Graphene-based liquid-gated transistors for biosensing

Adrien Hugo

To cite this version:

Adrien Hugo. Graphene-based liquid-gated transistors for biosensing. Biological Physics [physics.bio-ph]. Université Grenoble Alpes [2020-..], 2020. English. NNT : 2020GRALI010 . tel-03083947

HAL Id: tel-03083947

https://theses.hal.science/tel-03083947

Submitted on 20 Dec 2020

THÈSE

Pour obtenir le grade de

DOCTEUR DE L'UNIVERSITE GRENOBLE ALPES

Spécialité : **Matériaux, Mécanique, Génie civil, Electrochimie**
Arrêté ministériel : 25 mai 2016

Présentée par

Adrien HUGO

Thèse dirigée par **Pascal MAILLEY**, Directeur de recherche, CEA-LETI,
et codirigée par **Thomas ALAVA**, Ingénieur de recherche, CEA-LETI

préparée au sein du **Laboratoire Composants et Micro-Capteurs**
et de **l'École Doctorale I-MEP2**

Capteurs biologiques à base de transistors graphène à grille liquide

Graphene-based liquid-gated transistors for biosensing

Thèse soutenue publiquement le **27 février 2020**,
devant le jury composé de :

Mme. Catherine VILLARD Directrice de Recherche, CNRS-Institut Pierre-Gilles de Gennes, Paris	Présidente du jury
M. Jose A. GARRIDO Professeur, ICN2, Barcelone	Rapporteur
M. Christian BERGAUD Directeur de Recherche, LAAS-CNRS, Toulouse	Rapporteur
M. Vincent BOUCHIAT Directeur de Recherche, CNRS - Institut Néel, Grenoble	Examinateur
Mme. Pascale PHAM Directrice de Recherche, CEA-LETI, Grenoble	Invitée
M. Thomas ALAVA Ingénieur de recherche, CEA-LETI, Grenoble	Encadrant de thèse
M. Pascal MAILLEY Directeur de recherche, CEA-LETI, Grenoble	Directeur de thèse

Remerciements

C'est avec une grande fierté que je regarde ces trois dernières années de thèse qui furent d'une incroyable richesse, tant sur les plans personnel que professionnel. Jamais je n'aurais imaginé apprendre autant au cours de cette formidable aventure, qui a grandement participé à faire de moi la personne que je suis aujourd'hui. Je ne peux qu'être reconnaissant envers toutes les personnes qui ont contribué d'une manière ou d'une autre à rendre cette expérience inoubliable.

Je voudrais particulièrement remercier mon encadrant, Thomas ALAVA, ainsi que mon directeur de thèse, Pascal MAILLEY pour m'avoir fait confiance à la fin de mon stage ingénieur et m'avoir donné l'opportunité de poursuivre avec cette thèse. Travailler avec vous aura été un vrai plaisir. Merci pour votre bienveillance, votre aide et vos conseils, votre bonne humeur et votre sagesse ! C'est avant tout grâce à votre soutient que j'ai pu m'approprier ce projet et continuellement faire face aux nombreuses difficultés. Je me sens chanceux et fier en regardant ce que nous avons accompli ensemble, merci infiniment à vous deux !

Je tiens à remercier les membres du jury qui ont aimablement accepté de juger la qualité de mes travaux. Je tiens particulièrement à remercier José GARRIDO ainsi que Christian BERGAUD de m'avoir fait l'honneur de rapporter mon manuscrit de thèse. Je tiens à remercier Catherine VILLARD d'avoir présidé cette soutenance. Je voudrais aussi remercier chaleureusement Vincent BOUCHIAT d'avoir participé à ce jury. Merci pour ta gentillesse, ta disponibilité, ainsi que toutes ces discussions extrêmement enrichissantes au cours de cette collaboration. Enfin, je remercie Pascale PHAM d'avoir bien voulu participer à cette soutenance et à la supervision de cette thèse au travers du CSI. Merci pour ta disponibilité, tes conseils ainsi que ta grande bienveillance.

Un grand merci à Juliette SIMON. J'espère que ce travail pourra te servir de fondations pour toutes les belles choses que tu arriveras à accomplir grâce à ta détermination et ta rigueur. Je te souhaite bonne chance et bon courage pour ta thèse ! Merci également à Madhav KUMAR, pour m'avoir épaulé et m'avoir apporté ton regard avisé sur mes travaux. Ce fut un plaisir de travailler avec vous deux !

Je tiens à remercier chaleureusement Vincent BOUCHIAT, Julien RENARD, Antoine BOURRIER ainsi que Riadh OTHMEN de l'institut Néel du CNRS et de

Grapheal, pour cette collaboration très enrichissante, ainsi que pour votre aide et votre contribution essentielle tout au long de cette thèse.

Je remercie toute l'équipe de la PTA pour sa disponibilité ainsi que son aide tout au long du développement du process de fabrication en salle blanche. En particulier, je tiens à remercier Thierry CHEVOLLEAU, Jean-Luc THOMASSIN, Martine GRI, Marlène TERRIER, Thomas CHARVOLIN, Nicolas CHAIX, Christophe LEMONIAS et Frédéric GUSTAVO.

Ces travaux n'auraient pas été complets sans le travail effectué par l'équipe de la PFNC pour les caractérisations AFM, Raman et XPS. Merci à Denis MARIOLLE et Denis ROUCHON, pour votre rigueur, votre gentillesse et votre enthousiasme ! Merci également à Olivier RENAULT.

Je voudrais exprimer ma gratitude à la DGA pour avoir financé cette thèse, et plus particulièrement Rose-Marie SAUVAGE pour avoir suivit ma thèse avec intérêt, bienveillance et gentillesse.

Je voudrais également remercier William DICHTEL et son équipe de l'université de Northwestern pour avoir fourni le tripode au cours de cette collaboration.

Je tiens à remercier toutes les personnes au CEA qui m'ont aidé de près ou de loin au cours de cette thèse, et plus particulièrement, Caroline COUTIER, Sébastien HENTZ, Guillaume JOURDAN, Marc GELY, Paul-Henri HAUMESSER, Han Zheng, Guillaume NONGLATON, Henri BLANC, et Christine COURTOIS.

Ces trois années n'auraient pas été aussi joyeuses sans toutes ces virées inoubliables et ces bons moments passés avec vous, Maxime, Fédérico, Gabrielle, Marc, Martial, Sam, Bogdan et Ibrahima ! Merci à vous !

Je tiens à remercier mes parents et ma famille pour m'avoir toujours soutenu dans mes choix tout au long de ces années.

Enfin, je te remercie du fond du coeur, Clémence, pour ton soutient infaillible et inconditionnel. Tu es une source inépuisable d'inspiration qui m'a toujours poussé à tirer le meilleur de moi-même. J'espère réussir un jour à te remercier à la hauteur de tout ce que tu m'as apporté. Si tu tombes, je tombe !

Contents

Appendices

Acronyms

Notation	**Description**
$\mathbf{(NH_4)_2S_2O_8}$	Ammonium persulfate.
AFM	Atomic Force Microscopy.
Ag	Silver.
Al	Aluminium.
Ar	Argon.
Au	Gold.
C	Carbon.
$\mathbf{CH_4}$	Methane.
CNTs	Carbon Nanotubes.
Cr	Chromium.
CTE	Coefficient of Thermal Expansion.
Cu	Copper.
CVD	Chemical Vapor Deposition.
DIW	De-Ionized Water.
DNA	Deoxyribonucleic Acid.
DOS	Density Of States.
EDL	Electrochemical Double-Layer.
EIS	Electrochemical Impedance Spectroscopy.

Notation	**Description**
$\mathbf{Fe(NO_3)_3}$	Iron nitrate.
$\mathbf{FeCl_3}$	Iron chloride.
FET	Field-Effect-Transistor.
GO	Graphene Oxide.
$\mathbf{H_2}$	Dihydrogen.
$\mathbf{H_2O_2}$	Hydrogen peroxide.
$\mathbf{H_2SO_4}$	Sulfuric acid.
$\mathbf{H_3PO_4}$	Phosphoric acid.
HF	Hydrofluoric acid.
$\mathbf{HNO_3}$	Nitric acid.
HOPG	Highly Oriented Pyrolytic Graphite.
IBE	Ion Beam Etching.
ICP	Inductively Coupled Plasma.
IPA	Isopropyl Alcohol.
KOH	Potassium hydroxide.
L	Length.
$\mathbf{L_{cont}}$	Contact length.
$\mathbf{L_t}$	Transfer length.
LOD	Limit of Detection.
N	Nitrogen.
$\mathbf{Na_2HPO_4}$	Disodium Hydrogen Phosphate.
$\mathbf{Na_2S_2O_8}$	Sodium persulfate.
NaCl	Sodium Chloride.

Notation	**Description**
NaH_2PO_4	Sodium Dihydrogen Phosphate.
NHS	N-HydroxySuccinimide.
Ni	Nickel.
O	Oxygen.
O_2	Dioxygen.
PBASE	1-PyreneButyric Acid N-hydroxySuccinimide Ester.
PBS	Phosphate-Buffered Saline.
PCB	Printed Circuit Board.
Pd	Palladium.
PDMS	Polydimethylsiloxane.
PEG	Polyethylene Glycol.
PMMA	Poly(methyl methacrylate).
Pt	Platinum.
PTA	"Plateforme Technologie Amont" (or upstream technological plateform).
QCM	Quartz Crystal Microbalance.
R_c	Contact Resistance.
R_s	Sheet Resistance.
rGO	Reduced Graphene Oxide.
RIE	Reactive Ion Etching.
RNA	Ribonucleic Acid.
SAM	Self-Assembled Monolayer.
SEM	Scanning Electron Microscope.
SGFET	Solution-Gated Field-Effect-Transistor.
Si	Silicon.
SIMS	Secondary Ion Mass Spectrometer.

Notation	**Description**
SiNWs	Silicon Nanowires.
$\mathbf{SiO_2}$	Silicon Dioxide.
SNR	Signal-to-Noise Ratio.
SPR	Surface Plasmon Resonance.
SWNT	Single-Walled Carbon Nanotube.
THF	Tetrahydrofuran.
Ti	Titanium.
TLM	Transmission Line Measurement.
TMAH	Tretramethylammonium Hydroxide.
US	Ultrasound.
W	Width.
XPS	X-ray photoelectron spectroscopy.
Y	Yttrium.

Introduction

Considering a worldwide ageing population and the growing need for an improved healthcare in emerging countries, the demand for point-of-care diagnostics represents a major field of applications for biosensors [1]. As an example, diabetes is considered as one of the greatest healthcare challenges, according to the World Health Organization [2], accompanied with the rise of cardiovascular diseases, and cancers [3]. An early and/or real-time robust detection of the biomarkers associated to these diseases is particularly crucial for establishing a diagnosis and an efficient treatment. The development of biosensing devices with advanced transduction and bio-recognition technologies is therefore among the greatest driving forces of the scientific research.

The development of highly sensitive biosensors has been supported by the rise of the microelectronic, enabling the production of integrated devices at high throughput and low cost. In particular, nano-fabrication technological progress over the last decades made possible the fabrication and integration of low-dimensionality material presenting superior properties compared to bulky materials, such as carbon nanotubes and silicon nanowires. The isolation of graphene, a 2D layer of carbon atoms forming a honeycomb-like lattic,e have stimulated the scientific community for its exceptional properties. Indeed, graphene is highly conductive, lightweight, flexible, transparent, mechanically robust, and shows a high specific area due to its atomic thickness. This last property is particularly appealing for the detection of charged biological species, making graphene a great candidate for highly sensitive biosensing applications. Combining the enhanced electrical sensitivity of the Solution-Gated Field-Effect-Transistor (SGFET) technology in liquid environment with the outstanding graphene electrical properties is therefore promising to impulse a new generation of highly sensitive biosensors.

In order to specifically detect the analyte of interest, it is first necessary to functionalize graphene with bioreceptors. The simple adsorption of bioreceptors to the graphene surface is not viable since it has been demonstrated that biological objects which function rely on their 3D structure (such as proteins or antibodies) are prone to denaturation [4]. Besides, the covalent grafting of bioreceptors to graphene disrupts its honeycomb lattice, resulting in a drastically reduced charge carrier mobility impeding the biosensor performance. However, molecules presenting an aromatic moiety, such as the widely used 1-pyrenebutyric acid N-hydroxysuccinimide ester (PBASE), can adsorb on graphene without deteriorating its properties thanks to π-π interactions. Using the N-hydroxysuccinimide (NHS) reactive moiety of PBASE, bioreceptors are then grafted to this linker and maintained in the vicinity of the graphene surface without deteriorating its electrical properties.

Although PBASE is widely used, it is not systematically demonstrated that bioreceptors remain functional after being immobilized at the graphene surface. This concern originates from the fact that PBASE lacks the ability to precisely control both the orientation and distance of the pendant receptor relatively to the graphene surface, due to the existence of a rotational degree of freedom. Consequently, bioreceptors can possibly stack onto graphene and lose their biological function and specificity toward the analyte. The "tripod" is a molecule binding multivalently to graphene, thanks to three pyrene feet. Designed and synthesized through our collaboration with Dichtel's group from Northwestern university, this linker was demonstrated to project any active functionality away from the surface and form a predictable and robust self-assembled monolayer (SAM) on graphene [5].

Thesis objective & Outline

Combining a material with exceptional properties, with a simple yet highly sensitive biosensor architecture and an innovative non-covalent functionalization method, the objective of this thesis consists in proposing a first proof of concept of a tripod-functionalized graphene-based SGFET for highly sensitive biosensing applications.

The first chapter will first provide a brief overview of the vast world of biosensing, and detail the motivations for using graphene as an efficient transducer material. From the description of graphene and its exceptional properties, to the integration into SGFETs, and the non-covalent functionalization necessary for transforming devices into biosensors, the scientific knowledge and state of the art necessary to the comprehension of this work is also presented.

In order to achieve the objective, it was first necessary to establish a SGFET fabrication process in our clean-room facilities. As it will be recursively mentioned through this manuscript, graphene is highly sensitive to its environment. A non-optimized graphene transfer and device fabrication process are typically sources of reduced and highly variable sensor performance. Efforts were first dedicated to establish a stable and reproducible fabrication process to develop a robust SGFET platform. This process is presented in the second chapter, along with different fabrication methods which were explored during this thesis.

The topological and chemical nature of the surface contamination induced by the fabrication process, and the resulting impact on the graphene properties was assessed through a set of AFM, XPS and Raman characterizations conducted at each step of the protocol. The characterization of the fabrication process is presented through these experiments in the third chapter.

Before conducting biosensing experiments, the as-fabricated sensors were first electrically and electrochemically characterized in air and liquid environment respectively. Along with the developed experimental setup, these results are presented in the fourth chapter.

Finally, the non-covalent functionalization of the developed graphene-based biosensors, and the first biosensing experiment carried out in order to demonstrate a first proof of concept are presented in the last chapter.

Chapter 1

State of the art

An introduction to the complex world of biosensing will be presented in this first chapter. After describing the principle of a biosensor and its different elements, the discussion will present majors transduction techniques through some examples of label-free biosensors. In the context of a race toward higher performance, the development of biosensors based on nano and low-dimensionality materials has yielded promising results. We will unveil these results as well as tackling the challenge that have hindered their successful commercialization to this day. The potential of graphene and its exceptional properties, as a new transducing material alternative will be presented and details will be given on the promising application of the SGFET for biosensing in liquid. Finally, theoretical aspects about SGFET gating mechanism, electrochemical properties and functionalization of graphene will provide the context and motivations behind this work.

1.1 Introduction to biosensing

In 1962, Clark and Lyons published the development of the first "enzyme electrode" prototype for the detection of glucose [6]. Their invention consisted in immobilizing glucose-oxidase enzymes on a "Clark" electrode, previously developed for dioxygen (O_2) monitoring [7]. In presence of the enzyme and O_2, glucose is oxidized into gluconic acid and hydrogen peroxide. The concentration of glucose in the blood sample is indirectly determined by monitoring the O_2 consumption. This ingenious system is nowadays considered as the very first biosensor, and is essential for monitoring abnormal levels of blood glucose of people suffering from diabetes. Since this pioneer work, the development of biosensing devices with advanced transduction and bio-recognition technologies has been at the junction of multiple scientific domains, leading to numerous applications in food processing [8], environment [9], pharmacology [10] or biodefense [11].

1.1.1 Principle of a biosensor

A biosensor is defined as a self-contained analytical device, providing a selective and quantitative response upon a biological detection event [12] and combining the following elements (Figure 1.1):

- a bio-recognition (or bioreceptor) layer, that binds specifically the target analyte in the vicinity of the sensor surface
- a transducer element that converts the physical binding event (which typically leads to a physico-chemical change such as molecular flux, ionic balance, heat of reaction, bioluminescence or absorbance, pH shift, chemical product...) into a measurable signal
- a signal processing unit for signal amplification and analysis

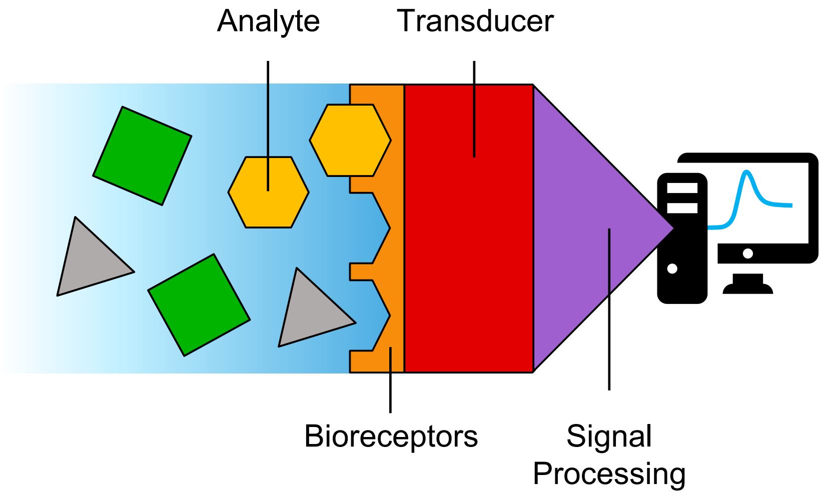

Figure 1.1: Schematic of the biosensor principle.

The performance of a biosensor for a given application is dictated by various parameters, the most important feature being the selectivity. This attribute represents the sensor's ability to detect a specific target in a mix of different analytes, while recognizing no other. The sensitivity and the limit of detection (LOD) are also key parameters, defined respectively by the transduced signal intensity upon a variation of the analyte concentration, and the minimal amount of analyte that can be detected. In addition, fast response time, high reproducibility, stability, linearity, reversibility, biocompatibility, portability, robustness, regeneration and low cost are the requirements that a biosensor must address.

The following discussion will be focused on affinity-based biosensors, which detection relies on the binding of a target analyte with a sensor-bound bioreceptors, leading to the formation of a biomolecular complex without any chemical (and eventually structural) modifications. The case of catalytic biosensors for which the analyte is converted into a product thanks to enzyme receptors will not be addressed here.

1.1.2 Biorecognition element

The biorecognition element provides the specificity of the biosensor. The choice of the receptor type obviously depends on the targeted analyte, but also on several parameters such as the stability, the sensor operational conditions, the cost and most importantly the affinity between the receptor and the analyte. Several classes of biorecognition elements exists: protein receptors, antibodies, nucleic acids and aptamers.

1.1.2.1 Protein receptors

Proteins are macromolecules consisting of polymer chains of amino acids arranged in a specific 3D configuration, called polypeptides, performing numerous cellular functions (structural, transport, regulation, signalisation, motor function) within organisms [13]. Each type of protein correspond to a defined amino acid sequence which dictates the protein folding into a unique four levels 3D structure (Figure 1.2): the primary structure corresponding to the polypeptide chain molecular level, the secondary structure consisting of local patterns stabilized by hydrogen bonds (α-helix, β-sheets and turns), and the tertiary structure revealing the overall shape of a single protein (stabilized by the formation of an hydrophobic core, hydrogen and disulphide bonds). Eventually, several proteins can form a complex called the quaternary structure.

The structure of proteins is composed of "domains", which are stable, folded, and compact 3D structures existing independently of the rest of the polymer chain. These domains can take the form of "pockets" or "depression" on the molecular surface and serve as anchoring site for binding other molecules. The interaction strength between a receptor (R) and a binding molecule, or ligand (L), is associated to the dissociation constant $\mathrm{K_D}$ of the reversible reaction between R and L [14]:

$$[R] + [L] \underset{\mathrm{k_{off}}}{\overset{\mathrm{k_{on}}}{\rightleftarrows}} [RL] \implies K_D = \frac{[R]\,[L]}{[RL]} = \frac{k_{off}}{k_{on}} \tag{1.1}$$

where k_{on} and k_{off} are the association and dissociation rate constant.

K_D is commonly used to describe the affinity between a receptor and a ligand: the lower K_D, the higher the affinity. In particular, the binding affinity is mediated by the protein tertiary structure, since binding interactions between the binding site and the ligand are ruled by intermolecular forces, such as ionic bonds, hydrogen bonds and Van der Waals forces.

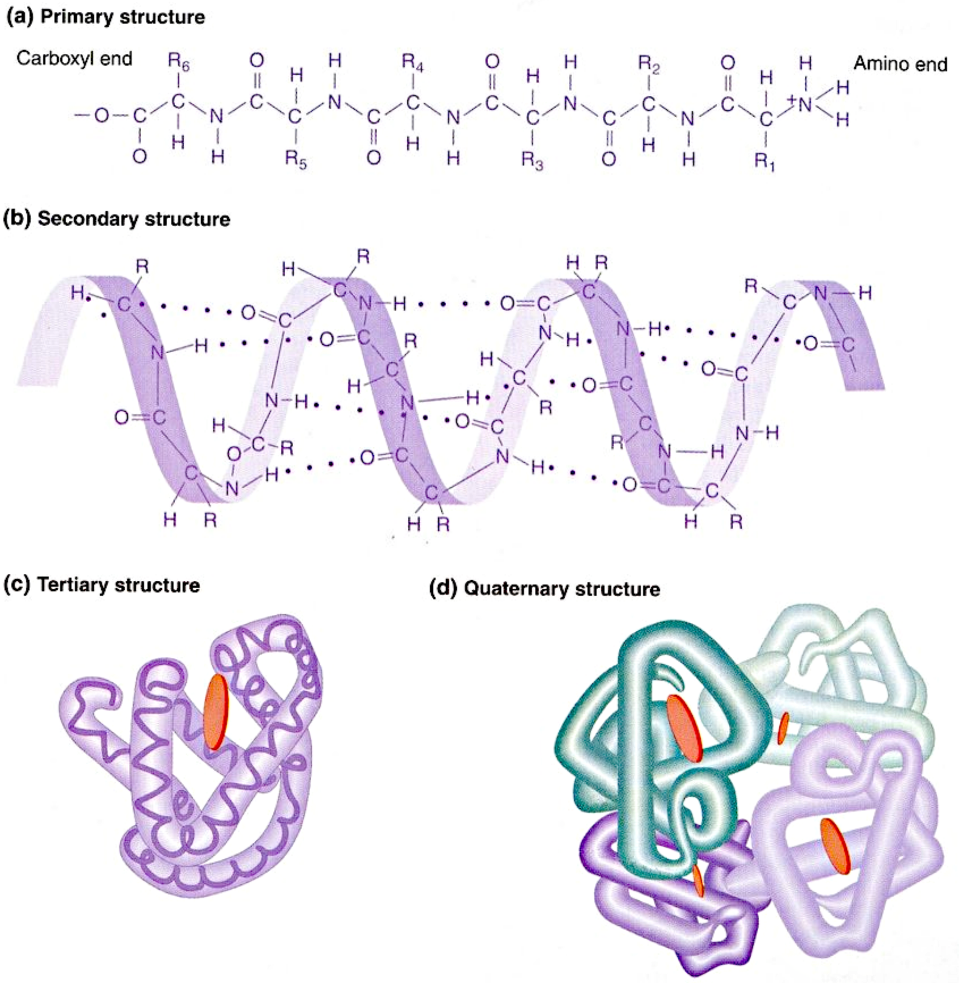

Figure 1.2: The four structure levels of a protein (from [13]).

The protein-ligand interaction is at the core of several biological processes. For instance, membrane proteins are involved in cell signalling and signal transduction: such proteins act as receptors, binding specific molecules and inducing a biochemical response to the cell they are attached. Another important function of proteins is transport: they bind with a high affinity to small biomolecules and transport them to a specific location of the organism (for example, the haemoglobin transports oxygen from the lungs to the organs and tissues). The role of recognition proteins, such as lectin, is to bind highly specifically to sugar groups of other cells or proteins. They are also involved in the binding process of bacteria or viruses with their target.

The protein-target binding affinity can reach the femtomollar level [15], which is the diagnostic level of significance for number of cancer biomarkers [16]. Using protein-receptors as biorecognition element of a biosensor is therefore attractive for highly sensitive biosensing and was used for various applications such as glucose sensing [17], artificial olfaction [18], drug development [19] and detection of cancer biomarkers [20].

1.1.2.2 Antibodies

Antibodies are Y-shaped proteins (Figure 1.3), also called immunoglobulins, produced during the immune response of an organism to neutralize pathogen such as bacteria or viruses. Antibodies are complex and large biomolecules (typically 10–15 nm), made up two heavy and light chains, and capable of binding specifically a unique type of antigen thanks to their variable "Fab" fragment. The tip of the "Fab" fragment shows a defined sequence of 5 to 10 amino acids constituting the binding site called paratope. Analogous to a lock, the paratope binds specifically the epitope on an antigen corresponding to a key. The constant fragment "Fc" is common to a given type of immunoglobulin and doesn't take part into the antigen recognition by the antibody, but binds with various cell receptors and proteins to activate the immune system.

Biosensors using antibodies as biorecognition element are called immunosensors, the most common being the enzyme-linked immunosorbent assay (ELISA), first described by Engvall and Perlmann in 1972, and widely used for HIV related antigen detection [21]. Antibodies suffers from costly isolation and production procedures, with binding capacities strongly dependant on assay conditions (temperature, pH). Sensor reuse is limited due to the generally irreversible antigen-antibody interaction, however, their implementation is simple and immunoassays are highly sensitive. Typical applications consisting in the detection of tumoral markers, pathogens, toxins and pollutants, and food analysis, have been reviewed in [22–24].

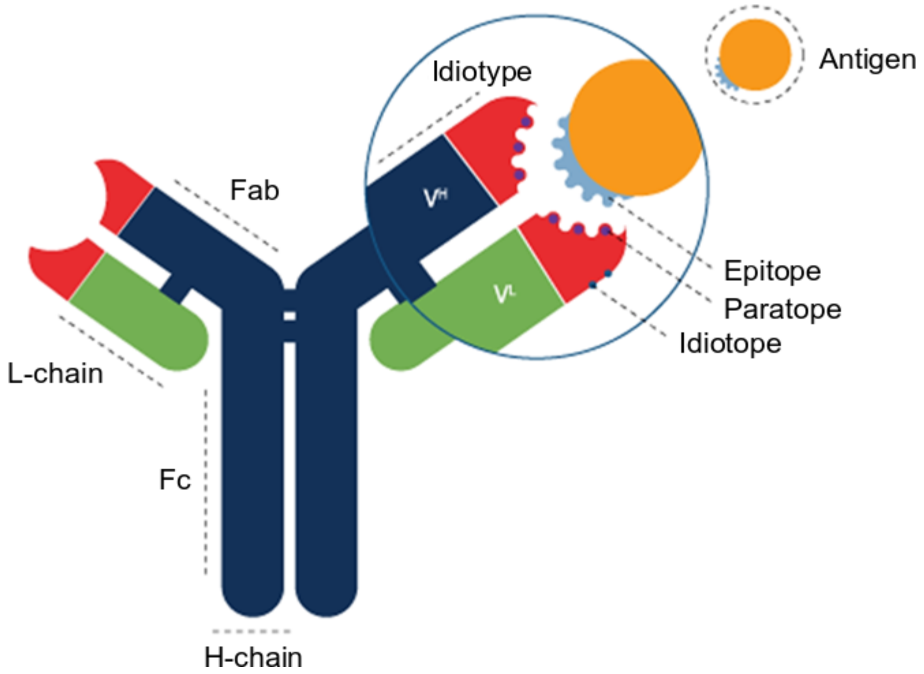

Figure 1.3: Schematic of the antibody structure (adapted from [25]).

1.1.2.3 Nucleic acids

Nucleic acids are biomolecules essential to all known forms of life, conveying the genetic information necessary for the development of all organisms. This overall name covers two types of biopolymer: deoxyribonucleic acid (DNA) and ribonucleic acid (RNA). They consists of polymer chains of nucleotides units arranged into a unique sequence. A nucleotide is composed of a nucleic base (adenine, guanine, cytosine in addition to thymine for DNA and uracil for RNA), a sugar group and a phosphate group. Alternating phosphate and sugar groups interact through phosphodiester bonds, constituting the sugar backbone of a single strand (Figure 1.4). While RNA is generally single stranded, DNA forms a double helix, resulting from the complementary base pairing between two single strands. This process, known as hybridization, is highly selective since a single base mismatch between two hybridized strands can strongly destabilize the complex [26]. This concept is exploited in genosensors, where immobilized single strand probe sequences are used as bioreceptors, binding complementary sequences as target analyte. The hybridization event is then converted into an electrical measurable signal by the transducer. Genosensors are highly sensitive and specific, attracting much interest in a wide range of applications such as gene sequencing [27], forensic [28], detection of pollutants [29], food analysis [30] or drug development [31].

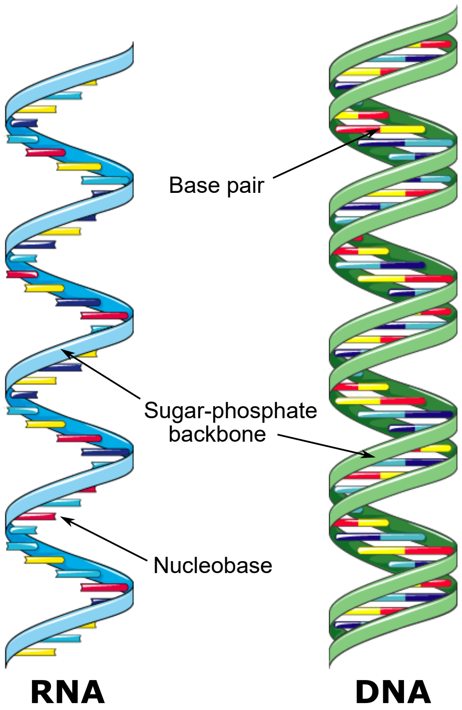

Figure 1.4: Deoxyribonucleic acid (DNA) & ribonucleic acid (RNA) structures.

1.1.2.4 Aptamers

Aptamers are oligonucleotides (short sequence of folded single stranded DNA or RNA) or peptides molecules capable of binding specifically a wide range of target analytes with nanomolar affinity. The binding interaction between the aptamer and the analyte results from physico-chemical interactions (electrostatic, hydrogen bonds, hydrophobic and dipolar). Upon folding, the single strand adopts a tertiary structure composed of linear parts resulting from base pairing, and constrained loops of bases interacting with the complementary shapes of the target binding site (Figure 1.5).

Aptamers can be in-vitro engineered through the SELEX method (systematic evolution of ligands by exponential enrichment) developed by Ellington [32] and Tuerk [33] in 1990. The aptamer probe is selected from a random library of $\sim 10^{15}$ sequences, by the iteration of the following successive steps: target binding, removal of unbound oligonucleotides, elution, amplification and purification steps. These variation, selection and replication steps are repeated until the desired affinity between the target and the probe is obtained. As opposed to antibodies which development depends on the immunization of animals and their production on cell culture techniques, aptamers are easily chemically synthesized, at low cost, and can be produced against a variety of target comprising amino acid, peptides, proteins, viruses, whole (or part of) cells, bacteria, metal ions and highly toxic target [34]. Aptamers are also more stable and can be reversibly denatured with temperature, allowing the regeneration of the sensor aptamer receptors after target binding.

Owing to their exceptional structure and properties, aptamers have been used in numerous biosensor applications including therapeutic [35], bio-imaging [36], food and water contaminant detection and therapy monitoring [37].

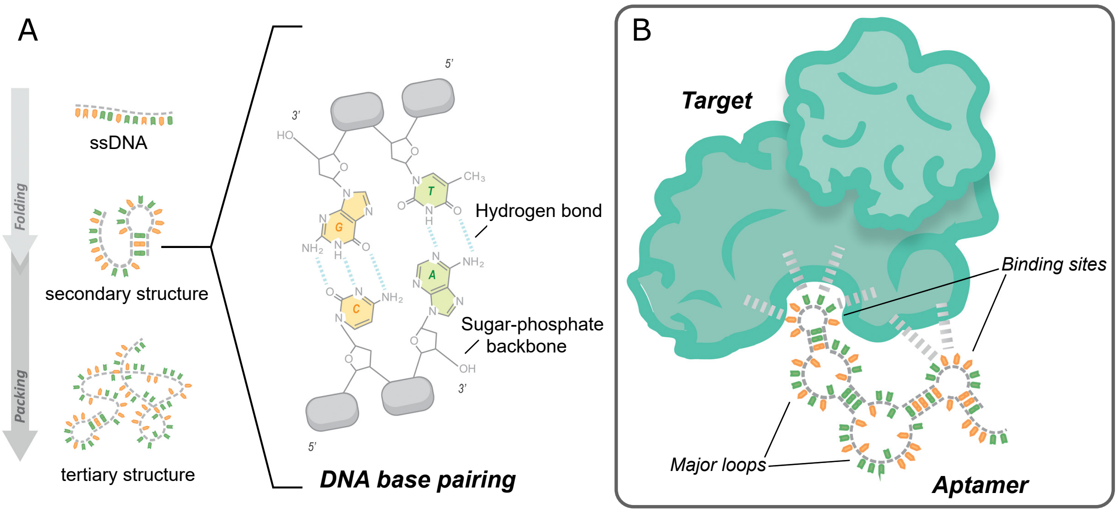

Figure 1.5: a) The aptamer structure resulting from base pairing, b) Aptamer binding the target through hydrogen bonding and dipolar interactions. (adapted from [38]).

Different types of bioreceptors were reviewed in the previous subsection, highlighting the need for a specific target immobilization at the sensor surface. However, a physical binding event do not induce a direct transformation of matter, but a physico-chemical property variation of the sensor environment. In order to detect the analyte binding, two different strategies can be adopted. Using labelling techniques, markers (such as enzymes or fluorophores) added to the system provide a measurable transformation of matter amplifying the signal. On the other hand, label-free techniques allow to directly probe the physico-chemical property variation of the sensor environment induced by the binding event. These two strategies, presented in the next subsections, offer different advantages and also drastically impact the sensor architecture, the transduction mechanism, measurement complexity, the sensor readout and performance.

1.1.3 Labelling techniques

Detecting an analyte in low abundance is far from being straightforward, irrespectively of the bioreceptor or transduction technique involved. Using labelling techniques, the signal and the sensitivity can be enhanced to reach satisfying detection levels. Labelling consists in the attachment of a foreign molecule to the target to enhance or induce a new physico-chemical property involved in the transduction mechanism. The most common technique is fluorescence labelling: fluorescent probes (protein [39], quantum dot [40], organic dyes [41]) are added to the target (either directly by covalent bonding or indirectly, by using an antibody label) allowing the bound target to be optically detected. This technique is inexpensive, simple and hazard-free but limited by the non-specific interactions, pH and temperature dependant probes quenching. Radioisotope labels offer robust and reproducible protocols, low LOD ($\sim$ pg.mL^{-1} [42]) and specificity but requires special precautions and licensing since radioactive substances are used. On the other hand, electrochemically active probes such as enzymes (horseradish peroxidase [43], alkaline phosphatase [44]) or metallic nanoparticles such as gold (Au) [45] or silver (Ag) [46]) act as catalyst, enhancing the electrochemical signal of the sensor. Enzymes always require a mediator added in the solution or immobilized onto the electrode surface to accelerate the electron transfer [47]. On the other hand, metallic nanoparticles require acidic conditions which can be a limitation depending on the application.

Issues regarding labelling biosensors development can therefore be pointed up: introducing a label can modify the target or the receptor, disturb the ligand-receptor interaction and not be representative of the initial specificity. This issue is particularly problematic for small molecules, which can undergo drastic physico-chemical modifications when bound to a larger molecule [48]. Moreover, labelling requires time-consuming, expensive and complicated additional experimental steps, procedures and equipments, drastically impeding real-time monitoring or field measurements.

1.1.4 Label-free biosensors: a variety of transducers

In label-free techniques, the analyte binding event induces a detectable physico-chemical property variation (mass, refractive index, electrostatic charge, steric hindrance, visco-elastic...) in the vicinity of the transducer, without any label, providing a simple, cheap, and real-time measurement. For the aforementioned reasons, label-free techniques have been preferred to label-based biosensors, since the sensing information is more accurate and closer to in-vivo conditions. However, the sensitivity and LOD of such biosensors might be lower since the signal is not amplified. In order to improve this performance without using labels, technological progress has been focused on developing highly sensitive transducing techniques.

1.1.4.1 Mechanical and optical transducers

The commercialization of the BIAcore system in 1990 by Pharmacia Biosensor was one of the major breakthrough in the development of label-free biosensors [49]. This system is based on the surface plasmon resonance (SPR) optical transduction, consisting in the resonant oscillation of conduction electrons at the interface between a dielectric (the sample) and a thin metal layer (typically gold) deposited onto a prism. When the oscillating electrons, called plasmons, are excited by an incident light satisfying wavelength, incident angle and polarization coupling conditions, an evanescent wave is created and a sharp decrease of the reflected light intensity is observed [50]. The underlying physical principle of SPR biosensors is the local variation of the refractive index at the metal surface, due to the target binding the immobilized bioreceptors. Since a variation of the refractive index induces a shift of the resonant incident angle proportional to the density of analyte detected, the sensor can be operated by monitoring the resonant incident angle shift (Figure 1.6.a). SPR is a very powerful technique, enabling real-time measurement of biomolecular interactions with high sensitivity for binding affinity monitoring [51], DNA strand separation [52] or mutation in proteins [53].

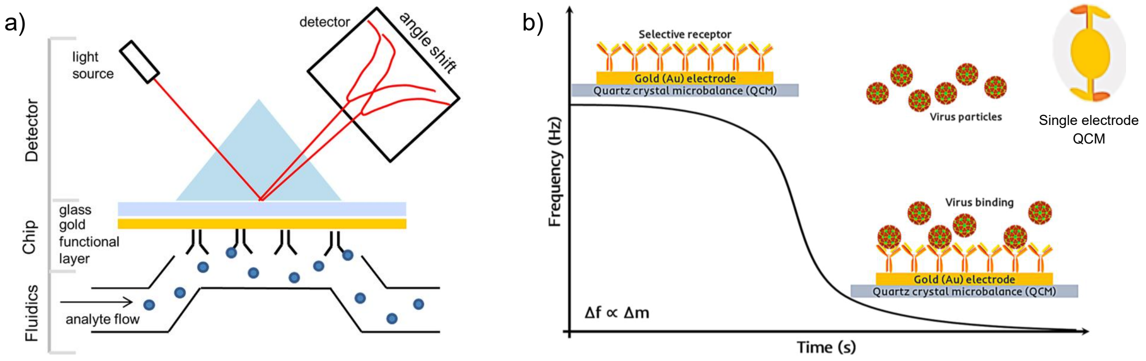

Figure 1.6: a) Principle of a SPR biosensor (adapted from [54]), b) Principle of a quartz crystal microbalance (QCM) biosensor and single electrode QCM cell as inset (adapted from [55])

An other major class of label-free biosensors is based on the mechanical transduction of oscillating resonators that can be achieved through piezoelectric effect. In particular, the QCM is a nanogram sensitive technique relying on the measurement of mass per unit area variations. An alternative electric field is applied to a quartz sandwiched between two electrodes, inducing expansion and contraction of the crystal lattice. The resonance frequency of the quartz is directly related to its thickness: the thinner the quartz, the higher the resonance frequency. In particular, Sauerbrey demonstrated in 1959 [56] that a resonance frequency variation is linearly related to the mass adsorbed on the quartz. His theoretical demonstration showed that is was possible to use the QCM as a mass scale. Later on, QCMs were used as biosensors [57], by monitoring the resonance frequency shift induced by the analyte binding to bioreceptors immobilized at the quartz surface (Figure 1.6.b). This technique has demonstrated its potential in various applications, including virus detection [58], interactions with disease related biomolecules [59], detection of cancer markers [60] or volatile compounds [61].

Nonetheless, these two canonical techniques present major disadvantages regarding integration. While very fast analysis time and high throughput by multiplexing approaches are achieved with the SPR, typical LOD values lie in the nanomolar range without labelling, far beyond the femtomolar range required for the detection of cancer biomarkers [16]. The QCM, on the other hand, is limited in terms of sensitivity, multiplexing and integration since it requires bulky instruments predominantly addressed to laboratory analysis. Finally, their cost per unit is a severe limitation for a successful industrialization.

Sensitivity and costs issues have been partially resolved by the collective fabrication of micrometric/nanometric devices at the wafer scale using techniques developed by the semiconductor industry. In particular, micro and nano electromechanical systems (MEMS/NEMS) benefit from both improved mass resolution and sensitivity due to their reduced size. These systems mostly consist of a micro/nano cantilevers that can be operated in two modes: in the static deflection mode, analyte binding on one side creates an unbalanced surface stress resulting in the cantilever measurable deflection (by optical, piezoelectric or capacitive read-out systems [62]), while in the dynamic (or resonant) mode, the increased mass induces a decrease of the resonance frequency in a similar fashion than the QCM. Both techniques show very high sensitivity in liquid, in the order of 100 pmol for an analysis time below one hour as reviewed by Arlett *et al.* [16]. Visco-elastic effects can be also probed, providing complementary and rich information during measurements [62–64]. However, the highly complex fabrication greatly influences the device performances and robustness, and the non-homogeneous residual surface stress results in a poor reproducibility.

Alternatively, various types of label-free biosensors based on optical transduction have been developed, such as optical ring resonators [65], fibres [66], wave-guides [67] or photonic crystals [68] (Figure 1.7). Similarly to SPR, in these techniques involving a coupling between the incident light and an optical transducer, target binding induces a shift in refractive index measured by a variation of the device optical resonant frequency. While the LOD of such biosensors can reach the picomolar limit [16, 69, 70], the optical transduction still requires complex experimental setups, including lasers which integration into lightweight and portable sensors can be challenging.

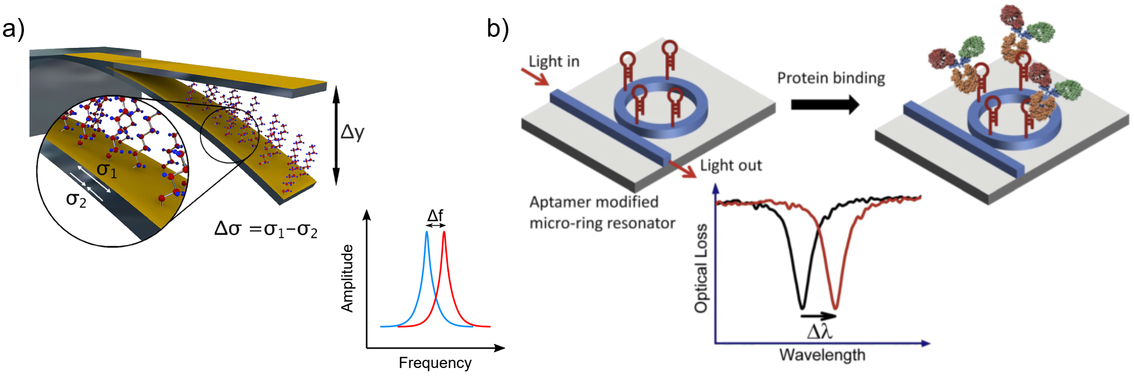

Figure 1.7: Principle of a) a micro-cantilever biosensor (adapted from [71]) and b) a ring optical resonator biosensor (adapted from [72]).

1.1.4.2 Electrochemical transducers

A few examples of optical and mechanical transduction techniques were discussed in the previous subsections. These techniques involved the transduction of the biological binding event into a final electrical measurable signal, thanks to variations of an intermediate physico-chemical property (mass, refractive index...). Electrochemical transducers provide a conversion of the biological event *directly* into an electrical signal. These transducers are therefore highly promising, mostly due to their simplified setup, for making lightweight, inexpensive and easily integrable biosensors.

(Volt)Amperometry

Among the existing electrochemical transduction techniques, the amperometry, which development started with the invention of the glucose sensor by Clark and Lyons (section 1.1), is the most widespread and commercially successful.

Amperometry is based on the measurement of the current resulting from the electrochemical oxidation or reduction of an electroactive species at the surface of a working electrode (sample), held at a constant potential with respect to a reference electrode. The bulk analyte concentration is deduced from the measured current. A subclass of widely used amperometric methods, referred under the term "voltametry", comprises different techniques consisting in scanning the potential over a set potential range. Such dynamic measurements are sensitive to interfacial processes and carry kinetics information. However, a large majority of affinity-based amperometric biosensors use secondary enzyme [73] or aptamer labels [74], since antibodies and most proteins doesn't naturally present a redox catalytic site electrochemically active in the potential range of measurement [75]. The amperometric detection is well suited to label-based sensors in which a current is generated. But as already discussed, labelling is a time-consuming and complex process. Instead, the label-free detection of an analyte by amperometry requires to modify the sensor surface, in order to enhance the charge transfer between the target and the substrate. Typical surface modifications consists in a 2D modification of the transducer surface using SAM [76,77].

Electrochemical Impedance Spectroscopy

Electrochemical impedance spectroscopy (EIS) is a powerful technique for probing the interfacial impedance of an electrochemical system. This method consists in measuring both the amplitude modulation and phase shift, between a small amplitude AC voltage input and the resulting current output. A variety of electrochemical phenomena inducing a dielectric constant or conductivity variation can be probed over a wide range of frequency, with or without an electrochemically reactive probe. In particular, it is possible to assess surface property modifications solely induced by the analyte binding at the sensor surface. Thus EIS is a technique very well suited for label-free biosensing applications, being richer in information, versatile (since not limited by the choice of the recognition element) and more sensitive than amperometric methods. Indeed, while typical LOD values are in the range of 0.01–100 ng.mL^{-1} for label-free amperometric biosensors [78], the LOD range of impedimetric biosensors is typically 3 order of magnitude lower [79].

BioFET

Field-Effect-Transistor (FET)-based biosensors (or BioFET) is a class of biosensors sensitive to surface potential variations induced by target binding. Originally, the first BioFET, called ISFET (for Ion-Sensitive Field-Effect-Transistor), was introduced by Bergveld [80]. It is derived from the MOSFET (Metal-Oxide Field-Effect-Transistor) structure which is considered at the core of modern electronics. An ISFET consist of a p-doped silicon (Si) substrate with two n-doped regions (source and drain) separated by a channel covered with a dielectric material (typically silicon dioxide (SiO_2)) (Figure 1.8.a). The transistor is operated by applying a positive gate potential between a reference electrode (immersed in the solution) and the Si bulk substrate, which creates a depletion region in the channel, electrically bridging the source and drains. When a potential difference is applied between the source and drain, mobile charge carriers (here electrons) flow through the channel. The channel current is modulated by the electric field developed across the device, between the gate and the substrate (Figure 1.8.b). In particular, charges at the dielectric surface alter the electric field, shifting the potential experienced by the transistor channel, thus modulating the output current (Figure 1.8.c). The ISFET is therefore a device transducing a surface charge variation into a current modulation, making it a practical application for pH sensing. Indeed, in aqueous solutions, the dielectric surface hydrolyses into ionizable sites (OH groups) capable of releasing or binding to H^+ ions, altering the interface potential as a function of pH.

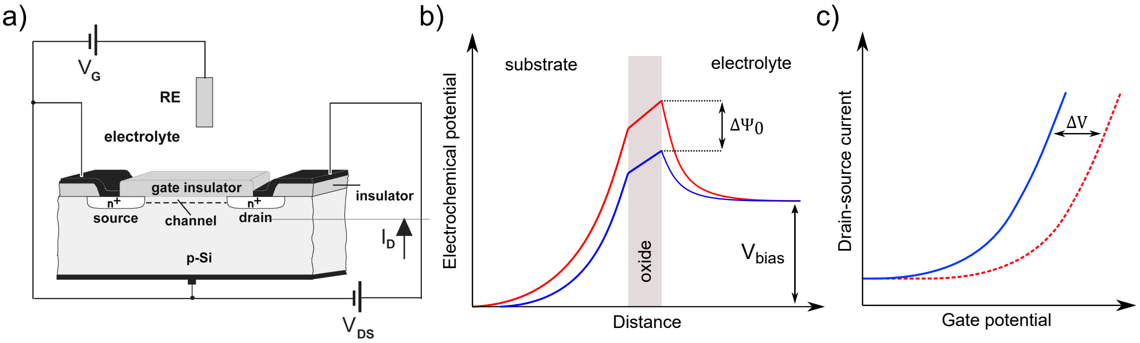

Figure 1.8: a) Structure of the ISFET (from [81]), b) Diagram of the potential distribution across the device structure (adapted from [82]) and c) Transfer curve of the ISFET showing the pH effect.

Since this structure is highly sensitive to any electrical interaction at the dielectric/solution interface, it can serves as a biosensor when coupled to a biorecognition element specifically immobilizing biomolecules at the sensor surface. The ISFET is therefore at the root of a variety of BioFETs, classified as a function of the biorecognition element they used: the EnFET (enzyme) for glucose [83], urea [84] and penicillin sensing [85], the ImmunoFET (antibody) for protein detection [86] or the DNA-FET (or GenFET) for the direct detection of DNA hybridization [87, 88]. Finally, ChemFET designates any ISFET modified with an ion-selective membrane for the detection of other ions than H^+, for example used in blood electrolyte monitoring [89].

These MOSFET-derived FETs technologies largely benefit from their compatibility with modern complementary metal-oxide semiconductor (CMOS) processing techniques, which provide advantages of large scale manufacturing and the possibility to integrate such devices in electronic circuits and systems. With the miniaturization of MOSFET devices, the development of nano-sensors based on low-dimensionality and high surface/volume ratio transducer materials has emerged as the next generation of biosensors.

1.1.5 Nano & low-dimensionality materials for highly sensitive biosensors

1.1.5.1 Carbon nanotubes

The rediscovery of carbon nanotubes (CNTs) by Sumo Injima in 1991 was a major breakthrough in the development of high performance biosensors [90]. Single-walled carbon nanotube (SWNT) are pseudo-1D cylinders made of sp^2-hybridized carbon atoms. Due to their nanometric size and peculiar atomic structure, metallic SWNT have exceptional properties. In particular, CNTs show a Young's modulus approaching 1 TPa, a thermal conductivity of $3500\,W.m^{-1}.K^{-1}$ at room temperature, and can carry a current density up to $10^9\,A.cm^{-2}$. In addition, SWNTs present a high specific surface area (or surface/volume ratio) due to their structure (typical lengths range from less than 100 nm up to a few centimetres, and typical diameters range between 0.8 and 2 nm) [91]. This last property is particularly appealing in biosensing, since the binding of biomolecules at the transducer surface can induce a large depletion or accumulation of carriers in the "bulk". Combining an excellent electrical conductivity and high specific surface area, SWNT-based FET biosensors therefore appeared as a promising solution for the highly sensitive and label-free detection of biomolecules in electrolytic environment.

Among the various methods developed to integrate single SWNT into FET devices, the Chemical Vapor Deposition (CVD) is the most widely used. Briefly, an hydrocarbon gas is decomposed at high temperature (600–1200 °C) in the presence of a metal catalyst deposited and patterned onto a substrate. Carbon atoms dissolve into the metal until the solubility limit is reached: dissolved carbon then precipitate and crystallize in the form of a cylindrical network, thus forming the nanotubes [92]. The metal catalyst is either dissolved using an acidic treatment, or covered by metallic contacts patterned on both ends of the nanotube to form the source and drain of the FET device (Figure 1.9.a). Finally, the SWNT is functionalized with bioreceptors for biosensing applications.

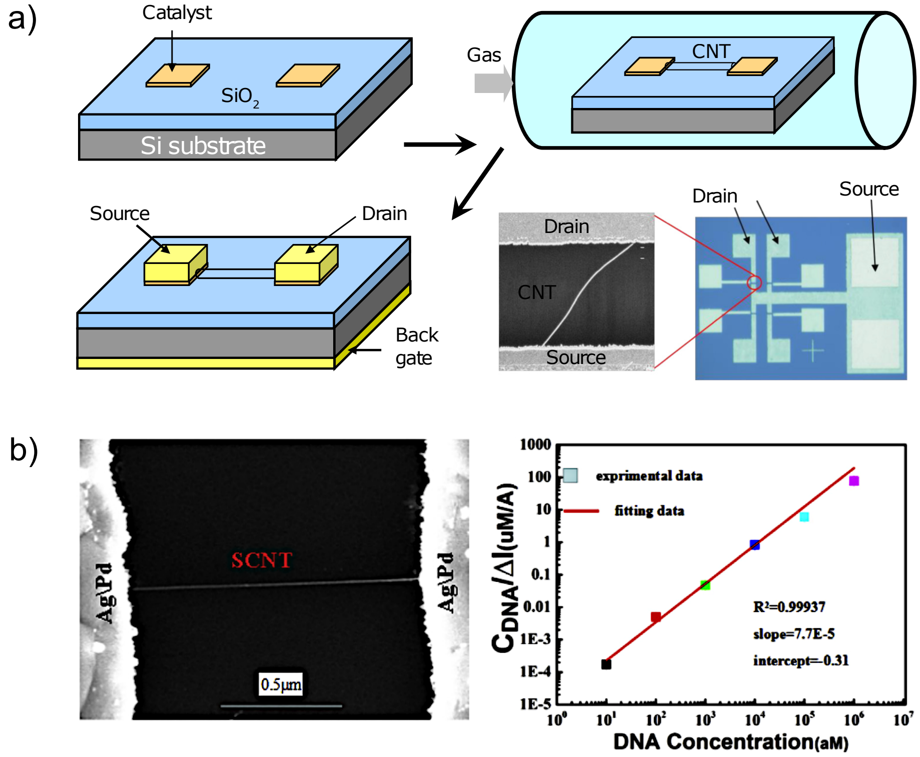

Figure 1.9: a) Fabrication process of a SWNT FET device by CVD (from [93]), b) Ultra-sensitive detection of DNA hybridization using a SWNT (adapted from [94]).

SWNT-based FET biosensors have been developed for the detection of prostate cancer biomarkers [95], cortisol stress biomarkers in saliva [96], or hepatitis C virus RNA [97], eventually reaching sub-pg.mL^{-1} LOD values. A striking application of highly-sensitive DNA hybridization detection using SWNT was recently demonstrated by Sun *et al.* , achieving LOD as low as 10 amol (Figure 1.9.b) [94].

Nonetheless, the commercialization of CNTs-based FET biosensors has been impeded by some limitations inherent to their fabrication, such as poor reproducibility resulting from nanotube chirality heterogeneity (leading to a mix of metallic and semi-conducting CNTs), diameter and growth yield [98,99]. In addition, the bottom-up integration of CNTs by CVD in complex device architectures is severely limited due to the harsh CNTs growth conditions. On the other hand, top-down fabrication approaches consisting in depositing networks of randomly distributed SWNTs overcome the non-reproducibility limitation thanks to statistical averaging over the CNTs properties [100]. However, using these structures remains challenging because CNTs networks require additional fabrication complexity to achieve a precise deposition on the substrate and a good CNT-CNT inter-connexion [101]. The performance of CNTs-based FET can be improved by horizontally aligning the SWNTs between the contacts [102] using Langmuir-Blodgett assembly [103], dielectrophoresis [104], or filtration [105]. Such post-process methods are however a limitation toward the scalable mass production of robust CNTs-based biosensors.

1.1.5.2 Silicon nanowires

Similarly to SWNT, other semi-conducting materials, such as silicon, have been used for the fabrication of highly sensitive nanoscale transducers using bottom-up approaches. Silicon nanowires (SiNWs) are grown catalytically by CVD, and into various shapes (round, square, or triangular) [106]. Subsequently, the nanowires can be suspended in an ethanol solution, deposited onto a substrate, and electrically contacted by patterning metallic contacts. The native oxide layer formed by exposing the nanowire to an oxygen environment provide a SiO_2 passivation layer which can be chemically modified for covalently grafting bioreceptors [107]. Even though high quality nanowires can be prepared using the bottom-up approach, the same limitations encountered for the production of SWNTs apply to SiNWs. Finally, the poor control of the surface chemistry of the native oxide layer results in a non-reproducible receptor grafting and variable sensor performance.

On the other hand, top-down approaches offer high reproducibility and control on the fabrication of SiNWs, benefiting from CMOS processes (e-beam lithography, ionic-implantation, and etching processes), and also from the availability of high quality silicon-on-insulator wafers. In particular, a typical process flow for FET device fabrication (Figure 1.10.a) include first a low-density doping of the top Si layer, followed by doping of patterned area to define the source and drain leads formed after an Reactive Ion Etching (RIE) step. The nanowire is subsequently patterned using e-beam lithography. Metallic contacts are evaporated and passivated before the SiNWs functionalization with bioreceptors. SiNWs produced from this top-down approach therefore overcome the property heterogeneity faced by nanostructured produced from the bottom-up approach. In addition, top-down fabrication techniques provide a better control of the SiNWs doping, a robust functionalization and allows to produce multiplexed arrays of SiNWs. Label-free SiNWs-FET biosensor thus achieved sensitivity levels down to $\sim 1\,\mathrm{fg.mL^{-1}}$ and short detection time ($<1\,\mathrm{min}$) for the detection of oral squamous cell carcinoma biomarkers in saliva [108], lung [109] and prostate cancer biomarkers [110] (Figure 1.10.b) among numerous examples reviewed in [111, 112].

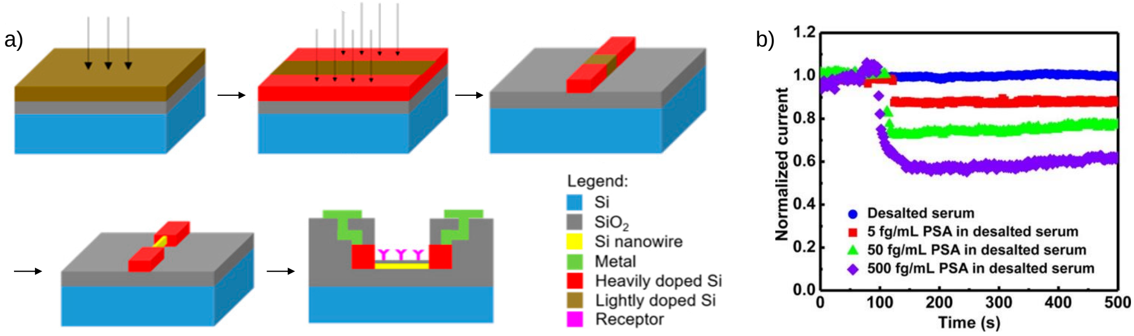

Figure 1.10: a) Top-down fabrication process of SiNWs-based FET label-free biosensor (adapted from [113]), b) Real-time detection of prostate cancer biomarkers with a SiNW-FET biosensor (from [110]).

1.1.5.3 How much do we need nano-miniaturization?

The implementation of nanomaterials as highly sensitive transducer elements led to an abundance of new device architectures (such as nanogap [114] or nanochannel [115]) combining a variety of nanomaterials. An exhaustive enumeration of all these technologies and a review of their performance cannot be produced here. We will focus on essential considerations arising from the miniaturization of biosensors to the nanometer scale, from both theoretical and practical perspectives.

As discussed before, the race toward nanosensing has been largely motivated by the enhanced sensitivity of structures with ultimate specific surface area, including nanowires and nanotubes. In fact, Shoorideh *et al.* [82] showed that it is the overall concavity of the structure, and the binding of biomolecules in concave area (corresponding to the regions between the nanowire/nanotube and the substrate) that increase the sensitivity, due to a weaker screening of the charged biomolecules by the ions in solution. When shrinking a nanowire width, concave area constitute a larger proportion of the total wire surface, which is partly responsible for the enhanced sensitivity. The sensitivity of such structures is therefore largely dependant on morphology at the nanometer scale which is only partially controllable by both top-down and bottom-up fabrication approaches.

Another important theoretical aspect is the sensor time response. Typically, the solution containing the analyte is supplied to the sensing area thanks to a microfluidic system. The solution flowing on top of the sensor channel at a given velocity, the diffusion of the analyte from the "bulk" solution to the sensor surface through concentration gradient, and the analyte-receptor binding/unbinding kinetics largely contribute to the sensor analysis time. In particular, reducing the sensing area to the nanoscale drastically reduces the bioreceptor density at the sensor surface, thus the number of biomolecules that can be captured from the solution [116]. For example, Squires *et al.* determined that a nanosensor with a 10 nm × 2 µm sensing area in a microfluidic channel with a 100 µm × 100 µm section would bind less than 1 % of the time to a *single* target molecule in a 10 fmol.L^{-1} analyte solution. On the other hand, a 50 µm × 50 µm sensor would bind 500 target molecules at any time at the equilibrium [117]. Experimentally, these theoretical sensor time response were not observed, which is attributed to the contribution of electrostatic effects enhancing the binding kinetics. Yet, these predictions shows that a nano sensing area is unfavourable in terms of number of biomolecules detected at low target concentration, which might represent a source of measurement uncertainty and stability issues.

From a practical point of view, using a microfluidic channel to supply such low concentration of analyte to a nanosensor any spoils miniaturization efforts. In particular, the optimal flow becomes close to zero when decreasing the sensing area toward the nanometer scale (Figure 1.11). Using nanofluidic systems might also be detrimental for the device integrity since the high hydraulic resistance requires a large input pressure. Finally, sub-micro optical lithography resolution needed for device fabrication are typically achieved using e-beam, which is expensive and time-consuming.

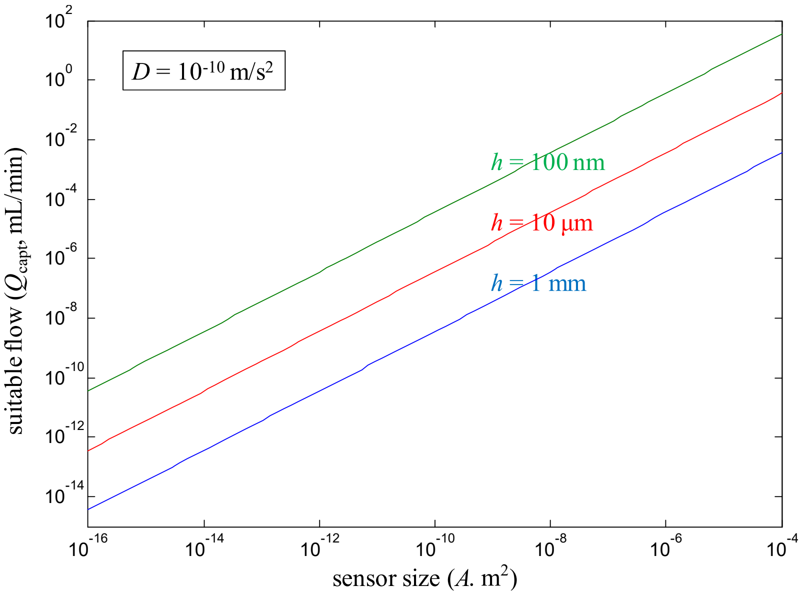

Figure 1.11: Optimal flow rate as a function of the sensor area and microfluidic channel height (from [118]).

To overcome the limitations associated to a reduced surface area, while still benefit from an enhanced sensitivity, an optimal transducer material should have a sufficiently large surface to fit within a micrometer channel and have no volume in order to exhibit a high specific surface area. A new class of single-layer materials, also referred as 2D materials, perfectly fit such profile. In particular, graphene, a 2D material composed of a single layer of carbon atoms, represents an highly promising candidate for addressing this challenge on building high performance biosensors.

1.2 Graphene for biosensing

Graphene, the last member of the carbon allotrope family comprising graphite, carbon nanotubes and fullerenes (Figure 1.12.a), is an atomically thin, single layer of carbon atoms. The existence of graphene was already predicted in 1947 [119], yet it was isolated for the first time by Geim and Novoselov only in 2004 [120]. Their method consisted in the mechanical exfoliation of a piece of highly oriented pyrolytic graphite (HOPG) using a scotch tape. As graphite is composed of graphene layers stacked and weakly coupled by van der Waals interactions, they could deposit graphene monolayers on a Si/SiO_2 substrate by repeatedly peeling graphite with a sticky tape. Isolating a 2D crystal at room temperature with such an ingenious technique came as a big surprise, since 2D thin films were predicted to be thermodynamically unstable at room temperature [121]. Geim and Novoselov received the Nobel prize in 2010 "for groundbreaking experiments regarding the two-dimensional material graphene", opening a new era of research on 2D crystalline materials.

1.2.1 Structure & properties

Graphene crystalline structure consists in carbon atoms arranged in a hexagonal network. Each carbon atom, in its ground state, possess four valence electrons distributed over a 2s, $2p_x$, $2p_y$ and $2p_z$ atomic orbital. The superposition of the 2s, $2p_x$, and $2p_y$ orbitals results in three sp^2 hybridized orbitals forming strong planar σ bonds between three nearest-neighbouring carbon (C) atoms. The remaining unmixed $2p_z$ orbitals each filled with one electron form π-bonds. These bonds extends perpendicularly from the graphene plane (Figure 1.12.b) and results in a delocalized π-electron cloud at the origin of exceptional conduction properties. In particular, the energy band diagram reveals a specific feature of the unique structure of graphene: the conduction and valence band intersect in some particular points in the reciprocal space of the hexagonal lattice (called K and K' points) (Figure 1.12.c). These points also coincide with the Fermi level of the neutral system in the energy spectrum, called the Dirac point. At the Dirac point, the density of states (DOS) is zero, and at the same time, there is no gap in the band structure. Therefore graphene is classified as a semi-metal, or a zero-gap semiconductor. In addition, the DOS increases linearly with the energy in the vicinity of the Dirac point: the interaction between the electrons and the honeycomb-like structure of graphene causes the electrons to behave as massless relativistic particles (like photons or neutrinos), travelling at a Fermi velocity only 300 times smaller than the speed of light. Combined with a ballistic charge transport over tens of microns [122], the transport properties properties exhibited by graphene are exceptional.

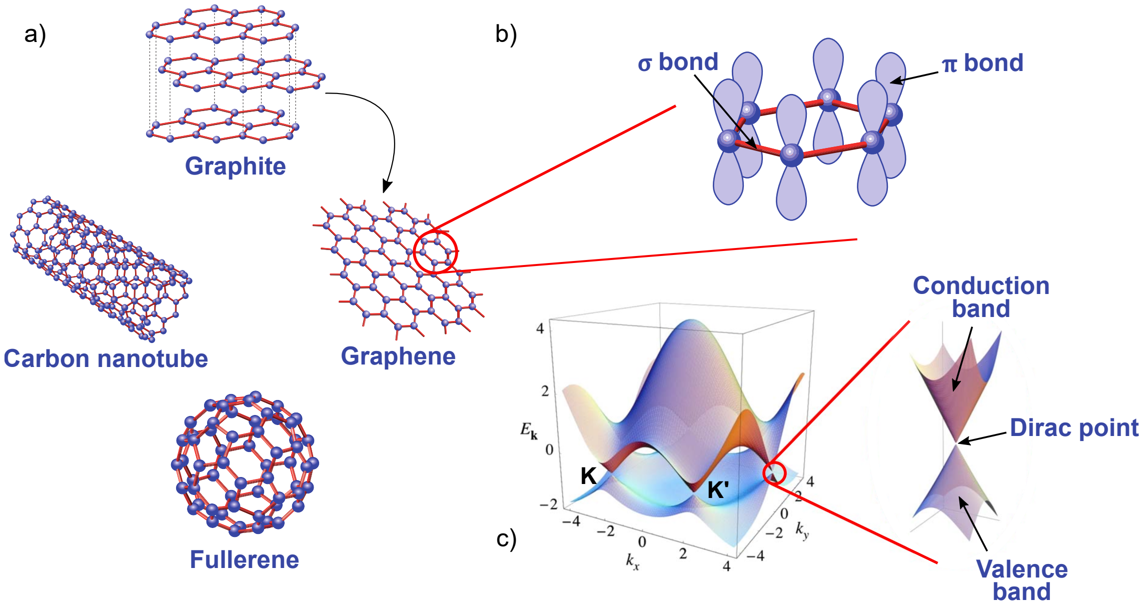

Figure 1.12: a) Carbon allotropes, comprising graphite, which is constituted of stacked graphene layers. Graphene can be seen as the building block of carbon nanotubes and fullerenes, b) σ and π bonds and c) band diagram of graphene (adapted from [123] and [124]).

For instance, while thin films of 3D semiconductors like Si suffer from surface roughness scattering that drastically reduces their charge carrier mobility when scaled down to sub-nanometer thickness, graphene presents mobility values several orders of magnitude higher (Figure 1.13.a), eventually reaching $5 \times 10^4\,\mathrm{cm.V^{-1}.s^{-1}}$ at room temperature [125], which is still far bellow the predicted intrinsic limit of $2 \times 10^5\,\mathrm{cm.V^{-1}.s^{-1}}$ [126]. Besides those superior electronic properties, graphene is also the thinnest (~0.4 nm) and strongest material ever tested, exhibiting a Young's modulus close to 1 TPa (similar to that of diamond) and a breaking strength of $42\,\mathrm{N.m^{-1}}$ [127]. Graphene has a theoretical specific surface area of $2630\,\mathrm{m^2.g^{-1}}$, much larger than that reported for carbon black ($\sim 900\,\mathrm{m^2.g^{-1}}$) or carbon nanotubes (from $\sim 100\,\mathrm{m^2.g^{-1}}$ to $\sim 1000\,\mathrm{m^2.g^{-1}}$), in addition to a thermal conductivity close to $5300\,\mathrm{W.m^{-1}.K^{-1}}$ [128] (approximately 10 times higher than copper of silver [129]) and an optical transmittance of ~97 % over the visible light spectrum [130] (Figure 1.13.b).

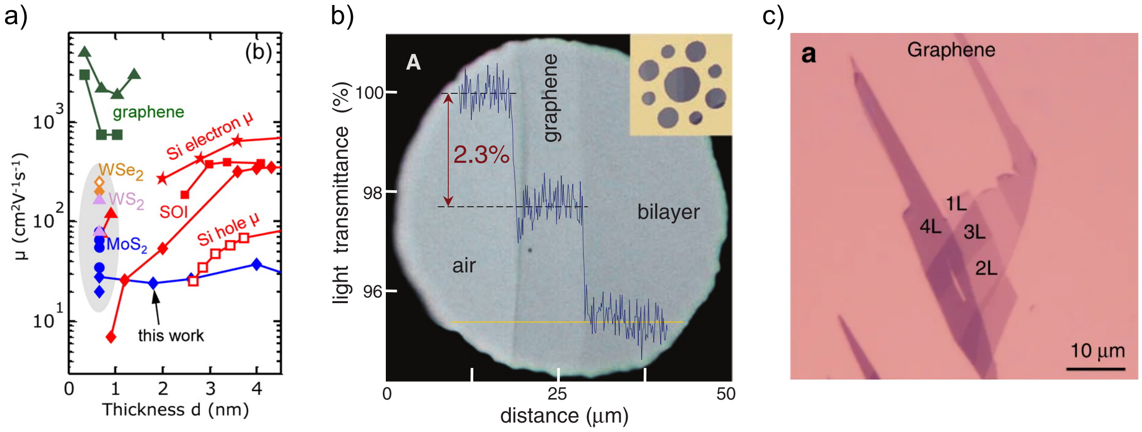

Figure 1.13: a) Mobility values as a function of thickness for different materials (from [131]), b) Optical transmittance of graphene layers (from [130]) and c) Optical microscope picture of graphene layers exfoliated on a 90 nm SiO_2 layer (from [132]).

1.2.2 Synthesis & transfer

The mechanical exfoliation of graphite developed by Geim and Novoselov has been extensively used for the preparation of high-quality graphene flakes for fundamental studies. The flakes are usually deposited on a Si/SiO_2 substrate which allow to see the graphene layers with a simple optical microscope. Indeed, each graphene layer adsorbing 2.3 % of the light adds an optical path with respect to the bare substrate surface, which results in an optical contrast between the reflected light on graphene layers and the top SiO_2 layer. The contrast is maximal in particular for a SiO_2 thickness of 90 nm or 280 nm under white light [133].

Although this technique provides graphene flakes with high charge carrier mobility ($\mu > 10^4\,\mathrm{cm.V^{-1}.s^{-1}}$), their size is typically limited to mm^2 which is not suitable for large scale integration. This method is also extremely tedious and time consuming since the graphene monolayers have then to be located with an optical microscope among the bi-/tri/multilayer graphene flakes present on the substrate (Figure 1.13.c).

Other techniques have been developed since, such as the graphitization from silicon carbide (SiC) substrate or the chemical exfoliation of graphite, providing a large choice in terms of cost, graphene layer size, and quality [134]. In particular, the thermal CVD growth of graphene is highly promising, as it can provide large area and uniform polycrystalline graphene of good quality.

1.2.2.1 CVD growth of graphene

The CVD growth of graphene on copper (Cu) was first introduced in 2009 by the team of S. Ruoff, reporting high quality ($\mu \sim 4 \times 10^4\,\mathrm{cm.V^{-1}.s^{-1}}$) single-layer graphene (>95%) over an area as large as cm^2 [135].

Experimentally, a piece of Cu foil is loaded in a quartz-tube chamber, the chamber is evacuated to insure the lowest O_2 concentration possible. The chamber is then heated between 950 °C and 1050 °C and a gas mixture of argon (Ar) and dihydrogen (H_2) is introduced to etch away the surface of the copper substrate, lowering the substrate roughness and removing contaminants. Subsequently, an hydrocarbon precursor (typically, a mixture of methane (CH_4) and H_2) is injected in the chamber and starts the graphene growth (Figure 1.14.1). Two mechanisms are involved during growth: a surface adsorption process, and a surface segregation/precipitation process (Figure 1.14.2). First, physisorbed CH_4 molecules at the surface of the catalytic Cu substrate are decomposed into C atoms and CH_x radicals. C atoms accumulate at the surface and eventually bind to form the sp^2 hybridized hexagonal lattice of graphene. The temperature, pressure and gas concentration conditions are maintained until the growing grains coalescence and the substrate surface coverage by a continuous polycrystalline graphene layer. At the same time, a proportion of C atoms can diffuse into the Cu bulk until the solubility limit is reached. Once the Cu bulk is saturated, the segregated C atoms can precipitate at the surface and form graphitic, multilayer patches during the final cooling process step [136].

The CVD growth of high-quality and large-area graphene therefore requires a thorough control of the process conditions, including the temperature, the pressure, the gas composition, the duration of each steps and also the substrate purity, surface crystalline orientation, roughness, chemical surface state. Indeed, these conditions can drastically affect the graphene nucleation, growth rate, layer number, the grain size and morphology, consequently altering the graphene physical and electrical properties. Various metal substrates have been used to grow graphene by CVD,

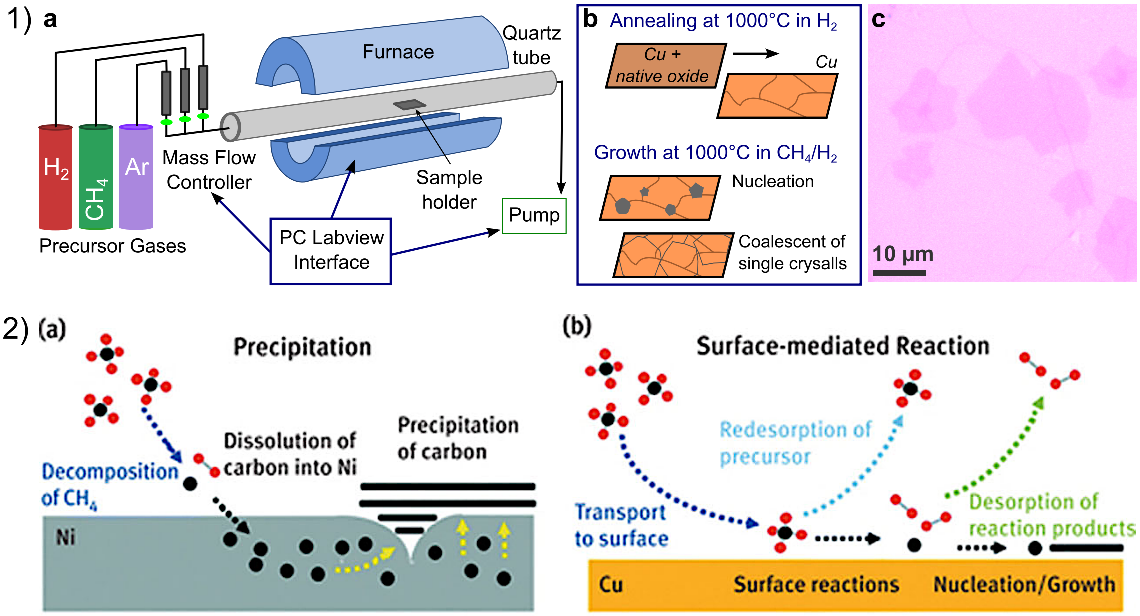

Figure 1.14: 1) a) Typical experimental setup for the CVD growth of graphene, b) Schematic representation of the growth principle and c) Optical picture of graphene (transferred on a Si/SiO$_2$ substrate after growth) showing the multilayer patches (from [137]), 2) a) Surface segregation mechanism and b) Surface adsorption process (from [138]).

such as nickel (Ni) [139], palladium (Pd) [140] or platinum (Pt) [141]. However, Cu is a significantly cheaper material and the solubility of C in Cu is low [142], which is primordial for the surface-adsorption mechanism to dominate during the growth, thus producing a graphene monolayer with a low multilayer patches density which drastically reduces the charge carrier mobility, as demonstrated by Han *et al.* [143].

After ten years of development, graphene CVD growth is becoming more and more mature, reaching high throughput and low costs, as recently demonstrated by both manufacturers LG [144] and Aixtron [145] with their cost-effective roll-to-roll production of CVD graphene.

1.2.2.2 Graphene transfer: from growth to device

Following the CVD growth, it is necessary to transfer the graphene film from the growth substrate to the desired substrate. As graphene exhibits a macroscopic characteristic lengths along two directions and a sub-nanometric thickness, it is thus challenging to transfer this film while preserving its structural integrity and surface cleanliness. Therefore, developing a robust and reproducible method to transfer graphene has been at the core of intensive research, with numerous techniques reported [146]. The polymer assisted wet-transfer method, which principle is presented Figure 1.15, has been largely adopted by the community for transferring large-area graphene onto any kind of substrate fitting the need of the desired application [147]. This method consists in first covering the graphene surface with a supporting layer (typically poly(methyl methacrylate) (PMMA)), and etching the underlying Cu growth substrate in an aqueous Cu etchant. Once the Cu substrate is completely etched, the graphene/PMMA stack floating at the etchant surface is transferred to a de-ionized water (DIW) bath by scooping it out with a piece of Si/SiO_2 or a glass slide, and releasing it carefully at the surface of water by immersing the sample. This step is performed several times in order to rinse and remove the impurities from the graphene bottom surface. The graphene/PMMA sample is then scooped out with the desired substrate and dried. Finally, the polymer supporting layer is removed to expose the graphene layer, which can then be patterned and electrically contacted to fabricate graphene-based devices.

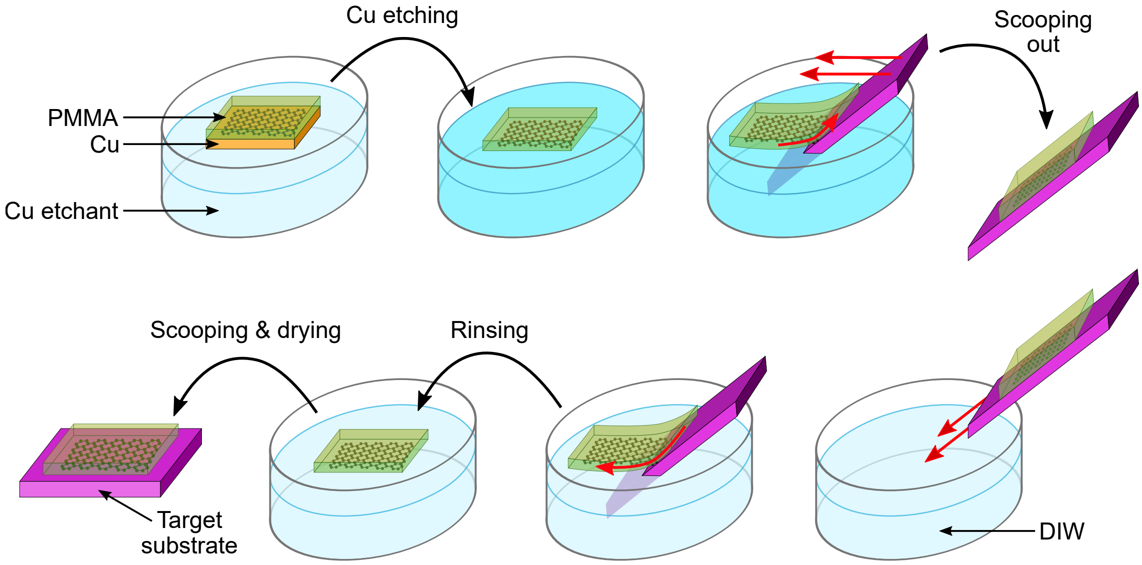

Figure 1.15: Schematic of the graphene transfer principle, from the Cu growth substrate to an arbitrary substrate.

1.2.3 Graphene FETs: principle & biosensing applications

The transfer of graphene onto any arbitrary substrate has enabled the fabrication of a variety of devices, such as FETs, using large-scale micro/nano-fabrication techniques. A typical graphene-based FET fabricated on a Si/SiO$_2$ substrate consists in a graphene channel contacted by two metallic contacts. The doped Si bulk is used as the gate, separated from the channel by a SiO$_2$ dielectric layer (Figure 1.16.a). Due to the linear band structure of graphene and the absence of charge screening in atomically thin layers, the charge carrier density and sign can be varied with an externally applied gate voltage over a large range, making graphene-based FET the first ambipolar atomically thin transistors [120], and showing a unique current-voltage transfer characteristic (Figure 1.16.b). Under large positive gate voltage, the channel conductivity is governed by accumulated electrons in the conduction band (n-type channel), while large negative gate voltage leads to a p-type channel. As a result, the transfer curve present two branches separated by a point of minimal conductivity corresponding to the Dirac point (or charge neutrality point).

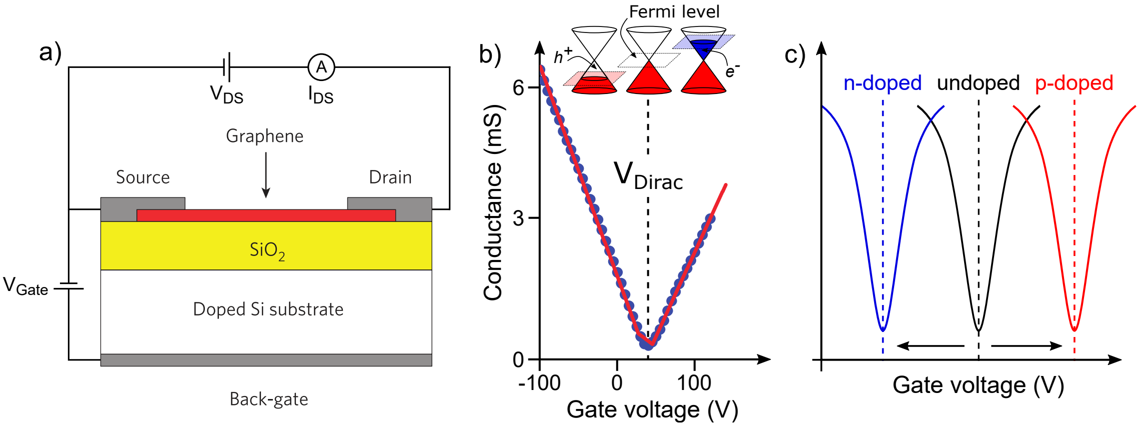

Figure 1.16: a) Graphene-based back-gated FET (from [148]), b) the associated typical transfer curve showing the ambipolar characteristic due to the peculiar charge injection by electrostatic gating (data from [120]) and c) the effect of doping on the Dirac point of the transfer curve.

From the transfer curve, several information can be extracted. First, the two branches can be asymmetric due to p-n junction at the electrode-graphene interface [149] or chemical doping impeding the mobility of one type of charge carrier [150]. The potential at which the Dirac point is reached (V_{Dirac}) gives indications about the doping of graphene by its chemical environment (Figure 1.16.c). at the top and bottom interfaces. This intrinsic doping is mainly induced by polymer residues left after stripping of the supporting layer used for transfer [151], and by charges trapped in the substrate induced by surface treatments [152]. The charge carrier mobility

μ is also a good indicator of the graphene quality and the impact of the transistor fabrication process on the graphene integrity. Indeed, the charge carrier mobility can be drastically affected by different charge scattering sources such as charged impurities, neutral defects, charge transfers or substrate roughness [153]. A good approximation of the mobility can be obtained from the method developed by Kim *et al.* , consisting of fitting the R_{tot}-V_{gate} transfer curve of the transistor [154]. For a back-gated transistor with a 290 nm SiO_2 layer, the induced surface charge carrier concentration in graphene by capacitive coupling is given by:

$$n_{unit} \;=\; \frac{\varepsilon_{ox}\varepsilon_0}{d \cdot e} \sim 7.4 \times 10^{10}\,\mathrm{cm}^{-2}.\mathrm{V}^{-1} \tag{1.2}$$

where ε_{ox} is the dielectric constant of the SiO_2 layer, ε_0 the vacuum permittivity, d the dielectric thickness and e the elementary charge.

The total charge carrier concentration is linked to the impurity related residual charge carrier concentration n_0 by:

$$n \;=\; \sqrt{n_0^2 + \left[n_{unit}\left(V_{Gate} - V_{Dirac}\right)\right]^2} \tag{1.3}$$

The conductance G and conductivity σ are related to n by:

$$G \;=\; \frac{1}{R_{tot} - R_c} \;=\; \sigma\frac{Wt}{L} \;=\; ne\mu\frac{W}{L} \tag{1.4}$$

where W is the transistor width, L the length, t the graphene thickness conventionally set equal to 1, and R_c the contact resistance. From Equation 1.3 and Equation 1.4, the mobility of the device can then be extracted from the device resistance as a function of the gate voltage following:

$$R \;=\; \frac{L/W}{e\mu\sqrt{n_0^2 \;+\; \left[n_{unit}(V_{Gate} - V_{Dirac})\right]^2}} \;+\; R_c \tag{1.5}$$

The device performance is therefore maximized by increasing the channel aspect ratio W/L, decreasing the contact resistance between graphene and the metallic contacts, and by promoting a high charge carrier mobility.

In particular, the contact resistance (R_c), graphene sheet resistance (R_s) and transfer length (L_t), defined as the effective contact length contributing to the injection of carriers in graphene, can be extracted from the Transmission Line Measurement (TLM) technique. By measuring the resistance of devices with same channel width and varying length, a linear $R_{tot} - L$ curve is obtained. R_s is extracted from the slope, and $R_{contact}$ from the intercept at $L = 0$ as shown in Equation 1.6 and illustrated in Figure 1.17:

$$R_{tot} = R_{sheet}\frac{L}{W} + \frac{2R_{contact}}{W} \tag{1.6}$$

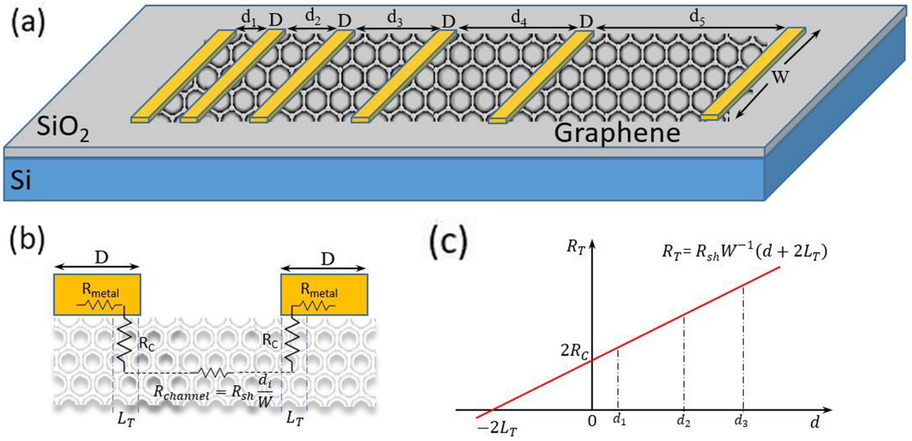

Figure 1.17: a) Device architecture for TLM measurement, b) the equivalent electrical model and c) the resulting linear behaviour of the total resistance as a function of channel length for extracting R_s, R_c and L_t (from [155]).

These methods are widely used to extract mobility and contact resistance as they require simple device architecture and electrical equipment. However, since both mobility and contact resistance are gate voltage dependant [156, 157], the values obtained should be regarded as first approximations.

The exceptional mobility of charge carriers readily exposed at the surface of graphene without any bulk inducing charge screening have naturally attracted a great interest for biosensing applications. When functionalized with bioreceptors, the graphene sensitivity to surface potential variation or charge transfer allows the transduction of the binding event to a current channel modulation of the transistor and a variation of V_{Dirac}. Back-gated graphene-based FETs have been used as immunosensors [158,159] and DNA sensors [160], showing promising detection limits as low as 1 fmol.L^{-1} [161] (Figure 1.18).

Although these devices benefit from the graphene exceptional conductivity, their electrical sensitivity remains limited. Indeed, the sensitivity S of the transistor to external potential changes is dictated by the transconductance g_m, which is proportional to the charge carrier mobility and the interface capacitance at the transistor/gate interface:

$$S = \frac{g_m}{V_{DS}} = \frac{1}{V_{DS}}\frac{\partial I_{DS}}{\partial V_G} = \mu \cdot C_{Ox} \cdot \frac{W}{L} \qquad (1.7)$$

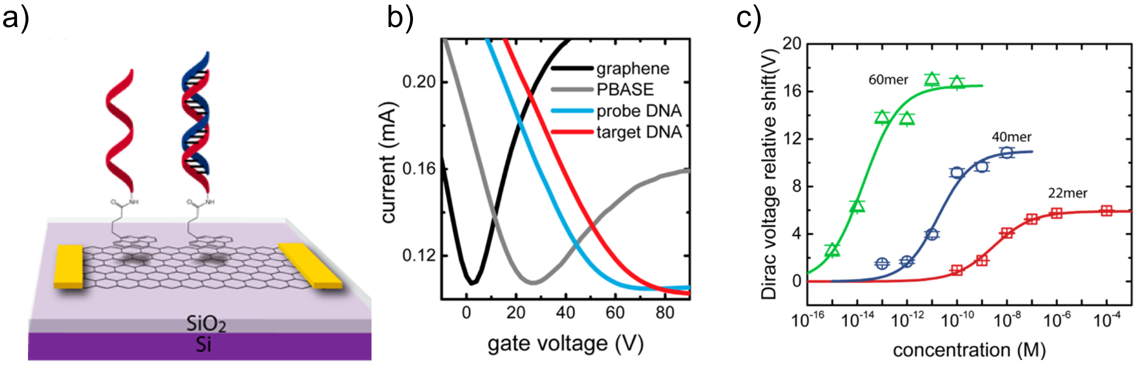

Figure 1.18: a) Example of graphene-based back-gated FET DNA biosensor, b) monitoring the target detection through Dirac point variation, c) demonstrating a LOD in the femtomolar range (from [161]).

The interface capacitance depends on the thickness and material of the dielectric, which is typically in the order of 12 nF.cm^{-2} for a thermally oxidized SiO$_2$ layer of 290 nm [162]. As a consequence, electrical sensitivity is limited, and it is necessary to apply a large gate potential (typically a few tens to hundred volts, see Figure 1.16.b and Figure 1.18.b) to induce a sufficient charge modulation for monitoring variations of V$_{\mathrm{Dirac}}$, which is not desirable for power consumption and integration purpose. Decreasing the oxide layer thickness to increase the interface capacitance is neither desirable as it would be detrimental in terms of leakage current and breakdown voltage for large area devices.

1.3 Graphene-based Solution-Gated FET

The SGFET consists in a graphene-based transistor device with the graphene channel directly exposed to the electrolyte containing charged species. Instead of using the Si bulk to electrostatically gate the graphene channel through the SiO_2 dielectric layer, a reference electrode is inserted in the electrolyte and used as an out-of-plane gate (Figure 1.19.a). This electrode maintains a fixed potential in the solution relatively to the vacuum level, shifting the Fermi level in graphene and modulating the drain-source current of the transistor, similarly to the back-gated FET (Figure 1.19.b). In particular, the gating mechanism relies here on the existence of a large capacitance at the graphene-electrolyte interface, induced by the formation of a so-called electrochemical double-layer (EDL). In the SGFET configuration, the exceptional mobility of the charge carriers directly available at the graphene surface is therefore exploited with a large interface capacitance, overcoming the sensitivity limitations faced by back-gated graphene FETs. The SGFET thus represents a promising solution for a highly sensitive detection of biomolecules in liquid environment.

Before going into more details about SGFET biosensors, it is first necessary to present the EDL structure, its application to the SGFET capacitance model ruling the graphene gating mechanism, and other important electrochemical considerations about graphene.

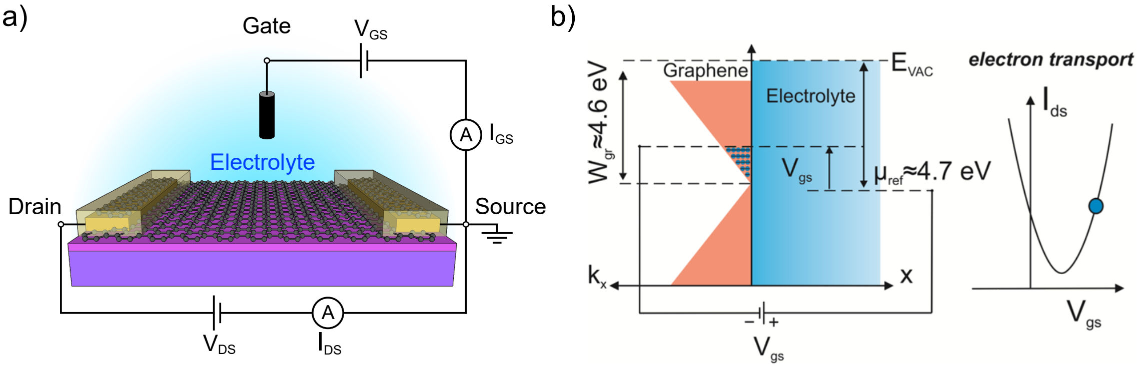

Figure 1.19: a) The graphene SGFET structure, comprising a graphene layer deposited on a Si/SiO_2 substrate and contacted by metallic contacts passivated from the liquid environment, in which an out-of-plane electrode is inserted to serve as a gate, b) Simplified energy diagram at the graphene-electrolyte interface, in the case of an Ag/AgCl reference electrode, showing the ambipolar characteristic of the graphene-based transistor in liquid, when biased positively from the Dirac point (from [163]).

1.3.1 The electrochemistry of graphene

1.3.1.1 Theory of the electrochemical double-layer

When an electrically conductive electrode is immersed in an electrolyte, ions from the solution accumulate at the electrode surface to maintain the charge electroneutrality of the system. This charge separation at the interface was first modelized by Helmholtz in 1879 as two compact layers of charges having opposite polarity, and separated by a distance corresponding to the ionic radius of the solvated ions (hence, the name "double-layer") [147]. The structure, equivalent to a parallel-plate capacitor, was thus assigned a constant capacitance C_{EDL}:

$$C_{EDL} = \frac{\varepsilon\varepsilon_0}{d} \tag{1.8}$$

However, this model was found to be insufficient to describe the variable capacitance observed experimentally in most systems, since it doesn't take into account important factors, such as diffusion and convection processes.

Later on, Gouy (1910) and Chapman (1913) introduced the model of the "diffuse layer", describing the charge repartition in the electrolyte side of the interface as an ion atmosphere, taking into account their thermal motion. This diffuse repartition of charges, with a potential decreasing exponentially away from the electrode surface is well described by the Poisson-Boltzmann equation in the 1D case:

$$\frac{d^2\phi}{dx^2} = -\frac{e}{\varepsilon\varepsilon_0}\sum_i c_i^0 z_i \exp\left(\frac{-z_i e\phi}{k_B T}\right) \tag{1.9}$$

where ϕ is the potential, x the distance from the electrode, k_B the Boltzmann constant, T the temperature, c_i^0 the bulk concentration and z_i the charge of the ion i. Solving Equation 1.9 with ϕ_0, the potential drop across the diffuse layer, as the potential at $x = 0$ for boundary conditions gives:

$$\frac{\tanh\left(\frac{ze\phi}{4k_BT}\right)}{\tanh\left(\frac{ze\phi_0}{4k_BT}\right)} = e^{-\kappa x} \tag{1.10}$$

where $\lambda = \kappa^{-1}$ or "Debye length" is the characteristic length of the decaying electric potential defined by:

$$\kappa^{-1} = \sqrt{\frac{\varepsilon\varepsilon_0 k_B T}{2 \times 10^3 N_A e^2 I}} \quad \text{with} \quad I = \frac{1}{2}\sum_i c_i z_i^2 \tag{1.11}$$

where N_A is the Avogadro number and I the ionic strength of the solution.

The diffuse layer thickness is thus ruled by the electrode potential, but also by the concentration and net charge of the ionic species: the higher the electrolyte concentration (or charge), the thinner the diffuse layer extends in the solution, as the charge excess is compensated more efficiently by the ionic cloud. The associated capacitance is no longer constant, inversely proportional to λ, thus dependant of the ionic strength (as shown (Figure 1.20.a):

$$C_{EDL} = \frac{\varepsilon\varepsilon_0}{\lambda} \cosh\left(\frac{ze\phi_0}{2k_BT}\right) \tag{1.12}$$

This refined model, however, doesn't modelize perfectly the double-layer phenomenon, as charges are considered as points without any limit of electrode surface approach which is unrealistic. Instead, Stern introduced in 1924 a combination of the former Helmholtz and Gouy-Chapman models, with a first compensation of the electrode charge by ions at a plane of closest approach (called outer Helmholtz plane, or OHP) immobilized close to the surface, and the remaining charge being compensated by the diffuse layer [164]. The resulting capacitance is thus simply equivalent to the Helmholtz (C_H) and diffuse capacitances (C_{EDL}) in series:

$$\frac{1}{C_{EDL}} = \frac{1}{C_H} + \frac{1}{C_D} \tag{1.13}$$

The composite capacitance C_{EDL} shows a complex behaviour, governed by the smallest of the two components, C_D being electrolyte concentration and charge dependant. As a consequence, at high concentration the diffuse layer is compressed (so $1/C_D$ is negligible compared to $1/C_H$) and the potential drops linearly in the Helmholtz layer. At low concentration and low polarization of the electrode, the capacitance of the diffuse layer is mainly contributing to the overall capacitance (Figure 1.20.b).

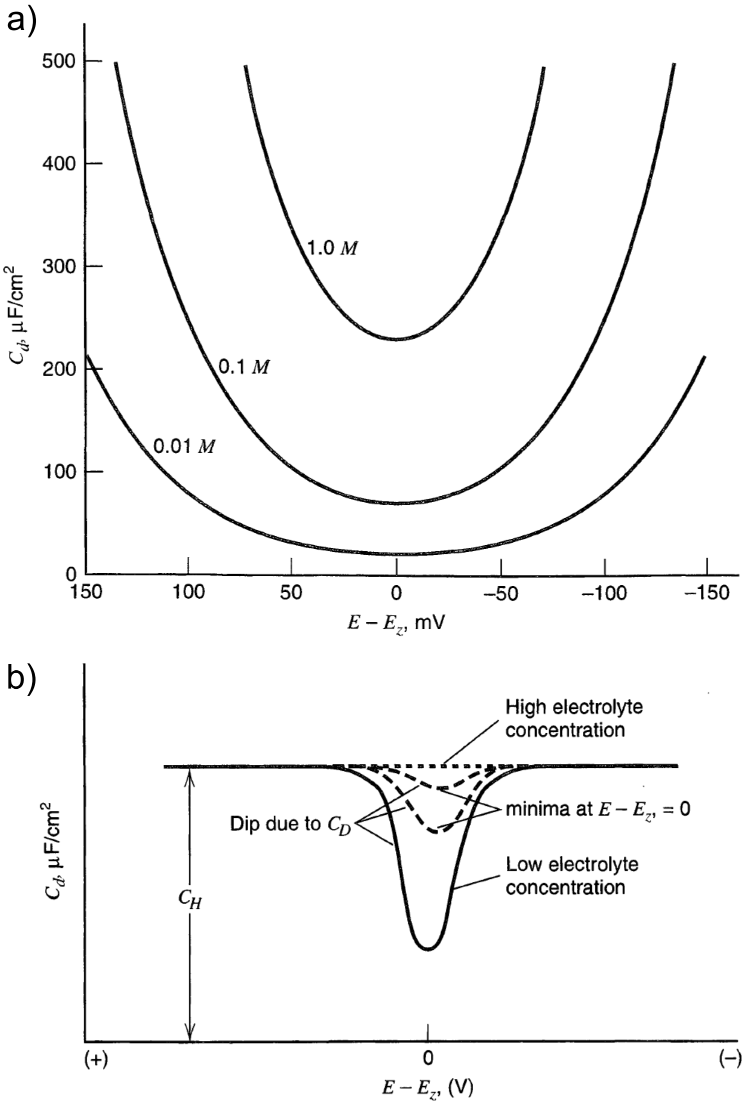

Figure 1.20: a) V-shape behaviour of the diffuse layer capacitance as a function of the electrode polarization and the ionic strength of the electrolyte, b) Capacitance behaviour in the Stern model, as a function of the ionic strength and electrode polarization (both figures from [165]).

This model predictions accurately fit the main features observed in real systems. The remaining discrepancies have been refined by taking into account other parameters such as the structure of the dielectric layer in the Helmholtz layer, dipole-electrode interactions, or the non-specific adsorption of ions at the electrode surface due to short range interactions. The locus of non-specifically adsorbed ions is called the inner Helmholtz plane (or IHP), which is often merged with the OHP for simplification. The structure of the double-layer, and the potential profile is illustrated Figure 1.21.

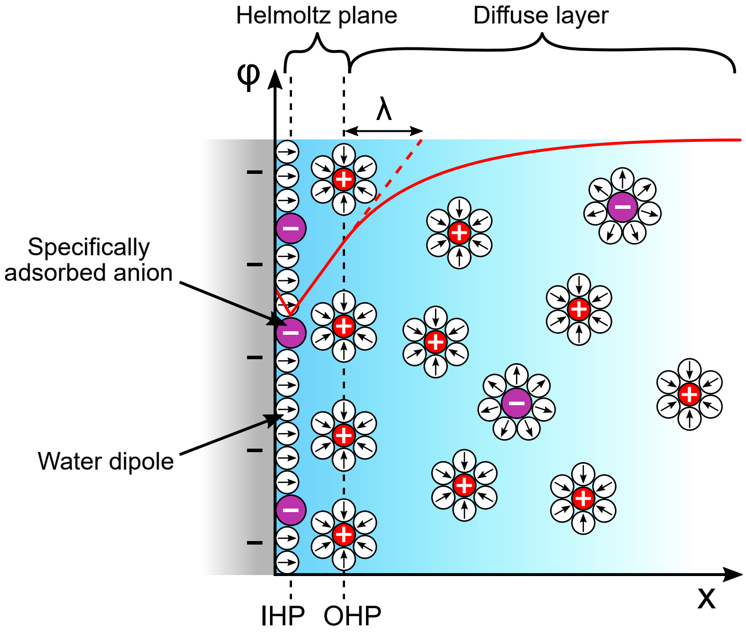

Figure 1.21: Schematic of the double-layer structure in the case of a negatively charged surface. The potential drop across the double-layer is depicted in red, and the Debye length indicated.

1.3.1.2 Capacitance model of the SGFET

Graphene exposed to an electrolyte is subjected to the same phenomenon previously described. The SGFET architecture takes advantage of the large double-layer capacitance to operate the device with a great electrical sensitivity. Indeed, this capacitance is typically in the order of 0.1–100 µF.cm^{-2}, which is at least one to three orders of magnitude higher than the 300 nm thick SiO$_2$ layer capacitance typically used for graphene FETs in the back-gating configuration. In addition, the quantum capacitance of graphene (C_Q), which is typical of 2D systems with a low DOS, has to be considered in the capacitance model. Indeed, Xia *et al.* showed that this capacitance was comprised between 5 and 10 µF.cm^{-2} (Figure 1.22.a), which is comparable to the double-layer capacitance [166]. This capacitance, neglected in the back-gated FET configuration due to the low SiO$_2$ layer capacitance (the $1/C_{Ox}$ contribution is preponderant), is therefore included in the graphene-electrolyte interface model of the SGFET:

$$\frac{1}{C_{tot}} = \frac{1}{C_H} + \frac{1}{C_D} + \frac{1}{C_Q} \tag{1.14}$$

In particular, C_Q is dependant to the charge carrier concentration n_G electrostatically induced by the gate potential and the charged impurity concentration n^* as:

$$C_Q = \frac{2e^2}{\hbar \nu_F \sqrt{\pi}} \sqrt{|n_G| + |n^*|} \quad \text{with} \quad n_G = \left(\frac{e\phi_{Gr}}{\hbar \nu_F \sqrt{\pi}} \right)^2 \tag{1.15}$$

where ϕ_{Gr} is the potential of graphene, $\hbar$ is the reduced Plank constant, and ν_F the Fermi velocity [166]. As shown Figure 1.22, the minimum of capacitance increases with the charged impurity concentration and the capacitance variation under graphene potential change is smaller. This additional component of the global capacitance is thus strongly affected by charged impurities.

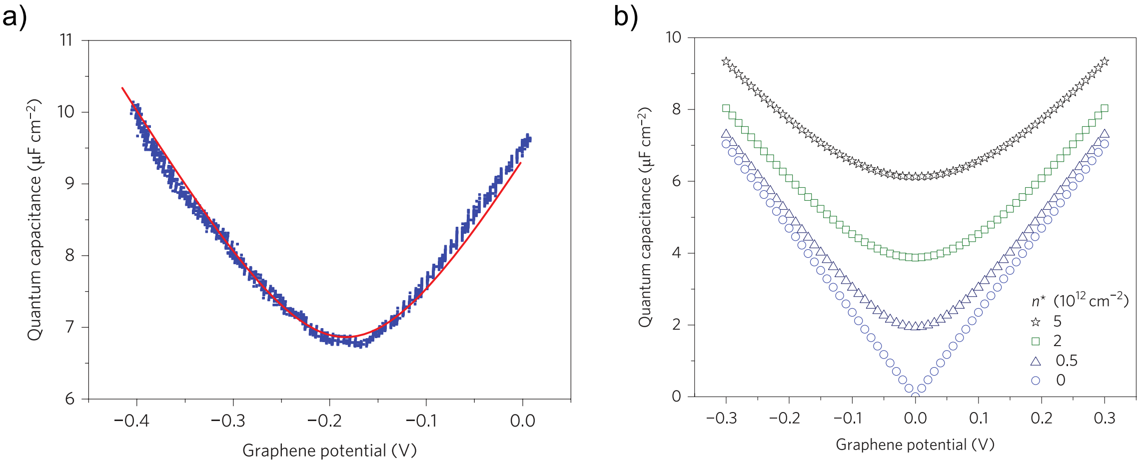

Figure 1.22: Graphene quantum capacitance, a) experimentally measured by Xia *et al.* and the effect of increasing the charge impurity concentration (from [166]).

In fact, the model is even more complex when considering the hydrophobicity of graphene. As shown by molecular dynamic simulations, the density of water strongly decreases at the surface of highly hydrophobic surfaces, creating a gap between the surface and the electrolyte with an effective dielectric constant drastically smaller than the bulk solution (Figure 1.23.a), thus resulting in an additional potential drop at the interface [167]. Such air-gap was introduced into an extended Poisson-Boltzmann model, developed by Hess *et al.* [168], and successfully applied to the description of SGFET capacitance-voltage experimental data [169] (Figure 1.23.b). The model was recently extended by Kireev *et al.* as a function of the main parameters of the total capacitance: I, V_{gate} and n^* [170] (Figure 1.23.c). These models show the importance of controlling these parameters, or at least knowing their effect in order to understand the gating mechanism involved in SGFET operation in liquid, and fabricate high performance biosensors.

1.3.1.3 Ionic strength effect

The example of the ionic strength effect is discussed in this subsection. As mentioned previously, the ionic strength directly affects the capacitance at the graphene-electrolyte interface. In particular, a variation of ionic strength will shift $\mathrm{V_{Dirac}}$ in liquid gating experiments. This effect is explained by first considering the charge electroneutrality of the system, which is always satisfied and at the core of the graphene sensitivity in electrolyte environment:

$$\sigma_{gra} + \sigma_{surf} + \sigma_{dif} = 0 \tag{1.16}$$

where σ_{gra} is the free carrier charge in graphene, σ_{surf} is a negatively surface-bound charge at the graphene-electrolyte interface due to specific adsorption [171] and the presence of ionizable groups [172], and σ_{dif} is the mobile charge in the diffuse layer. The surface charge is compensated from both the electrostatically induced charge carriers in graphene and the ionic charge in the diffuse layer. Therefore, any variation of the charge in graphene is related to charge variations in the diffuse layer:

$$\delta\sigma_{gra} = -\delta\sigma_{dif} \tag{1.17}$$

Moreover, the charge in graphene is coupled to the potential drop within the Helmholtz layer via the interface capacitance:

$$\sigma_{gra} = C_H\left(\varphi_{gra} - \varphi_{dif}\right) \quad \text{and} \quad \delta\sigma_{gra} = -C_H\delta\varphi_{dif} \tag{1.18}$$

where φ_{gra} is the potential in graphene, and φ_{dif} the potential at the interface, described in the first approximation by the Graham equation [165]:

$$\varphi_{dif} = \frac{2k_BT}{ze}\sinh^{-1}\left(\frac{\sigma_{surf}}{\sqrt{8\varepsilon\varepsilon_0 k_B T c_0}}\right) \tag{1.19}$$

where c_0 is the bulk concentration. From Equation 1.19, it appears that for a given surface charge, increasing the ionic strength induces a decrease of the interface potential φ_{dif}. The lower potential drop experienced by graphene consequently

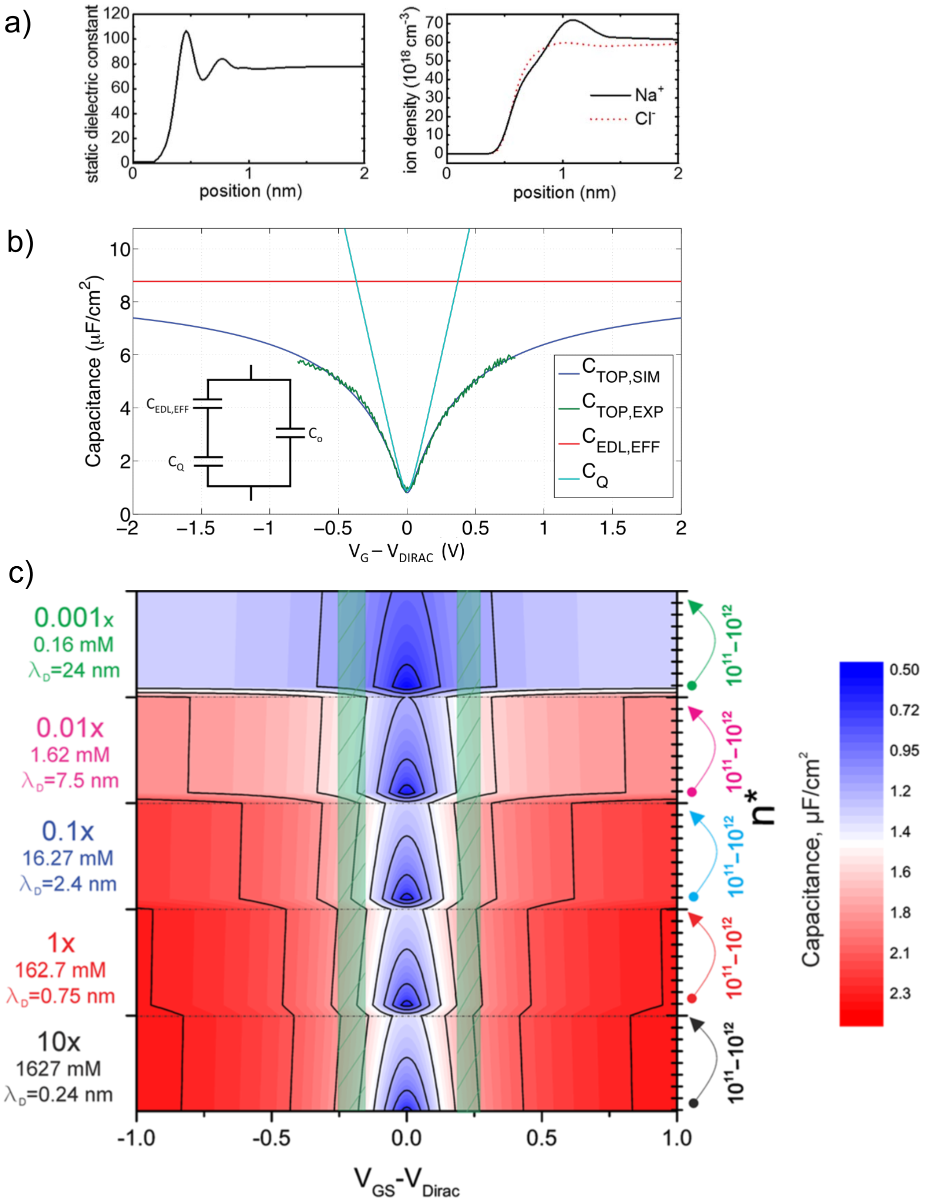

Figure 1.23: a) Molecular dynamic simulations of the dielectric constant (left) and the ion density close to a hydrophobic surface (right) (from [168]), b) the capacitance model of the graphene-electrolyte interface (blue, $C_{TOP,SIM}$) fitting the experimental data (green, $C_{TOP,EXP}$), comprising the quantum capacitance of graphene (light blue, C_Q), the EDL capacitance calculated with the extended Poisson-Boltzmann model (red, $C_{EDL,EFF}$) and an additional capacitance C_0 for the leads (from [169]), and c) the capacitance modelized as a function of the I, n^* and V_G. The green strips represents the maximal electrical sensitivity (from [170]).

results in a lower charge σ_{gra}. The gate potential required to reach the Dirac point is therefore lower, and V_{Dirac} is shifted toward more negative values (Figure 1.24). It is therefore necessary to set the ionic strength constant in biosensing experiments to insure that an observed shift of the transfer curve is resulting from the detection event and not an experimental artefact. In field measurement or for biological media, the ionic strength effect can be compensated by differential measurement with a secondary sensor.

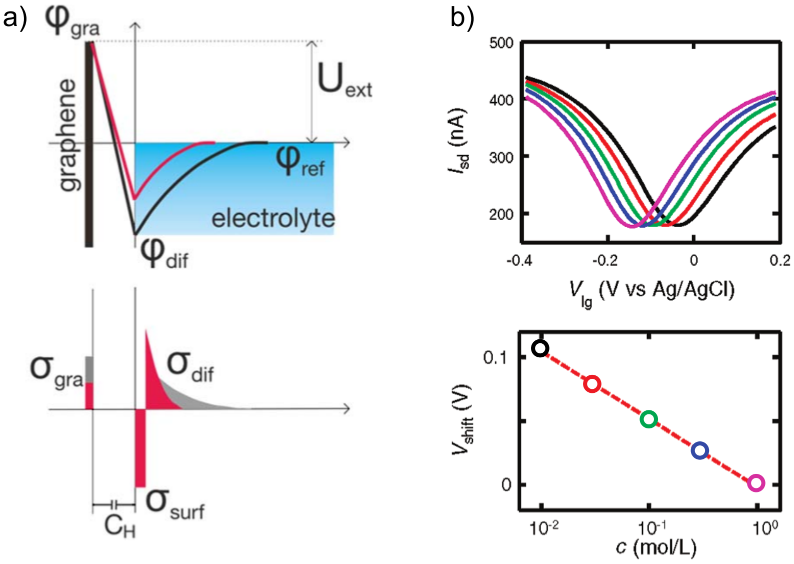

Figure 1.24: a) Representation of the potential (top) and charge (bottom) across the graphene-electrolyte interface showing the effect of increasing the ionic strength (red line) (from [168]) and b) the V_{Dirac} shift as a function of the ionic strength (adapted from [172]).

1.3.1.4 Graphene electrochemical reactivity

The former subsections were addressing only capacitive phenomena occurring at the graphene-electrolyte interface. Here, we will discuss about faradaic processes, related to charge transfers between reduced and oxidized species at an electrode, which could be involved in the electrochemical system represented by the graphene layer gated in an electrolyte environment.

Indeed, when the SGFET is operated, a potential difference is imposed between the graphene layer and the reference electrode. Such electrochemical energy provided to the system may be sufficient for electrochemical reactions to be thermodynamically promoted. In other words, a DC current, which magnitude depends on the gate potential and the chemical species involved in the reaction, could flow between the gate and the channel. In analogy with the back-gated FET where no current is supposed to flow through the dielectric, any faradaic current at the graphene-electrolyte interface can be considered as the transistor "leakage current". This current is not desirable in any transistor devices, as it represents a loss of energy, performance, and can interfere with the signal of interest. It is therefore important to understand the origin of this current, in order to minimize it to improve the device performance.

While the amplitude of this current (for a given species) can be related to diverse factors such as the concentration of the redox species, their transport to the electrode (diffusion, migration and convection) or time, we will rather mainly focus on the electrochemical reactivity of graphene, partially defined by its electron transfer rate constant k°, which is the figure of merit of the material ability to exchange charges with other species. When looking at the electrochemical reactivity of an electrode material, it is first important to distinguish between two types of electroactive species, called "outer-sphere" and "inner-sphere" redox probes. These two types of probes differ from their electron transfer kinetics, depending on the surface chemistry of the electrode material under investigation (defects, impurities, adsorption sites and oxygen containing groups). For example, the well-known outer-sphere redox probe $Ru(NH_3)_6Cl_3$ is "surface insensitive": the redox reaction with the electrode is not catalysed by any interaction with the surface but primarily sensitive to the electronic DOS of the electrode material (a higher DOS increases the probability that an electron is available to transfer to an electroactive species [173]). Conversely, an inner-sphere probe such as $K_4Fe(CN)_6$ is strongly "surface sensitive" and doesn't depend only the electrode DOS [174]. In any case, the electrochemical reactivity is dependant on either the electrode DOS or the surface chemistry.

Combining a robust and chemically inert sp^2 carbon network with a low DOS close to the Fermi level, pristine and continuous graphene layers should exhibit a very poor electrochemical response. However, the enhanced electro-catalytic behaviour of graphene has been reported for the detection of numerous molecules, including bisphenol A [175], dopamine, urea and acid ascorbic [176], or morphine and heroine [177]. The superior detection performance reported can be easily understood when considering that "graphene" is in fact used under two oxidized variants, called reduced graphene oxide (rGO) and graphene oxide (GO), rich in oxygen groups, points and line defects, and graphene edges due to small domain size (their structure are presented Figure 1.27.a). In these graphene alternative forms, the presence of oxygen groups and structural defects increases the graphene chemical reactivity and locally increase the DOS [178, 179]. In addition, it has been demonstrated by Yuan *et al.* that the graphene edges show a superior electrochemical reactivity compared to the basal plane, due to the presence of oxygen groups [180]. In addition, a "micro-electrode" effect enhances the diffusion of electroactive species at the edges, while the kinetics at the basal plane are diffusion-limited (Figure 1.25).

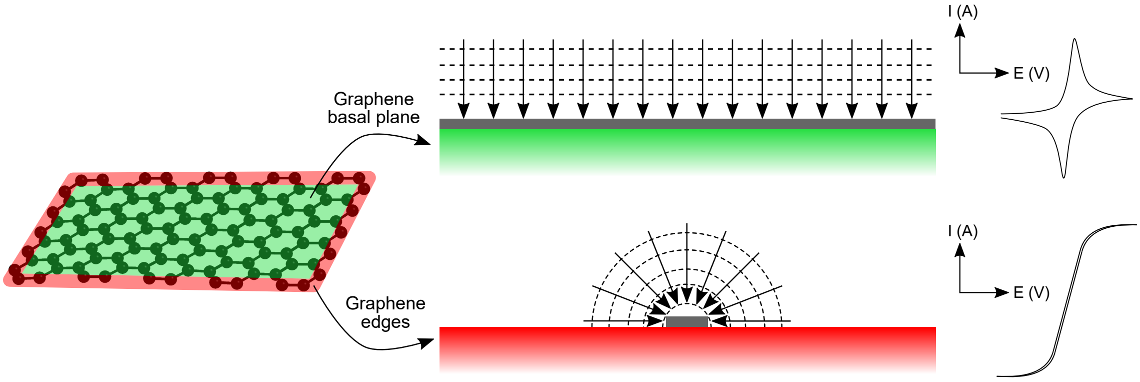

Figure 1.25: Schematic representation of (bottom) the micro-electrode convergent diffusion effect enhancing the electrochemical reactivity at the graphene edges, showing a typical sigmoid current density response, and (top) the basal plane macro-electrode linear diffusion profile of the species toward the surface, showing a typical diffusion limited current density response.

The enhanced electrochemical activity of dangling bonds at defects sites or at the edges is also responsible for the pH sensitivity of graphene. Indeed, such bonds are easily converted into hydroxyl chemical groups which can be protonated (deprotonated) into OH_2^+ (O^-) as the pH increases (decreases), leading to n-doping (p-doping) of graphene and a subsequent V_{Dirac} shift [181]. Pristine and continuous graphene should therefore show no pH response, and any pH sensitivity observed is reflecting the graphene surface state and quality [182].

Controlling the surface state of graphene, and in particular promoting a low defect density by optimizing the fabrication process, is therefore of primary importance to limit any undesired electrochemical reactions or large pH response, and maximize the device electrical sensitivity.

1.3.2 SGFET biosensing

SGFET devices have naturally attracted a great interest for biosensing over the years. In particular, lower LOD compared to previous technologies have been reported for the detection of insulin [183] or protein in physiological serum [184]. The biosensing mechanism is similar to back-gated graphene-based FETs or CNTs: bioreceptors interfaced with graphene provide a specific recognition and immobilization of charged biomolecules within the EDL. The presence of the target analytes electrostatically shift the Fermi level of graphene, resulting in V_{Dirac} variations in the transfer curve (Figure 1.27.a). The detection of the target can be also monitored by measuring in real-time the channel current at a constant gate potential (Figure 1.27.b).

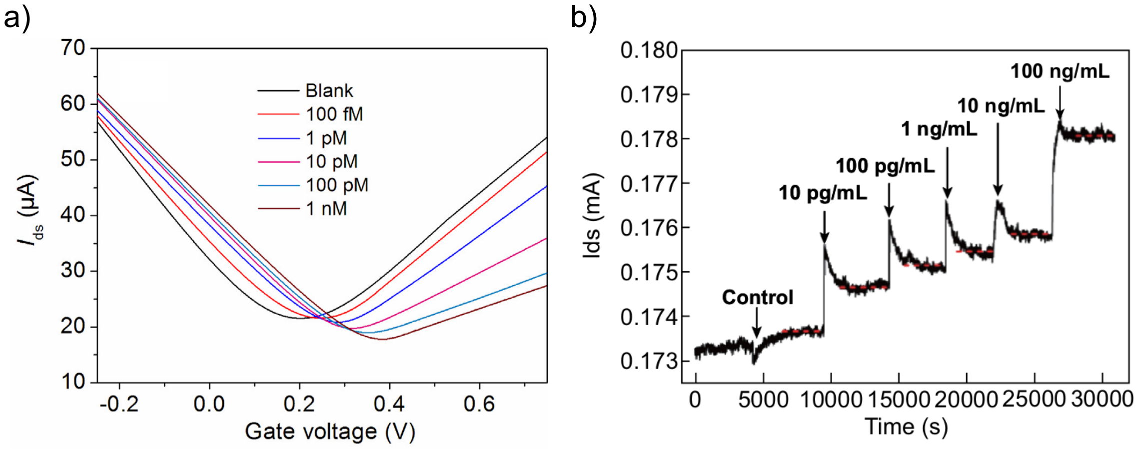

Figure 1.26: Examples of monitoring a) DNA hybridization through V_{Dirac} variations (from [185]), or cancer protein biomarker binding as a function of time at a working gate potential (from [186]).

1.3.3 Bio-functionalization of graphene

As discussed in section 1.1.2, interfacing the transducer element of the biosensor is essential to specifically detect the biomolecule of interest. The immobilization of bioreceptors at the surface of bulk materials, such as the SiO_2 layer at the surface of SiNWs, comprises a variety of bioconjugation techniques already well-established [187]. However, interfacing graphene (or CNTs) with bioreceptors requires a different approach which is detailed in the following subsections.

1.3.3.1 Physisorption

The direct physical adsorption of bioreceptors at the graphene surface through Van der Waals interactions is the simplest functionalization method. Indeed, aromatic amino-acid residues (such as histidine, phenylalanine, tyrosine, and tryptophan) found in peptides and proteins can interact with the highly hydrophobic graphene surface through strong π-π interactions, and orient parallelly to the graphene plane to maximize their interaction with the surface [188]. The non-covalent interaction of nucleotides (found in polynucleotides such as DNA and RNA strands), with the π-electron cloud of graphene was also found to be highly favourable [189]. Although this interaction is interesting for the robust immobilization of bioreceptors at the graphene surface, the receptor orientation can't be controlled, eventually blocking the binding sites. In addition, the physical adsorption of receptors can be detrimental for the structural integrity of such complex objects. Indeed, several theoretical studies have shown that the strong interaction with graphene competes and overcomes in some cases the intramolecular forces responsible for the 3D structure of the biomolecule. Since the bio-functionality of such receptors lies on their 3D structural arrangement, their specificity toward their target can be drastically affected when adsorbed onto graphene.

For example, Ou *et al.* have shown that α-helical peptides form functional dimers in solution, whereas the interaction between graphene and adsorbed peptides perturbs the native intra and inter-peptide interactions, leading to the α-helix unfolding into amorphous dimers [190]. In a similar manner, Zuo *et al.* showed that the villin headpiece (HP35) protein adsorbed onto graphene loses most of its native secondary and tertiary structures [191]. Hugues *et al.* showed that an adenosine target analyte bound to an adenosine-binding DNA aptamer receptor could detach, as a result of the competition between adenosine-graphene and aptamer-graphene interactions, in unfavourable adsorption configurations of the aptamer on graphene [192].

In addition, the protein loss of functionality after adsorption on graphene have been experimentally demonstrated by Alava *et al.* [4]. The adsorption on graphene of the lectin protein Concanavalin A (Con A), which is relatively stable with respect to denaturation and show a great affinity toward some polysaccharides, was studied under QCM experiments. In particular, the protein showed the same affinity levels toward α-D-mannopyranosyl moieties located on *Bacillus subtilis* cell walls as denatured Con A, indicating that the protein loses its biological function when adsorbed on graphene.

On the other hand, DNA strands adsorbed onto graphene can retain their specificity, but undergo desorption from the graphene surface upon hybridization with their complementary strand [193]. The simple adsorption of biological receptors at the surface of graphene is therefore not a suitable solution for functionalizing graphene.

1.3.3.2 Covalent grafting

The covalent binding of receptors to the graphene lattice is another route to be considered for the robust functionalization of graphene with bioreceptors. Because of its π electron cloud delocalized over its entire 2D network, graphene is fairly chemically inert, and requires highly reactive species to convert planar sp^2 carbon atoms into tetrahedral sp^3 lattice-points to further introduce chemical functionalities [194]. The most commonly used strategy consists in oxidizing graphite, and exfoliating it in acidic solutions to produce GO (Figure 1.27). The resulting dispersed GO sheets present a large variety of carboxyl, carboxylic acid, hydroxyl and ether reactive groups which can serve as anchor points for DNA or protein receptors grafting [195–198]. GO can also be reduced into rGO, partially restoring the aromatic carbon network of graphene while still containing unreduced covalently bonded oxy groups.

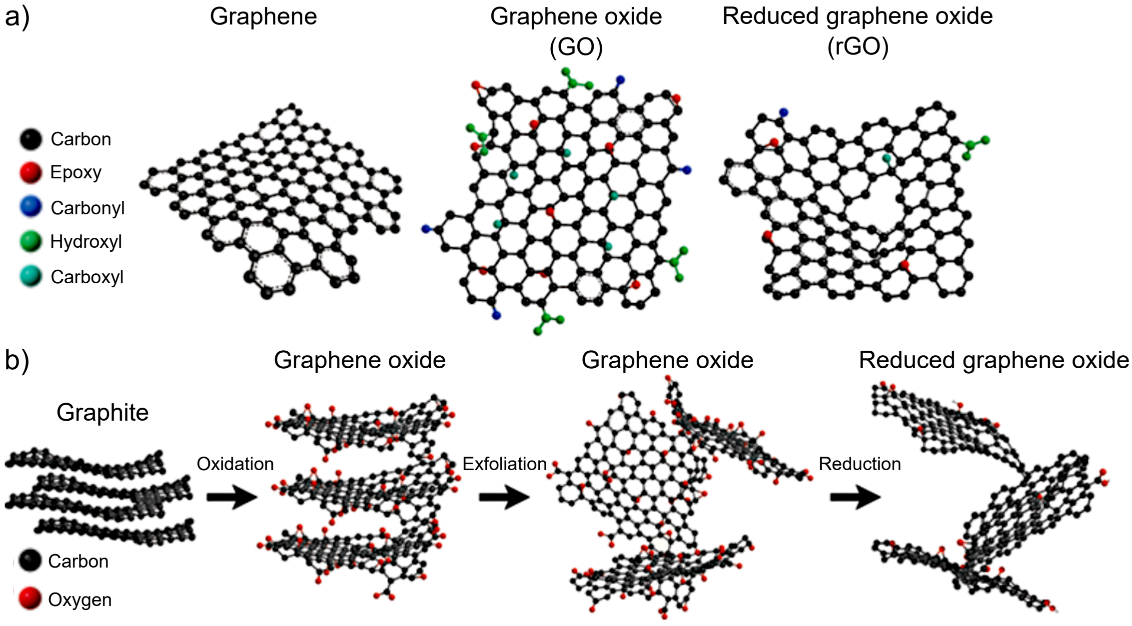

Figure 1.27: a) Chemical structures of graphene, graphene oxide and reduced graphene oxide, showing the diverse chemical functionality (and structural vacancies) introduced by b) the chemical exfoliation and oxidation/reduction from graphite (adapted from [199]).

The disruption of the hexagonal lattice of graphene through covalent functionalization is also significantly changing the graphene properties. The introduction of sp^3 carbon atoms removes a π electron per atom which reduces the carrier density, breaks the potential continuum, and can introduce a bandgap. The distorted planar lattice also induces a drastic charge carrier mobility reduction by a few order of magnitude [200, 201]. The covalent functionalization of graphene appears as a more robust technique than the physisorption method but at the cost of the graphene structural integrity and therefore the device performance. In addition, the graphene electrochemical properties (in particular the higher electrochemical reactivity due to the numerous oxygen groups and graphene edges) are drastically affected and not controlled due to the poor fabrication reproducibility, which complex process requires the manipulation of harsh and toxic chemical reactants [194].

1.3.3.3 Non-covalent functionalization

PBASE

PBASE has been widely used as a an alternative to the covalent functionalization of graphene for biosensing applications of SGFET [193,202–204]. This molecule, also called "linker", acts as a spacer interfacing bioreceptors with the surface of graphene. The aromatic pyrene feet of the linker interacts with the π electron cloud of graphene through π-π interactions (Figure 1.28.a), while the NHS ester group located at the opposite side of the molecule is a good leaving group upon nucleophilic reaction with primary amines (Figure 1.28.b). Such primary amine groups are notably found at the N-terminus of proteins and in the side-chain of lysine amino acid residues.

The PBASE thus provides an interesting bioconjugation strategy for maintaining protein, DNA or aptamer-based receptors in the close vicinity of graphene, preserving them from desorption without disrupting the extended π conjugation on graphene, creating sp^3 hybridized carbon atoms or lattice defects.

Nevertheless, it has yet to be unambiguously demonstrated that such spacers effectively prevent the covalently bound bioreceptors from denaturation. Indeed, PBASE lacks the ability to precisely control both the distance and orientation of the pendant functionality relatively to the surface of graphene, due to the presence of a rotational degree of freedom along the carbon chain (Figure 1.29.a). As a consequence, the receptors attached to monovalent linkers can possibly stack to the graphene surface and undergo loss of their functionality.

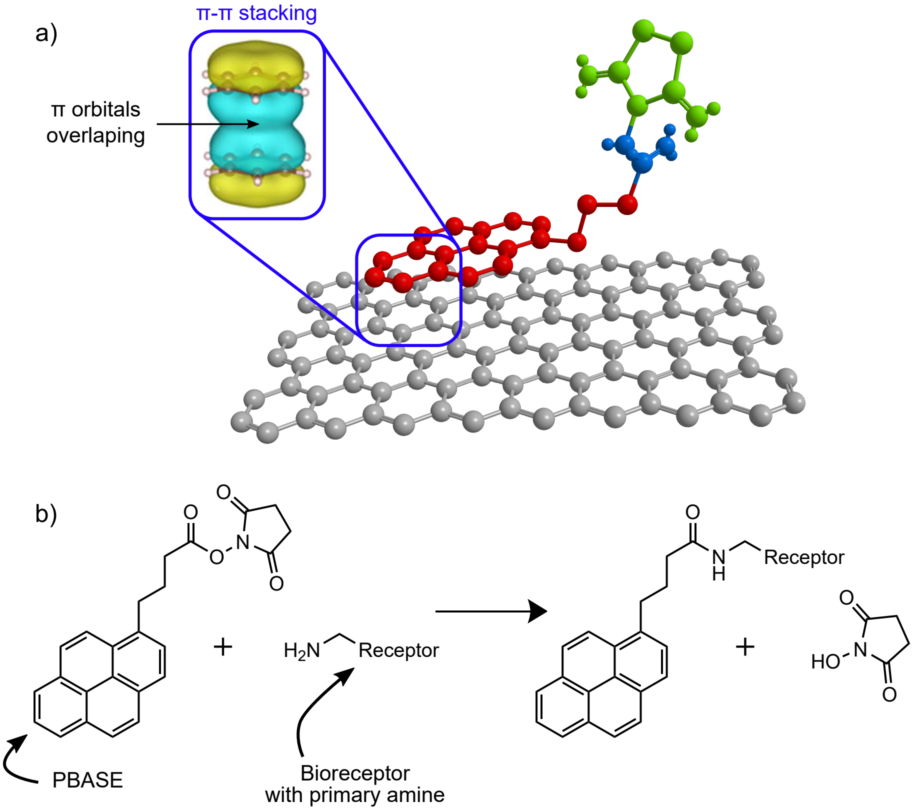

Figure 1.28: a) PBASE interacting with graphene by π-π interactions (orbitals from [205]), b) Chemical reaction of bioreceptor grafting to PBASE by nucleophilic attack of the primary amine on the NHS leaving group.

Tripod

Through a collaboration between LETI and Pr. William Dichtel from Northwestern university, initiated in our team, an innovative linker molecule called "tripod" (Figure 1.29.b), was designed to counter disadvantages of PBASE. The tripod can bind multivalently to the graphene surface thanks to three pyrene feet and effectively project its active functionality away from the graphene surface [5].

In particular, an electrochemically active redox complex ($[Co(tpy)_2]_2^+$) was incorporated to the tripod to measure its binding constant and surface coverage on a graphene electrode through electrochemical observation of the Co^{2+}/Co^{3+} redox couple. First, cyclic voltammetry experiments performed at varying scan-rate showed a quasi-reversible charge transfer kinetic between the redox probe and the graphene surface, indicating that the tripod is well confined to the graphene surface. The surface adsorption of both tripod and PBASE motifs, characterized by Laviron analyses, indicated a slower charge transfer rate for the tripod, consistent with the

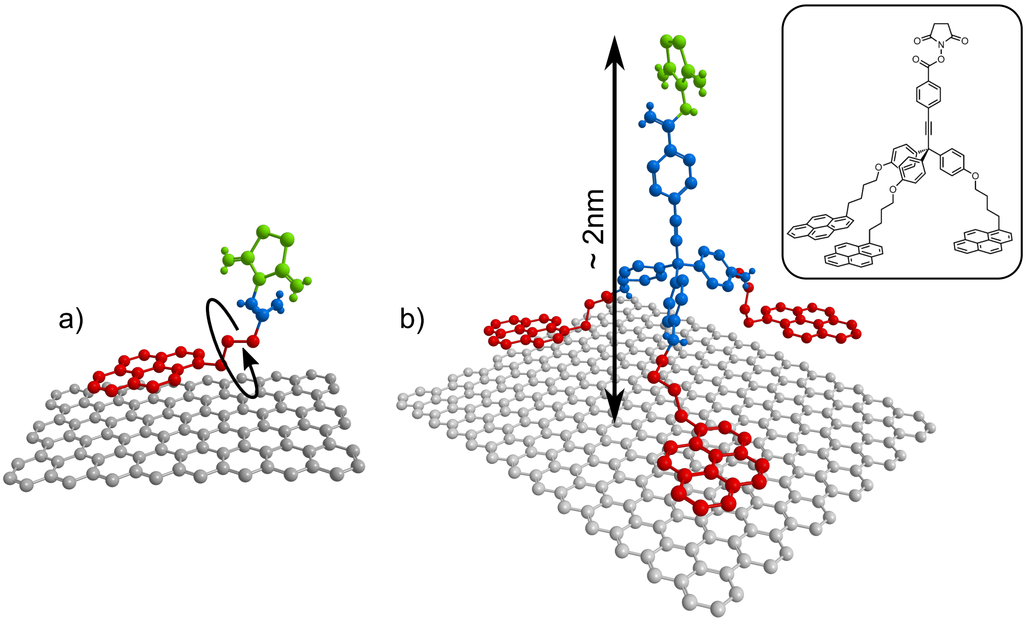

Figure 1.29: a) Presence of a rotational degree of freedom along the carbon chain of the PBASE linker, b) Representation of the tripod linker stacked on graphene thanks to its three pyrene feet (red) projecting its functionality (green) away from the graphene surface. The atomic structure is shown in inset (from [206]).

hypothesis that the multivalent motif projects its redox center further away from the graphene electrode surface compared to the monovalent model compound.

This hypothesis was further confirmed when exploring the influence of different molecular "foot motifs" (phenanthrene, naphthalene, or pyrene) (Figure 1.30) on the tripod molecular packing density and monolayer stability when exposed to organic solvents under infinite dilution conditions [207]. Indeed, a 2.3 nm^2 molecular footprint was extracted for the tripod with pyrene feet, and 1.7 nm^2 for PBASE which is significantly larger than the footprint of a single pyrene moiety (∼0.7 nm^2). This observation is consistent with the hypothesis that PBASE is likely to lie flat on graphene to maximize its Van der Waals interactions with the surface. In contrast, the tripod adopts an upright configuration, allowing for an improved orientational control of its functionality while maintaining comparable surface coverage. In addition, the tripod compound with pyrene feet was found to be exceptionally stable, as it retained 86 % of its initial coverage after 12 h, while the PBASE compound desorbed 1000 times faster in tetrahydrofuran (THF). The tripod stability was also confirmed in aqueous environment [208].

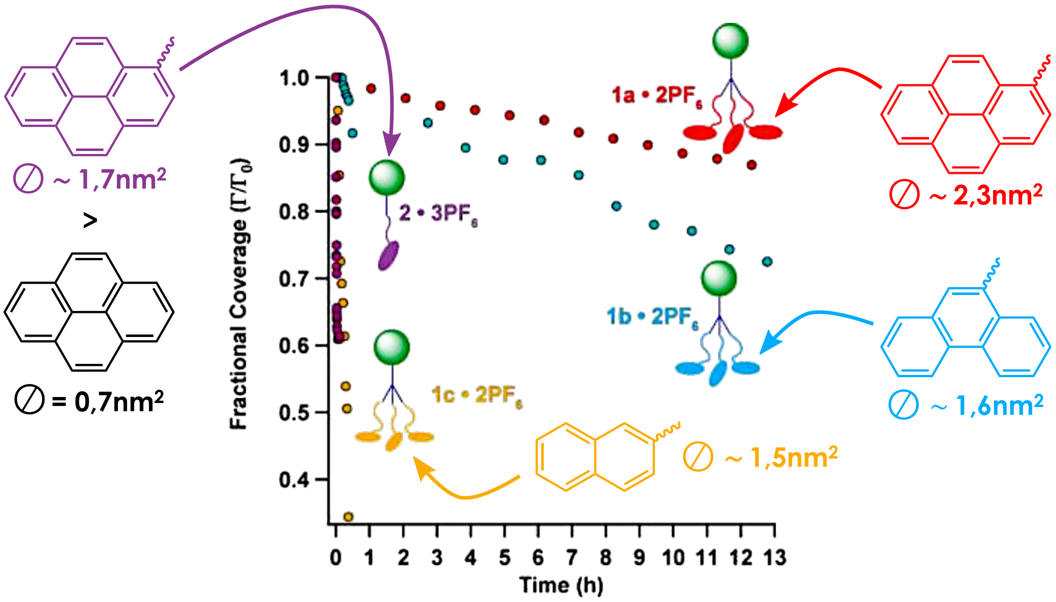

Figure 1.30: Stability of tripodal compounds with different foot motifs, compared with the PBASE (purple), under infinite dilution conditions. The calculated molecular footprints corresponding to each motif are indicated (from [207]).

In order to demonstrate that the tripod can effectively maintain biological objects onto graphene and preserve them from denaturation, anti-E.Coli antibodies were immobilized onto the tripod, onto PBASE, and without any linker by direct adsorption onto graphene [206] (Figure 1.31). The ability of anti-E.Coli antibodies to specifically recognize and bind to E.Coli cells was assessed under these different conditions, plus under two additional control tests : the first one consisting of tripods conjugated with a mismatched anti-BSA antibody, while the second one consisted of amide-tripods incapable of bioconjugation with anti-E.Coli antibodies. Once exposed to E-Coli cells, only the graphene surface functionalized with the functional tripod showed a cell density distinguishable from negative control experiments, demonstrating that anti-E.Coli antibodies exhibited little, or no specific E.Coli cell recognition when adsorbed onto bare graphene or conjugated to the PBASE linker. Yet they fully retained their function when conjugated to the tripod.

Similar results were obtained for proteins [4] and enzymes [209], with a biofunctionality preservation observed for tripod modified graphene surfaces, and a loss of activity or inhibition induced by structural changes for PBASE modified and bare graphene surfaces. The functionalization of graphene with the tripod linker is therefore a very promising bioconjugation strategy, insuring the preservation of the bioreceptors functionality, the graphene structure integrity, and the formation of a robust, stable and predictable biorecognition layer.

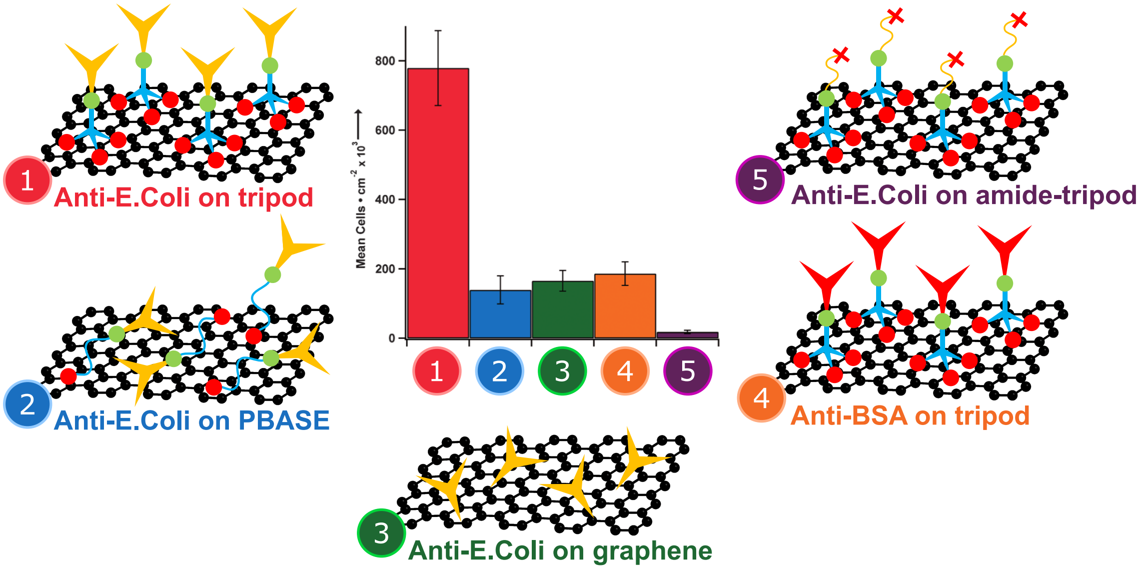

Figure 1.31: Captured E.Coli density for different graphene functionalized surfaces. Only the tripod functionalized surface shows a distinguishable response from negative controls (tests n°4 and 5) (adapted from [206]).

1.4 Conclusion

In this chapter, a brief overview of the context of graphene-based biosensors have been proposed. Due to its excellent electronic conductivity and an ultimate specific surface area, graphene appears to be an highly promising transducer material for the detection of biological objects in liquid environment. In particular, the SGFET architecture allows to fully exploit the potential of this unique material, benefiting from the high capacitance of the electrochemical double-layer. As for all biosensors, the graphene sensing area needs to be functionalized with bioreceptors to specifically detect an analyte in liquid. Among the different methods overviewed, the non-covalent functionalization using tripod linkers was demonstrated to be the most robust and stable technique, effectively preserving the graphene structure integrity and the bioreceptors functionality.

The objective of this thesis therefore consisted in proposing a proof of concept of tripod non-covalently functionalized graphene based SGFET for highly sensitive biosensing applications. The first challenge toward this demonstration, presented in the next chapter, was the development and optimization of a robust and reliable fabrication process of high performance SGFET devices.

Chapter 2

Fabrication of graphene SGFET

The fabrication of high-performance graphene-based devices, such as the SGFET operating in liquid environments, requires the thorough development of a robust fabrication process. Indeed, each fabrication step is critical when processing a 2D material such as monolayer graphene. Surface contamination or structural defects induced to the graphene sensing area due to a non-optimized process can drastically affect the sensor performance. During this thesis, different fabrication methods were explored to preserve the graphene layer and fulfil the requirements specification of the SGFET.

The optimized process developed and the alternative fabrication methods which were explored during this thesis will be presented in this chapter. The fabrication process was developed in a class 1000 (or ISO6) clean-room facility called "Plateforme Technologie Amont" (or upstream technological plateform) (PTA), shared by the major actors of the nanotechnology community of Grenoble and giving the opportunity to users to develop their own process according to their needs. Being flexible, this clean-room offers the possibility to work with small substrate sizes (up to 4 inches wafers), making possible the device design and fabrication process optimization through numerous iterations, at a high and fast throughput (typically, 9 chips each consisting of 38 devices within a week).

2.1 Development and optimization of SGFET fabrication process

2.1.1 SGFET structure, requirements and process flow

The architecture of the graphene-based SGFET developed in this work consists in a graphene layer electrically contacted by two in-plane metallic electrodes (namely source and drain), fabricated on a Si/SiO$_2$ substrate. The metallic electrodes are passivated with an electrically insulating material in order to limit any parasitic leakage current during the device operation in liquid. The SGFET structure is presented Figure 2.1 along with the following associated requirements specifications:

- Process robustness, reproducibility and simplicity
- Preservation of the graphene structure and integrity from lattice defects, and surface contamination by resist residues induced by the process
- Ohmic contact and low contact resistance between graphene and the metallic electrodes
- Robust and efficient electrical and physical insulation of the metallic contacts from the liquid environment of the sensor

The fabrication process was developed to fulfil as much as possible these specifications and achieve reliable and reproducible high sensor performance.

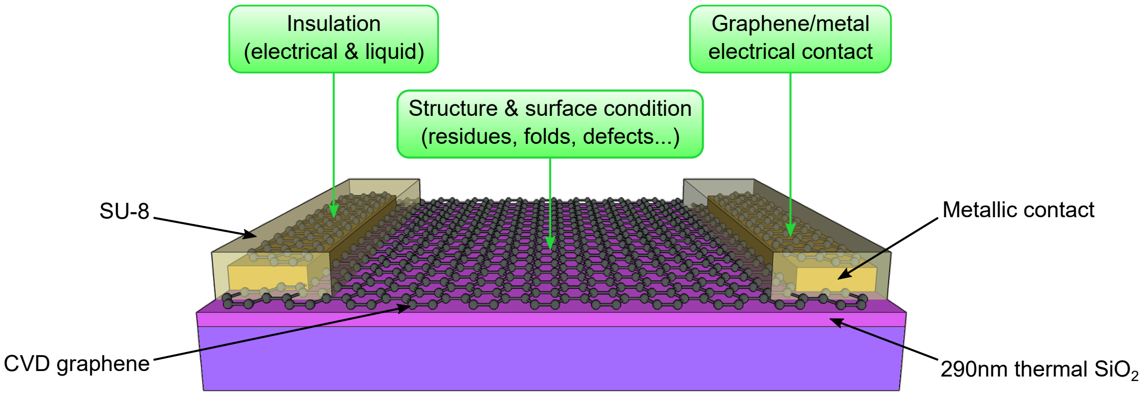

Figure 2.1: Requirements specification for the fabrication of SGFET devices.

The process developed and optimized to fabricate such structure comprise three main steps detailed in the next following subsections, summarized in Figure 2.2 and below:

1. Graphene transfer, from CVD growth Cu substrate to Si/SiO_2 substrate with pre-patterned metallic contacts, including the following steps:
    - (a) Fabrication of the metallic contacts by lift-off
    - (b) Preparation of the graphene sample (polymer supporting layer spin-coating and graphene back-etching)
    - (c) Substrate cleaning and plasma treatment
    - (d) Wet-transfer of graphene
    - (e) Supporting layer stripping
2. Graphene patterning for defining the transistors channel, including the following steps:
    - (a) Definition of the etching mask
    - (b) Etching graphene by O_2 plasma
    - (c) Mask stripping
3. Contact passivation and definition of the graphene sensing area

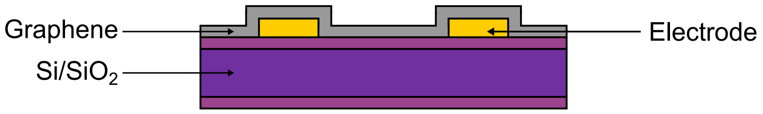

(a) Graphene transfer onto the substrate of interest.

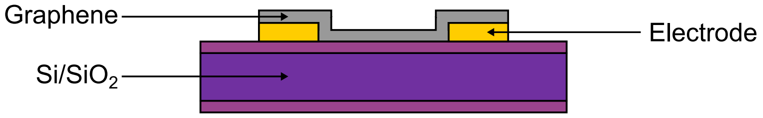

(b) Graphene patterning.

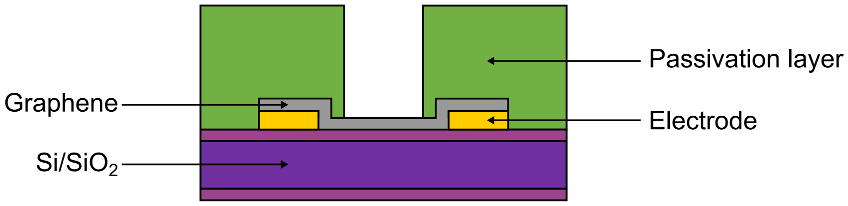

(c) Contacts passivation.

Figure 2.2: Main steps of the fabrication process developed and optimized.

2.1.2 Fabrication of drain and source electrodes

2.1.2.1 Substrate material considerations

For convenience during the fabrication process development, we first worked with Si/SiO$_2$ substrates. As mentioned in section 1.2.2, the atomically thin graphene layer is observable with an optical microscope under white light when deposited onto a ∼280 nm SiO$_2$ oxide layer on Si. In addition, an SiO$_2$ layer can be easily thermally-grown with sub-nanometer roughness, offering a planar surface for the graphene layer. Devices fabricated on Si/SiO$_2$ substrates with a p-doped Si bulk can also be operated as back-gated FETs in order to extract the charge carrier mobility.

2.1.2.2 Electrical contact surface considerations

Historically, graphene was isolated by mechanical exfoliation of HOPG on Si/SiO$_2$ substrate [120]. Because the location of the graphene layers were spatially determined by the method itself, the metallic contacts were thus fabricated on top of graphene, requiring a lithographic step before the metal deposition. Graphene is therefore exposed to a resist layer during this process, contaminating its surface with polymeric residues. Such resists residues are then trapped between the metal and graphene (Figure 2.3.a)), resulting in high device contact resistance. This non-reproducible surface contamination of the metal/graphene interface is also the source of large variations of the reported contact resistivity values [210].

Since large area CVD graphene is now commonly available, the fabrication of metallic contacts on top of graphene is no longer inevitable. Graphene can be then transferred on top of the metallic contacts right after their fabrication, preserving the graphene surface from resist residues. This method has the superior advantage to precisely control the cleanliness of the metal/graphene interface, since it is possible to perform any cleaning and/or surface treatment of the substrate prior to the graphene transfer. In addition, the graphene surface in contact with the metal is never exposed to resist during the process, assuring more consistent and reproducible contact resistivity values, as reported by Bharadwaj *et al.* [210] (Figure 2.3.b).

In the light of the reproducibility, robustness and simplicity benefits inherent to the graphene-on-metal architecture, we chose to transfer graphene on top of Si/SiO$_2$ substrates with pre-patterned metallic contacts for the first main step of the fabrication process.

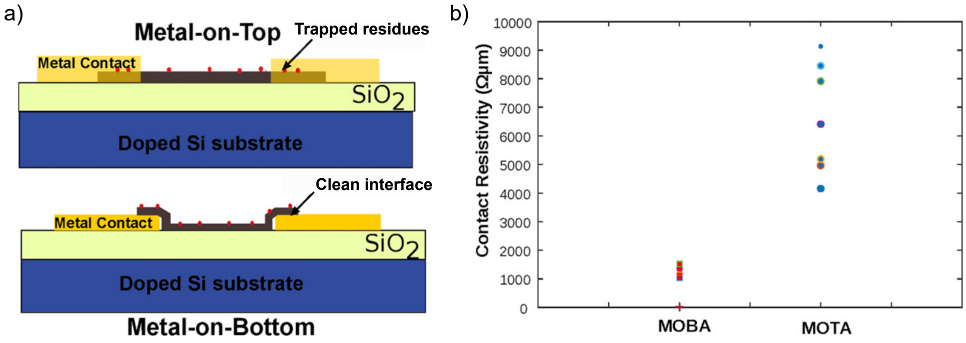

Figure 2.3: a) Comparison of metal-on-graphene (MOTA) (top) and graphene-on-metal (MOBA) (bottom) architectures and b) the associated contact resistivity values (adapted from [210]).

2.1.2.3 Contact material considerations

The contact resistance between graphene and the metallic contacts is a limitation of the device performance, hindering the exceptional electronic conductivity of graphene. Several mechanisms are involved in the graphene-metal contact resistance.

First, when graphene is brought into contact with a metal, its work function (∼4.5 eV) is pinned to the same value as the one of the metal. The resulting work function difference leads to a charge transfer at the graphene-metal junction (Figure 2.4.a), and the formation of an interfacial dipole increasing the contact resistance [211]. Moreover, the metal-graphene interaction shifts the Fermi level of the graphene in contact with the metal, potentially creating a p-n junction with the uncovered graphene (Figure 2.4.b). Depending on the material used, this phenomenon can significantly increase the contact resistance and induce a strong asymmetry between the electron and hole conduction [212].

As a consequence, a number of studies have focussed on graphene-metal interface engineering in order to achieve a low contact resistance, such as ozone/ultraviolet surface treatment of graphene [213], rapid-thermal-annealing of graphene-metal contacts [214], or contacting graphene along the edges [215, 216]. In particular, Song *et al.* observed that in the case of Au and Pd contacts, the graphene work function is pinned to an intermediate value of (∼4.6 eV), resulting in lower contact resistance [217]. Despite the fact that Pd shows a lower contact resistance with graphene than Au, Au was used for its permanent availability within the PTA facility and lower cost.

In particular, the metallic electrodes fabricated onto Si/SiO_2 substrates by lift-off during this work consisted of a 80 nm thick Au layer deposited over a 15 nm chromium (Cr) adhesion layer.

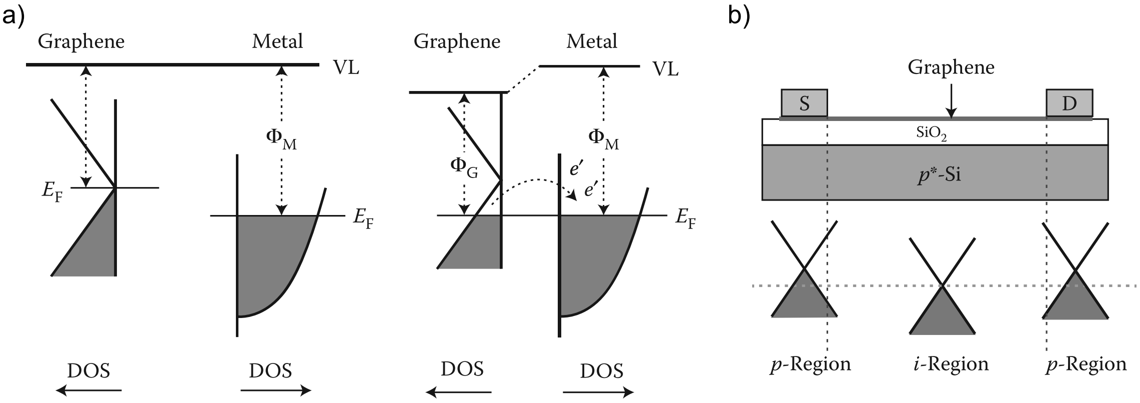

Figure 2.4: a) Energy dependency on DOS of graphene and metal without any interaction (left), and in contact (right), highlighting the resulting charge transfer between graphene and metal due to bands alignment (adapted from [218]), b) Schematic of back-gated graphene-based FET, showing the differently doped regions, the graphene channel doping being tuned by applying a gate bias, thus inducing p-n junctions.

2.1.2.4 Chip & device designs

As mentioned in section 1.2.3, the transistor channel width (W) and length (L) directly affects the electrical sensitivity of the device. In particular, the sensitivity is directly proportional to the aspect ratio W/L. Therefore, high electrical sensitivity can be achieved with devices having a high W/L ratio. The device area is also a parameter of importance, as it defines the the number of immobilized bioreceptors at the sensor surface which directly influences the target binding kinetics. Thus, a versatile set of devices with varying W/L ratio and channel area was designed to cover eventual different needs (Appendix: Devices design). Two sets of TLM structures, each consisting of 5 devices were added to this set in order to electrically characterize any fabrication induced effect on the graphene contact and sheet resistance.

The whole set of 38 devices fits at the bottom of a 2 cm × 2 cm chip, for immersion in liquid of the sensing area (∼8 mm × 5 mm), while the top of the chip is dedicated to wire-bonding (section 4.2.1) thanks to large pads connected to the devices by metallic tracks with a 40 µm width (Figure 2.5). Typically, 9 chips can be produced from a 4" Si/SiO_2 wafer.

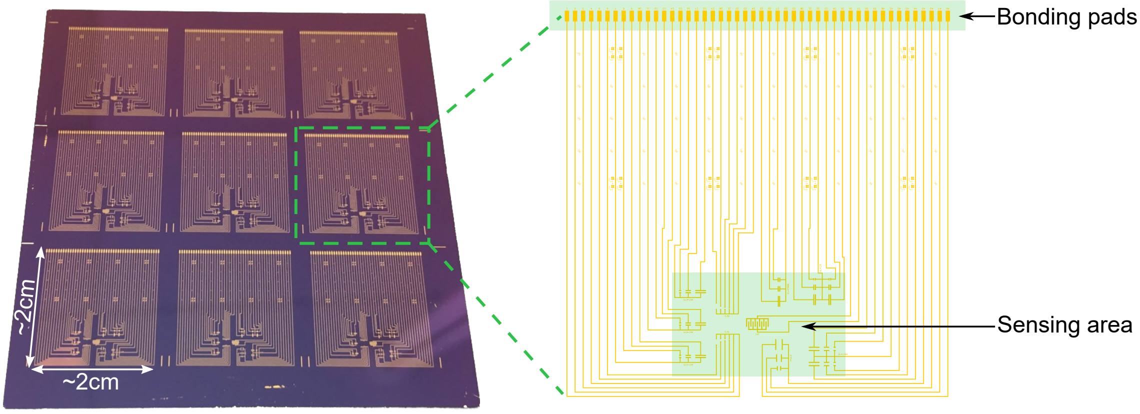

Figure 2.5: (left)Layout of the 9 chips fabricated on a 4 inches wafer and zoomed view (right) of a single chip showing the bonding and sensing area.

2.1.2.5 Substrate preparation & microfabrication of metallic contacts

200mm diameter, 725 µm thick, p-doped Si wafer (1-10 $\Omega.cm^{-1}$) with a (100) crystalline orientation were thermally oxidized in an O_2/HCl atmosphere at 1050 °C for 4h40 to provide a 295 ± 2 nm thick SiO_2 layer. The 200mm wafers were then diced into 70 mm × 70 mm (squared 1/4 of wafer) as the PTA equipments are limited to sample size up to 100mm. A cleaning step was performed on each wafer in order to insure the complete removal of dicing residues prior to any process. This second cleaning step consisted in dipping into a succession of solvents:

- Acetone at 25 °C for 10min in ultrasound (US) to remove Si dicing residues followed by a quick rinse in fresh acetone
- isopropyl alcohol (IPA) at 25 °C for 10min in US to remove the acetone from the sample surface followed by a quick rinse in fresh IPA
- Rinsing in DIW to remove IPA traces

The metallic electrodes were fabricated using a "lift-off" procedure. First, a 1.2 um positive resist (AZ1512HS) is spin-coated on the wafer using standard parameters. The wafer is soft-baked at 100 °C for 60 s on a hotplate to remove the excess of residual resist solvent before the UV exposure. The sample is then exposed to UV (365 nm) for 25 s using a MJB4 mask aligner (filtered at 6 $mW.cm^{-2}$). The exposed resist area are removed in a tretramethylammonium hydroxide (TMAH) based developer for 30 s, followed by a 1 min DIW rinse, revealing the patterns of the future metallic electrodes within the resist layer. Subsequently, the 15 nm Cr adhesion layer and the 80 nm Au layer are deposited over the sample, with an electron-beam evaporator, after a short Ar plasma to insure the cleanliness of the exposed substrate area. The Cr and Au deposition rate are respectively 0.1 nm.s^{-1} and 0.25 nm.s^{-1}. Finally, the sample is immersed in an acetone bath for at least 2h, in order to dissolve the sacrificial resist layer and reveal the metallic contacts. This step is followed by a 15 s short sonication step in fresh acetone, 5 min rinsing in fresh IPA and in DIW to remove resist residues. The sample is then diced into 9 individual chips, to make the handling easier for the wet-transfer of graphene films locally onto the sensing area.

2.1.3 Graphene transfer and PMMA stripping

This thesis work was achieved using two sources of CVD graphene. The major part of the fabrication development was achieved using high-quality graphene kindly produced and provided by the team of Vincent Bouchiat from the Néel Institut in Grenoble [143]. For supplying reasons, the other part of this work, including the fabrication and devices characterizations, and biosensing experiments was achieved using graphene bought from one of the largest European manufacturer, GRAPHENEA.

This subsection will present the first main step of the graphene processing: the transfer of graphene onto the substrate of interest (Figure 2.2a). Before transferring graphene, some precautions are necessary regarding both the surface state of the substrate, and the graphene sample preparation after its CVD growth. The following sections will detail them, as well as the transfer process established during this thesis.

2.1.3.1 Graphene sample preparation

During the CVD growth, both sides of the Cu foil are exposed to the gas flow, thus a second graphene layer grows from the bottom side (Figure 2.6a) that is necessary to remove before the transfer of the top layer. Prior to the the graphene bottom layer etching ("back-etching"), the top layer is first protected with a PMMA supporting layer.

PMMA coating

A ~70 nm PMMA layer (950K, 2% in ethyl-lactate) is spin-coated over the top graphene layer (Figure 2.6b), using standard parameters.

The Cu foil goes through significant surface reconstruction and tends to roughen due the high temperatures reached during the CVD growth process. The graphene growing at the surface follows the roughness of the underlying metal [219]. As a consequence, when graphene is transferred onto a flat surface (such as SiO_2), small gaps forms between the two surfaces, inducing folds and cracks and resulting in a non-continuous graphene coverage when stripping the PMMA layer. In order to improve the continuity of the transferred graphene layer, the contact area between graphene and the substrate must be maximized. Therefore, the supporting layer must be soft enough to allows graphene to relax and adapt to any rough features at the substrate surface, and robust enough to provide sufficient mechanical support during the transfer [220].

The sample is thus left to dry at room temperature overnight after PMMA spin-coating, in order to let the resist solvent slowly evaporate, preventing the PMMA layer to harden and improving the contact between graphene and the substrate [221].

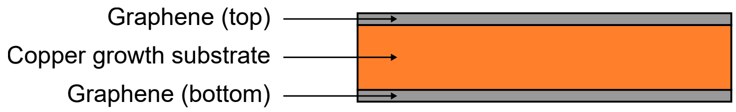

(a) Graphene sample after the CVD growth on Cu.

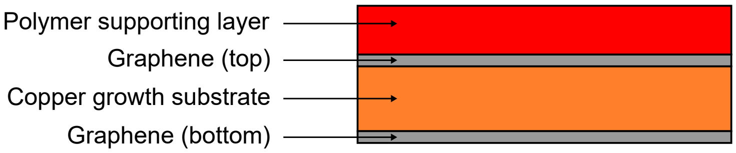

(b) Spin-coating of a PMMA supporting layer on top of the top graphene layer.

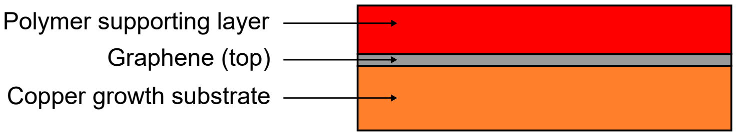

(c) Etching of the bottom graphene layer.

Figure 2.6: Sequential steps constituting the preparation of the graphene sample after the CVD growth on Cu, prior to the transfer on the desired substrate.

Back-etching

After PMMA drying, the graphene bottom layer was etched (Figure 2.6c) under an Ar/O_2 plasma in a RIE-Inductively Coupled Plasma (ICP) chamber:

- Gas flow: Ar (20 sccm)/O_2 (80 sccm)
- Pressure: 10 mtorr
- $P_{ICP} = 600\,W$
- $P_{RF} = 0\,W$

In particular, the RF power (P_{RF}), which controls the ion bombardment of the substrate, was set to 0 W to prevent further PMMA hardening due to excessive sample heating. The plasma etching time was extended to 2.30 min to insure the complete removal of the bottom graphene layer [222], as confirmed by Scanning Electron Microscope (SEM) and Raman spectroscopy (Figure 2.7)

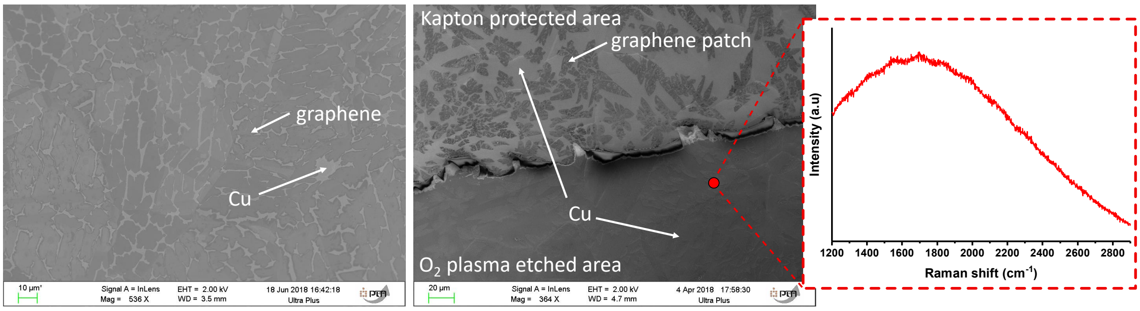

Figure 2.7: SEM observation of the non-continuous graphene bottom layer: before etching (left), after O_2 plasma etching (right), at the junction between an area protected from the plasma by kapton tape and an unprotected area. The absence of any graphene-related Raman peaks between 1200 cm^{-1} and 2900 cm^{-1} in this area indicates the complete removal of graphene. The background observed is due to the fluorescence of Cu.

2.1.3.2 Substrate surface state preparation

In a last step, the graphene/PMMA stack floating at the surface of water is scooped out with the Si/SiO_2 substrate (Figure 1.15). The substrate wetting will have a strong influence on the quality of the graphene transfer. Indeed, if the liquid on which the graphene/PMMA stack floats doesn't wet properly the substrate surface (contact angle > 0, high surface tension), some liquid can remain trapped between graphene and the substrate during drying, generate folds and micrometer cracks

(Figure 2.8.b). However, if the liquid wet perfectly the surface and forms an homogeneous film (contact angle ∼ 0, low surface tension), the graphene/PMMA stack can lie flat onto the substrate, preventing the liquid to be trapped (Figure 2.8.a). The homogeneous drying of the stack onto the substrate induces much less folds and cracks, resulting in a higher graphene continuity and a lowered surface roughness [223].

In our experience, an higher graphene continuity results in an enhanced resistance to the chemical solvent exposure, which is inevitable in the next steps of the process. This higher resistance can be explained by a limited graphene edge area where the solvent can induce graphene lift-off from the substrate. As a consequence, we have observed that the graphene final quality, the process robustness and the device performance reliability strongly depends on the surface state of the substrate right before the transfer.

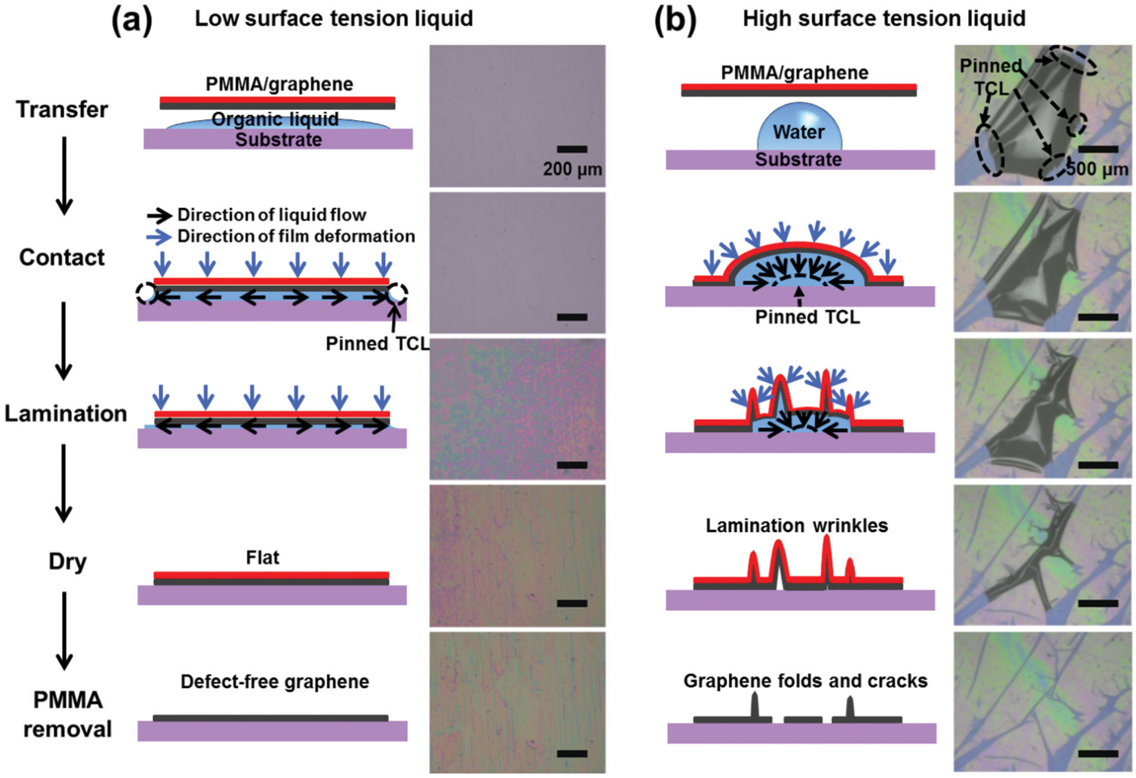

Figure 2.8: Influence of the surface tension of the liquid interfacing the substrate and the PMMA/graphene stack on the quality of the graphene transfer (from [223]). a) Liquid wetting the surface, resulting in "defect-free" graphene. b) Non-wetting liquid leading to folds and cracks to the graphene layer transferred.

In our case, the target substrate is an Si/SiO_2 individual chip with pre-patterned metallic electrodes. The SiO_2 surface is composed of Si−O−Si chemical bonds which shows a limited affinity to water molecules due to the absence of hydrogen bonds. As a consequence, water doesn't wet completely SiO_2 surfaces. The hydrophilicity of SiO_2 surfaces can be greatly improved in a two step surface treatment procedure:

1. Removal of hydrophobic organic contamination by "Piranha" cleaning [224]:
    - 10 min cleaning in a mixture composed of 1 part of hydrogen peroxide (H_2O_2) and 2 parts of sulfuric acid (H_2SO_4) heated at 140 °C in a quartz bath
    - 10 min long DIW rinsing in a "quick dump rinsing" bath to prevent the redeposition of particles on the surface
    - N_2 blow drying
2. O_2 plasma treatment, performed in a parallel plate RIE chamber, right after the "Piranha" cleaning. This plasma further remove surface contamination and create Si-OH bonds [225] capable of hydrogen bonding with water molecules, improving the substrate hydrophilicity:
    - 2 min exposure to a Ar (2.5 sccm)/O_2 (10 sccm) plasma at 120 W

As it can be seen from Figure 2.9, the Si/SiO_2 surface is effectively more hydrophilic (decrease of the contact angle) after "piranha" cleaning. However, the plasma step is necessary to achieve a complete water wetting of the surface (non-measurable contact angle). The surface treatment procedure was always performed right before the transfer step, as the effect is limited in time, due to the contamination by ambient particles. The Cr/Au electrodes were not damaged by this harsh surface treatment, as confirmed by profilometry measurements.

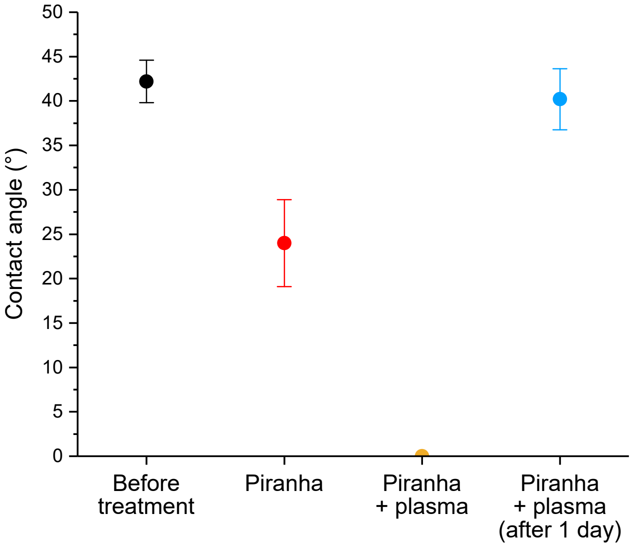

Figure 2.9: Combined effect of the "Piranha" cleaning with the plasma surface treatment on the contact angle of water with the surface of Si/SiO$_2$ single chips. Each point represents 5 measurements.

2.1.3.3 Graphene wet-transfer

The conventional wet-transfer technique was described in section 1.2.2.2, and the main steps are summarized Figure 2.10. The first step consists in etching the Cu growth substrate using an oxidative solution. Metallic impurities are then rinsed in DIW before the final transfer.

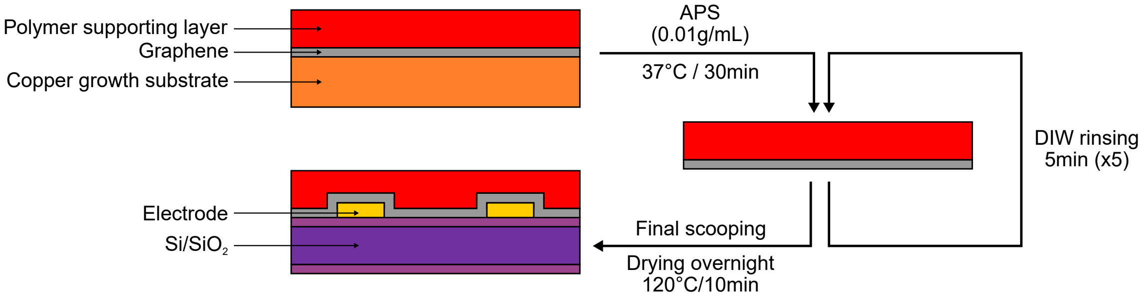

Figure 2.10: Schematic of the graphene transfer, from its growth substrate to the individual chip, starting with the Cu growth substrate etching, followed by repeated rinsing steps and finally the transfer of PMMA/graphene onto a single chip with pre-patterned electrodes.

Cu-etching

Cu can be etched in oxidative solutions such as iron nitrate ($Fe(NO_3)_3$), iron chloride ($FeCl_3$), sodium persulfate ($Na_2S_2O_8$) or ammonium persulfate ($(NH_4)_2S_2O_8$). $FeCl_3$ have been widely used among the groups working with CVD graphene, since it was commonly used in the printed-board industry [220, 226–228]. However, Wu *et al.* [229] and Yu Wang *et al.* [230] showed that the iron-based Cu etchants induce a strong p-doping of graphene, leading to high V_{Dirac}. Iron oxides and oxyhydroxides formed during etching also adsorb onto graphene and act as charge scattering centers. In the other hand, Cu etching in $Na_2S_2O_8$ or $(NH_4)_2S_2O_8$ results in cleaner graphene [137, 230], but Han Zheng demonstrated that $Na_2S_2O_8$ induced structural disorder, resulting in a degradation of the charge carrier mobility and a sheet resistance increase [231].

Therefore, $(NH_4)_2S_2O_8$ was used as Cu etchant during this thesis. A piece of the Cu/graphene/PMMA sample is first cut with dimensions slightly larger than the chip sensing area (∼9 mm × 6 mm), laid at the surface of the liquid etchant and heated at 37 °C on a hotplate to increase the etching rate. In our experience, the Cu film is longer visible after ∼6 min, indicating that the Cu bulk was etched. To insure the complete removal of Cu, the etching time is extended to 30 min. The temperature is limited to 37 °C in order to prevent the formation of bubbles under the graphene film that may result in non-homogeneous etching.

Rinsing

After 30 min, the beaker containing the floating graphene/PMMA film is removed from the hotplate. Since the etching solution contains metal ions, it is necessary to rinse the film prior to transferring it onto the final substrate. These impurities act as charge scattering centers degrading the electronic transport properties of graphene [221] and impacting its electrochemical properties [232]. The graphene surface is rinsed by repeatedly transferring the graphene/PMMA stack at the surface of large beakers containing DIW, in order to sequentially dilute and rinse off these residues.

The graphene/PMMA stack is transferred from one water bath to the next one by using an intermediate substrate, a small piece of Si/SiO_2 prepared with the same protocol as the target substrate. In particular, attention is paid not to let the water film separating the graphene from the SiO_2 surface to dry, in order to avoid damaging graphene.

These rinsing steps were repeated five times in our transfer process, each rinsing step during at least 5 min.

Transfer on the target substrate & Drying

After the final rinsing step, the graphene/PMMA stack is scooped with the target substrate to complete the transfer procedure. Finally, the sample is left to dry overnight at room temperature to insure that the graphene/PMMA stack can slowly fit to the substrate roughness and its features (here the metallic contacts), while inducing a minimal strain and preventing water to be trapped. Before striping the PMMA layer and moving on with the next fabrication step, the chip is baked at 120 °C for 10 min on a hotplate (Figure 2.11), to slightly re-flow the PMMA layer and improve the adhesion of graphene on the substrate [219].

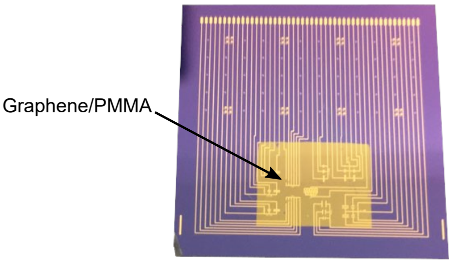

Figure 2.11: Picture of a graphene/PMMA stack transferred onto a chip after drying, and annealing on a hotplate.

2.1.3.4 PMMA stripping in organic solvent

The PMMA supporting layer stripping is a critical step in graphene processing (Figure 2.12). PMMA is usually dissolved in chemical solvents, acetone being the most popular as it is commonly employed in any micro/nano-fabrication process to dissolve photoresist layers or clean substrates from organic residues. During this thesis, we explored the use of another organic solvent to strip the PMMA supporting layer: THF. It is a moderately polar cyclic ether, miscible in a wide range of polar and non-polar chemical compounds (including water as opposed to acetone), and have already been used to dissolve PMMA [233, 234]. However, to the best of our knowledge, it has never been used to remove PMMA from the graphene surface.

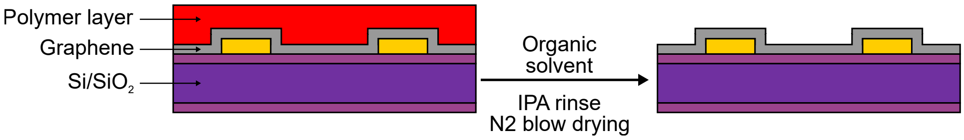

Figure 2.12: PMMA stripping step in organic solvent.

As a first approach into finding a chemical solvent capable of efficiently dissolve a polymer, comparing the Hildebrand solubility parameter (δ) of the solvent and the polymer gives a good prediction of their physical interactions. Indeed, two substances are mutually soluble and thermodynamically compatible if the associated free energy of mixing ΔG_M is negative [235]. ΔG_M is related to the enthalpy of mixing ΔH_M and the entropy of mixing ΔS_M through:

$$\Delta G_M = \Delta H_M - T\Delta S_M \tag{2.1}$$

As the variation of entropy between the new equilibrium state of the mixed substances and the equilibrium thermodynamic state of each substances separated is typically positive, ΔG_M sign is determined by the amplitude of the term ΔH_M, which is described by the Hildebrand equation:

$$\Delta H_M = V_S \phi_1 \phi_2 (\delta_1 - \delta_2)^2 \tag{2.2}$$

where V_S is the volume of solution, ϕ_i is the volumetric fraction of the substance i and δ_i its associated solubility parameter.

As it can be seen from Equation 2.2, ΔH_M strongly depends on the absolute difference of the solubility parameters of the two substances. In particular, ΔG_M is minimal (the solubility is maximal) if their respective δ values are equal. Typical values of acetone, THF and PMMA solubility parameter give the following differences [220, 235, 236]:

$$|\delta_{PMMA} - \delta_{acetone}| \sim 0.7\ MPa^{1/2}$$
$$|\delta_{PMMA} - \delta_{THF}| \sim 0.4\ MPa^{1/2}$$

In a first approximation, the lower difference of solubility parameters between PMMA and THF indicates that THF would be more efficient in solubilizing PMMA than acetone, and therefore could results in a cleaner graphene surface after PMMA stripping. With a view to optimize the fabrication process, the stripping of PMMA was tested in both acetone and THF solvents.

PMMA is typically stripped in acetone overnight, the sample is then rinsed in IPA and carefully dried by N_2 blowing. In the case of THF, the PMMA stripping time had to be optimized, since in our experience long exposure to THF induced some graphene lift-off. In particular, the PMMA stripping time was limited to 20 min, the sample rinsed and dried following the same method as for the stripping in acetone.

The quality of the graphene film transferred in terms of surface coverage, residues and folds strongly depends on the substrate surface state (cleanliness and hydrophilicity) and the graphene sample preparation (PMMA heat treatments). Both can affect the adhesion of graphene and introduce large macroscopic defects, which combined, can drastically decrease the graphene resistance toward the organic solvent exposure necessary for PMMA stripping. An optimal graphene adhesion is particularly required when stripping PMMA in THF, since it can induce graphene lift-off. Longer or higher temperature heat treatments can improve the adhesion of graphene, but also cure the polymer supporting layer, which is then harder to solubilize and leaves more surface residues after stripping. Accordingly, the optimization of the first part of this fabrication process is a complex and limited set of optimal conditions, regarding both the preparation of the substrate and graphene sample prior to the transfer, and the graphene transfer itself.

An illustration of how these conditions affect the resulting graphene layer is shown Figure 2.13. On the left picture, large folds, residues covering the whole surface and large defects can be observed after PMMA stripping in acetone, consequently to non-optimized PMMA heat treatment. Cu residues are also observed due to incomplete etching in $FeCl_3$. On the right picture, graphene was transferred using the previously described process, except that PMMA was not baked after the overnight drying step. As a result, the graphene surface is relatively cleaner, but a low surface coverage is obtained after PMMA stripping in THF due to the poorer adhesion of graphene. Finally, before moving on with the next fabrication step, chips were baked for 5 min at 180 °C on a hotplate, to increase the adhesion of graphene with the substrate.

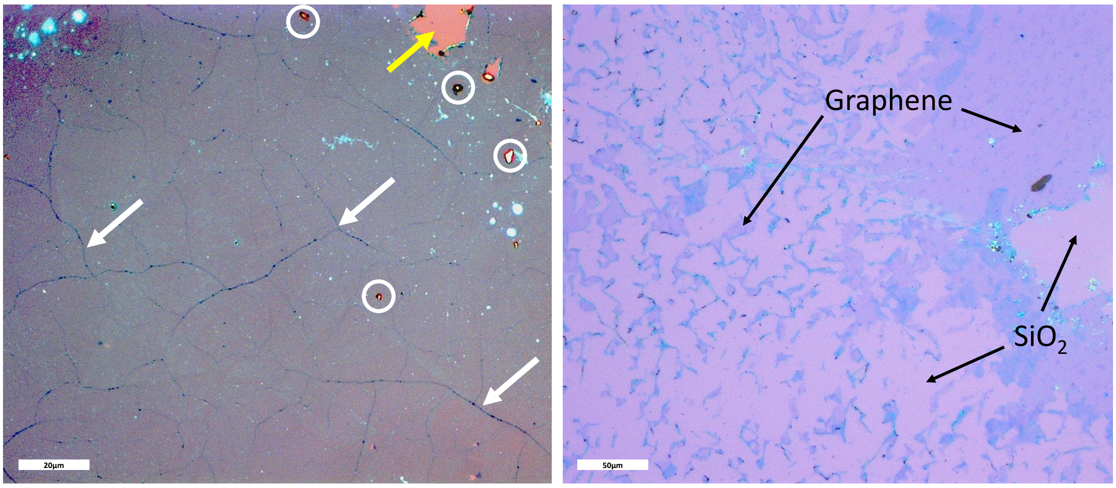

Figure 2.13: Two examples of non-optimized transfer conditions resulting in poor graphene quality. White circles shows Cu residues, white arrows large folds, yellow arrow macroscopic defect. Scale bars are 20 µm (left) and 50 µm (right)

We achieved large graphene surface coverage and low (microscopic) resist contamination through our optimized graphene transfer process, for PMMA stripping in both acetone and THF (Figure 2.14). The stripping in acetone is a reference since it has been widely used in the literature, while stripping in THF represents a new alternative which efficiency remains to be established. The PMMA stripping efficiency of these two solvents will be further discussed in chapter 3.

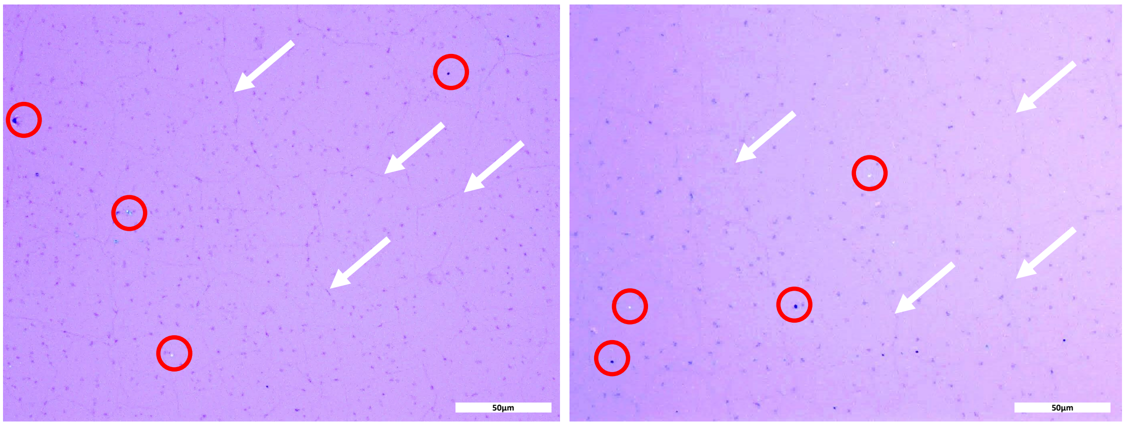

Figure 2.14: PMMA stripping in acetone (left) and THF (right) of chips fabricated with the optimized process. Red circles indicate optically visible microscopic resist residues, white arrows indicate graphene folds. The darkest, small dots covering both films are bilayer graphene patches resulting from the CVD growth (scale bar: 50 µm).

2.1.4 Graphene patterning

The patterning of graphene is the second main step of the fabrication process (Figure 2.2b). This step is necessary for isolating each transistor channel from the others, as the graphene covering the metallic tracks can cause short-circuits between the different devices. Thus the patterning of graphene enables the fabrication of a large number of devices in a limited area.

2.1.4.1 Design considerations

The transistor channel geometry should be precisely defined, as the width and length of the transistor affects the global resistance of the device. In particular, since graphene is transferred on top of the metallic contacts, the area of graphene covering the contacts dictates the contact resistance of the device. Nagashio *et al.* found that the contact resistance at the graphene-metal interface is contact width dependant rather than area dependant. Therefore the contact area between graphene and the metal shouldn't be a limiting factor in graphene-based devices [212]. However, this assumption holds only if the contact length (L_{cont}) between graphene and the metal is larger than the L_t, defined as the effective length required to inject the carriers from graphene to the metal. If L_{cont} is smaller than L_t, the whole contact area participates in the carrier injection [155].

All the metallic contacts were designed with a contact length L_{cont} of 50 µm, and variable width (W) depending of the device design (Appendix: Devices design). Graphene was patterned to cover the full contact length, which is larger than typical L_t values lying in the micrometer range.

Moreover, graphene edges show a two order of magnitude superior electrocatalytic activity than the basal plane (as discussed in section 1.3.1). As a consequence, exposing these edges within the transistor channel could results in a parasitic current, promoted by oxidative/reductive electrochemical reactions of species present in the solution. Therefore, graphene was patterned with an additional width (W_{supp}) of 50 µm relatively to the channel extremities. A typical graphene patterning design is shown Figure 2.15.

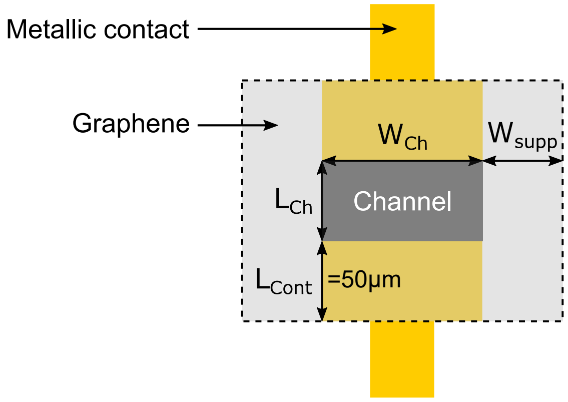

Figure 2.15: Graphene patterning design, showing the additional L_{cont} and W_{supp} to the channel extremities. Graphene edges are represented as doted lines.

2.1.4.2 Resist mask on graphene

The typical method to pattern graphene consists in protecting graphene by a resist mask, etching the exposed graphene by an O_2 plasma treatment and finally strip the resist mask in chemical solvent (Figure 2.16).

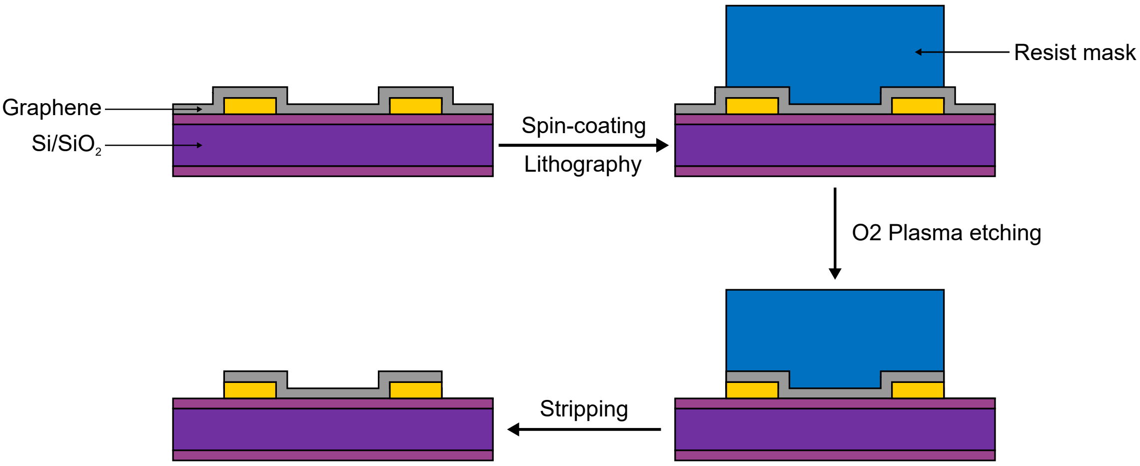

Figure 2.16: Procedure steps for patterning graphene with a resist mask.

The etching mask was pattern using a positive resist (AZ1512HS), and graphene was etched using the same RIE-ICP plasma chamber used for the back-etching step (section 2.1.3.1), with the same parameters. The resist was stripped in acetone overnight, the sample rinsed in IPA for 5 min and DIW for 1 min.

In our experience, this method resulted in optically visible resist residues covering the whole graphene surface (Figure 2.17 (left)) and/or large defects (Figure 2.17 (middle)). We could achieve optically clean and defect free graphene patterns (Figure 2.17 (right)), but it was hardly reproducible between chips processed in the same batch. Changing the gas ratio, the RF/ICP power or reducing the etching time to avoid heating effects of the resist mask didn't improve these results.

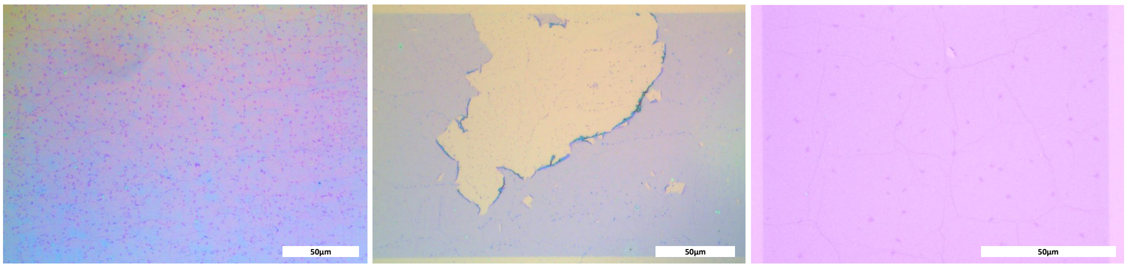

Figure 2.17: Graphene patterning using a resist mask, non-reproducibly resulting in large resist contamination (left), and/or large defects (middle), or in clean and continuous graphene pattern (scale bars are 50 µm).

The contamination of the graphene surface by photoresist residues after photolithography processing is a major problem that has been partially solved by performing annealing treatments at high temperature, under Ar/H_2 or N_2/H_2 atmosphere. Even though this technique effectively removes a large part of the resist contamination, some residues remain at the surface, due to strong van der waals interactions, or covalent bonding with graphene of radicals created at high temperature [237]. In addition, it has been reported that graphene is heavily p-doped [238], the charge carrier mobility is degraded [239–241], and large mechanical stress is induced to graphene after such treatments [240].

Instead, sacrificial metal layers such as Au [137, 242], aluminium (Al) [243, 244], titanium (Ti) [245] or Yttrium (Y) [246], have already been successfully used to protect the graphene surface from contamination induced by the resist mask during the etching step. As opposed to the post-fabrication methods cited before, the optimization of the fabrication process appears as a more reproducible and straightforward method. Therefore, we explored the use of a metal sacrificial layer to overcome the non-reproducibility issues faced with the resist mask method for patterning graphene.

2.1.4.3 Cu sacrificial layer

The removal of the sacrificial layer should ideally be trivial and not affect graphene surface state and electronic properties, the metallic electrodes, or the SiO_2 surface (which could in turn induce graphene lift-off). Ti is typically etched in hydrofluoric acid (HF), which drastically complicate the process as it is highly corrosive and toxic, and also etch SiO_2. Since graphene is transferred on top of Au electrodes, using a sacrificial Au layer is not conceivable either. Al is etched in basic solutions such as potassium hydroxide (KOH) or TMAH, which are typically used in photoresist developer. Thus etching Al could induce over-development of the resist mask and a severe loss in patterning resolution. These etchants also slowly attack SiO_2 which is not desirable. Al can be etched in acidic solutions such as phosphoric acid (H_3PO_4) or nitric acid (HNO_3) which could damage graphene. Finally, Y is less common and was not available within the PTA facility.

Instead, we introduce the use of Cu as a sacrificial layer to protect graphene from resist contamination. Cu is a common CVD graphene growth substrate which is etched during the graphene transfer step (section 2.1.3.3). Etching a Cu layer which is in contact with graphene is thus already a part of the fabrication process. Therefore, protecting the graphene surface using a Cu sacrificial layer is highly promising since it has the great advantage not to introduce a new type of contamination, and the ammonium persulfate etchant $(NH_4)_2S_2O_8$ is compatible with Au, Cr, SiO_2 or positive resists.

The global principle is presented Figure 2.18. A 100 nm layer is first deposited by e-beam evaporation over the sample, at a $0.5\,nm.s^{-1}$ deposition rate. The layer thickness value is chosen to insure that the 95 nm thick metallic contacts sides are covered, so that graphene is protected along the contacts sidewalls. Then, the resist mask is patterned on top of the metal sacrificial layer. During this thesis, two procedures were developed to etch the Cu sacrificial layer, by dry-etching using Ion Beam Etching (IBE) and wet-etching.

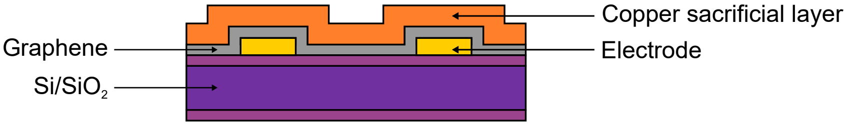

(a) Cu sacrificial layer deposition.

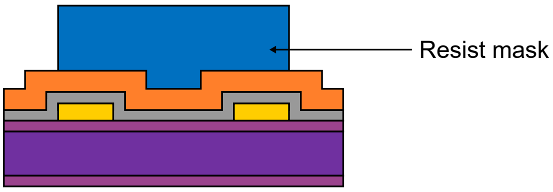

(b) Resist mask patterning.

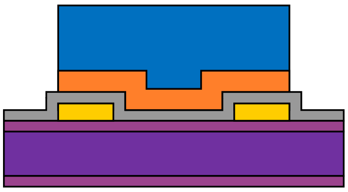

(c) Cu etching.

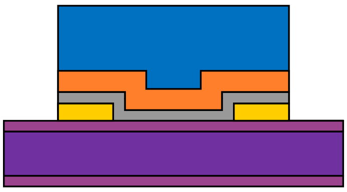

(d) Graphene etching.

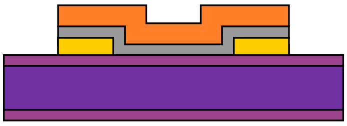

(e) Resist mask stripping.

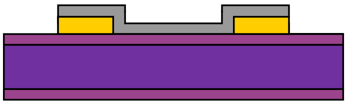

(f) Cu sacrificial layer stripping.

Figure 2.18: Procedure for patterning graphene using a sacrificial Cu layer.

Dry-etching of Cu by IBE

The Cu layer was etched with an Ar beam accelerated at 600 V, and the etching process was followed by tracking the Cu element with a Secondary Ion Mass Spectrometer (SIMS) detector. The 100 nm Cu layer was typically completely etched within 3 min. Because it is a physical etching process, the selectivity of IBE is poor, meaning that once the Cu is completely etched, the underlying graphene layer exposed to the beam can also be etched in the same process which allows to combine two fabrication steps at once. However, a graphitic layer is also formed at the surface of the resist mask during the process. As this layer is not soluble is organic solvents, a O_2 plasma is performed in order to remove the resist mask (Figure 2.19 (left)), eventually etching any graphene remaining at the surface of the substrate. Finally, the Cu mask is stripped in a 0.02 g.mL^{-1} $(NH_4)_2S_2O_8$ solution for 2 min to insure its complete removal (the 100 nm Cu bulk being stripped within 40 s). The Cu etching time was not extended to prevent a possible graphene lift-off. As it can be seen from Figure 2.19 (right), an optically clean and microscopical defect-free graphene surface can be successfully and reproducibly obtained with this technique.

While the poor selectivity of IBE is an asset for etching Cu and graphene during the same fabrication step, it represents a drawback regarding the metallic contact integrity as they are also etched. As a consequence, the resistance of the metallic tracks connecting the devices to the bonding pads can drastically increase, depending on the over-etching amplitude.

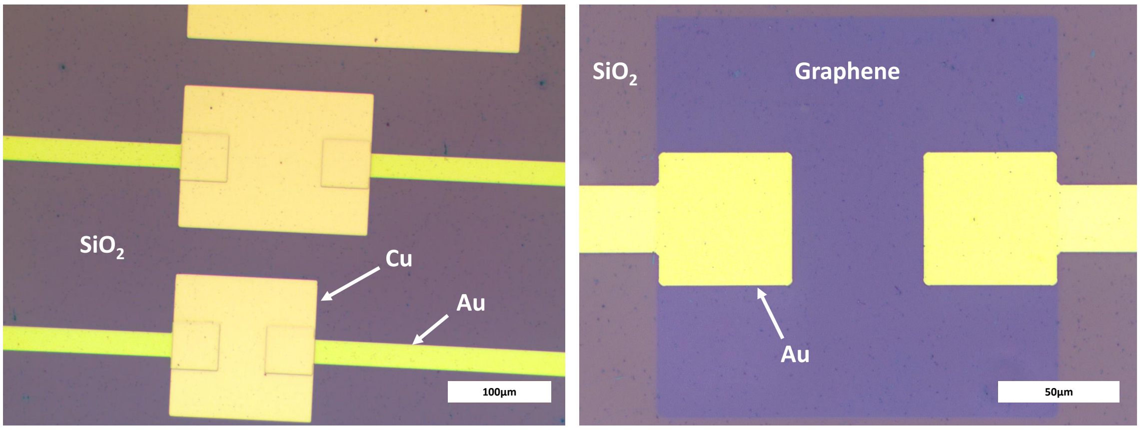

Figure 2.19: Graphene patterning using a Cu sacrificial layer, (left) after Cu etching and resist stripping, (right) after Cu stripping revealing the optically clean and microscopic defect-free graphene surface. A great contrast can be observed between graphene and the substrate, due to the etching of SiO_2 at the end of the IBE process. Scale bars are (left) 100 µm and (right) 50 µm.

Wet-etching of Cu

From these preliminary results, using a Cu sacrificial layer appears as an efficient solution to preserve the graphene surface from resist contamination. However, we developed an alternative to the Cu dry-etching process in order to preserve the metallic contact from being etched, aiming at improving the robustness and reproducibility of the fabrication process.

The Cu sacrificial layer is etched in a $0.02\,\mathrm{g.mL^{-1}}$ $(NH_4)_2S_2O_8$ solution for 60 s, and the sample rinsed in DIW to remove the metallic impurities. Wet-etching techniques are easier, low cost and highly selective compared to dry-etching techniques, but are also isotropic and can induce a large undercut. The resist adhesion is particularly problematic in wet-etching procedures, as a poor adhesion on the material being etched can result in resist delamination, drastically increasing the undercut. As a consequence, the patterning resolution is also significantly affected. As it can be seen from the micrometer undercut after Cu etching Figure 2.20 (left), the adhesion of the AZ1512HS resist on Cu is relatively low when processed under standard conditions. The adhesion of resist was greatly improved by using an adhesion promoter and an heat treatment. First, the adhesion promoter (VM652) is spin-coated on the sample prior to the resist, enhancing the resist adhesion on the oxidized copper surface. A second bake is performed right before the metal etching step, at 120 °C for 5 min to slightly re-flow the resist layer, mechanically relax the resist structure and reduce the undercut Figure 2.20 (right). This bake was limited to 120 °C for 5 min to avoid inducing mechanical stress to graphene due to mismatch thermal expansion coefficient with the top Cu layer and the SiO_2 surface.

This optimized procedure led to reproducible Cu etching and a complete protection of the whole graphene surface from contact with the resist mask. After O_2 etching of the unprotected graphene, the resist mask is easily stripped in acetone, the sample rinsed in IPA and DIW. Finally, the Cu sacrificial layer is stripped in $(NH_4)_2S_2O_8$, following the same conditions used for the dry-etching process. As it can be seen from Figure 2.21, this procedure led to large optically clean graphene surface while protecting the integrity of the metallic contacts.

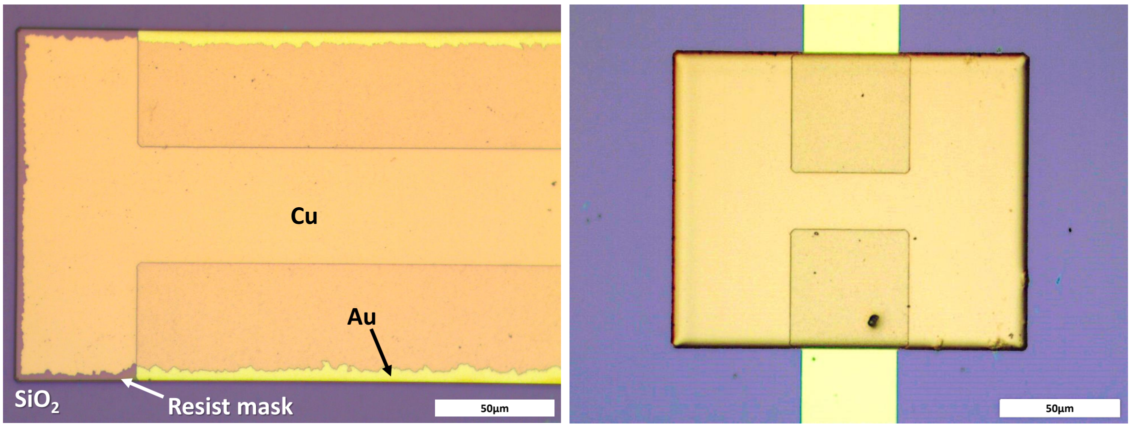

Figure 2.20: Wet-etching of the Cu sacrificial layer for graphene patterning, (left) micrometer undercut due to resist delamination, (right) resist adhesion improved by heat treatment, drastically reducing the undercut. Scale bars are 50 µm.

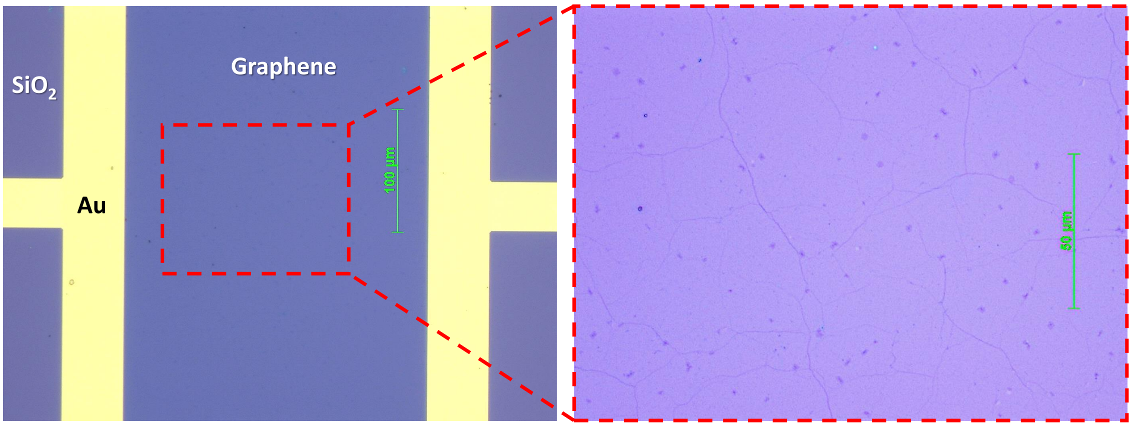

Figure 2.21: Large area, optically clean and continuous graphene resulting from the optimized patterning process using a Cu sacrificial layer. The electrodes integrity is preserved as opposed to the dry-etching process presented before. Scale bars are (left) 100 µm and (right) 50 µm.

2.1.4.4 Graphene lift-off

In addition to the aforementioned patterning procedures developed, we explored an elegant and simple technique proposed by Trung *et al.* , the graphene lift-off [247]. As opposed to deposition/etching processes, it has the great advantage to be an additive method making it simpler, cheaper and less time consuming. This technique is perfectly adapted to cases where the direct etching of the target material would induce undesirable effects to the other layers, and where no less than micrometer resolution are required.

This method (Figure 2.22), analogous to the classic lift-off procedure, consists in the following: first, a resist layer is patterned on the substrate. The material to be patterned, here graphene with its PMMA supporting layer, is deposited onto the resist. A 2 min bake at 150 °C is then performed to re-flow the photoresist and the PMMA layer supporting the suspended graphene regions, so the graphene layer is completely in contact with the substrate surface. When immersed in an organic solvent, the photoresist *and* the PMMA layer are dissolved. The graphene area which were lying on the resist are released from the surface, but still attached to the graphene regions adhering to the substrate. Graphene is subsequently cut off along the resist walls by an ultrasonic treatment, lifting-off the unwanted graphene area. Finally, the sample is rinsed in IPA and dried under N_2 blowing. This technique is extremely promising, as it combines both the stripping of the PMMA supporting layer *and* the patterning of graphene in a single easy and fast step.

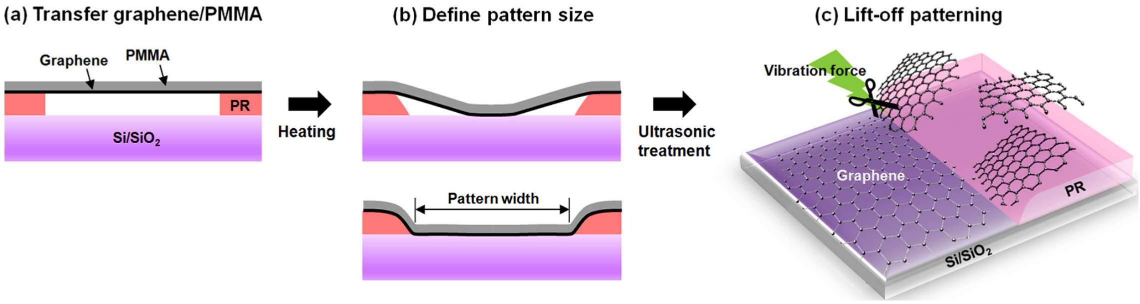

Figure 2.22: The graphene lift-off procedure proposed by Trung *et al.* (from [247]).

This technique was tested by first transferring graphene with its PMMA supporting layer on top of the AZ1512HS positive resist, in which a 50 µm wide trench was patterned (Figure 2.23 (left)). Before baking the sample for 2 min at 150 °C, a ~5 µm long graphene/PMMA suspended region can be observed. The graphene/PMMA is fully in contact with the substrate surface after re-flowing the resist layers, accordingly to the authors results (Figure 2.23 (right)).

Instead of using acetone for the lift-off step, we used THF, motivated by the ability of this process to combine graphene cleaning and patterning. The sample was immersed in THF until the resist dissolved (∼15 s) before the ultrasonication was applied for 15 s. The sample was then immersed in THF for 20 min, in order to compare the cleanliness of graphene obtained through this technique, with the samples simply transferred and cleaned in THF (section 2.1.3.4). Indeed, the mechanical energy brought by the ultrasonication would be expected to improve the removal of PMMA residues from the graphene surface. The sample was then rinsed in IPA and dried by N_2 blowing. The resulting graphene (Figure 2.24 (left)) shows no microscopical PMMA residues, but some large defects are introduced by the sonication, and the patterning resolution appears lower than for lithography/O_2-based processes since here only a mechanical action is involved. Nonetheless, large area, patterned graphene can be easily obtained (Figure 2.24 (right)) and the technique remains highly promising for fast and low-cost graphene processing.

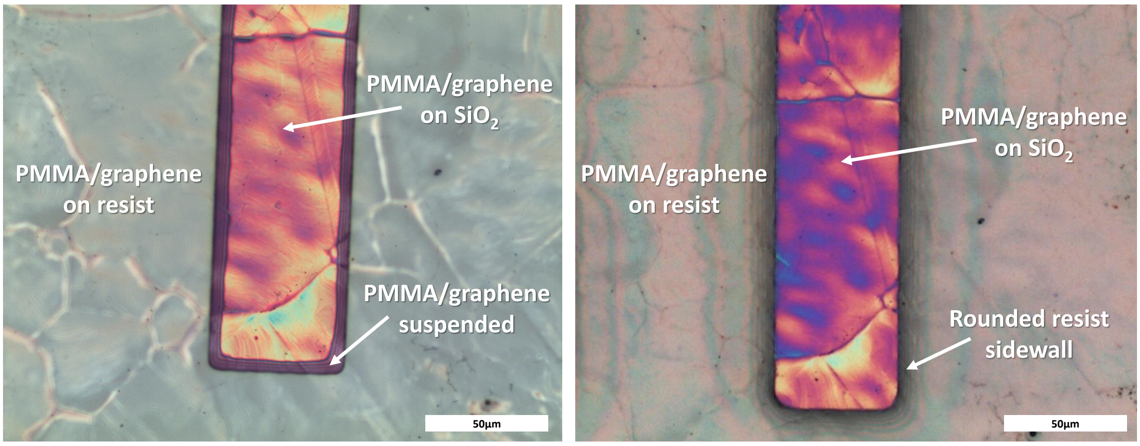

Figure 2.23: (left) graphene/PMMA stack transferred on the patterned resist layer showing the suspended region, (right) after baking on hotplate the resist sidewalls are rounded and the graphene is fully in contact with the substrate.

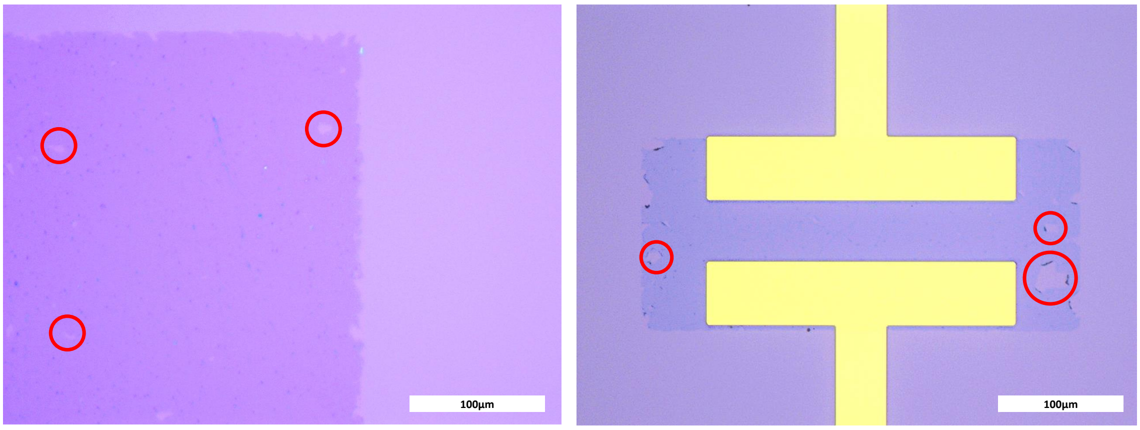

Figure 2.24: Graphene lift-off in THF, (left) zoomed view, (right) large area graphene patterned on top of metallic contacts, showing the potential for devices applications. Red circles show microscopic defects. Scale bars are 100 µm.

2.1.5 Contact passivation for liquid operation

The passivation of the metallic contacts is the third and last step of the fabrication process (Figure 2.2c). As discussed in section 2.1.1, it is necessary to cover the apparent gold metallic contacts to prevent any electrochemical reaction to occurs during the sensor operation in liquid.

Indeed, gold is commonly used as a working electrode in electrochemistry: when a sufficient potential is applied to the electrode in an electrolyte solution, the electrode acts as a sink/source of electrons. The electroactive ions exchange their charges with the metal (they are oxidized or reduced), generating a faradaic current which amplitude depends on the nature and concentration of the dissolved ions, the area of the electrode and its microstructure [248]. Considering the fact that the surface area of the metallic contacts of a device is approximately 2 order of magnitude larger than the channel active area, any faradaic current generated at the metal surface could be significantly larger than the drain-source current of the transistor. Passivating the metallic electrodes with an insulating and chemically robust material is therefore of primary importance to limit the possibilities of electrical paths between the gate and the device, and measure a transistor current carrying analytical information rather than artefacts.

During this thesis, the metallic contacts were passivated using a 5 µm thick SU-8 layer. SU-8 is an epoxy-based negative photoresist commonly used in biosensing applications [249, 250] for its excellent biocompatibility [251, 252], flexibility [163], chemical stability [253] and in particular for graphene-based SGFET biosensors [169, 254, 255]. When properly processed, SU-8 presents a highly cross-linked structure extremely resistant to chemical solvents, as opposed to other negative resist formulations. This chemical resistance is particularly interesting for durable operation of the sensor in liquid and its functionalization in organic solvent (section 5.2.1). The use of a photoresist as an insulating material also greatly simplify the fabrication process, as it only requires a photolithography step, whereas the use of oxide such as SiO_2 as passivation material requires at least three fabrication steps (deposition, photolithography, etching) further complicating the process and enhancing the risk of damaging graphene.

2.1.5.1 Design considerations

The main purpose of the SU-8 passivation layer is to insulate the contacts, but also to define the dimensions of the devices sensing area by limiting the surface of graphene exposed to the electrolyte. We first designed the SU-8 openings as shown Figure 2.25, with a 5 µm spacing between the extremities of the metallic contact and the SU-8 in the channel, in order to insure that the full coverage of the contact.

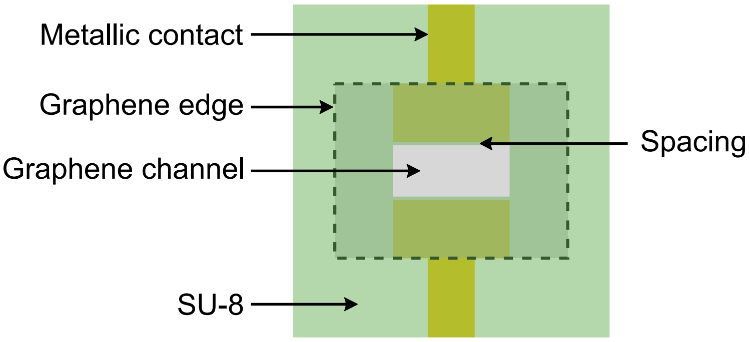

Figure 2.25: Top view of the passivation layout, representing the design of the SU-8 opening within the transistor channel.

2.1.5.2 SU8 processing

SU-8 consists in an epoxy monomer dissolved in an organic solvent containing a photo-acid generator, which under UV exposure triggers the polymerization. On average, each monomeric chain contains 8 epoxy rings, that can be opened by the photo-acid and initiate the cationic polymerization. As a consequence, a high degree of cross-linking can be obtained after activation of the reactive groups. The cross-linking kinetic, thus the mechanical properties and the resolution of the polymer, are strongly dependent on the photo-acid diffusion within the polymer network which, in turn, is dependant on the resist thickness and the solvent content during the polymerization [256].

The process is composed of different steps: first the resist is spin-coated using a 2-steps program to promote a good uniformity of the viscous resist on the sample surface. A first bake (soft-bake) is performed in a 3-steps procedure to evaporate the solvent. A second bake (post-bake) is performed to accelerate the polymerization induced by the acid generated during the UV exposure. The baking time and temperature are critical as they affect both the diffusion of the acid, and the polymerization kinetic. The sample is slowly heated in order to minimize the *intrinsic* tensile stress induced by the formation of the strong polymeric network, and the polymer shrinkage due to the solvent evaporation. Then the sample is slowly cooled down to minimize the *thermal* stress $\sigma_{thermal}$ which is directly proportional to the coefficient of thermal expansion (CTE) difference between the film and the substrate:

$$\sigma_{thermal} = (\alpha_{substrate} - \alpha_{SU-8})\frac{E_{SU-8}}{1-\nu_{SU-8}}\Delta T \tag{2.3}$$

where α is the material CTE, E and ν the Young's modulus and Poisson's ratio, and T the temperature [257, 258]. The unexposed region are then developed by dissolution of the monomers in an organic solvent, and the remaining solvent is evaporated during a final bake (hard-bake) which re-flow the polymer, further reducing mechanical stress and enhancing the robustness and the chemical stability.

Processing of SU-8 is particularly challenging, as every step can induce large tensile or compressive stress causing cracks, resist delamination, and induce mechanical stress to the other layers present on the sample, which in our case include the underlying graphene layer. The protocol of the SU-8 optimized process is provided at the end of this manuscript (Appendix: SU-8 process).

The residual thermal and intrinsic tensile stress generated during the post-bake is particularly high in the corners of the openings patterns, inducing cracks that are visible before the hard-bake Figure 2.26 (left). The cracks are no longer visible after the hard-bake, indicating that re-flowing the resist effectively relax the stress Figure 2.26 (right). This observation is further confirmed by resistance measurements, as shown Figure 2.27: the sheet and contact resistance of graphene both increase after the SU-8 post-bake, as a consequence of the tensile stress induced to graphene by the SU-8 layer [259]. As a part of the strain is released by the hard-bake which re-flows the SU-8 layer, the graphene sheet and contact resistance both decrease. This clearly demonstrates that the SU-8 layer directly affect the graphene electrical properties through strain-induced effects, and that an optimized process is required for minimizing such impact on the device performance.

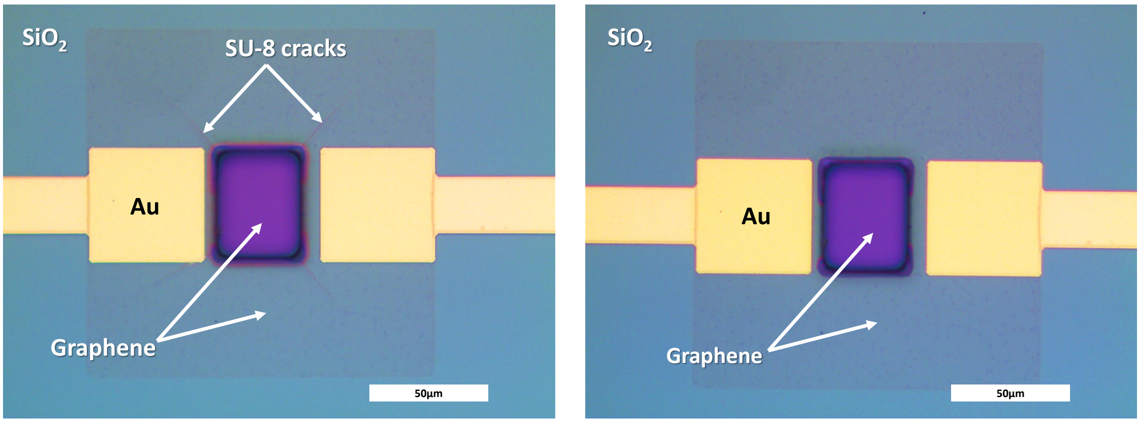

Figure 2.26: SU-8 passivation of the devices and the hard-bake effect on cracks induced by mechanical stress during the process, before (left) and after hard-bake (right). Scale bars are 50 µm.

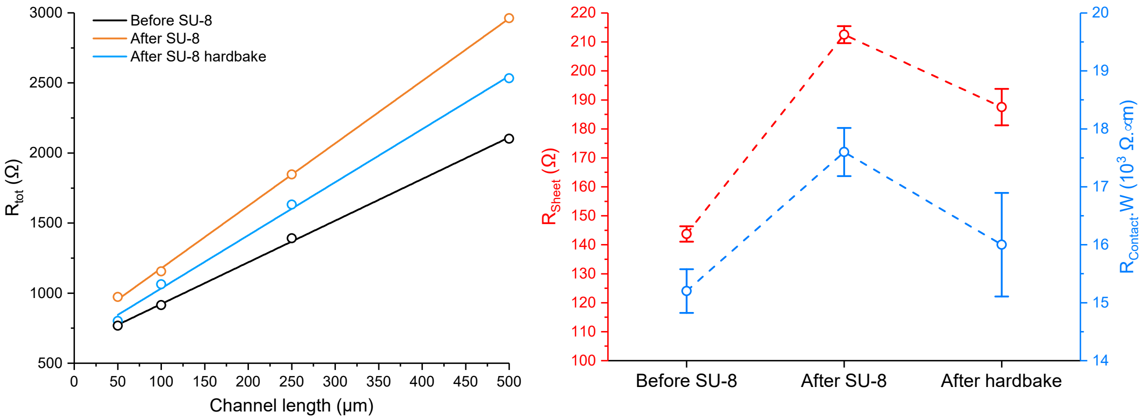

Figure 2.27: Effect of metallic contacts passivation with SU-8 processing on graphene resistance: TLM measurements (left), sheet and contact resistance of graphene extracted from TLM (right). Error bars were calculated from the TLM data fitting error.

2.1.5.3 SEM observations of the graphene/SU-8 interface

In the vicinity of each device, SU-8 is in contact with different material: Au and SiO_2 with positive CTE (respectively $\sim 14 \times 10^{-6}\,K^{-1}$ [260] and $\sim 0.5 \times 10^{-6}\,K^{-1}$ [261]), and graphene with a negative CTE at room temperature ($\sim -8 \times 10^{-6}\,K^{-1}$ [262]). Using Equation 2.3, with a CTE of $\sim 52 \times 10^{-6}\,K^{-1}$ for the SU-8 [263] and considering an homogeneous cross-linking of the polymer, we can expect the thermal *tensile* stress σ_{SiO_2-SU8} induced at the SiO_2/SU-8 interface to be ∼4 times higher than the σ_{Au-SU8} *tensile* stress, and ∼6 times higher than the $\sigma_{Graphene-SU8}$ *compressive* stress generated at the SU-8/graphene interface. This unbalanced repartition of tensile and compressive stress could affect the SU-8 adhesion and locally damage graphene.

We conducted SEM observations of the SU-8 opening patterns sidewalls on graphene to investigate possible damages. As it can be seen from Figure 2.28, the SU-8 layer is deformed, and lifted from the substrate surface, revealing the SiO_2 surface and tearing the graphene layer below along the SU-8/graphene contact line. Because the SU-8 covers graphene in the transistor channel, such tearing along the graphene/SU-8 contact line could drastically deteriorate the electrical conduction and the graphene properties. In order to solve this issue, the SU-8 adhesion has to be improved by optimizing the process.

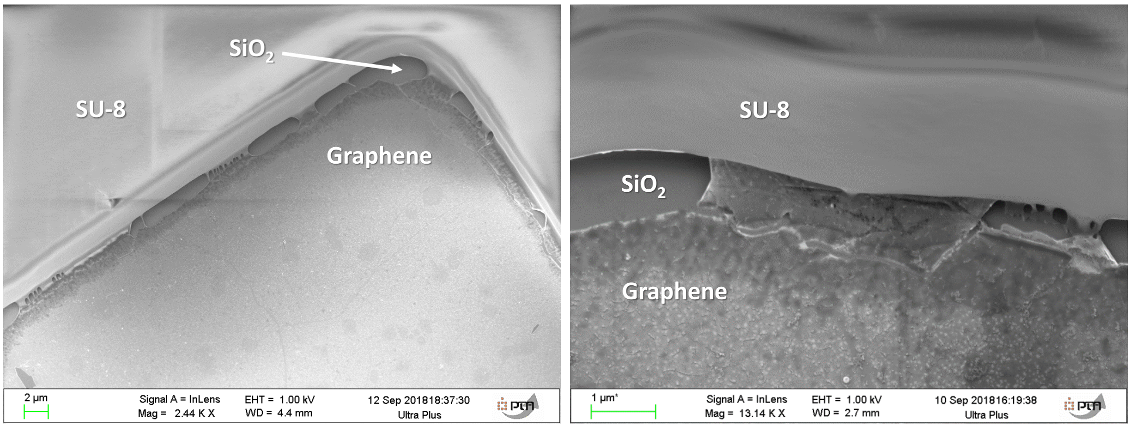

Figure 2.28: SEM observations of the SU-8 opening patterns on top of the transistor channel, revealing the delamination of the SU-8 layer and tearing of the graphene layer.

2.1.5.4 Optimization of SU8 processing & passivation design

The delamination of SU-8 has been reported for high aspect-ratio structures or thin films [256,264,265]. The delamination of photoresists due to low adhesion (typically on SiO_2, glass, Au, or Ag) is often easily solved by performing surface treatment or using an adhesion promoter. With the graphene layer exposed before passivation, performing harsh surface treatments such as piranha or plasma is not conceivable: either the process have to be optimized or an adhesion promoter has to be used.

Adhesion promoter

The OMNICOAT adhesion promoter has been developed to enhance the low adhesion of SU-8 on substrates such as Au, Cu or quartz [266]. The OMNICOAT layer is coated on the sample prior to the SU-8 spin-coating and baked at 1 min at 200 °C on a hot plate following the manufacturer recommendations. The SU-8 is then processed following the same procedure as described before (Figure 2.29 (left)), the OMNICOAT layer is then developed in an alkaline developer to reveal the graphene surface and the sample is finally rinsed in DIW. However, in our experience, the OMNICOAT development step lifted the graphene layer (Figure 2.29 (right)). The presence of cracks before the hard-bake also indicate that the promoter doesn't significantly reduce the thermal stress induced to the SU-8 during its processing.

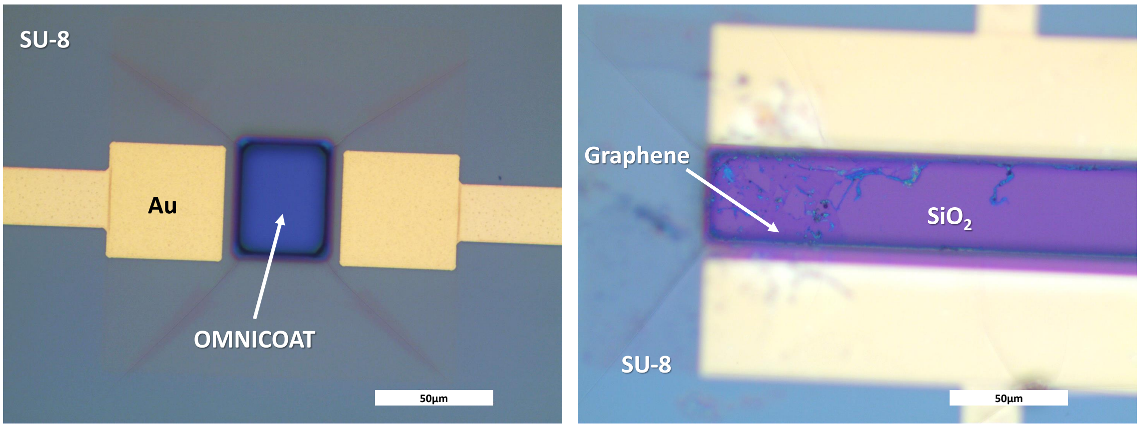

Figure 2.29: OMNICOAT for promoting the adhesion of SU-8, before OMNICOAT development (left), after development (right) showing the lifted graphene.

Dehydration step

Performing a dehydration step before the induction of the hydrophobic resist can drastically improve its adhesion as the remaining water molecules are removed from the surface. By implementing a 5 min dehydration step at 180 °C on a hotplate before the SU-8 spin-coating, we obtained a better adhesion on the substrate. The SEM observations reveals that the SU-8 is not deformed and in close contact with the graphene surface, but also graphene tears in the vicinity of the graphene/SU-8 contact line indicating that the residual stress is still significantly high.

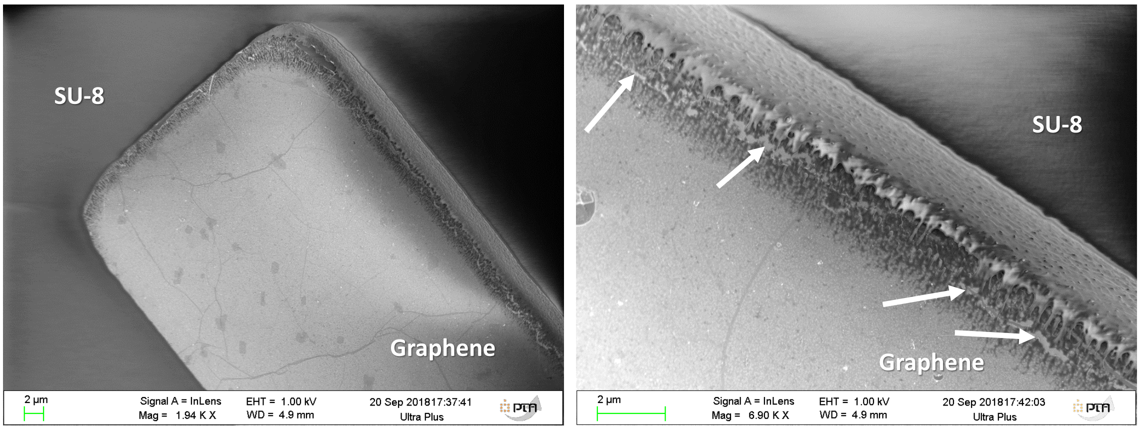

Figure 2.30: SEM observations showing the SU-8 adhesion improvement by adding a dehydration step prior to the spin-coating step. White arrows shows the graphene tears.

Recessed passivation design

In order to decrease the residual stress causing tearing of graphene close to the contact line at the graphene/SU-8 interface, the design of the opening patterns was changed following the "recessed channel passivation" design introduced by Makin *et al.* [169]. As opposed to the "partial channel passivation" that we first adopted, where the SU-8 is covering a part of the graphene in the channel (section 2.1.5.1), this alternative design leaves a portion of the metallic contact uncovered (Figure 2.31 and Figure 2.32 (left)). This design presents several advantages: first, it suppresses the series resistance induced by the presence of SU-8 within the channel. It also reduces the contact area between graphene and the SU-8, leading to smaller thermal compressive stress and better adhesion of SU-8. In addition, the corners of the opening patterns (where mechanical stress is concentrated, as seen from the presence of cracks) can be moved away from the metallic contact extremities, further decreasing the SU-8 intrinsic stress caused by the metallic contact step height (see top views Figure 2.31). Finally, the graphene/SU-8 contact line is no longer within the channel but on top of the metallic contact, thus reducing the effect of graphene tears on the measured drain-source current.

The SEM observations of the graphene/SU-8 contact line show no SU-8 delamination or graphene tears Figure 2.32 (right), indicating that the recessed passivation effectively promote a better SU-8 adhesion by reducing the intrinsic stress accumulated in the vicinity of the graphene/SU-8 contact line.

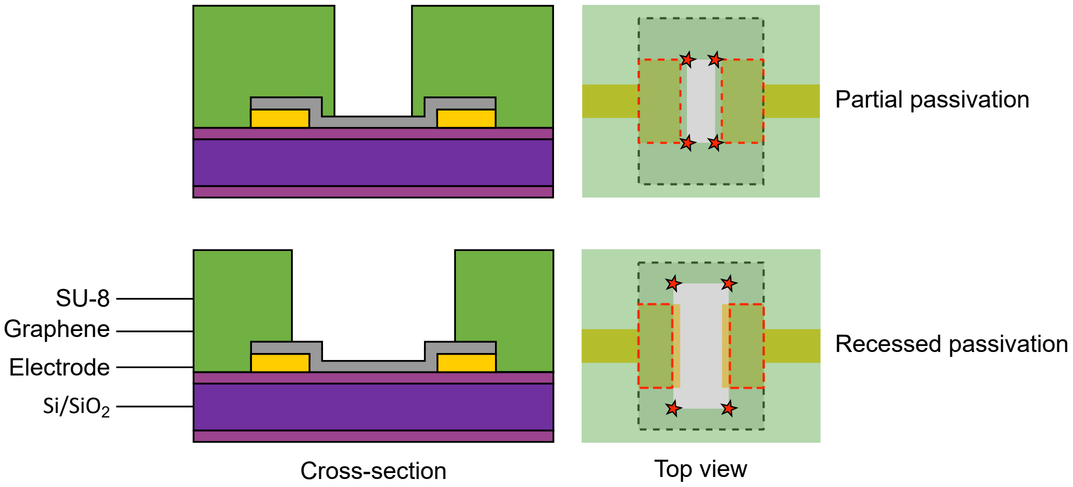

Figure 2.31: Cross-sections and top views of the recessed and partial passivation designs. Green doted lines indicates graphene edges, red doted lines indicates the step-height induced by the metallic electrode to the SU-8, and the red stars indicates the SU-8 opening corners.

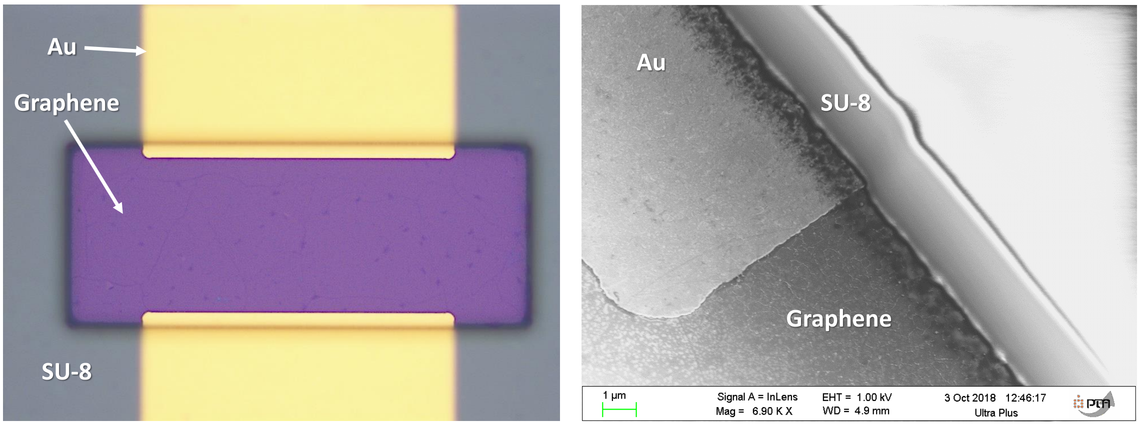

Figure 2.32: (left) Picture of a device passivated with the new design and (right) SEM observation of the graphene/SU-8 contact line showing no delamination or graphene tears.

2.1.6 Conclusion

A substantial part of this thesis was dedicated to the development and optimization of a SGFET fabrication process, which could be robust, stable and serves as a reliable base for producing high performance graphene-based devices for operation in liquid. Such groundwork was presented in this chapter, including the different methods which were explored to develop this process (summarized in Figure 2.33). THF, which is theoretically an efficient solvent for solubilizing PMMA, was proposed as an alternative to the classic PMMA stripping procedure in acetone. Graphene was patterned using a sacrificial copper layer for preserving the graphene integrity and its contamination from resist residues. In particular, this alternative allowed us to drastically improve the process reproducibility issues faced with the conventional resist-mask patterning method. The promising graphene lift-off procedure developed by Trung *et al.* for both PMMA striping *and* graphene patterning in the same step was also tested and adapted using THF. Finally, the procedure for passivating the metallic electrodes was optimized to promote the adhesion of the SU-8 resist layer, and prevent damaging graphene.

In order to probe the graphene cleanliness, possible doping effects, or defects induced by each fabrication method explored, Atomic Force Microscopy (AFM), X-ray photoelectron spectroscopy (XPS) and Raman experiments were conducted at each main step of the fabrication process. The following chapter will present the results of these experiments.

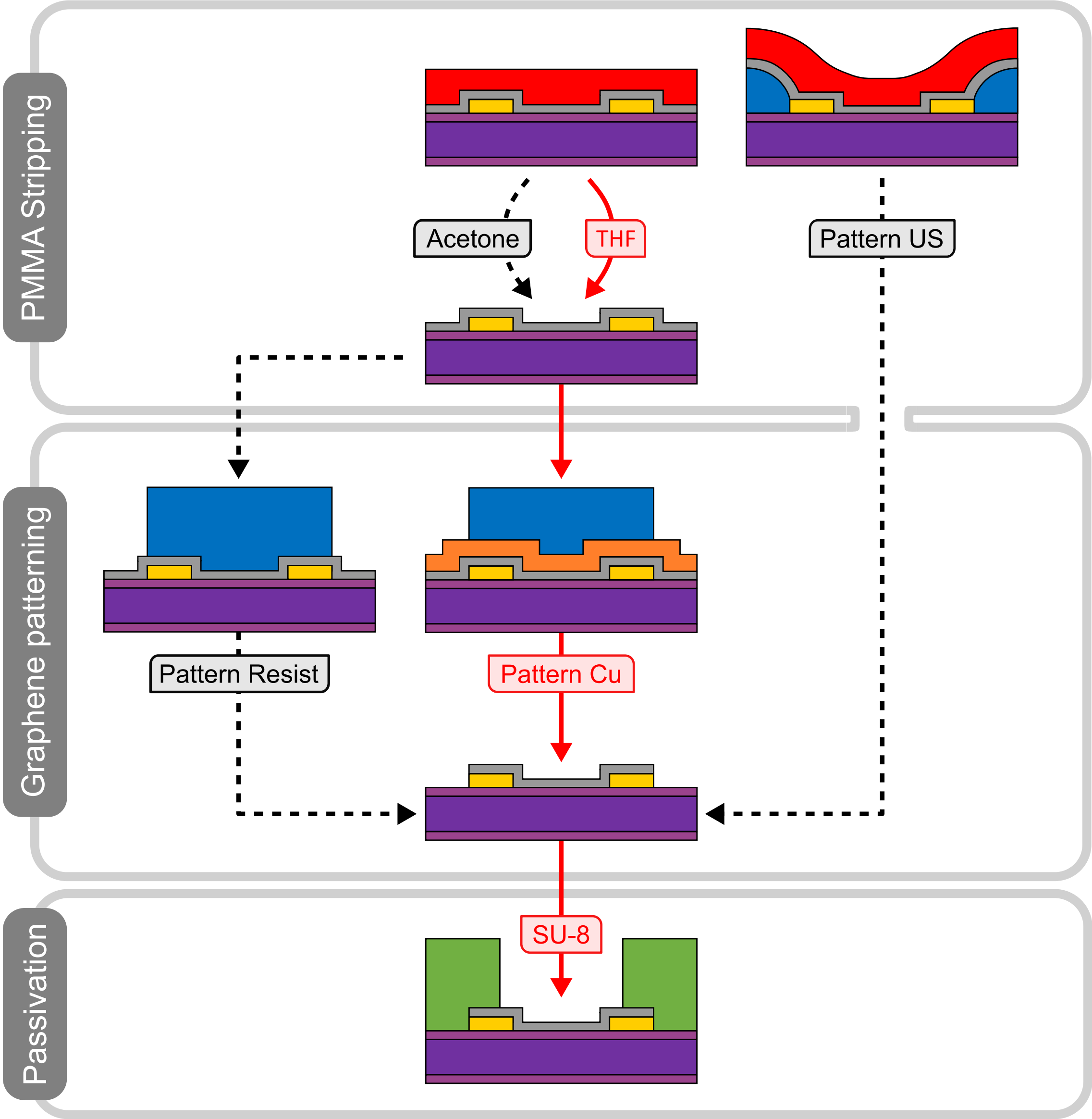

Figure 2.33: Recap of different fabrication methods tested and developed. Red arrows indicate the "main" process, dashed arrows indicate "variants" for a given step of the fabrication process (for example: the "Pattern Resist" sample corresponds to the patterning of graphene with a resist etching mask, with the PMMA stripped in THF at the previous fabrication step).

Chapter 3

Topographic and spectroscopic characterizations of graphene

Microscopic and SEM observations gave useful information during the numerous iterations required for the process optimization. However, more powerful and complete characterizations are needed to assess the impact of the process on the quality of the transferred and processed graphene films.

Size and shape of resist residues induced by incomplete PMMA stripping, or graphene folds generated during the transfer contribute to the surface morphology of the sample. 3D images obtained by AFM scans can reveal these features, their geometrical shapes and thickness. The chemical composition of the surface contamination can be identified using XPS, while chemical doping, mechanical strain and lattice defect can be revealed in the Raman spectrum of graphene. These tools were used to determine the efficiency of the different fabrication methods developed during this thesis and discussed in the previous chapter.

In particular, three different PMMA stripping methods were used (in acetone, in THF, and the graphene lift-off), as well as three graphene patterning methods (with or without a Cu sacrificial layer, and the graphene lift-off), and the passivation of the contact using SU-8. Altogether, six samples were analysed, allowing to compare these methods and their impact on graphene. The sample names and their corresponding fabrication method are summarized in Figure 2.33: a "main" process (red arrows) is distinguished from "variants" (black dashed lines) in order to indicate the fabrication sequence used for each sample: for example, the sample **Pattern Resist** was fabricated by stripping the PMMA layer in THF in the first fabrication step, and by using a resist mask directly on top of graphene for the patterning step.

3.1 Atomic Force Microscopy

AFM played a role in early graphene research for its ability to determine the number of graphene layers in exfoliated graphene samples. AFM is a high-resolution scanning probe microscopy in which a sharp tip on a cantilever scan the sample surface. When in proximity with the sample surface, the cantilever deflects due to forces between the tip and the surface, giving topological information of the sample surface.

Different imaging technique exist, but the most frequently used when operating in ambient air, and used during this thesis, is the "Tapping" mode. The cantilever is driven to oscillate at or near its resonance frequency and the amplitude kept constant. When the tip interact with the surface through Van der Waals or electrostatic forces, the amplitude of the oscillation changes. An height image of the sample is then produced by adjusting the amplitude of the cantilever to maintain its height constant over the sample surface thanks to a feedback-loop system.

The six samples were characterized by performing two types of AFM scans: a step height scan realized at the interface between the graphene layer and the SiO_2 substrate surface, and a large 2D map of the graphene surface. These two types of measurements gives complementary information. A step-height scan provides a *thickness* measurement of the graphene layer and eventually contaminants at its surface. In particular, such scans were obtained across macroscopic graphene defects, to avoid edge effects and obtain an authentic view of the in-plane graphene topology. On the other hand, the 2D map of a continuous surface provides a *roughness* information, independently of the step-height with the substrate surface. The experimental methods description is provided at the end of this manuscript (Appendix: AFM methods).

3.1.1 PMMA stripping AFM analysis

The 2D maps at the graphene/SiO_2 interface and the corresponding step height of **THF**, **Acetone**, and **Pattern US** samples are presented Figure 3.2. The step height is extracted by calculating the difference between the two mean planes corresponding to the SiO_2 substrate and the graphene layer. Both **THF** and **Pattern US** samples show a step-height close to the thickness of graphene ($\sim$0.4 nm) within margins of error, indicating that THF can efficiently remove the PMMA residues from the graphene surface. Interestingly, the mechanical energy brought by the ultra-sonication used during the **Pattern US** sample fabrication doesn't result in a significantly lower step-height than the simple THF cleaning, except on the SiO_2 surface. It can be explained by the fact that a simple chemical treatment can't solely remove completely PMMA residues from the graphene surface. As discussed in section 2.1.4.2, some PMMA residues strongly interacting with the graphene surface are impossible to remove, and are expected to contribute to the measured thickness. In contrast, PMMA stripping in acetone results in a ∼2 nm step-height, indicating that acetone is effectively less efficient in removing PMMA residues from the graphene surface than the THF solvent, and that the whole surface is in fact covered with a ∼2 nm thick resist layer.

2D maps of continuous surfaces gives a roughness information independently of the step-height relatively to the surface. As a consequence, the height distributions of the **Acetone** sample 2D maps (Figure 3.3 (bottom)) reflects the resist layer roughness rather than particles on a graphene apparent surface. In fact, the zoom view of the acetone sample reveals large residues with random shapes and a distribution of small round shape (red colour, higher than 3 nm), which can be attributed to the rough surface of the remaining resist layer. However, both **THF** and **Pattern US** show narrower distributions (Figure 3.3 (top & middle)), with most of the shapes located at the intersection between line shapes, attributed to graphene folds. These shapes are more visible on **Pattern US**, since the surface of the sample is not perfectly clean and hydrophilic prior to the graphene transfer, as opposed to the **THF** sample. As a consequence, water or residues can remains trapped between the substrate and graphene, inducing even more folds of the graphene layer.

Since these samples have different morphologies, extracting a roughness value is not trivial and would certainly not reflects the actual topology of these surfaces. Instead, the height distribution (normalized) are presented Figure 3.1. **Acetone** shows a wider distribution of heights, up to a few nanometres due to the resist roughness, whereas **THF** and **Pattern US** samples show narrower distributions attributed to a lower resist residues density, due to a more efficient cleaning, with the apparent graphene folds contributing to the height distribution.

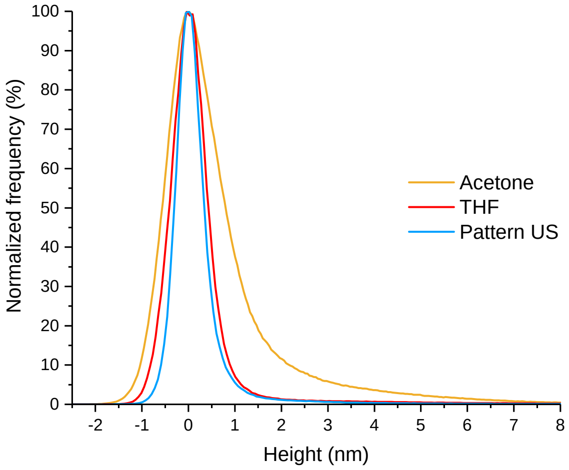

Figure 3.1: Normalized height distribution of the samples after PMMA stripping.

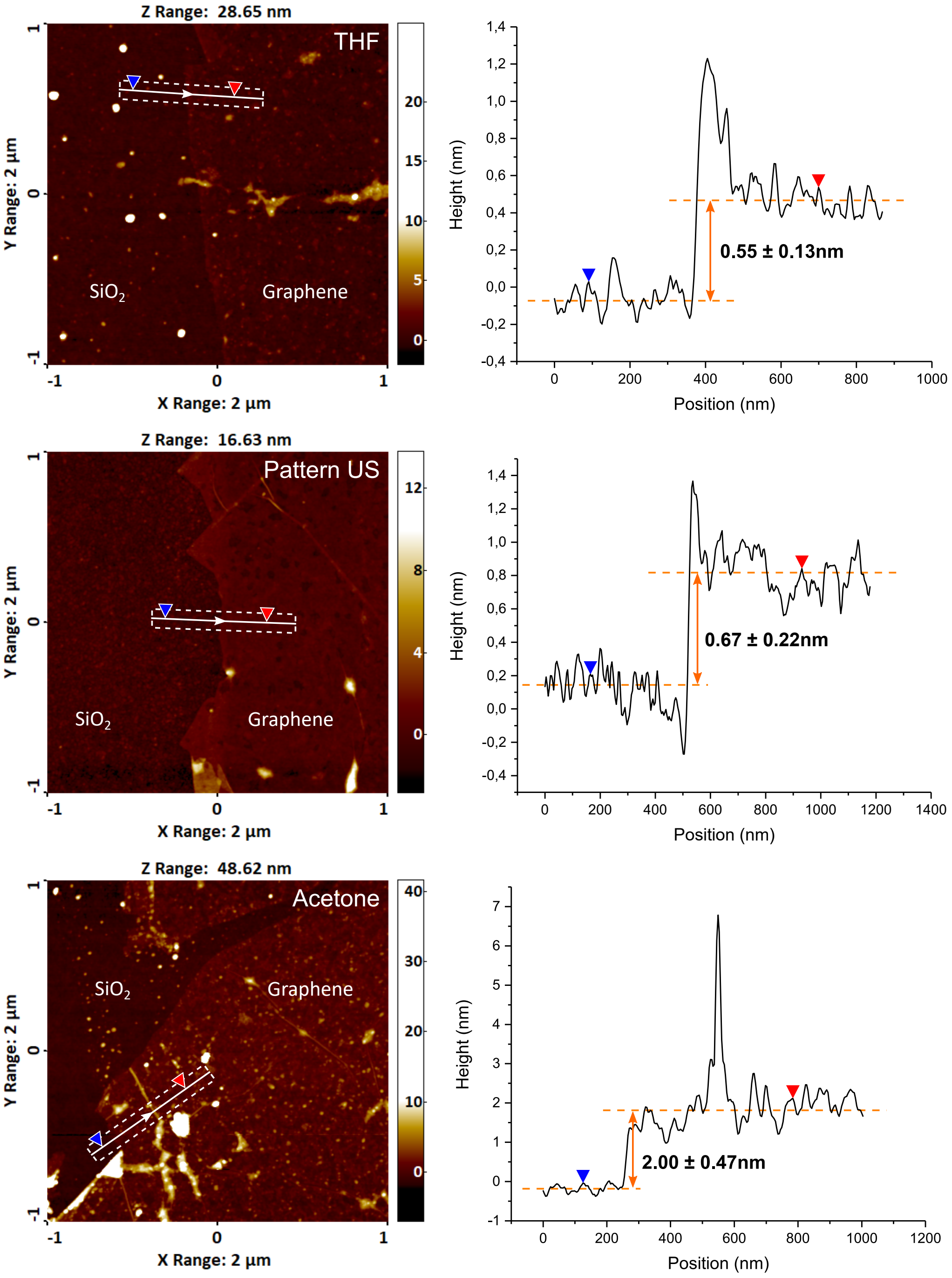

Figure 3.2: 2 µm × 2 µm scan (left) at the graphene/SiO$_2$ interface and the associated step height (right) after acetone and THF cleaning and graphene lift-off. Colormaps are harmonized (white spots are higher than 10nm).

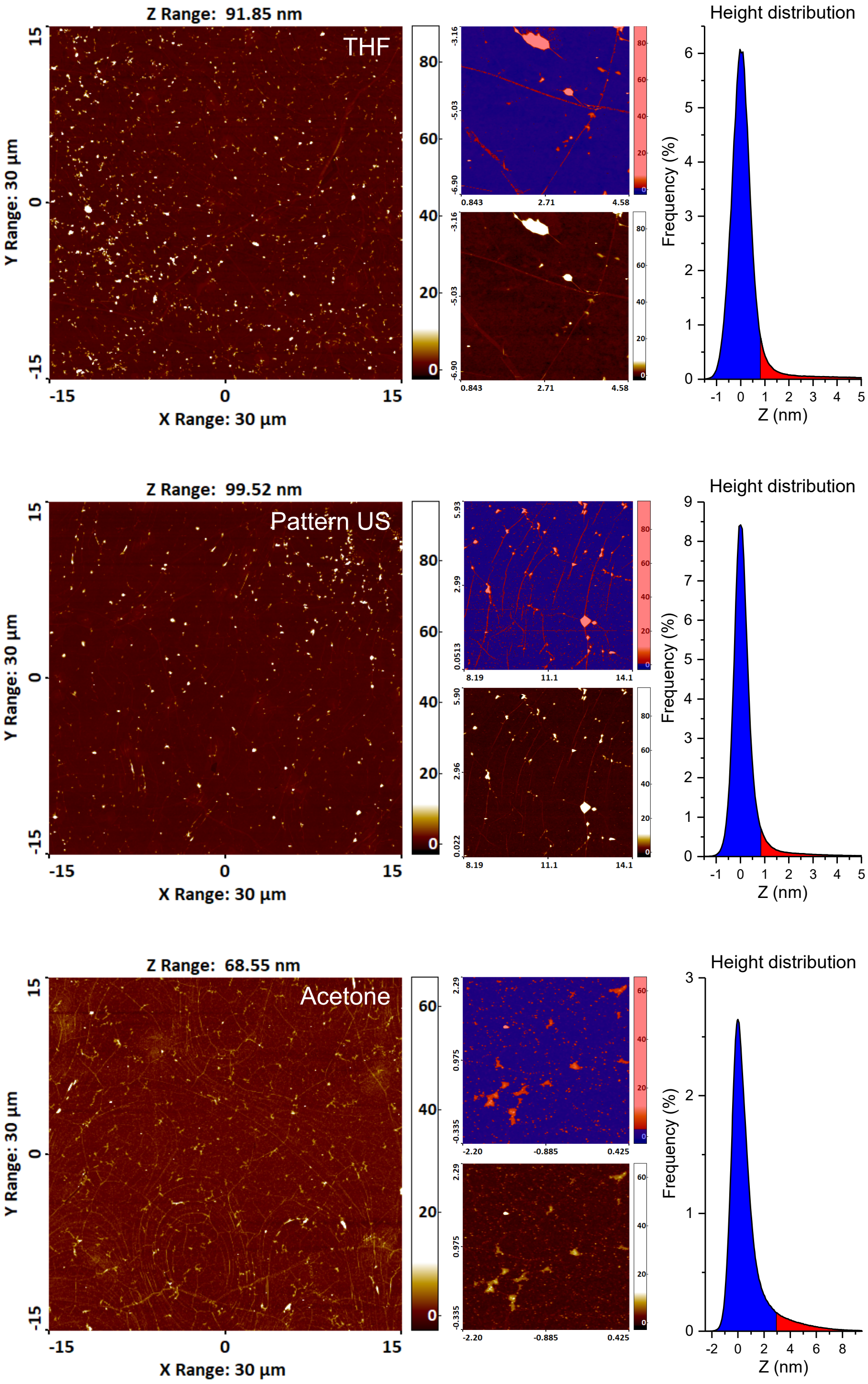

Figure 3.3: 30 µm × 30 µm 2D maps of the graphene surface (left), raw zoomed view (middle-bottom) and colourized (middle-top) with the associated height distribution (right) of THF and acetone cleaning and graphene lift-off.

3.1.2 Graphene patterning AFM analysis

The step height scans and 2D maps of **Pattern Resist** and **Pattern Cu** are presented Figure 3.4 and Figure 3.5. A ∼3.8 nm step height is observed for **Pattern Resist**, showing that the associated patterning method leaves an homogeneous resist residues layer on graphene after mask stripping in acetone. Similarly to **Acetone**, the height distribution is reflecting the resist residue roughness rather than a graphene apparent surface with local residues. Concerning **Pattern Cu**, the cross-section reveal the existence of ∼2 nm thick "islands" (green marker) distributed on the graphene apparent surface (red marker) with a ∼1 nm thickness. Since these islands are not observed on **THF**, they are attributed to Cu residues left after the mask stripping. The existence of two mean planes is further evidenced by both the zoomed view of the 2D map and the height distribution, with the first peak corresponding to the graphene apparent surface, and the second to the Cu residues. Compared to the resist mask in direct contact with graphene, the Cu metal sacrificial layer leaves a non-homogeneous contamination at the surface after mask stripping, with similar thickness, but also leaves apparent the graphene surface with a sub-nanometer contamination.

From these AFM results, the graphene lift-off (using THF) appears as the most efficient technique concerning surface contamination, since graphene is only exposed to the PMMA layer after its growth and PMMA is well dissolved in THF.

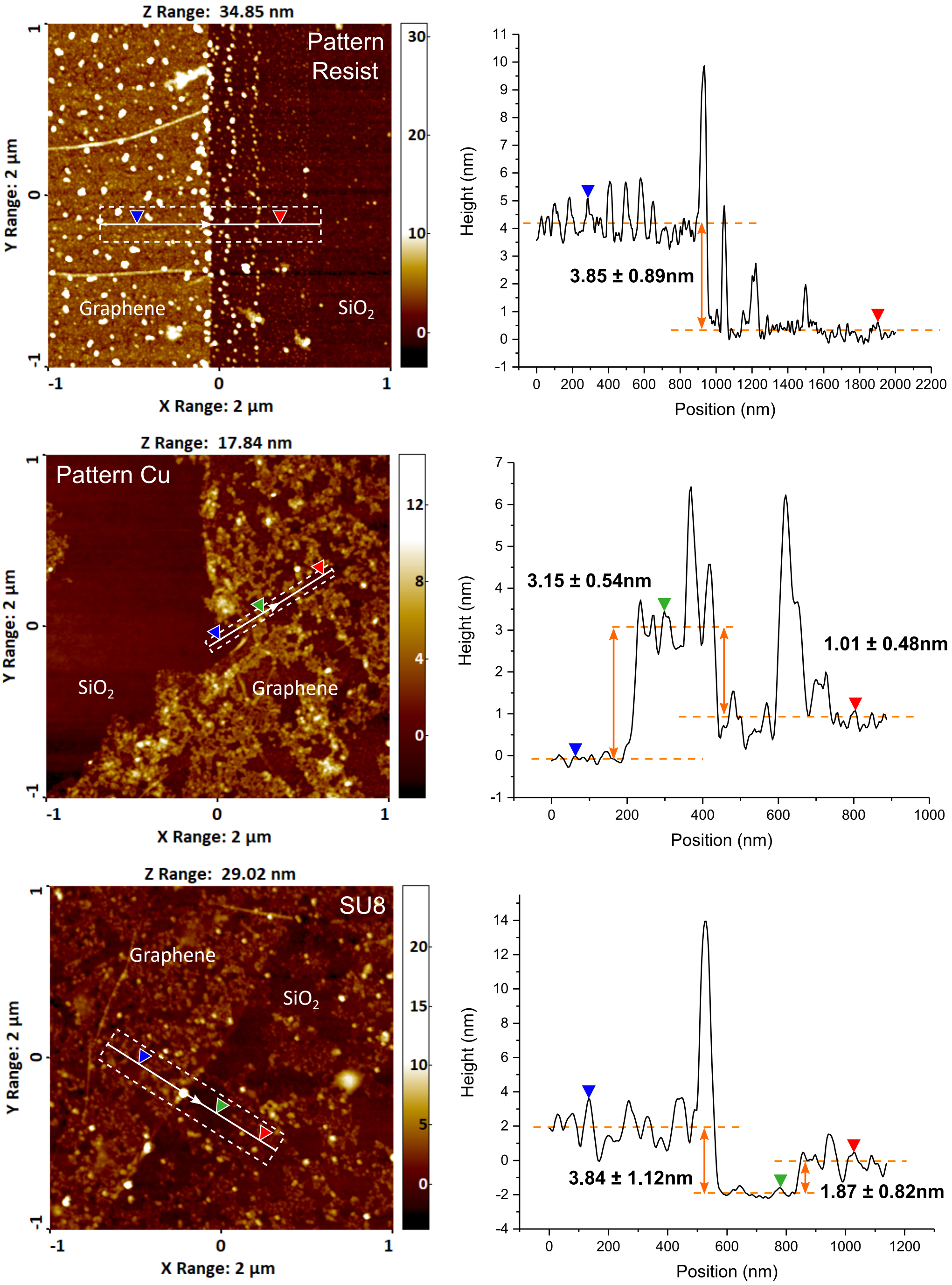

Figure 3.4: 2 µm × 2 µm scan (left) at the graphene/SiO$_2$ interface and the associated step height (right) after graphene patterning and passivation. Colormaps are harmonized (white spots are higher than 10nm).

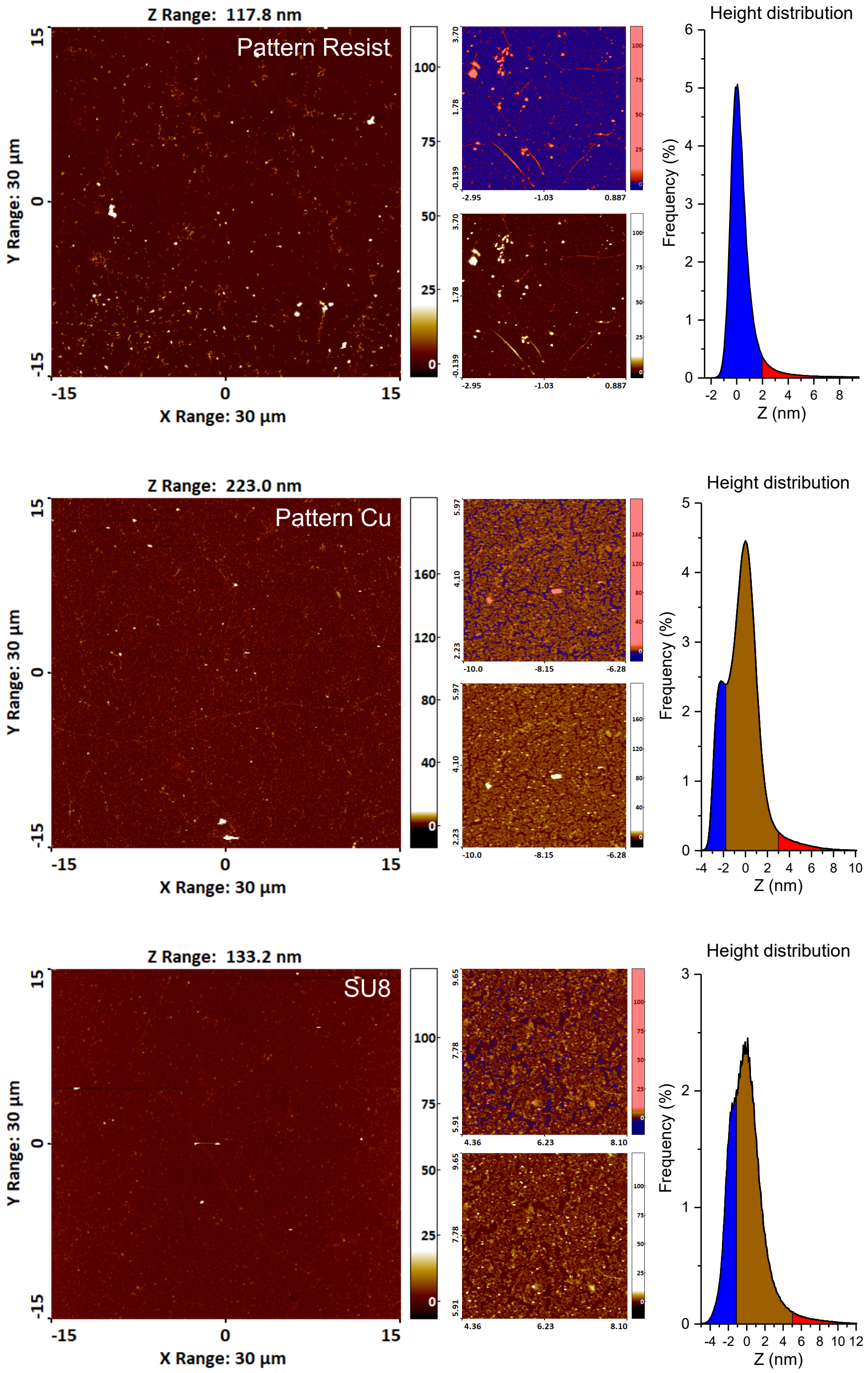

Figure 3.5: 30 µm × 30 µm 2D maps of the graphene surface (left), raw zoomed view (middle-bottom) and colourized (middle-top) with the associated height distribution (right) after graphene patterning and passivation.

3.1.3 SU-8 passivation and process AFM analysis

The **SU-8** sample step height scan and 2D map are presented Figure 3.4 (bottom) and Figure 3.5 (bottom). The step height scan reveals a ∼3.8 nm on the graphene surface. Since the SU-8 covers the graphene edges, the step height was realized across a macroscopic defect within the graphene layer. Because graphene was patterned using a Cu sacrificial layer, the Cu islands observed on **Pattern Cu** are also found on the **SU-8** sample. As a consequence, the height distribution after SU-8 passivation shows a smoother yet similar line profile compared with **Pattern Cu**, due to the surface coverage by SU-8 resist residues (Figure 3.6 (left)).

It should be noticed that the step-height of **SU-8** and **Pattern Resist** are similar (Figure 3.6 (right)), demonstrating that patterning graphene using a Cu sacrificial layer effectively promote a lower resist contamination of the graphene surface. In addition, this result indicates that passivating a graphene surface after patterning it using a resist mask would result in step-height larger than ∼3.8 nm, since SU-8 residues appear to be inevitable.

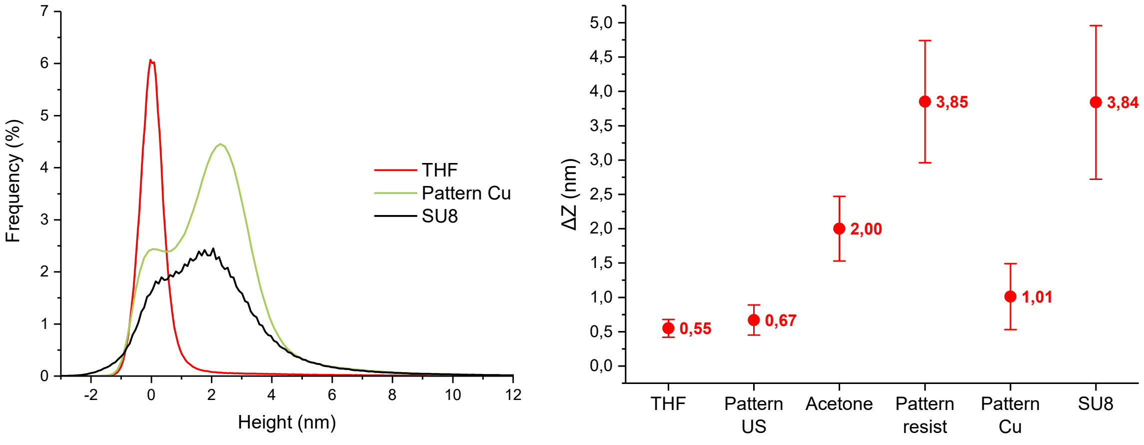

Figure 3.6: Height distribution evolution through the main process (left). The profiles are adjusted so the first peak corresponds to 0 nm for better visualization. Step heights for the six samples analysed (right).

3.2 X-ray photoelectron spectroscopy

X-ray photoelectron spectroscopy (XPS) is a powerful analytical technique, providing a quantitative identification of the elements present at the surface of the analysed material. The material is bombarded by a highly energetic X-ray beam, ejecting photoelectrons from the surface with a kinetic energy E_k defined by:

$$E_k = E_b + \phi - h \times \nu \tag{3.1}$$

where E_b is the binding energy of the excited electron relative to the Fermi level, $h \times \nu$ is the energy of the incident beam and ϕ is the analyser work function.

Because the binding energy of the excited electron is characteristic of the nature of the bombarded atom, the sample composition can be deduced from the measured kinetic energy of the emitted photoelectrons using a velocity analyser. In addition to the quantification of the probed element, the binding energy gives information on the chemical environment of the atom from which was emitted the core electron of a given molecular orbital. The C1s spectra is of particular interest while studying carbon-based materials such as carbon blacks [267], carbon nanotubes [268,269] and in particular graphene [270, 271], which hexagonal lattice mainly composed of sp^2 hybridized carbon atoms shows a characteristic peak at ∼284.6 eV on the C1s spectrum. The introduction of lattice defects generates sp^3 carbon atoms (amorphous $C{-}C$ or $C{-}H$ bonds) which signature appears at ∼285 eV [272]. Thus the C1s XPS spectrum is a powerful tool to probe the graphene structure integrity by looking at the sp^2/sp^3 ratio, as well as the presence of surface contamination since this technique is sensitive to the chemical environment of the probed element. In particular, the contamination of graphene by PMMA residues was studied [242, 273, 274], and the resulting XPS spectrum shows peaks typical of $C{-}O$ or $O{-}C{=}O$ bonds typically found in polymer structures [275].

Experimentally, a wide scan (0–1000 eV) is first measured, giving a snapshot of all the elements present in the sample. The resulting "survey" spectrum shows a good signal-to-noise ratio (SNR) but a poor peak resolution. A second scan in a narrower energy range, focused on the peak of interest, is thus necessary for a proper peak analysis with higher resolution (but poorer SNR). The experimental methods description is provided at the end of this manuscript (Appendix: XPS methods).

3.2.1 PMMA stripping XPS analysis

A survey spectrum showing the global atomic composition of the samples after PMMA stripping is shown Figure 3.7. As expected, the C element is detected predominantly (48.1%) with oxygen (O) (35.1%), Si (15.8%), and Nitrogen (N) traces (1.0%). The relative atomic quantification shows a proportion of O atoms larger than 2 (relatively to the Si element), suggesting that the SiO_2 substrate surface is not solely composed of Si−O−Si bonds. This stoichiometry larger than 2 is explained by the formation of Si−OH bonds during the SiO_2 surface treatment prior to the graphene transfer [276]. In addition, the absence of peak (within the limits of detection) between 930 eV and 955 eV related to the Cu element indicates that the Cu growth substrate was completely etched during the transfer step.

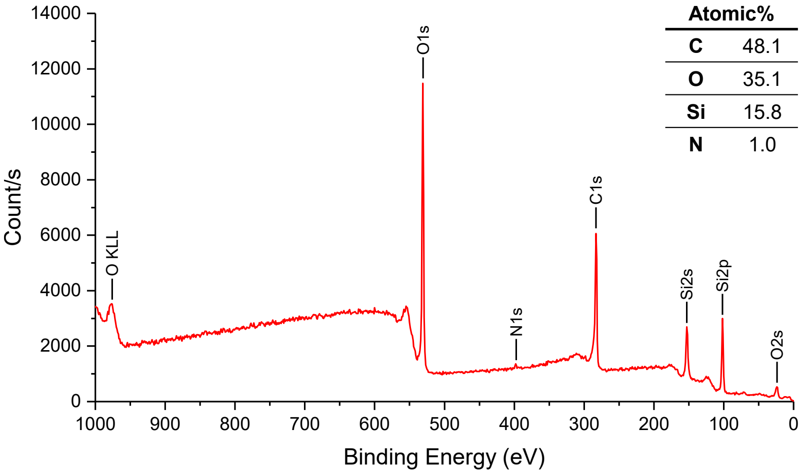

Figure 3.7: Survey spectrum after PMMA stripping and relative atomic composition.

The high-resolution C1s spectra of **THF**, **Pattern US** and **Acetone** samples are shown Figure 3.8. The spectra were analysed following a standard procedure (Appendix: XPS methods). The three samples present a main sp^2 contribution related to the graphene sp^2 hybridized lattice. While both **Acetone** and **THF** samples show a similar sp^3/sp^2 ratio (∼10 %), a large sp^3/sp^2 ratio (∼48 %) is observed for **Pattern US**, which is attributed to the generation of lattice defects by the ultra-sonication used during the associated fabrication process.

Peaks attributed to C−C and C−H (286.3–286.6 eV), C−O (287.4–287.7 eV), and O−C=O (288.9–290 eV) chemical bonds are found to contribute to the C1s spectra. Interestingly, PMMA-related components are detected for the THF sample, in larger quantity than the acetone sample which shows a 2 nm thick residue layer evidenced by AFM. Nonetheless, these contributions remains weak in both cases and are found to be comparable to XPS signals reported after different PMMA removal strategies such as thermal annealing [237, 274, 277], plasma cleaning [272, 278, 279], or laser annealing [280]. This result shows that independently of the solvent used to strip the PMMA supporting layer (i.e THF or acetone), the low contamination is rather a result of the graphene sample preparation and transfer procedure optimizations, which are known to strongly affect the removal of PMMA residues, as discussed in section 2.1.3.4.

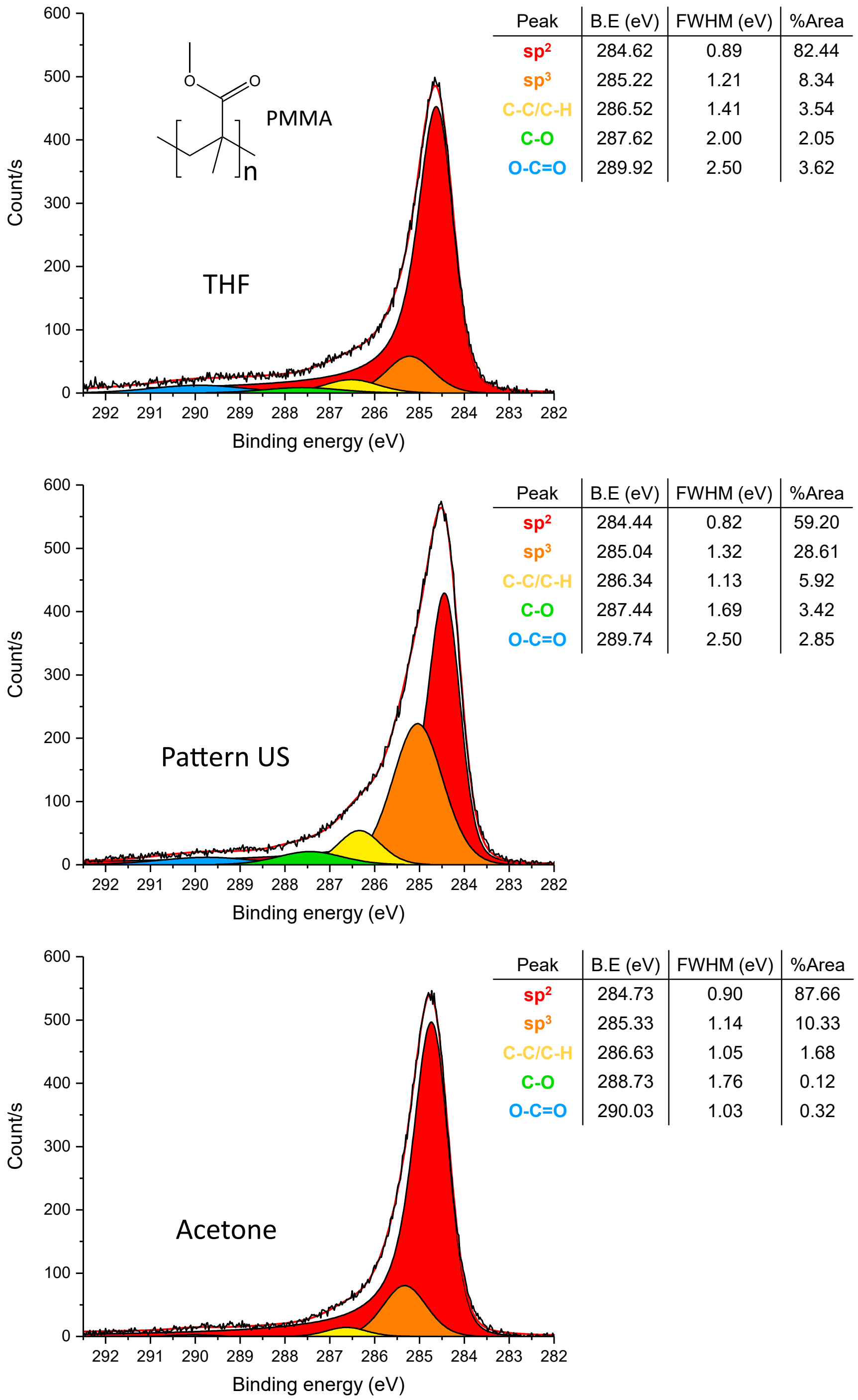

Peak	B.E (eV)	FWHM (eV)	%Area
sp^2	284.62	0.89	82.44
sp^3	285.22	1.21	8.34
C-C/C-H	286.52	1.41	3.54
C-O	287.62	2.00	2.05
O-C=O	289.92	2.50	3.62

Peak	B.E (eV)	FWHM (eV)	%Area
sp^2	284.44	0.82	59.20
sp^3	285.04	1.32	28.61
C-C/C-H	286.34	1.13	5.92
C-O	287.44	1.69	3.42
O-C=O	289.74	2.50	2.85

Peak	B.E (eV)	FWHM (eV)	%Area
sp^2	284.73	0.90	87.66
sp^3	285.33	1.14	10.33
C-C/C-H	286.63	1.05	1.68
C-O	288.73	1.76	0.12
O-C=O	290.03	1.03	0.32

Figure 3.8: High-resolution C1s spectra of the samples after PMMA stripping. The PMMA chemical structure is shown in inset for visualization of the different contributions.

3.2.2 Graphene patterning XPS analysis

The survey spectrum of the pattern Cu sample is shown (Figure 3.9). The small peak at 930 eV is attributed to the presence of Cu $2p_{3/2}$ and represents 0,6% of the global atomic composition of the sample surface. This peak is absent from the other samples, indicating that it results from the process and is not solely due to some environmental contamination. This observation also confirms that the "islands" evidenced by the AFM step height are indeed Cu residues resulting from an incomplete removal of the hard mask.

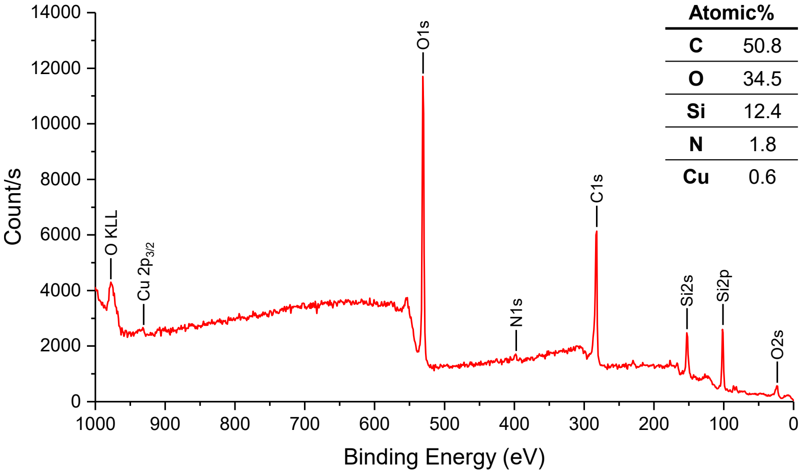

Figure 3.9: Survey spectrum of the pattern Cu sample, showing the presence of the Cu element and the relative atomic composition.

The C1s spectra of the **Pattern Cu** and **Pattern Resist** samples (Figure 3.10) both show a significant increase of the sp^3 contribution relatively to the **Acetone** and **THF** samples, with sp^3/sp^2 ratios of ∼25% and ∼44% respectively. For **Pattern Resist**, it represents a 34% increase relatively to **THF**, and a 15% increase for **Pattern Cu**. The large increase of the sp^3 contribution observed for **Pattern Resist**, with the presence of a peak at high energy (289.6 eV) typical of O=C−O bonds, is attributed to the presence of polymeric residues left from the incomplete resist mask stripping, as evidenced by the AFM step height. **Pattern Cu** also shows significant C−O and C=O components, which can be attributed to the generation of oxidized defects during the stripping of Cu in ammonium persulfate. Nonetheless, the patterning of graphene with a Cu sacrificial layer results in a higher proportion of sp^2 hybridized C chemical bonds, which is ascribed to a more efficient protection of the graphene surface from the mask contamination after stripping.

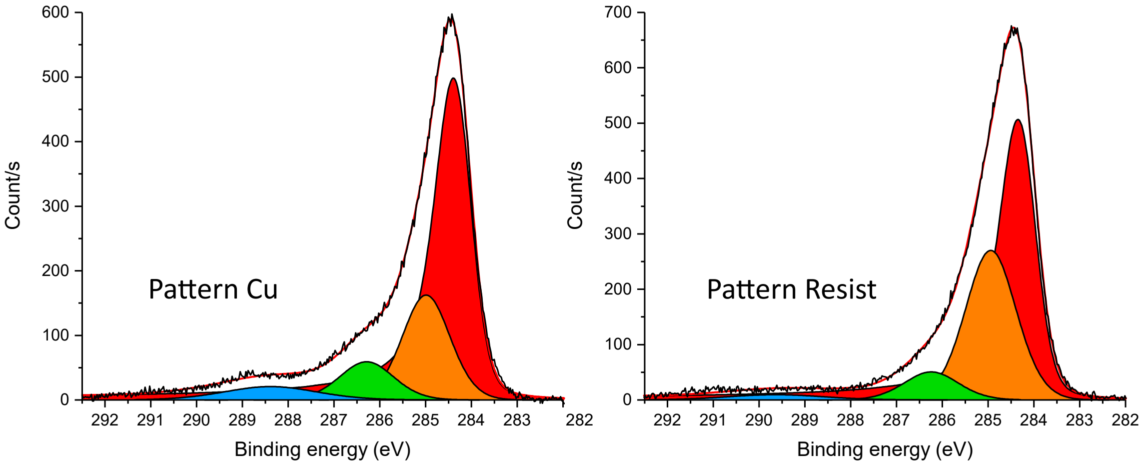

Peak	B.E (eV)	FWHM (eV)	%Area
sp^2	284.39	0.91	70.03
sp^3	284.99	1.23	17.91
C-O	286.29	1.40	7.40
C=O	288.69	2.38	4.42

Peak	B.E (eV)	FWHM (eV)	%Area
sp^2	284.34	0.91	64.03
sp^3	284.94	1.31	28.39
C-O	286.24	1.40	5.68
O-C=O	289.64	2.50	1.90

Figure 3.10: High-resolution C1s spectra of the pattern Cu and pattern resist samples with contributions of the different chemical bonds.

3.2.3 SU-8 passivation XPS analysis

The survey spectrum of **SU-8** shows a large proportion of C (65%) and O (26.4%) elements compared with **Pattern Cu** (respectively 50.8% and 26.4%, see yellow and red curves of Figure 3.11). A survey realized on bare SU-8 on SiO_2 (see green curve of Figure 3.11) reveals an even higher proportion of C (83.2%) and O (16.8%) elements, indicating that the additional source of C and O originates from SU-8 residues left on the graphene surface after development of the resist.

The proportion of the Si element is also reduced to 8.6% after SU-8 passivation, and is completely masked by the 5 µm resist layer (see yellow curve of Figure 3.11) on the bare SU-8 sample, which is explained by the limited XPS probed depth of ∼5 nm. Therefore, the presence of Si peaks observed for all the six samples demonstrates that the surface contamination thickness is on average below ∼5 nm, as confirmed by the AFM step heights.

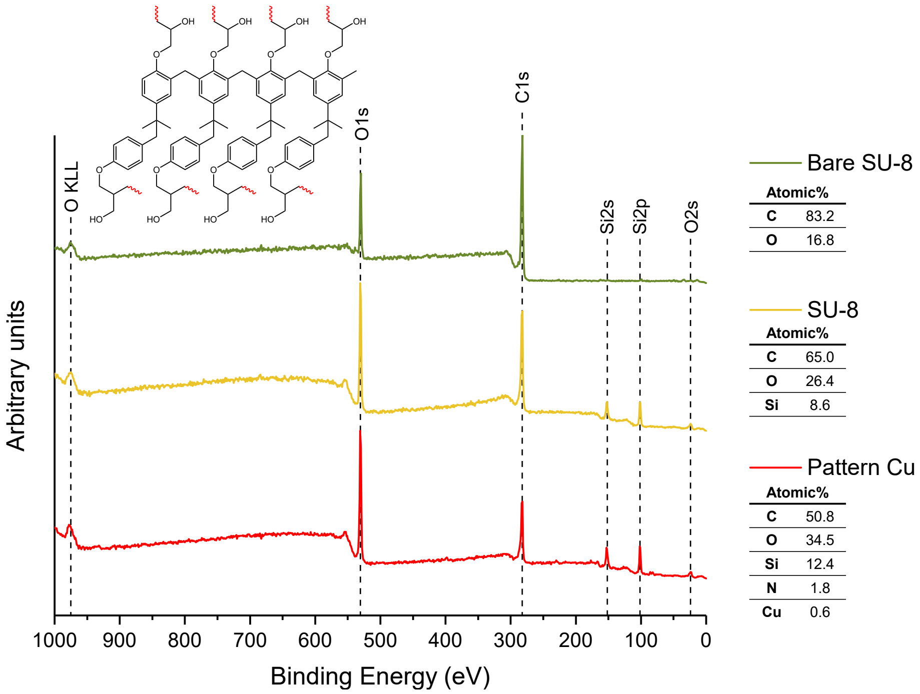

Figure 3.11: Survey spectra after SU-8 passivation (yellow) and on the surface of bare SU-8 on SiO_2 (green) and the relative atomic compositions. The survey spectrum of **Pattern Cu**, corresponding to the previous fabrication step was added for comparison. The monomer constituting the cross-linked SU-8 polymer is also shown (the red bonds are cross-linked to other polymer chains).

The presence of SU-8 residues is also revealed by the C1s spectra of the **SU-8** sample, and also on bare SU-8 on SiO_2 (Figure 3.12). The bare SU-8 spectrum shows large contributions of sp^3 C atoms and C−O bonds, accordingly to the SU-8 structure after polymerization, and a peak at 291.3 eV which is characteristic of a “shake-up” satellite, typical of polymers having an unsaturated backbone or an aromatic side-chain [281–283]. The apparition of the "shake-up" peak on the spectrum of **SU-8**, and the large increase of the sp^3 signal is a further indication of the presence of SU-8 resist residues at the graphene surface, in accordance with the AFM step height revealing a ∼3.8 nm step-height after passivation.

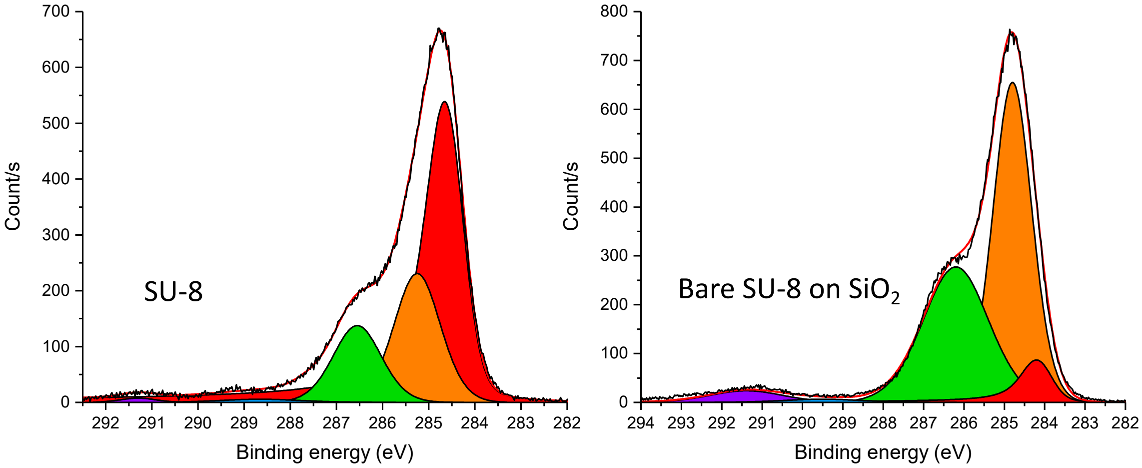

Peak	B.E (eV)	FWHM (eV)	%Area
sp^2	284.65	0.94	65.51
sp^3	285.25	1.18	20.43
C-O	286.55	1.23	12.67
C=O	288.65	2.08	0.87
Shake-up	291.30	0.91	0.52

Peak	B.E (eV)	FWHM (eV)	%Area
sp^2	284.20	0.88	8.93
sp^3	284.80	1.13	50.49
C-O	286.20	1.92	36.13
O-C=O	289.50	2.30	1.01
Shake-up	291.39	2.14	3.46

Figure 3.12: High-resolution C1s spectra after SU-8 passivation, and on the surface of bare SU-8 on SiO_2 with the different contributions.

3.3 Raman spectroscopy

Raman spectroscopy is a non-invasive, fast and powerful technique to probe the crystallographic structure and the electronic properties of a given material. The Raman effect consists in the inelastic scattering of light, associated with an energy gain or loss during the light-matter interaction. The probed material is excited using a monochromatic light source (laser) into a transitory and unstable virtual energy state. The incident photon interacts with the electron cloud of the material, and a part of its energy is scattered through the generation (Stokes scattering) or the annihilation (anti-Stokes scattering) of a phonon during the process. The relaxation of the molecule then results in the emission of a photon with a different energy from the incident photon, following the energy and momentum conservation principles. The electron-photon interaction occurring during the scattering process is governed by the polarizability of the probed material. In turns, the polarizability depends on characteristic vibrational modes related to the material chemical and structural properties. A Raman spectrum is therefore a spectroscopic fingerprint of the analysed sample, and allows for probing structural defects or doping effects. In practice, the diffused light is collected, and its intensity is plotted against the Raman *shift* δ (in cm^{-1}) (difference between the inversely proportional incident wavelength and the diffused wavelength). Typically, only the Stokes scattering is reported, since the anti-Stokes process requires the system to be in a fundamental excited vibrational state, which is unlikely at room temperature. The main features of the graphene Raman spectrum are the following:

- the G (for "graphite") band ($\sim$1585 cm^{-1}) is an in-plane sp^2 C$-$C stretching mode, common to all the carbon-derivative materials (graphite, nanotubes, amorphous carbon). This band is highly sensitive to strain effects [284, 285] since any modification of bond length or angle breaks the hexagonal lattice symmetry of graphene. In particular, the band is blue-shifted (δ increases) for both hole and electron doping [286, 287] and also vary with temperature [288].
- the 2D band ($\sim$2700 cm^{-1}) is the main feature of the graphene spectrum, and is associated to the in-plane breathing mode of the carbon sp^2 lattice. Such as the G peak, the band lineshape and spectral position vary with strain [284, 289] and temperature [290]. However, the band is blue-shifted for hole doping, while it is red-shifted for electron doping.
- the D (for "defect" or "disorder") band ($\sim$1350 cm^{-1}) is originating from the same breathing mode as the 2D peak, but requires a lattice defects to be active, such as sp^3 defects, grain boundaries, atomic vacancies [291] or edges [292]. The presence of this peak is often accompanied by a D' band around 1620 cm^{-1}, seen as a shoulder of the G peak.

One of the main interest of Raman spectroscopy while working with graphene-related material lies in the determination of the number of graphene layers. As the G peak intensity is monotonically increasing with the number of graphene layers [293], the ratio of the G and 2D peaks intensity (I_G/I_{2D}) varies accordingly. However, this ratio serves only as an indication as it increases for both hole and electron doping [286]. This ratio, (close to 0.5) has to be combined with a 2D peak having a single Lorentzian lineshape with a ~30 cm^{-1} width (the 2D peak splits into four peaks and broadens to ~60 cm^{-1} for bilayer and more). The graphene used during this thesis was predominantly monolayer, as shown Figure 3.13.

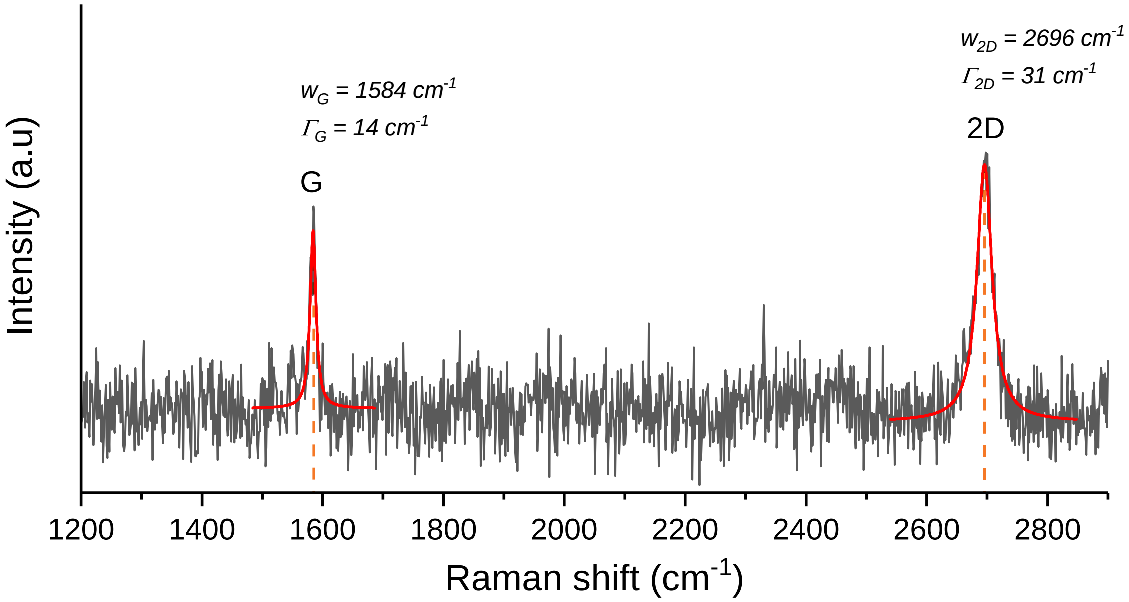

Figure 3.13: Raman spectrum of graphene on Cu. The background due to the Cu photoluminescence [294] was removed prior to spectrum analysis.

The second main interest relies in the presence of the D peak, indicating lattice defects which is therefore useful for quality assessment during the fabrication of graphene-based devices.

Raman spectra can be obtained in single point measurement (defined by the laser spot diameter, here ~0.9 µm), but might lack of reproducibility due to local variation of the sample properties caused by doping, defects or residues. Instead, we realized 2D maps of the six samples to be characterized, by measuring Raman spectra step-by-step using a X-Y microcontroller (a detailed description of the experimental methods is given in Appendix: Raman microscopy methods). 2D maps are more representative of the sample surface as they covers large area (typically 30 µm × 30 µm), and allows to compute statistics.

3.3.1 Defect density analysis by Raman spectroscopy

An example of defective graphene Raman spectrum is presented Figure 3.14, superimposed with a typical spectrum obtained on continuous and non-defective graphene sample transferred onto SiO_2 substrate. A large D peak is observed for the defective graphene, as well as a D'. A weak D peak was always observed for other typical graphene samples, which is attributed to the presence of local defects induced by the transfer procedure, and by graphene grain-boundaries (the grain size is up to 20 µm according to the manufacturer).

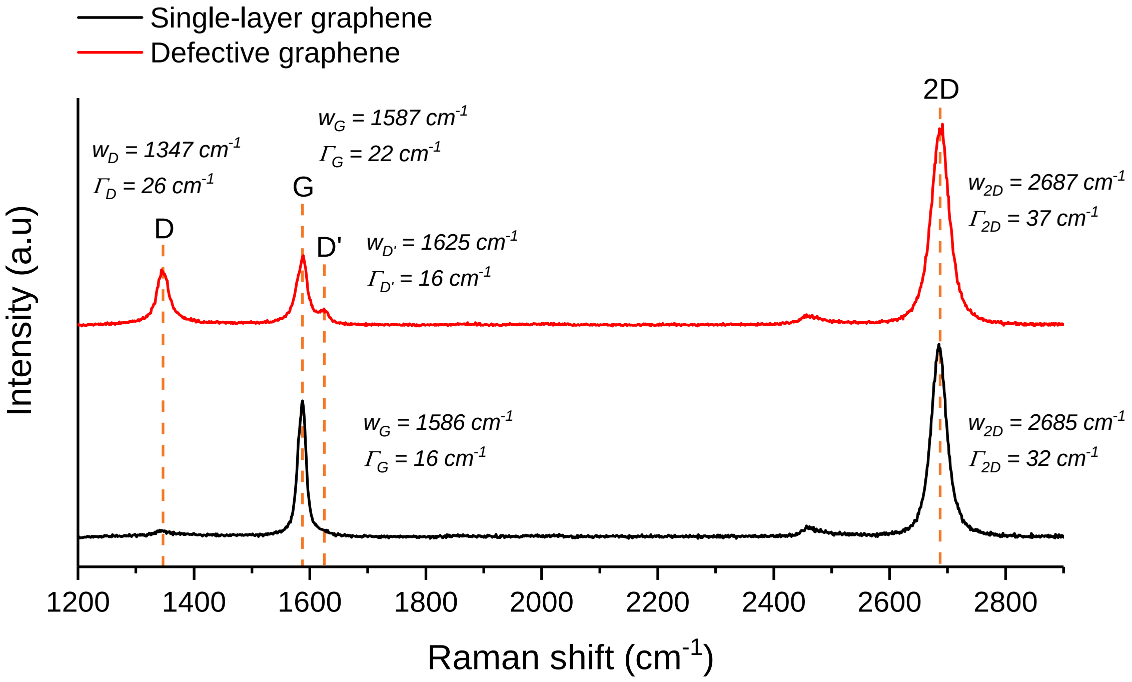

Figure 3.14: Raman spectra of typical graphene single-layer transferred onto SiO_2 substrate, and defective graphene.

I_D/I_G ratio and 2D maps of the six samples depicting the main step of the fabrication process are shown Figure 3.15 and Figure 3.16 respectively. Both **THF** and **Acetone** samples show a relatively uniform homogeneity and similar I_D/I_G ratio values indicating the presence of lattice defects which are attributed to the transfer procedure. However, **Pattern US** shows some inhomogeneity and large I_D/I_G ratio values that can be attributed to defects induced by the ultra-sonication, as evidenced by the XPS results. The defect density increases after graphene patterning independently of the method used. However, **Pattern Cu** shows a more homogeneous I_D/I_G ratio than **Pattern Resist** over the scanned area. In fact, the defect density of **SU-8** is similar to **Pattern Resist**, with high I_D/I_G ratio values locally. In both cases, graphene is in direct contact with a resist layer which is later stripped in organic solvent: the defects observed for the pattern resist is thus attributed to this resist stripping step. This result shows that patterning graphene with a sacrificial Cu layer is more efficient to prevent the generation of lattice defects induced by resist stripping.

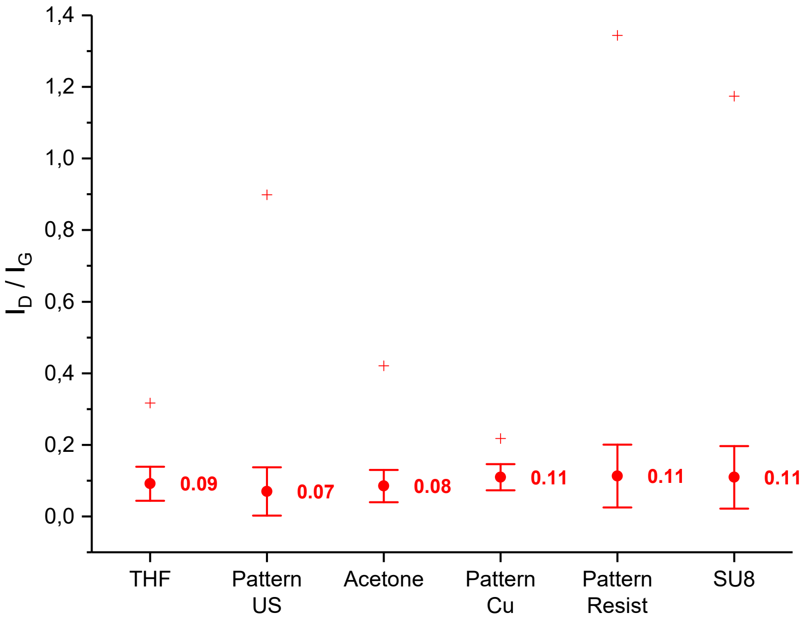

Figure 3.15: Mean values of the I_D/I_G ratio of the six samples, with standard deviation, min (minus sign) and max values (plus sign).

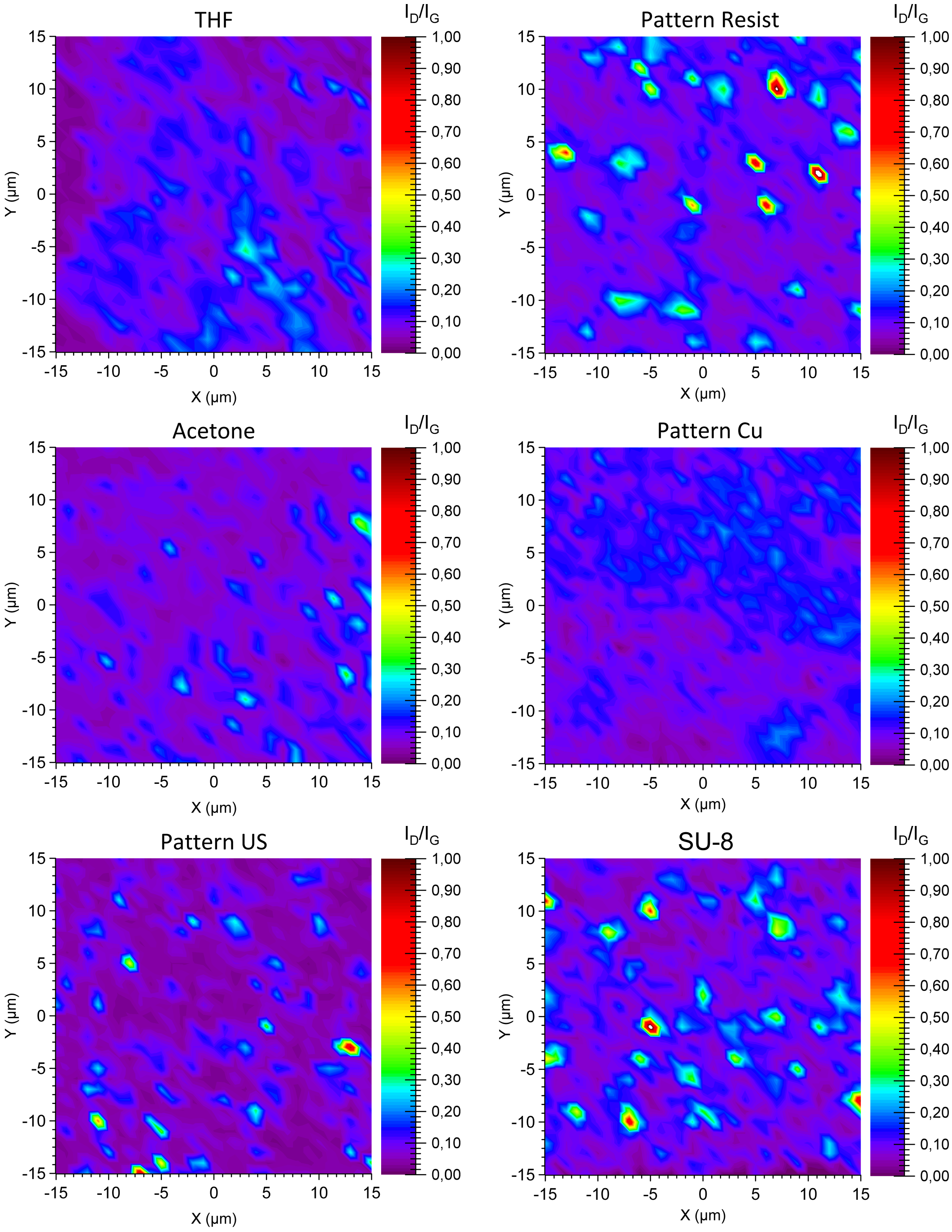

Figure 3.16: 2D maps of the samples I_D/I_G ratio.

3.3.2 Doping and strain analysis by Raman spectroscopy

Graphene is highly sensitive to its environment, particularly to mechanical strain induced during processing [295, 296], thermal annealing [288], and chemical doping by surface contaminants [286]. These effects are visible by Raman spectroscopy since the 2D and G peaks are both strain and doping sensitive, as discussed above. Decorrelating strain to doping effects from raw Raman spectra is thus non-trivial and require a more sophisticated analysis. In particular, a correlation analysis have been introduced by Lee *et al.* in order to separate these two concurrent effects. This method is based on a vector model, in which the frequency of the 2D peak (w_{2D}) is plotted as a function of the G peak frequency (w_G) [285]. The quasi-linear dependency of the ratio of the 2D and G frequency variations under pure uniaxial strain ($(\mathit{\Delta} w_{2D}/\mathit{\Delta} w_G)_{strain} \sim 2.2$) or pure hole doping ($(\mathit{\Delta} w_{2D}/\mathit{\Delta} w_G)_{doping} \sim 0.75$) are used to defined strain and doping unit vectors. The origin of these vectors corresponds to the w_{2D} and w_G values of free-standing graphene (respectively $1581.6\,\mathrm{cm}^{-1}$ and $2676.9\,\mathrm{cm}^{-1}$). The electron doping case is excluded from the model, since most of the transport and Raman studies showed that pristine and annealed graphene are predominantly p-doped. Doping and strain value can then be estimated from the repartition of the scattered raw w_{2D}, w_G data.

We used this method to obtain a *qualitative estimation* comparison of strain or doping induced effects within our samples through the fabrication process. Indeed, as pointed out by Mueller *et al.* , the strain induced to graphene by its transfer onto a substrate is neither purely uniaxial nor biaxial in practice [297]. Since the $\Delta w_{2D}/\Delta w_G$ factor sensitivity for biaxial strain (~ 2.8) is larger than the uniaxial case, the uncertainty from the extracted values could be non-negligible. Mueller *et al.* established a method to use this strain-doping analysis for arbitrary strain configurations, by recording Raman spectra with circular corotating polarization. However, this technique is beyond the scope of our work, so we made the assumption of uniaxial strain as a first approximation and considered the resulting data qualitatively.

The strain-doping plots of the six samples are presented Figure 3.17. First of all, both **THF** and **Acetone** samples show a small dispersion of compressive strain (approximately -0.1%), but have different doping concentration. The **Acetone** sample appears less doped than **THF**, which is contradictory with the thicker resist contamination evidenced by AFM. The same doping concentration is observed for **Pattern US**, indicating that the higher doping observed for **THF** is a consequence of the PMMA stripping in THF. This large doping concentration variations observed between THF or acetone based PMMA stripping could simply be explained by THF doping graphene, or O_2 adsorption. O_2 is known to strongly p-dope graphene [298], which could explain the higher doping observed for both **THF** and **Pattern US** samples, since the graphene surface of these samples is more exposed to the ambient atmosphere, compared to the **Acetone** sample which is fully covered by a ∼2 nm thick resist layer. Nonetheless, the three samples after PMMA stripping are all p-doped, which is attributed to charges trapped at the graphene-SiO_2 interface [298]. This doping effect is particularly enhanced by harsh surface treatment of the substrate prior to the transfer of graphene [299]. In addition, the sample **Pattern US** shows a larger dispersion of compressive strain, attributed to the transfer of graphene on top of the resist layer prior to the ultra-sonication step.

The samples after the graphene patterning step also show a larger dispersion of compressive strain, compared to the sample **THF**, attributed to the heating steps required for resist baking and sample heating during the plasma etching steps, as thermal annealing induces compressive strain to the graphene layer [285, 300]. Interestingly, the **Pattern US**, **Pattern Resist** and **Pattern Cu** samples show no variation of doping concentration compared to **THF**, corresponding to the previous fabrication step.

Finally, the passivation with SU-8 seems to drastically reduce the hole-doping concentration, and induce a larger dispersion of the doping values. SU-8 was used by Al-Mumen *et al.* to encapsulate graphene and stably n-dope it [301]. Therefore the hole-doping observed before passivation could be compensated by the n-doping of graphene induced by the SU-8 layer.

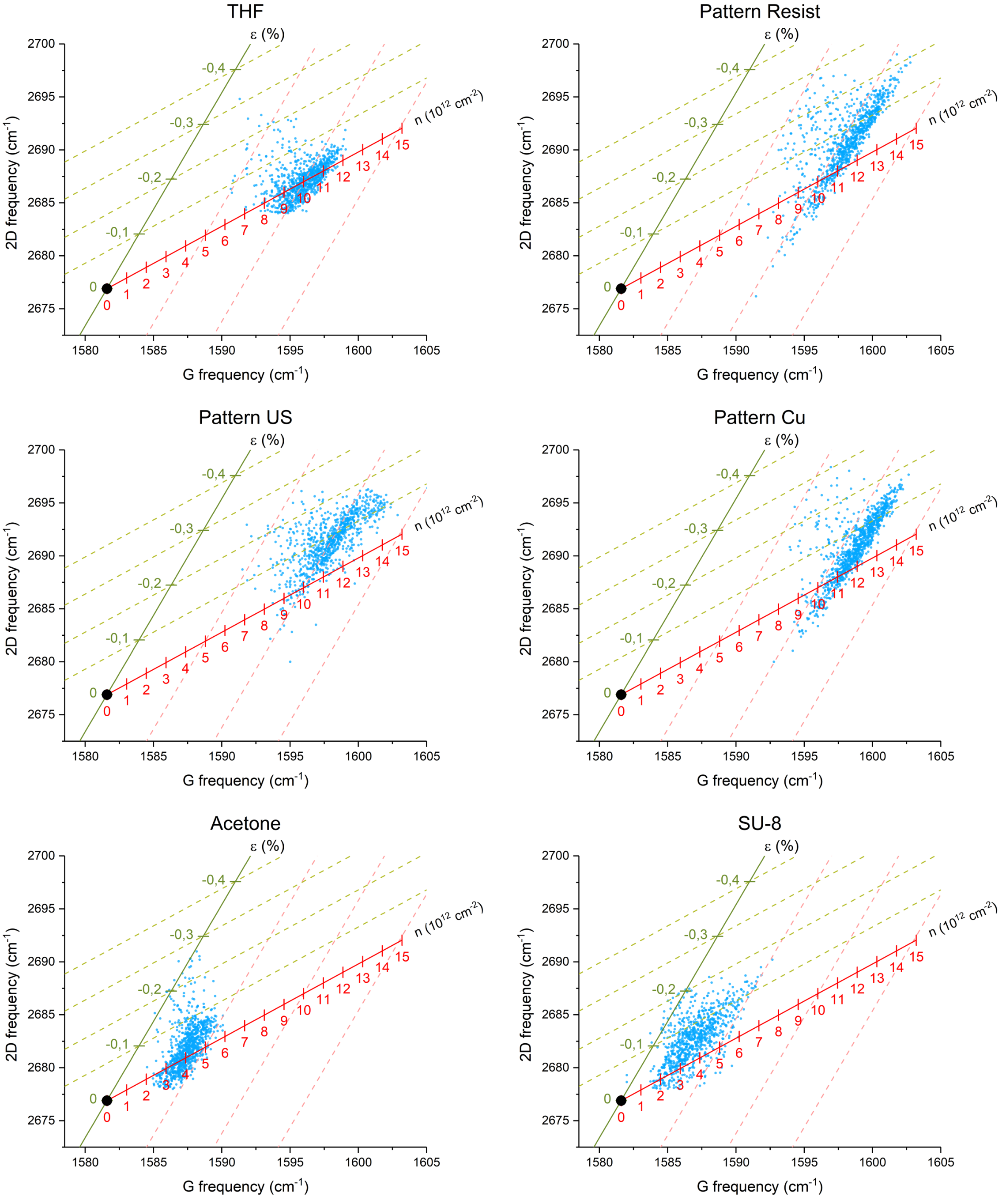

Figure 3.17: Strain-doping plots for the different step of the fabrication process, based on the method developed by Lee *et al.* The experimental (w_{2D}, w_G) data are plotted as blue points, the strain main axis in green and the hole-doping axis in red. The dark point indicates the origin corresponding to suspended graphene.

3.3.3 Conclusion

The AFM, XPS and Raman characterizations were performed at each step of the process and for different fabrication method variants.

The AFM step height measurements demonstrated that THF can remove the PMMA supporting layer more efficiently than acetone, which is commonly used in the literature. Together with a stripping time reduced to 20 min in THF (compared with *at least* a few hours in acetone), THF is therefore a promising solvent for removing PMMA from graphene.

The graphene lift-off is a versatile technique which combines both PMMA stripping and graphene patterning, reducing drastically the cost and time for graphene-based device fabrication. However, the XPS and Raman analysis revealed that the ultra-sonication step is detrimental for the graphene structure integrity as it induces a substantial amount of lattice defects. As these defects show a higher electrochemical reactivity than the basal plane, potentially enhancing the transistor leakage current, this fabrication method appears to be less adapted for devices meant to be operated in liquid environment.

The patterning of graphene is also a critical fabrication step. The conventional method using a resist mask in direct contact with graphene leaves, in our experience, an homogeneous and nanometer-thick resist residue layer evidenced by AFM. Patterning graphene using a Cu sacrificial layer was found to be reproducible and robust, compared to the resist mask technique. AFM and XPS analysis showed that some Cu is left after mask stripping. However, the surface coverage of graphene is not homogeneous, as it is the case with the resist mask technique, effectively leaving some graphene regions exposed to the environment. Moreover, the Cu mask stripping time was limited in time, and only tested for a low concentration of Cu etchant during this thesis. These highly promising results could therefore be improved by optimizing the etching time and solution concentration.

The passivation of the metallic contacts with SU-8 leaves resist residues at the graphene surface, evidenced by the three characterization techniques. These residues seems inevitable while using SU-8. However, using a resist as a passivation material remains more advantageous than using a material that needs to be patterned by etching techniques such as oxide materials. The resist processing needs to be optimized for each application, especially for adhesion issues as evidenced by the delamination observed by SEM which damaged graphene. Even though the passivation layer appears structurally robust after process optimization, the electrical and physical insulation efficiency remains to be demonstrated. Electrical characterizations both in air and liquid will be presented in the next chapter. The results further presented in this work were obtained from SGFET devices produced with the optimized fabrication process consisting in: PMMA stripping in THF, graphene patterning with a Cu sacrificial layer and passivation of the contacts with SU-8.

Chapter 4

SGFET electrical characterizations

After characterizing the impact of the process on graphene properties, the as-fabricated SGFET devices were characterized in air and liquid environments to evaluate their electrical performance. For this purpose, a complete experimental set-up was developed during this thesis. Different types of measurements were carried out in order to find reference conditions prior to the functionalization of graphene and the biosensing experiments. These measurements also complete the characterizations conducted to assess the robustness and reproducibility of the fabrication process.

4.1 Charge carrier mobility, contact & sheet resistance

SGFET fabricated on Si/SiO_2 substrates can be operated in a back-gating configuration by using the Si bulk as a gate for tuning the Fermi level of graphene. As discussed in section 1.2.3, some parameters can be extracted from these measurements, such as the charge carrier mobility μ and the residual carrier concentration n_0 which are additional indicators of the quality of a given fabrication process.

A typical transfer curve obtained by back-gating for a device fabricated with our optimized fabrication process (before SU-8 passivation) is presented Figure 4.1 (left). The Si bulk was contacted using Ag paste and the gate/drain-source potentials applied with a probe station and two sourcemeters.

The devices show a strong p-doping, with typical V_{Dirac} values lying in the 80–150 V range (Figure 4.1 (lower right)) and n_0 in the range of 1–3 × $10^{12}\,\mathrm{cm}^{-2}$. The gate potential was kept below 150 V to avoid the SiO_2 layer breakdown, and the leakage current between the gate and the source was at least 3 order of magnitude lower than the channel current in this potential range. Graphene FET devices are typically p-doped due to polymeric residues or O_2 adsorption on graphene when operated in ambient atmosphere. However, such high V_{Dirac} values are less common and can't be solely explained by resist contamination. We also found similar values for graphene transferred on SiO_2 and cleaned in acetone, indicating that the THF cleaning might not be the cause. The doping is thus attributed to charges trapped at the graphene-substrate interface, generated by the O_2 plasma and piranha cleaning surface treatments, which induce dangling bonds, defects, free-radicals and the accumulation of polar molecules [299]. These charges typically results in a dipole between graphene and the underlying substrate which p-dope graphene [302, 303].

Hole mobility values are comprised between 500–1700 $cm^2.V^{-1}.s^{-1}$ (Figure 4.1 (upper right)). The extracted electron mobility values were not consistent due to the lack of data point on the n-branch side of the I-V curve because of the strong p-doping. Nevertheless, the hole mobility values are typical of large area CVD graphene on SiO_2 [254, 274, 304–306]. Indeed, grain boundaries in CVD graphene are limiting the charge carrier mobility (similarly to point defects, wrinkles or contamination) as they act as strong charge scattering centers [307]. These defects represent highly resistive area, inducing a potential barrier that drastically reduces the carrier mobility [306]. Thus we expect grain boundaries to play a predominant role in our devices, since the grain size of the graphene used in this work is up to 20 µm, which is *at best* in same order of magnitude than the transistor channel length.

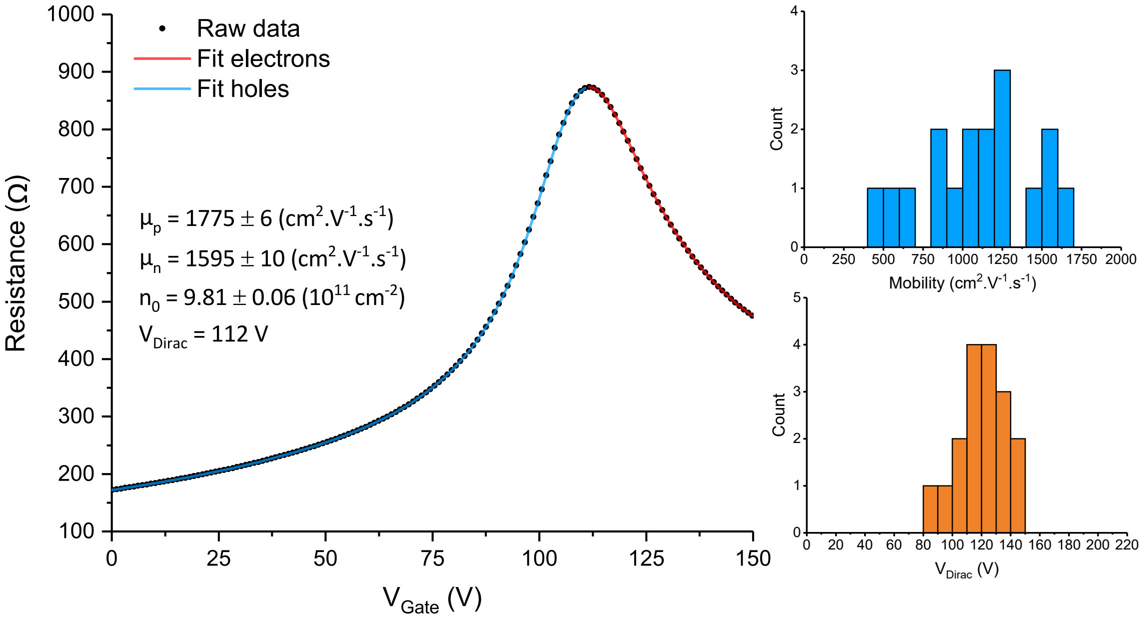

Figure 4.1: Transfer curve of a 250 µm × 50 µm device before SU-8 passivation (left), with typical hole mobility (upper right) and V_{Dirac} potential values (lower right) obtained with our process.

The graphene-metal contact resistance was extracted by TLM at 0 V gate voltage (Figure 4.2). Very low sheet resistance and contact resistivity values of $169 \pm 11\,\Omega.\square^{-1}$ and $1219 \pm 246\,\Omega.\mu m$ respectively are ascribed to the strong graphene p-doping, evidenced by the back-gating and Raman measurements. Since the contact resistance is gate-voltage dependant, the transport at the graphene-metal interface is ruled by the DOS in graphene and its doping [308, 309]. The cleanliness of the graphene-metal interface is also a cause of such low values which are a great asset for electrical sensing.

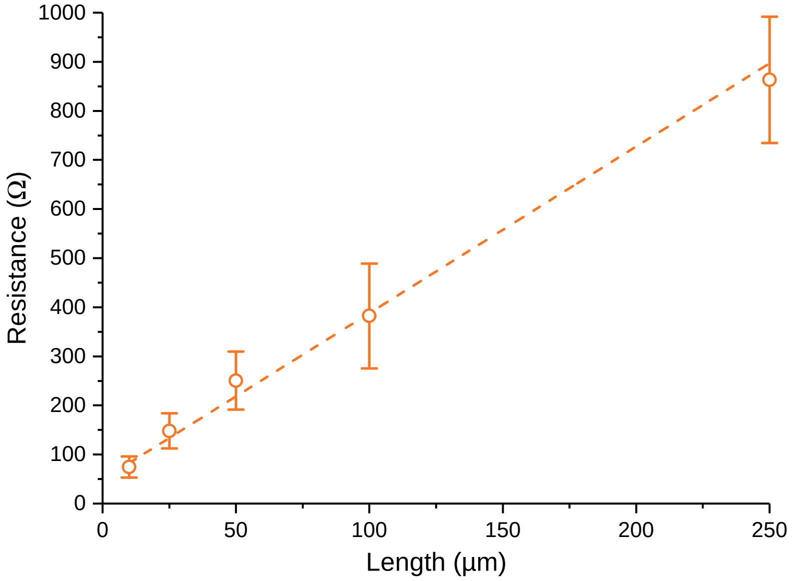

Figure 4.2: Extraction of the sheet resistance and contact resistivity by TLM, from a set of 10 TLM structures each consisting of 5 devices.

4.2 Characterizations in liquid

4.2.1 Experimental setup

The design of the chips (presented Figure 2.5) was motivated by the possibility to directly immerse the sensing area in a beaker which contains the electrolyte, while maintaining the bonding pads and wires outside of the liquid environment. SGFET experiments are typically performed by maintaining the liquid on top of the devices thanks to a polydimethylsiloxane (PDMS) mold [230], or by depositing a single droplet on top of the sensing area [310]. In both cases, the limited amount of liquid (especially for droplets) is a sever limitation for the gate electrode insertion. Moreover, droplets dry really fast, drastically limiting the experiments duration. Finally, the extremely small volume involved (typically in the µL − mL range) can induce undesired concentration gradients or thermal diffusion effects.

In the configuration developed during this thesis, only the part of the chip which is covered by the SU-8 is immersed (Figure 4.3.C), allowing to use large beaker or insert multiples electrodes for electrochemistry purposes. The chip is bonded on a printed circuit board (PCB) for mechanical support (Figure 4.3.B), and the PCB is maintained by a home-made substrate holder (Figure 4.3.A). The individual metallic contacts on the chip are wire-bonded (at the top of the chip) to metallic tracks on the PCB, which are connected to a pin header. The connection between any electrical apparatus and the PCB is possible thanks to a simple breadboard and wire-jumpers. This setup allows to directly and easily address any individual metallic contact on the chip, with a negligible access resistance (<1 Ω). The height of the chip/PCB ensemble can be adjusted, as well as the distance between the electrode inserted in liquid and the chip (typically set to 10 mm). This setup is highly convenient for performing any electrochemical measurements, including long term experiments without being limited by volume-induced effects. A python program was also developed to easily manage all the files thanks to a database, facilitating the data treatment and the extraction of any parameter of interest.

For SGFET measurements (Figure 4.3.D), a modular PGSTAT128N potentiostat from Metrohm was used and equipped with: a bipotentiostat module for control of both drain-source and gate potential/current measurements, a low current amplifier for additional measurement ranges up to 100 pA, and an EIS module. Using a potentiostat for liquid measurements is mandatory, since the potential applied to the "working electrode" needs to be precisely controlled. This is achieved in any electrochemical system by using a so-called "reference electrode", which potential is maintained constant at its known equilibrium potential defined by the Nernst relation.

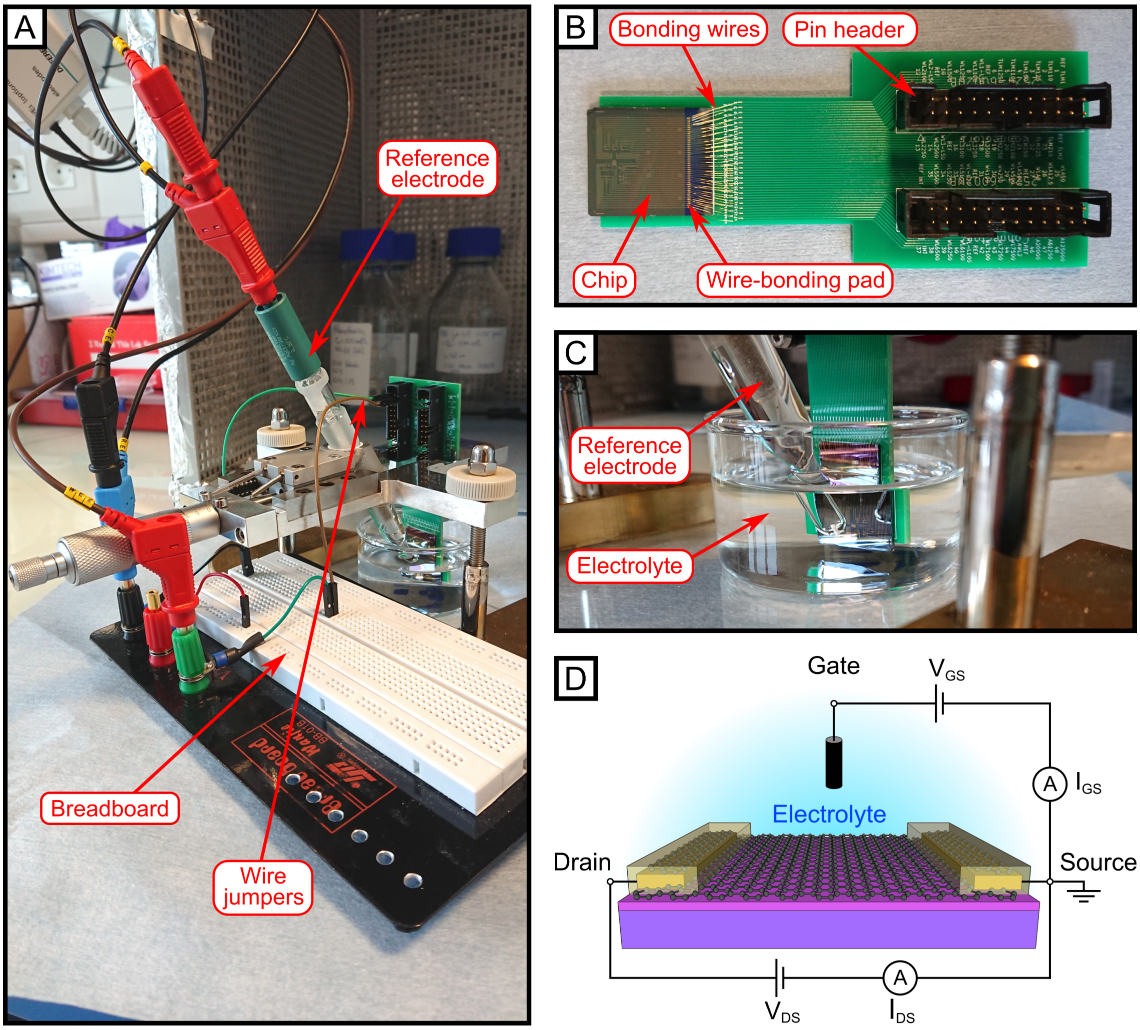

Figure 4.3: a) SGFET experimental setup, showing the reference electrode and the PCB mounted on the home-made substrate holder, and immersed in a beaker containing the electrolyte. The PCB and the potentiostat (not shown in the picture) are connected to the breadboard, respectively thanks to wire-jumpers and banana cables, b) Picture of the chip glued and wire-bounded to the PCB, showing the pin headers for addressing each device independently, c) Zoomed view of the chip immersed in the electrolyte with the reference electrode and d) Electrical schematic of the setup.

Not being limited by the volume of liquid, we used a Ag/AgCl reference electrode in our system. This ideally "non-polarizable second-species electrode" is widely used in electrochemistry, due to its high potential stability in aqueous solutions. On the contrary, "ideally polarizable" Pt pseudo-reference electrodes (largely used in the wire form for easier insertion in liquid droplet) have an unstable potential due to the existence of a mix-potential and the formation of an EDL at the electrode-electrolyte interface, which induces a potential drop. Consequently, the potential of such electrode can significantly vary during experiments, depending on the experimental conditions [248].

This point is further illustrated Figure 4.4, where a 500 µm × 50 µm device was operated in 0.1 mol.L^{-1} sodium chloride (NaCl), by sweeping the gate potential for 5 scans between −0.5 and 0.8 V, with each of the two aforementioned "reference" electrodes. A stable minimal current is observed at ∼0.08 V with the Ag/AgCl electrode, corresponding to the potential at which the Dirac point of graphene is reached (V_{Dirac}). However, when using a Pt electrode, V_{Dirac} is moving toward more negative value over the scans, up to a value of ∼0.46 V. In addition to be less stable, the V_{Dirac} is considerably higher (+0.38 V) when using a Pt electrode, which is not desirable for liquid operation, as high overpotential can promote parasitic electrochemical reactions. Since graphene and the Ag/AgCl electrode have similar work function values (respectively ∼4.5 eV and ∼4.6 eV), the Dirac point is expected to be close to 0 V against this electrode [168].

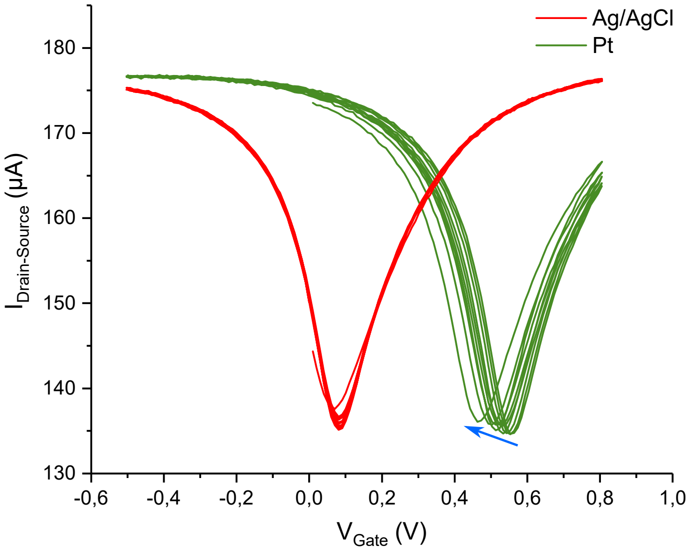

Figure 4.4: Stability comparison between Ag/AgCl and Pt gate electrode for SGFET measurements. V_{DS} was set to 0.1 V, the gate potential was swept 5 times between −0.5 and 0.8 V, at a scan rate of 50 mV.s^{-1} in 0.1 mol.L^{-1} NaCl electrolyte.

4.2.2 SU-8 passivation & leakage current

Considerable effort were dedicated to the fabrication process optimization, in order to achieve a robust and reliable metallic contacts passivation with the SU-8 layer (section 2.1.5) for limiting the devices leakage current when operated in liquid. In our setup, the leakage current is measured between the gate electrode and the transistor source, simultaneously with the drain-source current thanks to the bipotentiostat module.

The necessity of an optimally processed passivation layer is highlighted through the I-V curves (Figure 4.5) of 250 µm × 50 µm devices in 0.1 mol.L^{-1} NaCl electrolyte. Without any passivation, a symmetric transistor transfer curve, and a large and non-reversible leakage current is observed. Current peaks at -0.11 V and -0.32 V are the footprints of reduction reactions occurring either at the graphene or the Au surface.

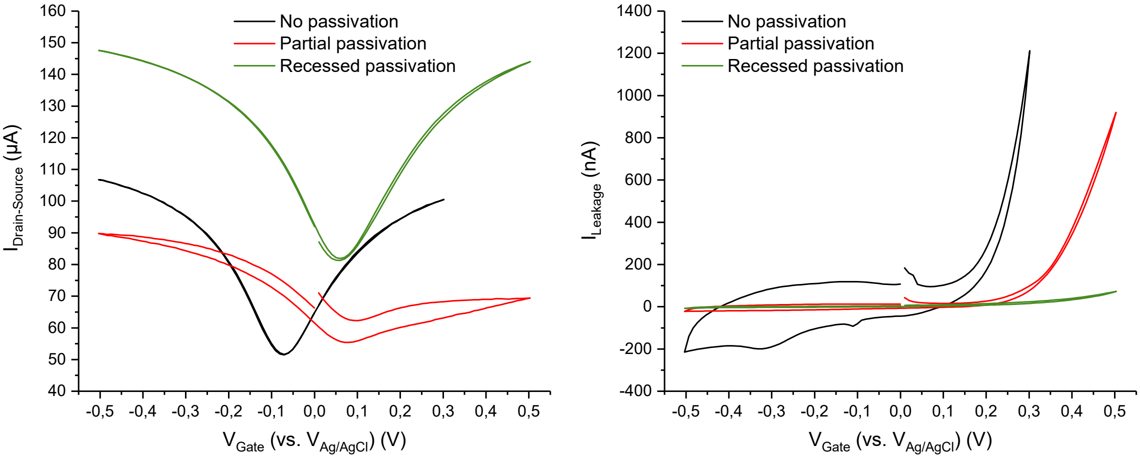

Figure 4.5: Comparison of devices not passivated (black), passivated with the "partial passivation" design (red) and "Recessed passivation" design (green) through drain-source (left) and leakage (right) I-V curves. V_{DS} was set to 0.1 V, the gate potential was swept at a scan rate of 50 mV.s^{-1} in 0.1 mol.L^{-1} NaCl electrolyte.

The device processed with the "partial passivation" design (SU-8 fully covering the metallic contacts and 5 µm of the transistor channel) shows almost no hysteresis, and the signal of the reduction reaction is suppressed. This results demonstrates that the signal observed for the un-passivated device was promoted on the Au contacts. The transfer curve is also asymmetric, due to the non-gated graphene located below the SU-8, in the channel. A p-n junction between this region and the graphene exposed to the electrolyte limits the carrier injection, resulting in an additional series resistance in the electron conduction regime ($V_{Gate} > V_{Dirac}$) and suggesting that the un-gated graphene region is p-doped [304]. In addition, the maximal leakage current remains significant (∼1 µA) compared to the non-passivated device. The leakage current measured during the backward scan crosses the forward scan leakage current at ∼0.37 V, which is typical of a modification of the exchange surface. Such modification is in agreement with the graphene being damaged along the graphene/SU-8 contact line evidenced by SEM observations (Figure 2.30), and visible in the transfer curve, with a large drain-source current hysteresis.

In contrast, the leakage current is drastically reduced (<70 nA) with the "recessed passivation" design (5 µm of the metallic contact is not passivated), the symmetry of the transfer curve is restored, and the hysteresis drastically reduced.

These electrical results first demonstrate that a passivation layer is required to insure a low leakage current and prevent parasitic electrochemical reactions promoted by the Au metallic contacts. The detrimental effect of the mechanical stress induced by a non-optimized passivation process is also highlighted by an asymmetric charge transport, a large hysteresis and a significant leakage current. Such effects are no longer observed when optimizing the device passivation, further validating the fabrication development realized during this thesis.

4.2.3 Experimental conditions optimization

SGFET transfer curves are typically obtained by performing a cyclic voltammetry measurement, consisting in linearly and cyclically sweeping the gate potential between two extreme values. The gate potential range and the sweep speed are two parameters of great importance in such experiments, yet they are not often reported. The effects of these two parameters on the device performance were therefore investigated in order to establish experimental reference conditions. The following experiments were performed in 0.1 mol.L^{-1} NaCl supporting electrolyte.

4.2.3.1 Scan rate effect

As it can be seen from Figure 4.6, the scan rate drastically affects both drain-source and leakage current at high scan rate, with a large increase of the hysteresis at V_{Dirac} and of the leakage current.

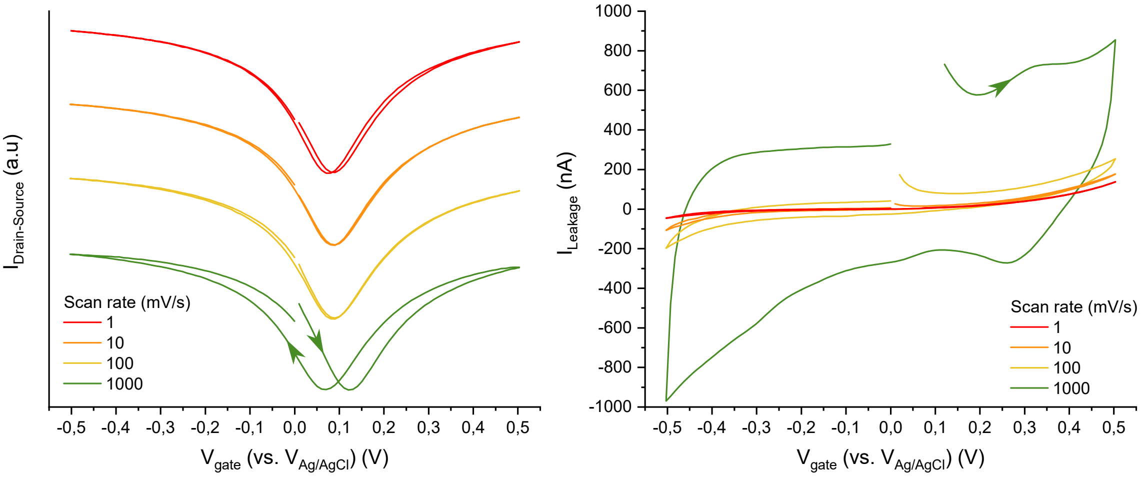

Figure 4.6: Scan rate effect on (left) the transistor current and (right) leakage current. V_{DS} was set to 0.1 V, the gate potential was swept between −0.5 and 0.5 V in 0.1 mol.L^{-1} NaCl electrolyte.

Hysteresis in the transfer curve has been observed in back-gated graphene FETs operated in air. This phenomenon was attributed to charge traps at the graphene-SiO_2 interface, the adsorption of dopants on graphene (oxygen, water, or organic residues) and graphene defects [151, 311]. Charge traps results in additional sites in the DOS of graphene, inducing an asymmetric charge injection upon the forward and backward gate potential sweeps [312]. In the case of the SGFET, the graphene-electrolyte interface is at the core of the gating mechanism. Therefore, the EDL formation kinetics, or surface electrochemical reactions might play a role in the current hysteresis.

In order to clarify such effect, the transient leakage current induced by a gate potential step was measured (Figure 4.7 (left)). The leakage current immediately shows a peak after the potential step, and exponentially decays until reaching a steady state. Such response results from different contributions [248]. First, the diffuse layer adapts to the electric field following the potential step, resulting in an exponentially decaying capacitive current due to the movement of ions (similarly to the discharge of a capacitor in a RC electrical system). An additional contribution is highlighted from the total charge generated during the time interval (Figure 4.7 (right)). Indeed, electro-active species diffusing in the solution and reacting at the electrode surface generate a charge transfer (Q_D), usually observed at longer time scale than the EDL formation. Such charge transfer typically shows a $\sqrt{t}$ dependency, as observed from the linear region of the curve. On the other hand, electro-active species already adsorbed at the surface readily exchange charges after the potential step, without being limited by diffusional effects. Such contribution (Q_{ADS}), if present, is mixed with the EDL charging process (Q_{EDL}), and typically measured from the intercept of the linear region with the y axis.

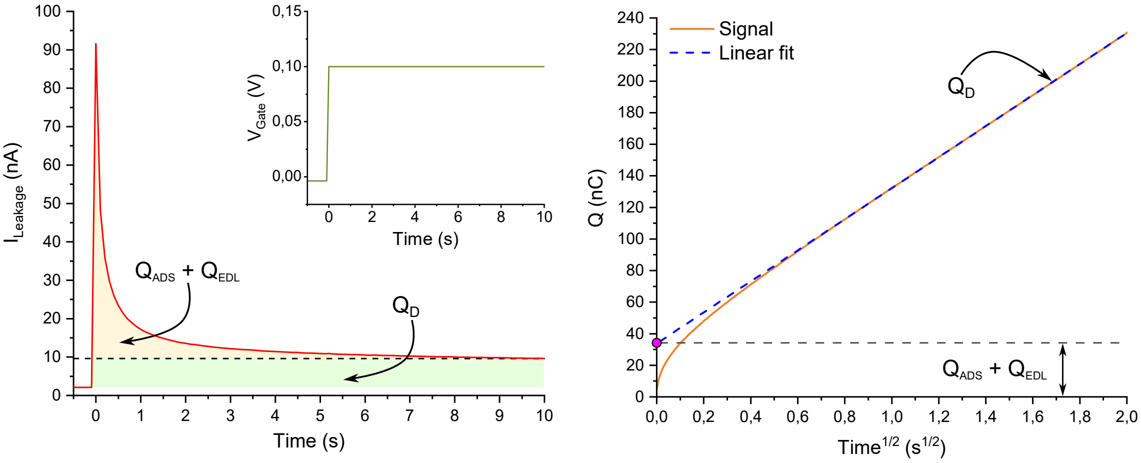

Figure 4.7: (left) Leakage current response (in red) when applying a potential step (inset) in $0.1\,\mathrm{mol.L^{-1}}$ NaCl electrolyte. The different contributions are highlighted from (right) the total charge generated during the interval, plotted as a function of $\sqrt{t}$.

Among the three process mentioned above, the EDL charging process might represent a large part of the leakage current hysteresis observed at high scan rate (1000 mV.s^{-1}), since the resulting capacitive current is directly proportional to the scan rate ν:

$$I_{EDL} = \frac{dQ_{EDL}}{dt} = C_{EDL}\left(\frac{dE}{dt}\right) = C_{EDL} \times \nu \tag{4.1}$$

The EDL formation kinetics might also induce the transistor current hysteresis observed at high scan rate. Due to the fast potential variation, the EDL is never completely established, and the potential drop at the graphene-electrolyte is consequently offset from its steady state value. Since the potential at the graphene-electrolyte interface governs the charge injection in graphene, the transistor current is also offset, leading to the hysteresis observed between the forward and backward scans.

In addition, the two peaks observed in the leakage current at ∼0.33 V and ∼0.26 V are typical of diffusion limited oxidation/reduction reactions. The amplitude of such faradaic current is typically proportional to the square-root of the scan rate, explaining their observation at high scan rate [165]. The origin of such redox reaction could be attributed to the oxidation and the subsequent reduction of graphene defects during the forward and backward scans [313].

At slow scan rate, the leakage current is completely reversible, and the amplitude of the maximal (I_{Ox}) and minimal (I_{Red}) leakage current values are both drastically reduced (Figure 4.8 (left)). On the other hand, the transfer curve hysteresis shows an optimal scan rate range between 10 mV.s^{-1} and 25 mV.s^{-1} (Figure 4.8 (right)).

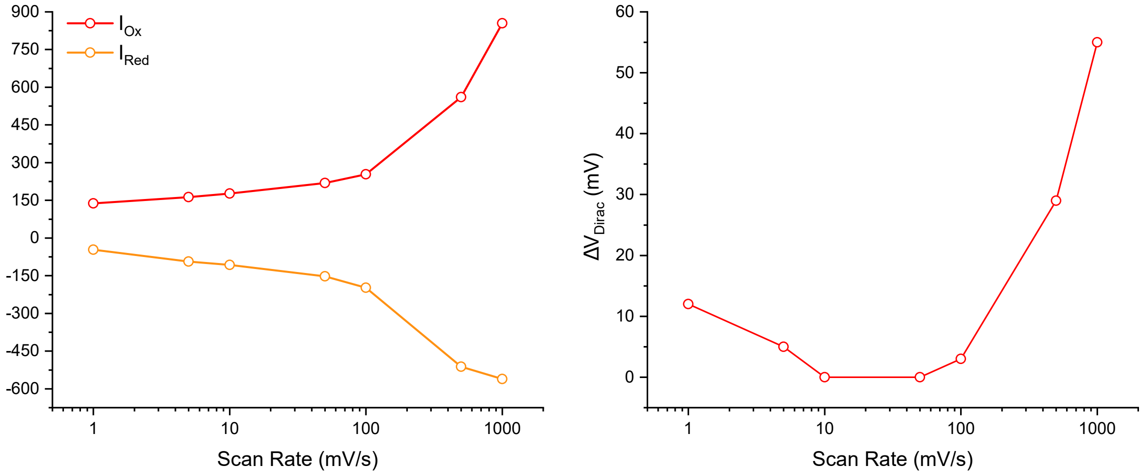

Figure 4.8: Evolution of (left) the hysteresis at V_{Dirac} and (right) of the maximal (I_{Ox}) and minimal (I_{Red}) transistor leakage current. V_{DS} was set to 0.1 V, the gate potential was swept 5 times between −0.5 and 0.5 V in 0.1 mol.L^{-1} NaCl electrolyte.

At lower scan rate (<10 mV.s^{-1}), the transistor current hysteresis increases. In particular, the shift of V$_{\text{Dirac}}$ toward more negative values indicates that graphene is n-doped during the scan. A possible explanation of this effect could involve the sustained polarization of graphene at low scan rate. The durable polarization at large positive gate voltage could promote a surface modification at the graphene-electrolyte interface. The generation of negatively charged oxygenated defects in graphene would induce graphene p-doping, thus can't explain the negative V$_{\text{Dirac}}$ shift observed [314]. The desorption of residues at the surface of graphene resulting in a lower graphene p-doping, could explain this effect. Nevertheless, the scan rate was limited to 10 mV.s^{-1} in the next experiments, in order to insure a low leakage current, and minimize the hysteresis of the transfer curve which could induce artefacts when monitoring V$_{\text{Dirac}}$ variations during biosensing experiments.

4.2.3.2 Electrochemical window effect

Charge transfer kinetics exponentially increase with the potential in the absence of diffusion processes [165]. In aqueous solutions, applying large overpotentials notably induce water electrolysis, producing O_2 and H_2, respectively for the oxidation and reduction reactions. The generation of these gases at the surface of graphene could deteriorate the device. An irreversible hysteresis was effectively observed after sweeping the gate potential up to 1 V, with a drastic increase of the leakage current (Figure 4.9) indicating damages to graphene. It is therefore crucial to operate the device in a limited gate potential range (electrochemical window) where such electrochemical reactions are not promoted in order to preserve the device integrity.

In order to find optimal potential conditions, the gate potential range was increased from −0.1/+0.1 V to −0.5/+0.5 V by −0.1/+0.1 V increments (Figure 4.10). When the electrochemical window is increased, the hysteresis at the Dirac point increases accordingly. The leakage current also increases exponentially when the gate potential is above ∼0.25 V, but remains reversible due to the low scan rate. Consequently, the electrochemical windows was always limited (when it was possible) to a gate potential range of −0.25/+0.25 V in order to limit the leakage current and the hysteresis.

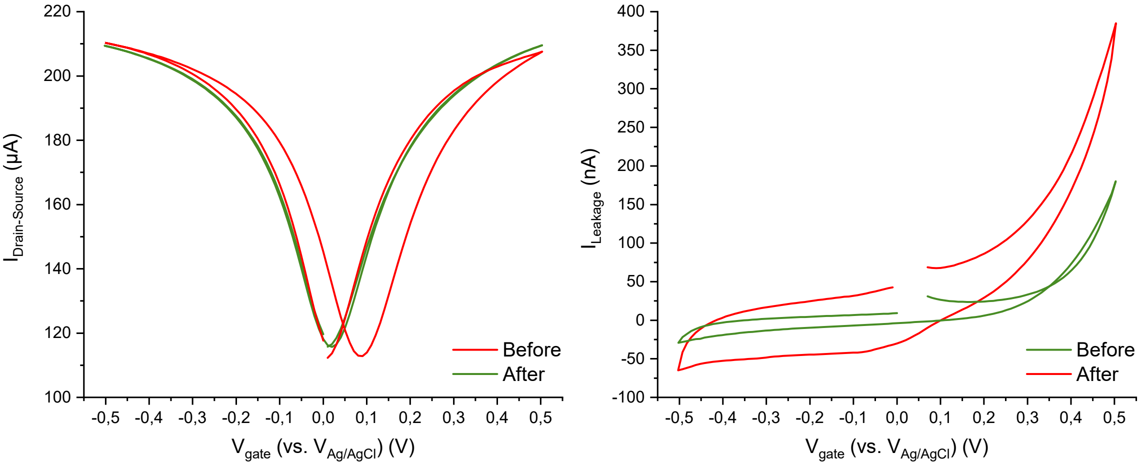

Figure 4.9: Transfer curves (left) and leakage current (right) before (green) and after (red) scanning the gate potential up to 1 V. V_{DS} was set to 0.1 V, the gate potential was swept between -0.5 and 0.5 V, at a scan rate of 10 mV.s^{-1} in 0.1 mol.L^{-1} NaCl electrolyte.

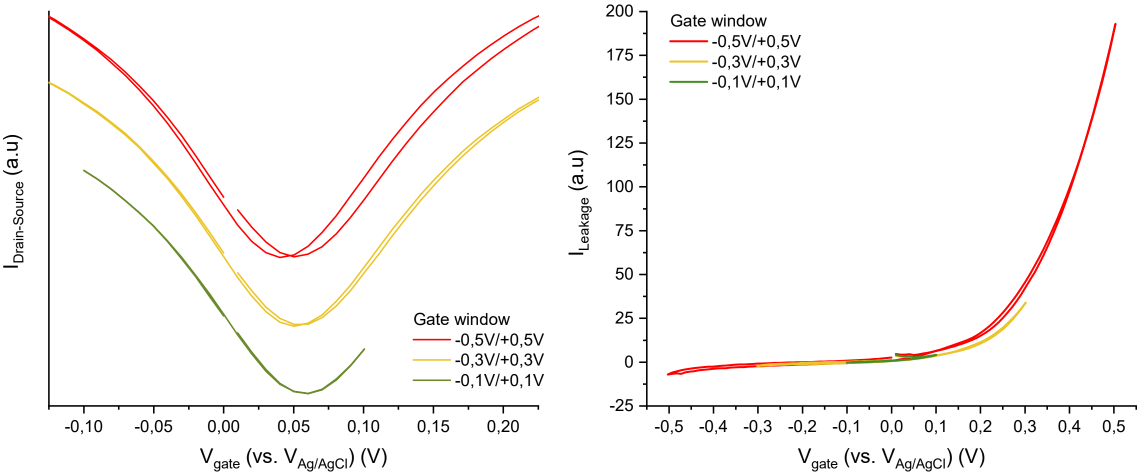

Figure 4.10: Transfer curves (left) and leakage current (right) for different gate potential windows, with V_{DS} set to 0.1 V a scan rate of 10 mV.s^{-1} in 0.1 mol.L^{-1} NaCl electrolyte. The curves for $-0.2/+0.2$ V and $-0.4/+0.4$ V gate windows are not shown for clarity.

4.2.4 Dirac point & electrical sensitivity

Before any electrochemical experiment or biosensing test, every chip was tested in the reference conditions established previously. Statistical data of device electrical performance were obtained from 72 devices from 5 chips, produced through the *last* iteration of the fabrication process optimization. Unless stated otherwise, the next experiments were carried out in 0.1 mol.L^{-1} NaCl solutions, with a drain-source polarization of 0.1 V, at a scan-rate of 0.01 V.s^{-1}. The gate window was limited to -0.25 V/ $+0.25$ V, or extended to $+0.4$ V in order to reach the Dirac point when it was necessary.

As mentioned in section 1.2.3, the potential at which the Dirac point is reached (V_{Dirac}) and the electrical sensitivity (S) are the performance metrics of graphene-based FETs. V_{Dirac} values follow a normal distribution centered around 0.3 V, with a standard deviation of ±25 mV (Figure 4.11). This result indicates that graphene is p-doped, accordingly to the back-gating measurements (section 4.1). In particular, this effect was attributed to the presence of charges trapped at the graphene-SiO$_2$ interface. Nevertheless, the low standard deviation is indicative of a good reproducibility across the different chip tested.

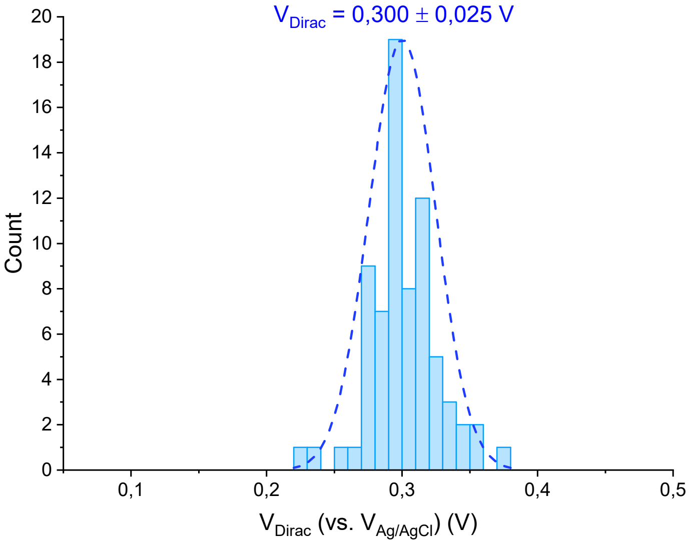

Figure 4.11: V$_{\text{Dirac}}$ distribution of 72 devices following a normal distribution.

Since the electrical sensitivity is directly proportional to the device aspect ratio W/L, the design of a device directly impact its electrical performance, as shown Figure 4.12. In particular, an increasing sensitivity induces steeper conduction branches slopes in the transfer curve.

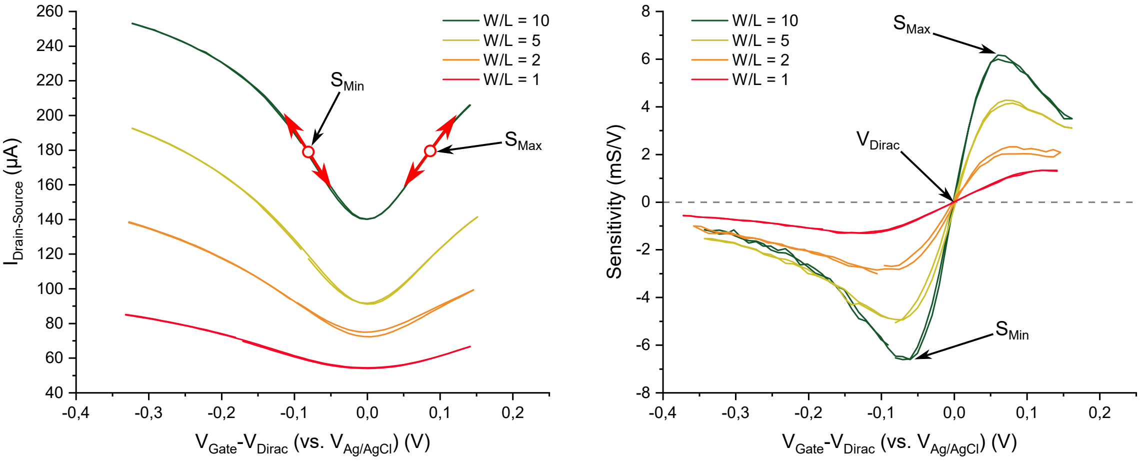

Figure 4.12: Transfer curves (left) and corresponding electrical sensitivity (right) of devices with different W/L ratio. The intercept of the sensitivity with the x axis gives the Dirac point, while both peaks correspond to the points of the transfer curve where the slope is maximal. V_{DS} was set to 0.1 V, the gate potential was swept between -0.25 and 0.25 V, at a scan rate of 10 mV.s^{-1} in 0.1 mol.L^{-1} NaCl electrolyte.

However, experimental sensitivity values are not perfectly proportional to W/L, especially for devices with large aspect ratio (Figure 4.13 (left)), indicating an heterogeneity of the graphene electrical properties. In particular, normalizing the sensitivity by the device aspect ratio gives:

$$S_{norm} = S\left(\frac{W}{L}\right)^{-1} = \mu C_{int} \tag{4.2}$$

where S is the sensitivity, μ the charge carrier mobility, and C_{int} the capacitance at the graphene-electrolyte interface.

As shown Figure 4.13 (right), the normalized electrical sensitivity is dependant on the devices area: small devices show heterogeneous performance and the maximal sensitivity decreases as the device area increases. A similar dispersion was reported by Kireev *et al.* , suggesting an heterogeneous repartition of mobility values attributed to graphene grain boundaries [170]: as the device area increases, the grain boundary density increases accordingly, reducing the charge carrier mobility (as discussed in section 4.1), and sensitivity (Equation 4.2). The dispersion of sensitivity values for small area devices could therefore be attributed to the heterogeneity of grain boundary density across the graphene sample.

These electrical performance are surpassing typical values reported for graphene SGFET on SiO$_2$ [170, 254, 315–317], our best devices reaching $\sim$3.6 mS.$\square^{-1}$.V^{-1} (see inset of Figure 4.13). Kwon *et al.* recently showed that the capacitance at the graphene-electrolyte interface was enhanced for SGFET fabricated on hydrophilic substrates [315]. The substrate hydrophilicity promoted by the surface treatments performed prior to the transfer of graphene could therefore explain the such high performance.

To the best of our knowledge, these results are approaching the highest SGFET sensitivity ($\sim$4.5 mS.$\square^{-1}$.V^{-1}) reported by Brown *et al.* [318], demonstrating the efficiency of the fabrication process.

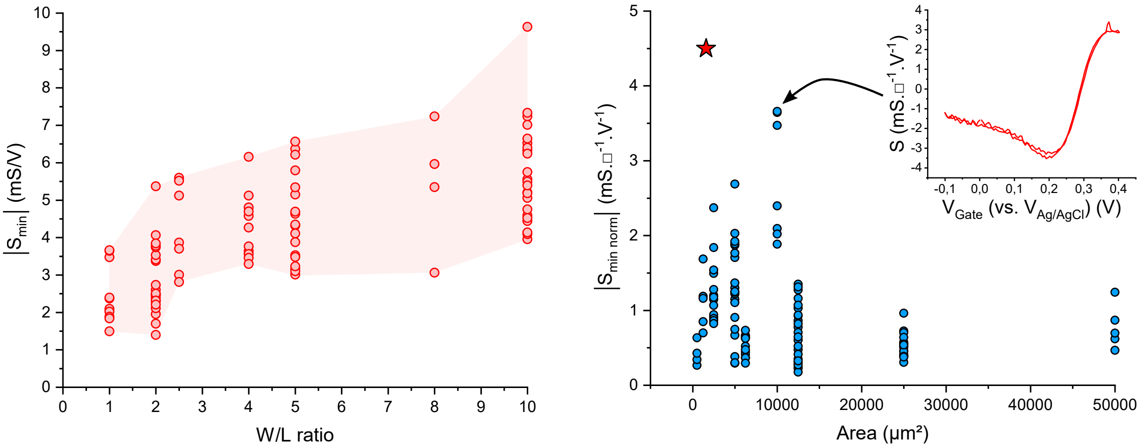

Figure 4.13: Electrical sensitivity repartition as a function of device aspect ratio (left). The normalized sensitivity as a function of devices area (right) highlight the highest transconductance achieved in this work (inset) and the best example found in the literature (red star).

4.2.5 Robustness & drift

The robustness is an important structural property required for the long term operation of biosensors in biological media. Being highly hydrophobic, graphene sheets are unstable in aqueous environment, and prone to aggregation [319,320]. Although the graphene layer is immobilized when integrated into the SGFET, its stability when durably exposed to liquid environment remains to be demonstrated.

In order to investigate the devices robustness in liquid, an experiment consisting of 1000 gate potential scans was carried out. This experiment was realized over three consecutive measurement sessions, and the chip was rinsed in DIW and carefully dried between the sessions. The resulting transfer, sensitivity and leakage current curves are presented Figure 4.14 (left).

During the first 150 scans, the device electrical performance is monotonically varying: the Dirac point is shifting toward negative values, the sensitivity is increasing, and the leakage current is drastically reduced (Figure 4.14 (right)). At the beginning of the second session, these parameters are slightly shifted back toward their initial values, before following the same stabilization observed during the first session. At the beginning of the last session, only I_{Ox} is not stabilized. At the end of the experiment, V_{Dirac} shifted by $-111\,\mathrm{mV}$, S_{min} increased by $37\,\%$ and I_{Ox} decreased by $76\,\%$.

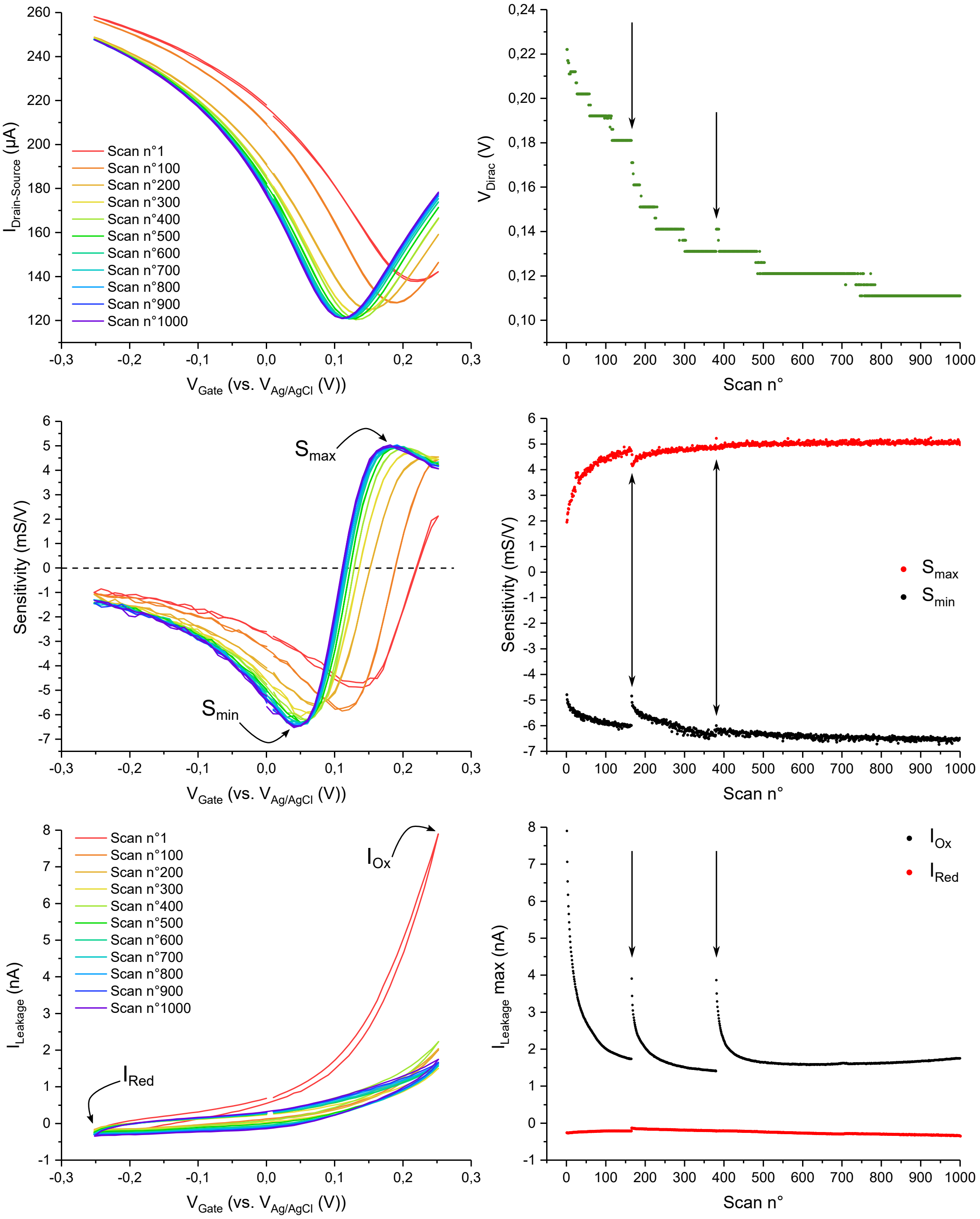

Figure 4.14: (left, from top to bottom) Transfer, sensitivity and leakage current curves evolution over 1000 scans, and (right, from top to bottom) variations of V_{Dirac}, S_{min} and S_{max}, and I_{Ox} and I_{Red}. The black arrows indicates the beginning of a measurement session. V_{DS} was set to 0.1 V, the gate potential was swept between −0.25 and 0.25 V, at a scan rate of $10\,\mathrm{mV.s^{-1}}$ in $0.1\,\mathrm{mol.L^{-1}}$ NaCl electrolyte.

From these experiments, two different behaviours can be distinguished: a global performance stabilization after ~500 scans, and a transient evolution at the beginning of each measurement session. The later effect might be explained by the slow desorption in liquid of O_2, N_2 and other possible ambient contamination adsorbed on graphene between two sessions. Interestingly, the devices which were not electrically connected during the experiment also showed a performance drift (Figure 4.15 (left)). This result suggests that the drift could originate from a surface modification induced by the prolonged immersion of the chip in NaCl, rather than the repeated gate potential scans.

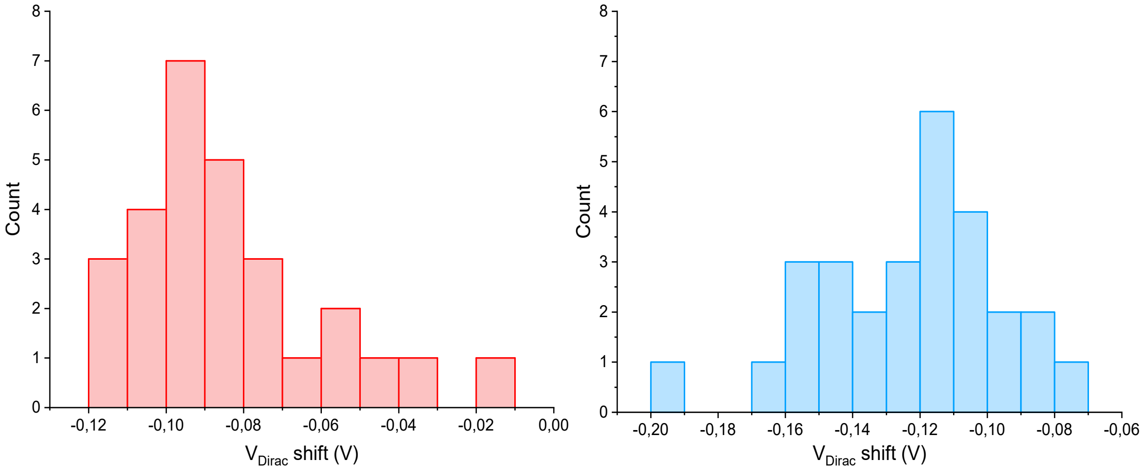

Figure 4.15: V_{Dirac} shift of (left) devices not electrically connected after 1000 scans, and (right) devices after 2 days of immersion in NaCl without scanning the gate potential.

A fresh chip was therefore let in the NaCl solution for two days, without carrying any electrical test, in order to investigate the influence of the gate potential scans on the drift. As shown Figure 4.15 (right), the Dirac point similarly shifted toward negative values, showing that sweeping the gate potential is not preponderant in the drift mechanism.

The device performance was then checked to be stabilized by performing two consecutive measurements consisting of 50 and 150 additional scans. A drift of the Dirac point was still observed during the first measurement (Figure 4.16 (left)), with a shift back toward the initial value at the beginning of the second measurement. V_{Dirac} then drifted at a slower rate, until reaching a stable value (Figure 4.16 (right)).

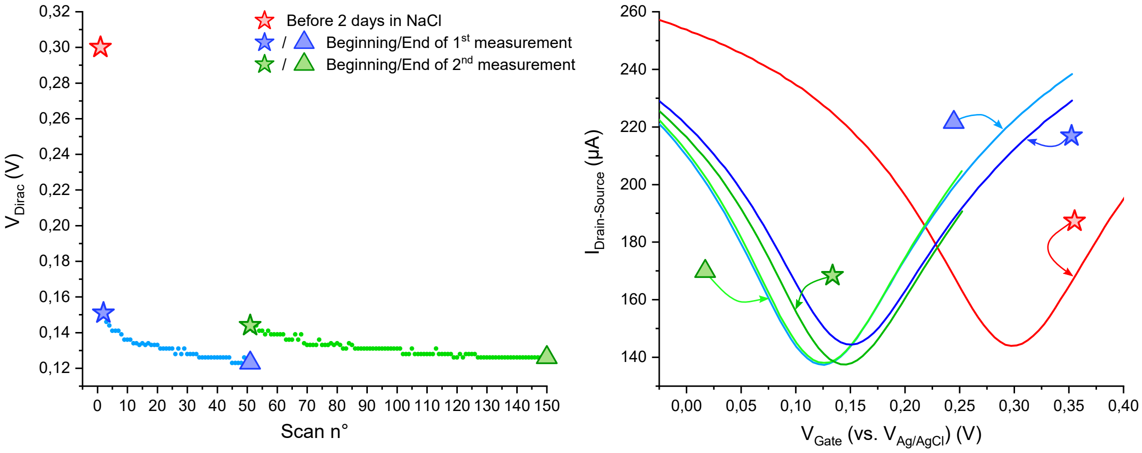

Figure 4.16: (left) V_{Dirac} slow drift between consecutive measurements, after 2 days in NaCl, and (right) the corresponding transfer curves (see symbols on the left figure). V_{DS} was set to 0.1 V, the gate potential was swept at a scan rate of 10 mV.s^{-1} in 0.1 mol.L^{-1} NaCl electrolyte.

An hypothesis can be drawn from the previous experimental results, in order to explain the drift mechanism. First, a large drift is observed when the chip is immersed in NaCl, independently of gate potential sweeps. This drift of graphene properties include a shift of V_{Dirac} toward negative values, an increase of the electrical sensitivity and a reduction of the leakage current. These observations could be attributed to the intercalation of a water molecular layer between graphene and the substrate. This phenomenon was evidenced by Lee *et al.* thanks to AFM and in-situ Raman experiments [321]. In particular, it was observed that water molecules intercalating at the graphene-SiO_2 interface affect the electrical properties of graphene, by removing hole-doping oxygen species, as well as doping effects induced by the substrate. Similarly to our results, a shift of V_{Dirac} toward negative values and an increase of SGFET electrical sensitivity were also observed, which is consistent with the graphene un-doping and a weaker graphene-SiO_2 interaction caused by the intercalation of the water layer [322, 323]. In addition, Lee *et al.* demonstrated that the substrate hydrophilicity and the presence of nanopores could drastically increase the intercalation rate. In our case, graphene edges are completely sealed by the SU-8 passivation layer, which could explain the slow drift rate observed, as water could penetrate between graphene and the substrate only through pinholes.

The slow desorption of p-doping residues at the surface of graphene could also play a role in the performance drift [324]. However, the transient behaviour observed at the beginning of each measurements remains unclear. Such effect could involve the slow re-organisation of the EDL, induced by both the graphene hydrophobicity and the device polarization at the beginning of each test. In order to stabilize the electrical performance prior to any experiment, chips were therefore let 2 days in a $1\,\mathrm{mol.L^{-1}}$ NaCl solution, and the devices were tested by sweeping the gate potential until V_{Dirac} reached a stable value ($\pm 5\,\mathrm{mV}$).

Nonetheless, the devices can be tested for days in liquid environment, while enduring hundreds of gate potential scans without showing loss of performance. In addition, the electrical sensitivity is enhanced and the leakage current reduced after two days in NaCl. The shift of V_{Dirac} toward $0\,\mathrm{V}$ is also a great asset, as the gate potential window can be narrowed, promoting a low leakage current and limiting eventual device degradations.

4.2.6 Ionic strength & pH

Graphene-based SGFETs are sensitive to the pH [172, 181, 325], and the ionic strength (I) of the electrolyte [172, 326]. As discussed in section 1.3.1.3, the ionic strength influences the diffuse layer capacitance, which in turns affects the surface potential at the graphene-electrolyte interface and shifts V_{Dirac} (Figure 4.17).

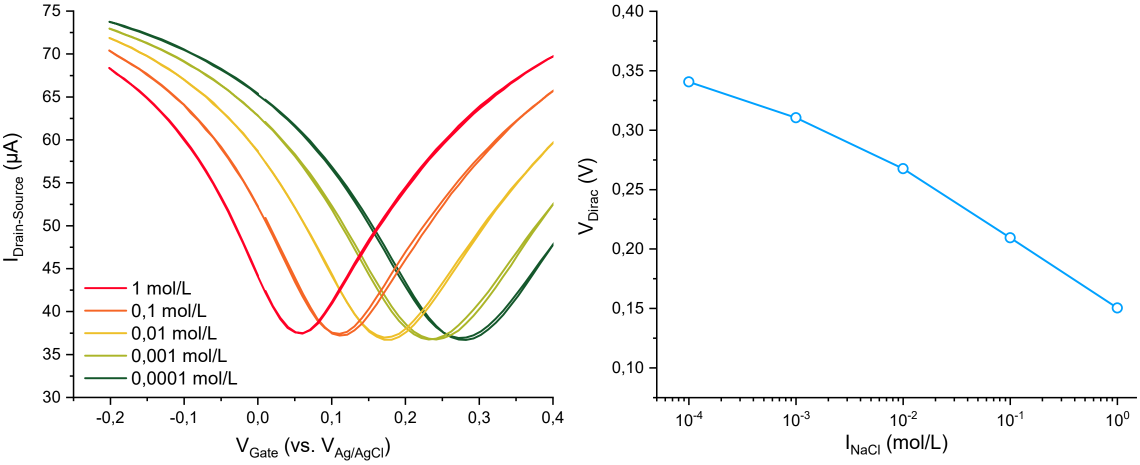

Figure 4.17: Influence of the ionic strength of a NaCl solution, shifting the transistor curves (left) and V_{Dirac} (right) (mean value extracted from 5 devices). $\mathrm{V_{DS}}$ was set to $0.1\,\mathrm{V}$, the gate potential was swept between -0.2 and $0.4\,\mathrm{V}$, at a scan rate of $10\,\mathrm{mV.s^{-1}}$ in NaCl electrolyte.

On the other hand, the devices pH dependency ($\sim$16 mV.pH^{-1}, see Figure 4.18) is governed by the formation of H-bonds, the proportion of ionizable oxygen groups and defects in graphene (as discussed in section 1.3.1.4). It is therefore necessary to control both the ionic strength and the pH in electrical characterizations in liquid environment, in order to prevent any parasitic sensor response upon an ionic strength or pH variation. In addition, working in such controlled conditions is necessary for biosensing experiments, as biological species are highly sensitive to these two physiological factors [327–331]. The pH is set constant in experiments using buffer solutions. In particular, phosphate-buffered saline (PBS) buffers are typically used in biological research when working at pH $\approx$ 7 ± 1. PBS buffers were therefore designed to adjusts and set constant both the pH and the ionic strength for the biosensing experiments (the protocol is provided in Appendix: PBS buffer protocol).

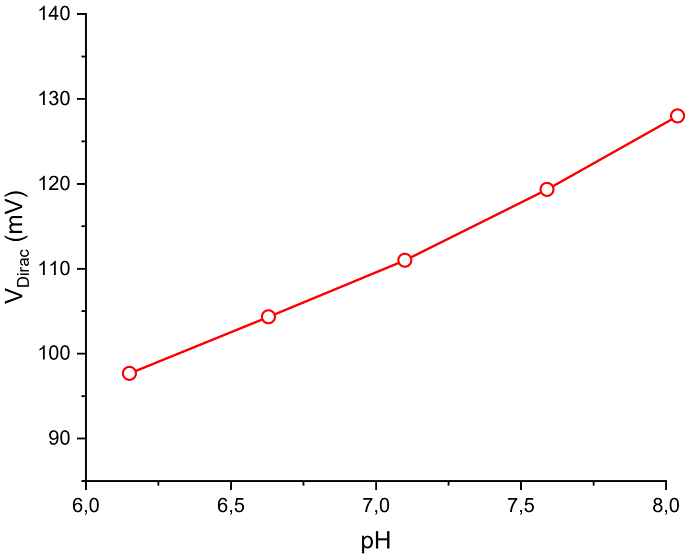

Figure 4.18: Influence of pH on V_{Dirac} (mean value extracted 5 from devices).

4.3 Conclusion

This chapter was dedicated to the electrical characterizations in air and in liquid of the devices after their fabrication. An experimental setup was fully developed, including a sample holder, a PCB, as well as a data treatment program based on Python. This versatile setup allows all kind of electrochemical measurements in liquid thanks to a bipotentiostat, and provides a systematic measurement of the leakage current. The setup is also particularly convenient for testing a great number of devices.

Although the contacts passivation is a critical fabrication step with potential detrimental effects on devices performance with an un-optimized process, it remains inevitable for limiting the parasitic leakage current. Preliminary characterizations in liquid demonstrated the robustness and the efficiency of the passivation design and the associated fabrication process developed during this thesis.

In the same manner that the process development, significant efforts were dedicated to establish experimental conditions in which the devices could be operated reproducibly and stably. To this purpose, the hysteresis was studied and minimized by finding optimized scan rate and gate potential window conditions.

Using these conditions, the performance of a great number of devices fabricated using the last iteration of the process optimization was assessed. Electrical sensitivity values among the best reported were demonstrated, showing the efficiency of the process. These high performance are also ascribed to the surface treatment performed to enhance the hydrophilicity of the substrate before the transfer of graphene. This fabrication step might also be the cause of a strong p-doping observed in back-gating measurements. However, this surface treatment also promote a clean graphene-metal interface, resulting in a low contact resistivity. Graphene grain boundaries seems to limit the charge carrier mobility and electrical sensitivity of the devices. Cu residues at the surface of graphene could also act as charge scattering sites. Using a graphene source with larger grain size, and optimizing the etching of the Cu sacrificial layer could greatly improve these highly promising results.

The devices robustness was also demonstrated, and a drift effect was evidenced and attributed to the intercalation of water between graphene and the substrate. Performing in-situ observations with both AFM and Raman techniques could clarify this phenomenon. Nevertheless, the devices were routinely tested in liquid during several days without showing performance loss, demonstrating that the process developed during this thesis is a strong base for fabricating graphene-based devices which can be operated and characterized in liquid. The next and last chapter will present the non-covalent functionalization of graphene, and the biosensing experiments realized to demonstrate the potential of these devices as biosensors.

Chapter 5

Biosensing with non-covalently functionalized graphene SGFETs

A biosensor is composed of a transducer, and a biorecognition layer providing a specific detection of the target. The SGFET transducer fabrication process and characterizations were presented in the previous chapters. In particular, electrical measurements performed in liquid environment demonstrated a superior device performance and robustness, which are two important requirements for biosensing applications.

In order to demonstrate the potential of these devices as biosensors, it is necessary to first immobilize bioreceptors at the graphene surface. The non-covalent functionalization of graphene with aromatic linkers appears to be the best method for preserving the graphene electrical conductivity and prevent the denaturation of the bioreceptors (as discussed in section 1.3.3). In particular, the tripod multivalent linker was identified as an highly promising alternative to the widely used PBASE, enabling the formation of a stable and predictable SAM at the graphene surface.

This chapter will present the biosensing experiments realized in order to fulfil the thesis objective, consisting in establishing a first proof of concept of tripod-functionalized SGFET biosensing.

5.1 Experimental design

The SGFET sensing mechanism lies on the modification of the electric field in the diffuse layer, induced by the analytes binding to the receptors at the graphene surface. The diffuse layer potential exponentially decays from the sensor surface with the characteristic Debye length, which is ionic strength dependant: the higher the ionic strength, the thinner the diffuse layer (see graph of Figure 5.2). The Debye length is consequently below 1 nm in physiological media, due to the high ionic strength (~0.1 mol.L^{-1}). Detecting large biomolecular objects such as antibodies, which are typically 10–15 nm, is therefore challenging and requires to work in highly diluted buffers in order to extend the diffuse layer deeper into the solution [332]. However, working at extremely low ionic strength (<10^{-3} mol.L^{-1}) is also a source of gate potential instability and measurement uncertainty [333].

As a result, there is a trade-off when choosing the buffer concentration, between the diffuse layer minimal thickness required for detecting the target, and the sensor performance. For these experiments, PBS buffer solutions were prepared with an ionic strength of 10^{-3} mol.L^{-1}, leading to a Debye length of ~9.6 nm. The choice of the bioreceptor/target couple was thus dictated by the thickness of the biorecognition layer including the tripod (~2 nm) for the functionalization of graphene, the bioreceptor and the target.

Streptavidin and biotin were used as ligand and receptor for this first proof of concept. These two bioconjugates are widely used in biochemistry for their exceptional binding properties [334]. Biotin, also called "vitamin B$_7$", is a small water-soluble organic molecule (~244 Da) specifically binding avidin and its derivative including streptavidin, a 52.8 kDa (~5 nm) tetrameric protein, with an exceptionally high affinity (K$_\mathrm{d}$ ~ 10^{-14}–10^{-16} mol.L^{-1}) [334]. Such affinity is promoted by numerous hydrogen bonds and Van der Waals interactions within each of the four binding sites of streptavidin (Figure 5.1).

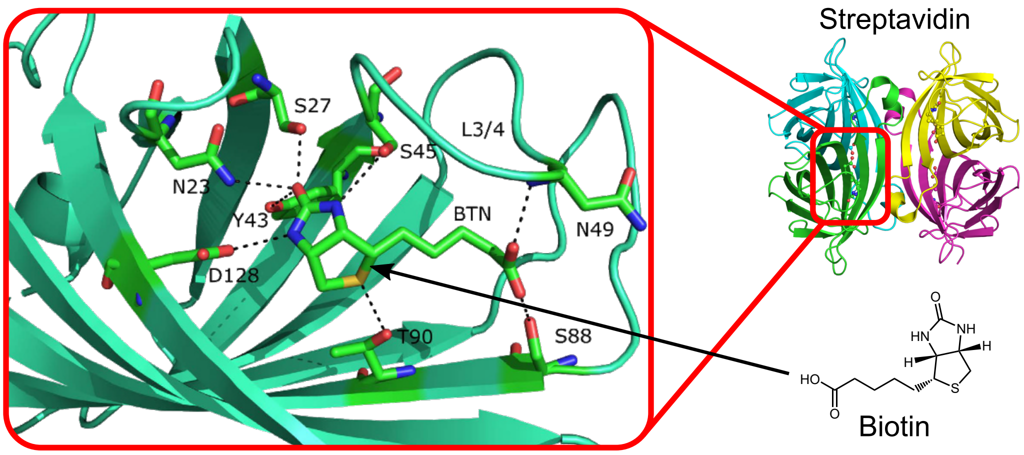

Figure 5.1: 3D representation of the structure of streptavidin and zoomed view of biotin-streptavidin interactions in one of the binding sites, through hydrogen bonds and Van der Waals forces (from [335]).

Streptavidin is negatively charged at pH ≈ 7, having an isoelectric point close to 5, and was therefore used as the target in these charge-sensitive biosensing experiment. On the other hand, biotin was used as receptor to immobilize streptavidin within the EDL, while benefiting from its small size. Interestingly, this biorecognition layer scheme provides the possibility to detect biotin in a second biosensing experiment, using the available binding sites of the immobilized streptavidin. The full biorecognition layer, comprising the tripod, the biotin receptor and the streptavidin target fit within the EDL formed in a 10^{-3} mol.L^{-1} PBS buffer solution (see Figure 5.2).

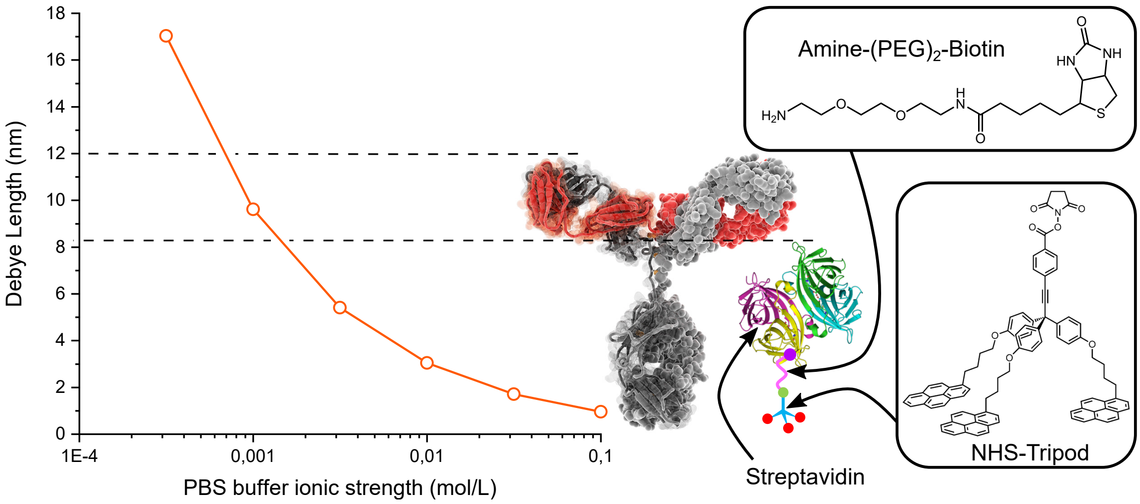

Figure 5.2: Debye length as a function of the ionic strength of the PBS buffer, and scaled representation of the biorecognition layer including the streptavidin target. An antibody is shown for size comparison (from [336]).

The transport of biomolecules toward the sensing area by diffusion and convection, and the binding kinetics involved in the detection play a critical role in the biosensor response time and its performance [117]. Such effects should therefore motivate the experimental design and interpretation in any biosensing experiment. The experimental conditions are well controlled when using an optimized microfluidic channel supplying a constant flow of fresh analytes at the sensor surface. In particular, the sample volume and the biosensor response time are drastically reduced [337]. Working in such conditions could lead to highly efficient biosensors, but the implementation of a microfluidic system requires long development time that could not fit within the necessary timeline of this work. Therefore its completion was not considered during this thesis. The following experiments were performed with the setup used for the electrical characterizations in liquid, presented in the previous chapter. In order to circumvent long response time faced in the absence of flow, we worked with reagent concentrations several order of magnitude above saturation levels, and the experiments duration were extended to the maximum. Such experiments do not provide the possibility to study binding kinetics. However, the qualitative response obtained at saturation still represents a first step toward the demonstration of a biosensor performance and its proof of concept.

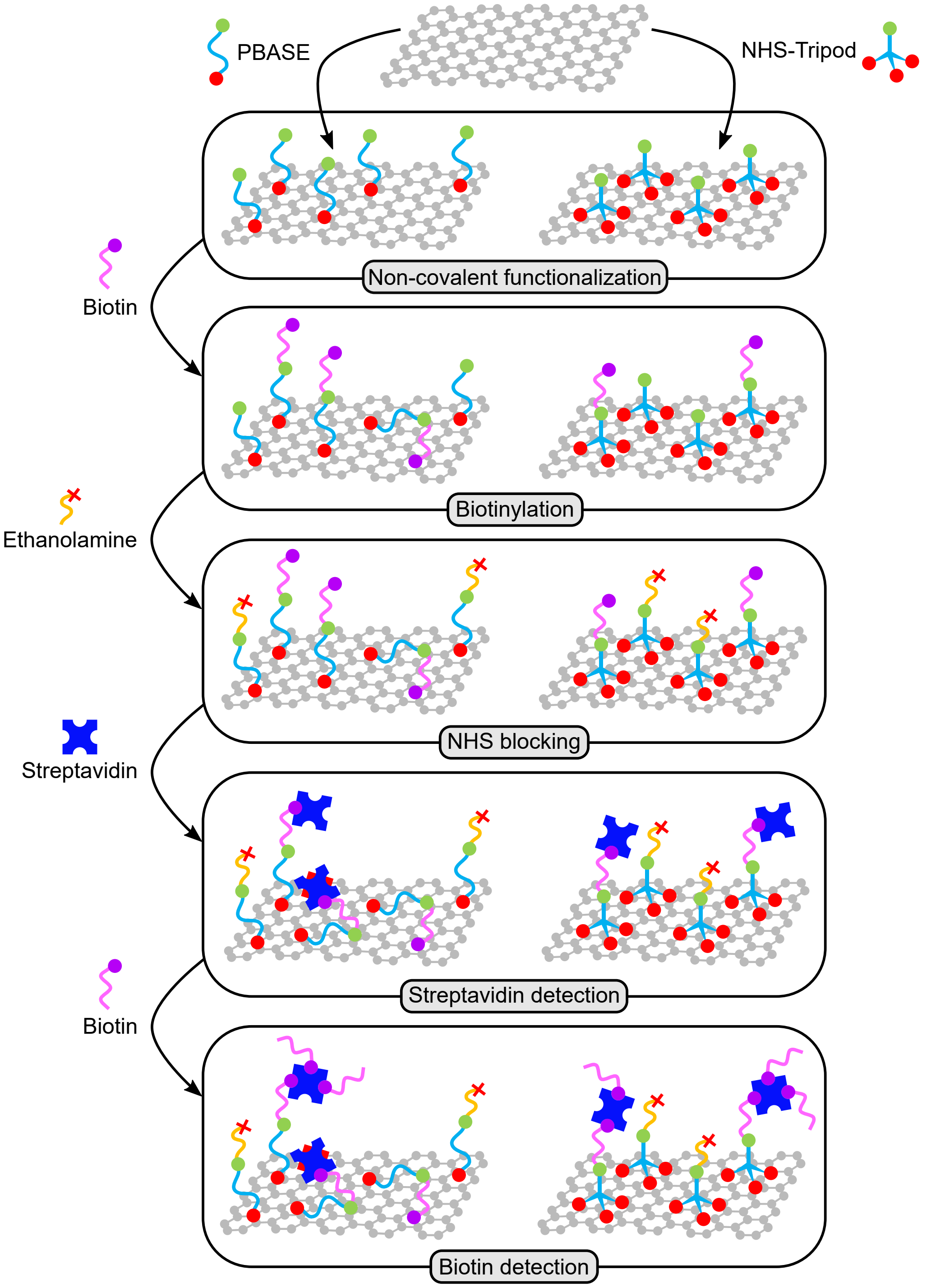

Figure 5.3: Schematic of the main steps of the procedure followed for both biosensing experiments carried out with either the tripod or PBASE.

5.2 Materials & protocol

Two streptavidin detection experiments were carried out during this thesis, one based on SGFET non-covalently functionalized with tripod, the other one with PBASE. The protocol of these experiments comprises several steps, from the functionalization of graphene to the detection of streptavidin and biotin. These steps, summarized in Figure 5.3, will be further detailed in the next subsections.

5.2.1 Non-covalent functionalization of graphene

The non-covalent functionalization of graphene is a promising technique for interfacing graphene with biological objects (as discussed in section 1.3.3.3). This first step, carried out before grafting bioreceptors, consists in adsorbing the linker molecule at the graphene surface. The highly promising tripod and the widely used PBASE were both tested during this thesis.

NHS-tripod was produced and provided through our collaboration with the team of William Dichtel from Northwestern University, Illinois. The complete synthesis procedure of this complex molecule, including nuclear magnetic resonance spectroscopy (NMR) characterizations has been reported elsewhere [206]. 100 µmol.L^{-1} NHS-tripod solutions were prepared in THF solvent (>99.9 %, anhydrous, purchased from Sigma Aldrich), and stored under N_2 atmosphere when not used. PBASE was purchased from Santa Cruz Biotechnology (95 %). 100 µmol.L^{-1} PBASE solutions were prepared and stored following the same procedure as for the tripod. The non-covalent functionalization of graphene-based biosensors with both tripod [4] and PBASE consists in:

1. Immersing the chip in the tripod or PBASE solution for 1 min
2. Rinsing in fresh THF for 1 min to remove weakly bound molecules
3. Rinsing in DIW for 30 s, performed two times to insure the complete removal of THF

The chip is finally rinsed with the solution used in the next experiment (here, 10^{-3} mol.L^{-1} PBS (pH $\approx$ 7.6) prepared following the protocol provided in Appendix: PBS buffer protocol), and inserted in the sample holder for electrical characterizations in PBS.

5.2.2 Biotinylation

The receptors grafted to the NHS-tripod or PBASE linkers consisted of a derivative of biotin. NH_2-$(PEG)_2$-Biotin is a water-soluble biotin compound containing a polyethylene glycol (PEG) spacer arm and a terminal primary amine. The hydrophilic PEG arm provides a long (∼2 nm) and flexible connection to minimize steric hindrance involved with binding to streptavidin. The terminal amine group is necessary for the covalent binding reaction with the NHS ester functionality of tripod and PBASE (Figure 1.28.b). The biotin derivative was purchased from Fisher Scientific and dissolved in PBS to prepare 1 µmol.L^{-1} solutions. The solutions were stored at 4 °C when not used. The biotinylation of the tripod or PBASE functionalized SGFET sensors consists in:

1. Rinsing the chip in PBS for 5 min
2. Immersing the chip in the biotin solution for 5 min
3. Rinsing the chip in PBS for 5 min

5.2.3 NHS blocking

After grafting the biotin receptors, it is necessary to block eventual free NHS ester chemical functions, in order to prevent any non-specific interactions possibly inducing a false positive signal during the detection of streptavidin. These NHS moieties are blocked by chemical binding with the primary amine of ethanolamine, a linear molecule presenting an alcohol function at the other extremity of its carbon chain. 0.01 mol.L^{-1} ethanolamine solution ($pH \approx 7$) were prepared by dissolving ethanolamine hydrochloride (>99 %, purchased from Sigma Aldrich) in PBS. The protocol for blocking the NHS moieties with ethanolamine consists in:

1. Rinsing the chip in PBS for 10 min
2. Immersing the chip in the ethanolamine solution for 10 min
3. Rinsing the chip in PBS for 10 min

5.2.4 Streptavidin detection

Streptavidin was purchased from Fisher Scientific, and a mother solution was prepared according to the manufacturer. 1 nmol.L^{-1} streptavidin solutions were prepared by diluting the mother solution in PBS. Such concentration is at least five orders of magnitude higher than the dissociation constant of the binding reaction (K_d), insuring that the biosensor response time is not limited by the binding kinetics [117].

The streptavidin detection experiments were carried out by:

1. Rinsing the chip in PBS for 5 min
2. Immersing the chip in the streptavidin solution for 60 min
3. Rinsing the chip in PBS for 5 min

5.2.5 Biotin detection

The protocol followed for the biotin detection experiment was the same as the biotinylation step:

1. Rinsing the chip in PBS for 5 min
2. Immersing the chip in the biotin solution for 5 min
3. Rinsing the chip in PBS for 5 min

5.3 Experimental results & discussions

Electrical characterizations were carried out after each steps of the protocol presented above. These measurements consisted in cycling the gate potential until the device performance was stabilized, in order to prevent artefacts induced by an eventual drift effect. The resulting transfer curve, leakage current and electrical sensitivity obtained for both tripod and PBASE functionalized SGFET will be presented together for clarity purpose. The devices tested were 500 µm × 50 µm, V_{DS} was set to 0.1 V and ν to 0.01 V.s^{-1} in both experiments.

5.3.1 Graphene functionalization

The effects of graphene functionalization with tripod and PBASE on devices performance are shown Figure 5.4. Before functionalization, both devices V_{Dirac} values are close to ∼0.2 V. After functionalization of graphene with PBASE, V_{Dirac} is shifted toward more positive values (0.272 V), indicating a p-doping effect. Graphene p-doping upon adsorption of aromatic molecules carrying an electron withdrawer group such as the NHS ester functionality of PBASE has been reported [202,203,338–340]. Negligible modifications of the devices electrical sensitivity, leakage current and drain-source minimal current indicate that the graphene structure is also preserved after the non-covalent functionalization.

Similarly to PBASE, the adsorption of NHS-tripod induces a shift of the transfer curve without drain-source current loss or a significant electrical sensitivity alterations. In particular, V_{Dirac} is shifted toward negative values (0.149 V), indicating that graphene is n-doped after the tripod adsorption. The two opposite p-doping and n-doping effects, respectively observed after the graphene functionalization with PBASE and tripod further confirm that PBASE tends to lie flat on graphene, while the NHS-tripod projects its functionality away from the surface [5]. The pendant NHS electron withdrawer group of PBASE in the vicinity of the surface could effectively pulls out electrons from graphene and induce p-doping. Yet, this effect seems hindered with the tripod, resulting from the projection of the NHS group $\sim$2 nm away from the surface. Explaining the origin of the n-doping effect is however not trivial. This result was reproduced within our group, suggesting that it is not a simple artefact. The presence of the hydrophobic pyrene feet and aliphatic legs of the tripod close to the graphene surface could induce a reduction of the permittivity at the graphene-electrolyte interface, resulting in a shift of the transfer curve toward negative values [339].

This hypothesis is further supported by preliminary results obtained with tripod functionalized SGFET in concentrated PBS-1X buffer ($\sim$0.17 mol.L^{-1}). In these conditions, a similar n-doping effect was observed (Figure 5.5). Since the diffuse layer is highly compressed in such concentrated buffer ($\lambda_{Debye} \sim 0.7$ nm), the upper part of the tripod is screened. As a consequence, the shift of V_{Dirac} toward negative values observed in both diluted and concentrated buffer can be assigned to the presence of the pyrene feet and the lower part of the molecule in the vicinity of graphene. The fact that the shift of V_{Dirac} in diluted buffer (-60 mV) is 6 times higher than in concentrated buffer (-10 mV), indicates that the upper part of the tripod also participates to the doping effect in diluted conditions. In particular, such polar moiety could locally induce a modification of the ionic distribution, resulting in an excess of positive charges in the diffuse layer compensated by negatives charges in graphene.

Finally, the leakage current is drastically reduced after tripod adsorption. The tripod seems to act as a passivation layer, screening the eventual graphene defects, which could be the source of leakage current. This effect could also be attributed to the modification of the water layer at the graphene-electrolyte interface induced by the hydrophobic tripod feet and legs.

Nonetheless, these results show that both PBASE and tripod-based functionalization strategies are promising for interfacing graphene with receptors without altering the electrical sensitivity. However, the tripod appears to be more advantageous, since it reduces the leakage current and shifts V_{Dirac} toward negative values, allowing to narrow the gate potential window and eventually operate the device at low gate voltage.

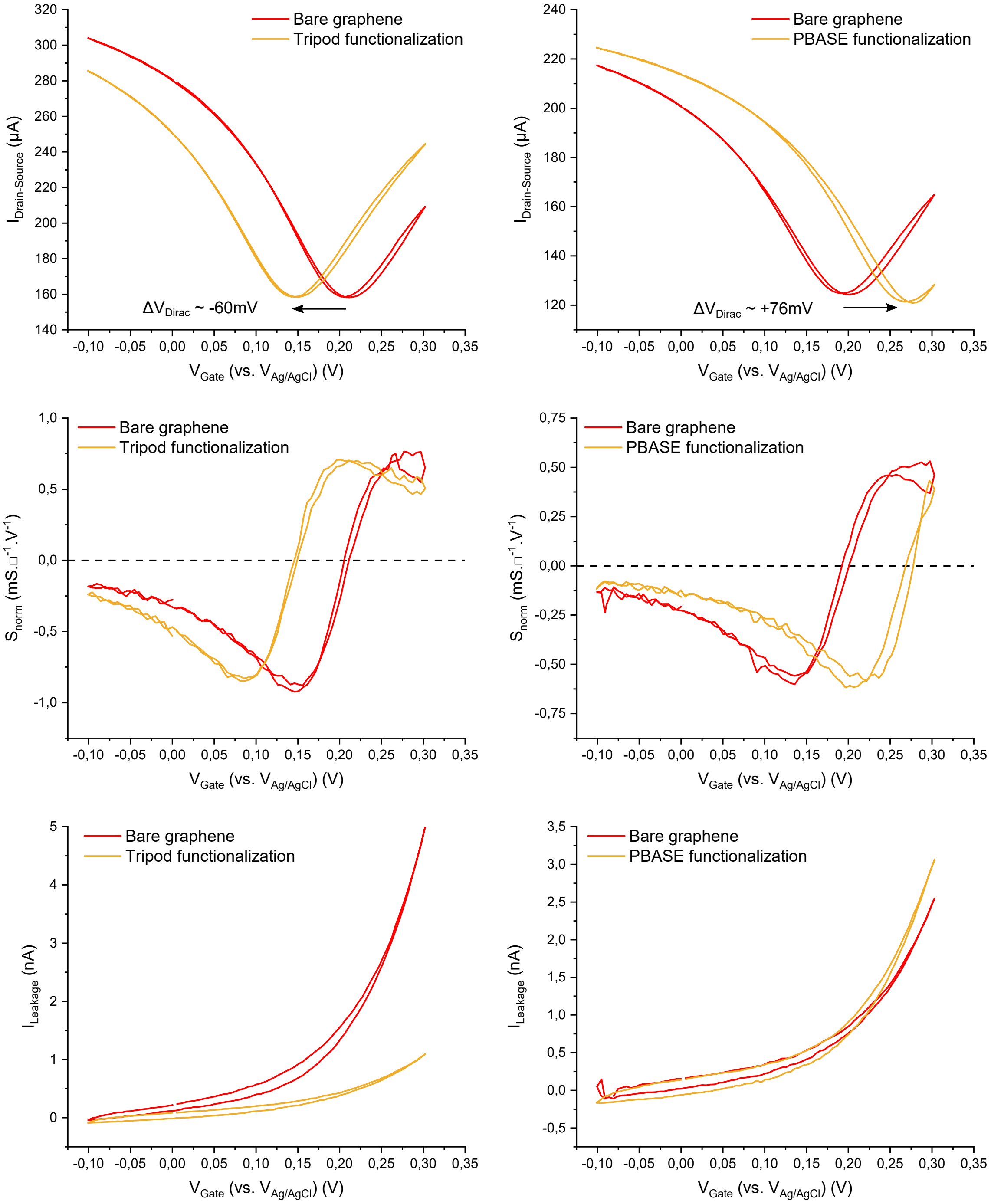

Figure 5.4: Transfer curves, normalized electrical sensitivity and leakage current curves of SGFET before (red) and after (orange) non-covalent functionalization of graphene with tripod (left) and PBASE (right).

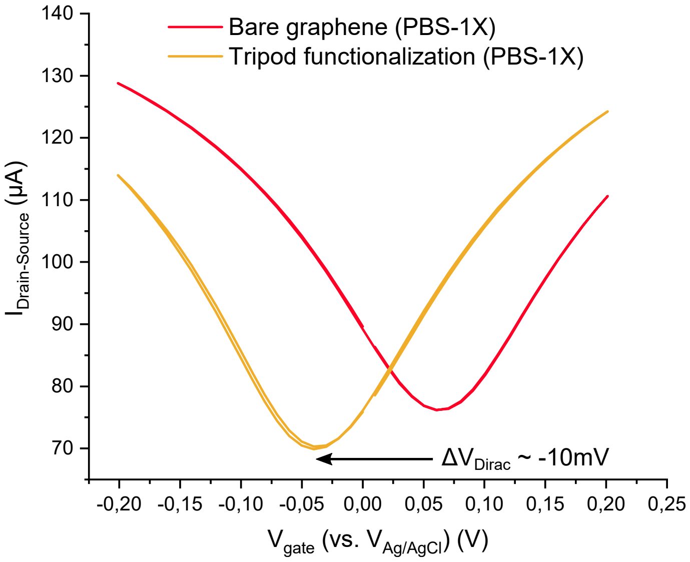

Figure 5.5: Transfer curves of SGFET before (red) and after (orange) non-covalent functionalization of graphene with tripod in PBS-1X (~0.17 mol.L).

5.3.2 Biotinylation and NHS blocking

Binding of biotin and NHS blocking by ethanolamine effects on devices performance are presented Figure 5.6. Biotinylation of the sensors induced a similar small positive shift of V_{Dirac} for both tripod (+7 mV) and PBASE (+6 mV) functionalization methods. Blocking the NHS groups with ethanolamine induced also a similar shift (−5 mV) in both experiments. Within a ±5 mV margin of error on the determination of V_{Dirac}, these two steps seems to have a negligible influence on graphene doping and devices electrical sensitivity. However, the maximal leakage current value of the tripod functionalized device increases significantly after both biotinylation and ethanolamine steps. The capacitive current also increases with the ethanolamine step. This increase, not observed for the PBASE functionalized device, could be attributed to the non-specific adsorption of these small molecules on graphene, since the tripod shows a lower saturation coverage than PBASE [207].

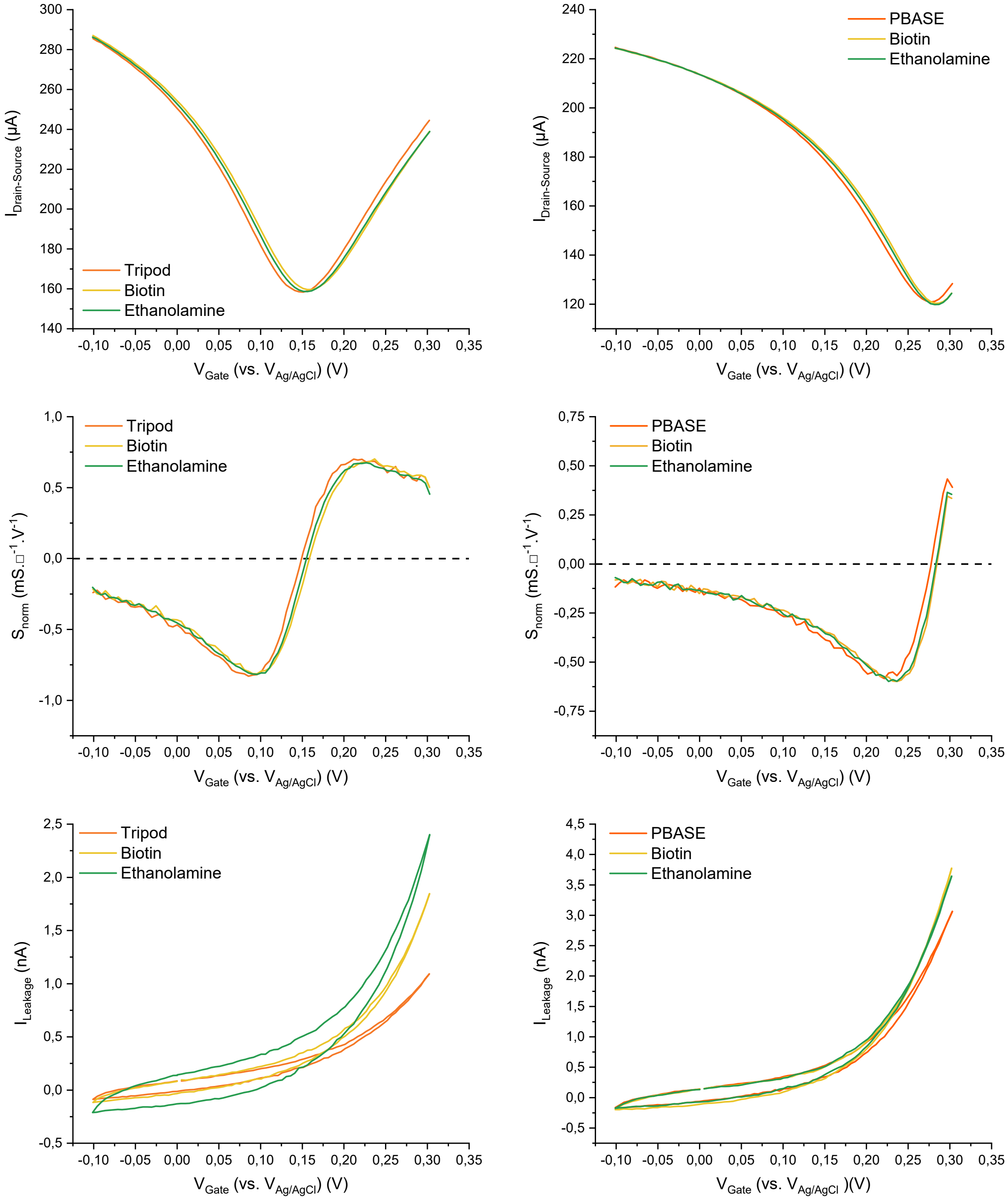

Figure 5.6: Transfer curves, normalized electrical sensitivity and leakage current curves after non-covalent functionalization of graphene (orange), after biotinylation (yellow) and after NHS blocking with ethanolamine (green) of tripod (left) and PBASE (right) functionalized SGFET.

5.3.3 Streptavidin & biotin detection

Devices performance after saturation with streptavidin is presented Figure 5.7. The main features of this detection experiment lies in the transfer curves of both sensors. The tripod-based sensor shows a large negative shift ($-45\,\mathrm{mV}$), while the device functionalized with PBASE shows a small positive shift ($+13\,\mathrm{mV}$). Since streptavidin is negatively charged, its binding to biotin receptors should p-dope graphene, which is effectively observed for the sensor functionalized with PBASE [193]. The large shift observed with the tripod-based sensor suggests the existence of another mechanism. The desorption of tripod molecules can't be involved since its adsorption induced graphene n-doping as well. Graphene n-doping upon streptavidin adsorption has been observed with CNTs-based FETs and attributed to the existence of a charge transfer [341], but the absence of leakage current increase in our case doesn't support this hypothesis.

Similarly to the n-doping effect observed after tripod adsorption, the immobilization of negatively charged proteins by the tripod at a fixed distance from the surface ($\sim$9 nm), could eventually affect the ionic distribution in the EDL region between graphene and the layer of immobilized proteins (Figure 5.8). Since the electric field exponentially decays from the graphene surface, the excess of cations between the negatively charged streptavidin and the tripod could have a more pronounced effect on the potential drop within the diffuse layer than the protein negative charge itself. Consequently, the graphene n-doping effect could result from this excess of cation close to the graphene surface, while for PBASE the opposite effect could be due to the presence of streptavidin directly at the graphene surface, since this linker lacks the ability to project its functionality away.

This result remains unclear without any additional experiments to unveil this underlying mechanism. Interestingly, the amplitude of the shift induced by the streptavidin for the tripod-based sensor is 3 times larger than for the sensor functionalized with PBASE. Reproducing these experiments with different buffer concentrations (thus varying diffuse layer thickness) could provide more information about such charge confinement effect.

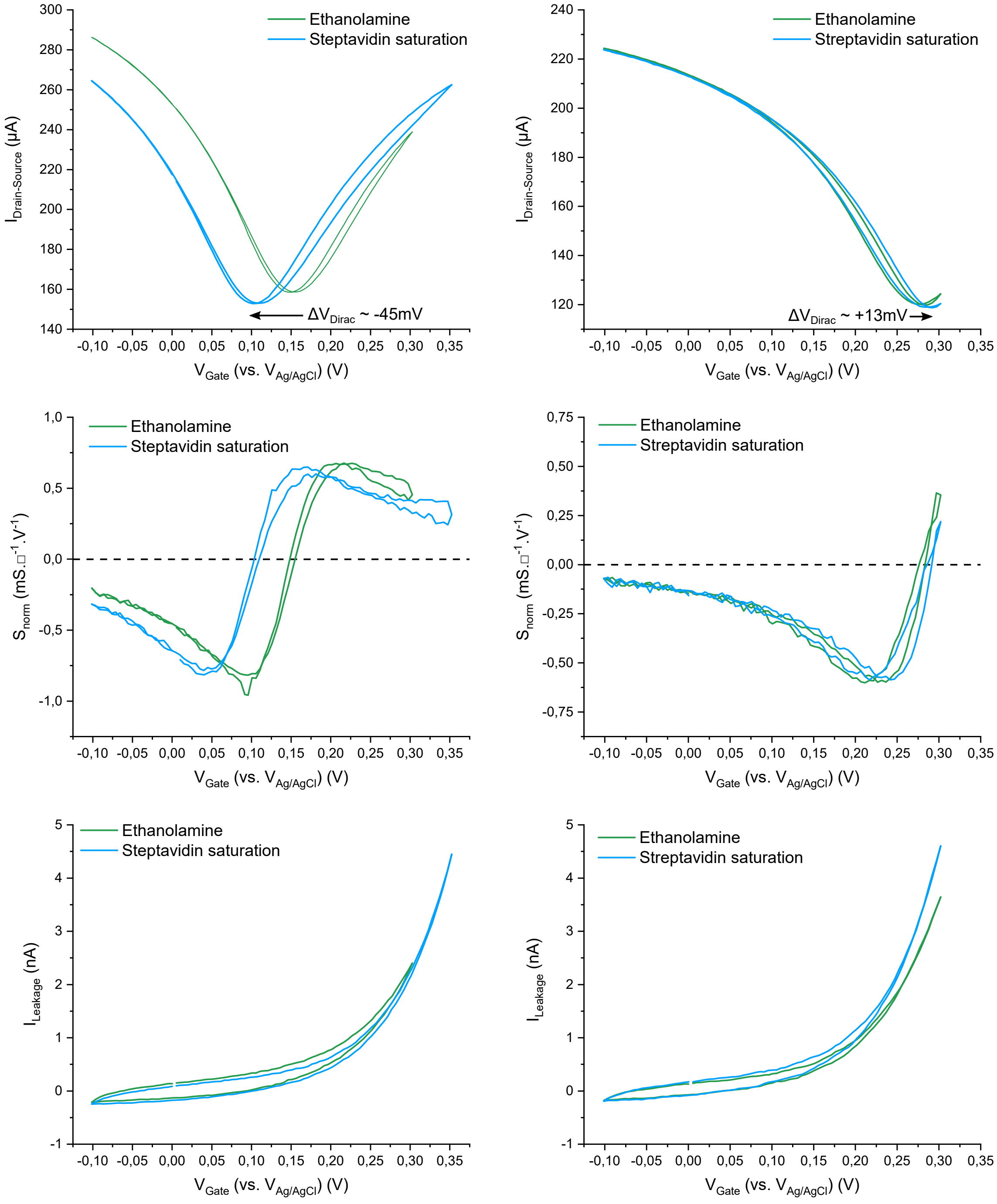

Figure 5.7: Transfer curves, normalized electrical sensitivity and leakage current curves of SGFET before (green) and after (blue) the sensor saturation with streptavidin of tripod (left) and PBASE (right) functionalized SGFET.

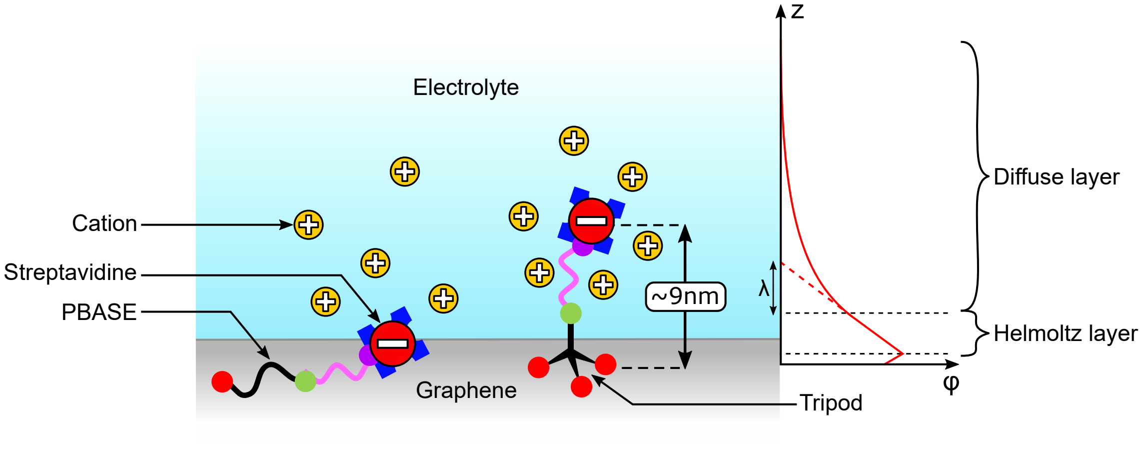

Figure 5.8: Illustration of the charge distribution induced by the binding of streptavidin on PBASE (left) and on tripod (right). The negative charge of streptavidin is maintained close to the graphene surface with PBASE, and projected at approximately 9 nm with the tripod. Cations in the diffuse layer should therefore affect predominantly the exponentially decaying potential within the diffuse layer, resulting in the n-doping effect observed.

Finally, saturating both sensors with biotin induced noticeable V_{Dirac} shift of +13 mV and −12 mV respectively for the tripod and PBASE functionalized sensors. Similarly to the biotin receptor grafting step, the tripod-based sensor shows an increase of the leakage current which is not observed for the other sensor, and can be again attributed to non-specific adsorption. However, both sensors shows a significant V_{Dirac} shift, with opposite graphene doping effects. Upon biotin binding with streptavidin, the protein might undergo conformational changes affecting its net charge or charge distribution. However, the two opposite effects can't be solely explained by the biotin binding, and reveal the presence of two distinct mechanisms involved in both biosensing experiments. Interestingly, such doping effect remains effective after two days in fresh PBS solution, indicating that the immobilization of the different elements composing the sensor biorecognition layer are strongly adsorbed at the graphene surface.

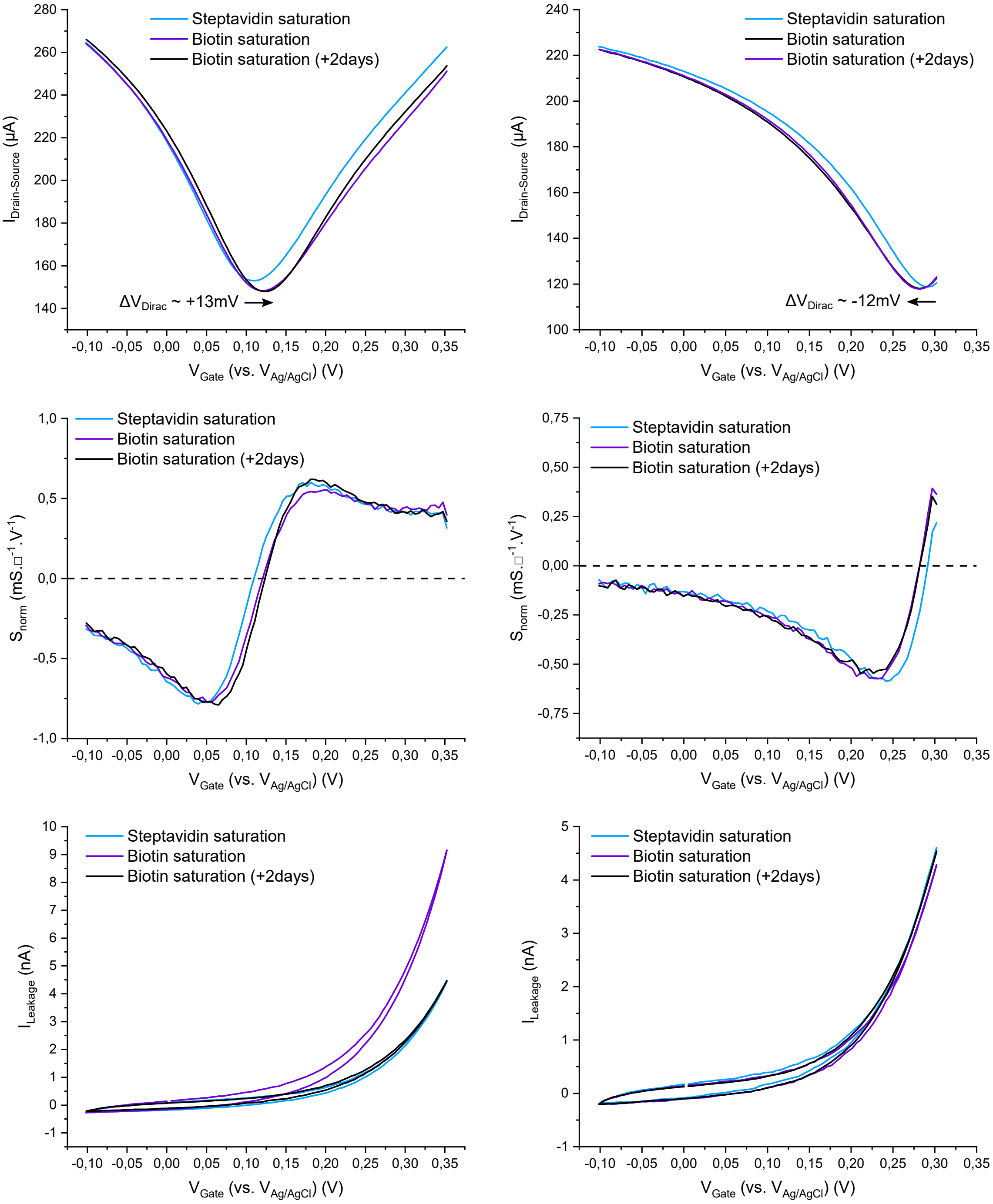

Figure 5.9: Transfer curves, normalized electrical sensitivity and leakage current curves after the sensor saturation with streptavidin (blue), after saturation with biotin (purple) and 2 days after (black) of tripod (left) and PBASE (right) functionalized SGFET.

5.4 Conclusion

The last part of this work was dedicated to evaluating the potential of the devices fabricated during this thesis for biosensing applications. Two streptavidin detection experiments were performed, with both PBASE and tripod non-covalently functionalized SGFET sensors.

The adsorption of the two linker molecules on graphene by π-stacking didn't alter significantly the electrical sensitivity of the devices, demonstrating the efficiency of the non-covalent functionalization strategy for preserving the graphene integrity. Comparing the results obtained with the PBASE linker and the tripod revealed interesting features. In particular, the tripod adsorption reduces the leakage current and induces graphene n-doping, while PBASE induced graphene p-doping. It was demonstrated by Mann *et al.* that PBASE tend to lie flat onto graphene, while the tripod can effectively project its functionality away from the surface. The two contrary doping effect observed with both linkers is a supplementary confirmation that the NHS moiety of PBASE is effectively at the origin of the graphene p-doping effect. The doping mechanism involved in the tripod adsorption was attributed to a modification of the dielectric constant and the ionic distribution within the EDL. However, these important results need to be strengthen with complementary analysis. In a possible next step, probing the impedance of the graphene-electrolyte interface by EIS could reveal such physico-chemical modifications induced by the tripod at the graphene surface.

As it can be seen from Figure 5.10, the streptavidin and biotin detections induced contrary shifts of both devices transfer curve, demonstrating for the first time the impact of the non-covalent functionalization in the biosensor transduction mechanism. However, these two experiments are not sufficient to conclude about the biosensors specificity. In order to demonstrate this essential aspect, negative control experiments should be performed. A first experiment could consist in using a protein incapable of conjugation with the biotin receptors. In a second experiment, the NHS functionality could be blocked with ethanolamine prior to receptors grafting. Finally, functional biotin receptors could be exposed to a streptavidin analyte already saturated with biotin. Under these conditions, the biosensor should show a non-specific response necessary for the demonstration of the biosensor specificity. Eventually, two other experiments could be performed in order to clarify the SGFET charge detection mechanism with both linkers, by detecting avidin and neutravidin analytes. These two molecules shows a similar affinity toward biotin, except that avidin would be positively charged (pI $\approx$ 10) and neutravidin almost neutral (pI $\approx$ 6.3) in the same pH conditions. Finally, such results could be correlated with EIS experiments and simulations, eventually providing insightful information.

Nevertheless, the substantial efforts dedicated to the development of a robust and reproducible fabrication process were necessary for achieving high device electrical performance and robustness. These experiments have paved the way for using these sensors as biosensing platforms, benefiting from the versatile non-covalent functionalization of graphene with the highly promising tripod linker.

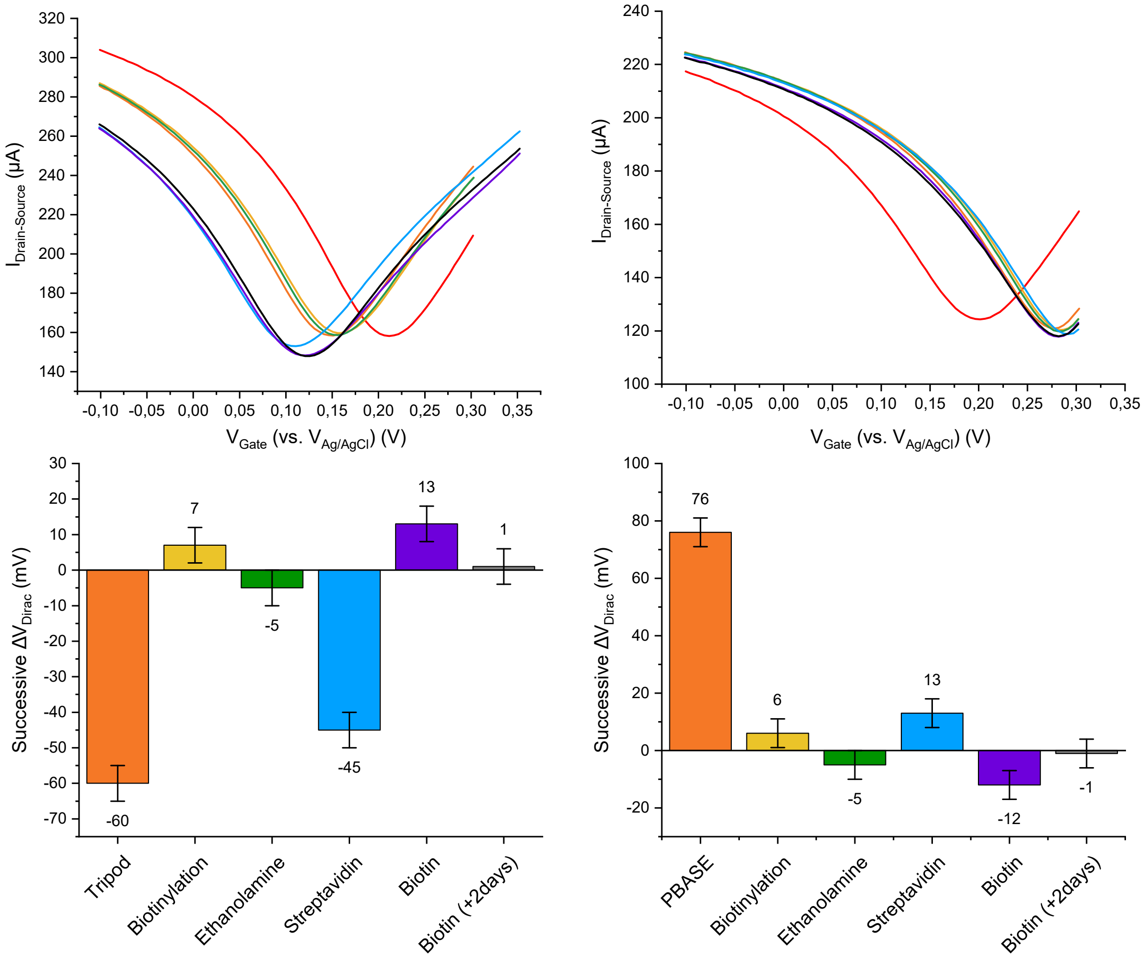

Figure 5.10: Transfer curves (top) and successive V_{Dirac} shifts (bottom) through the whole biosensing experiment of tripod (left) and PBASE (right) functionalized SGFET.

Conclusion & perspectives

This thesis work was focused on the development of tripod functionalized SGFET for biosensing applications. The potential of the tripod multivalent linker for efficiently interfacing graphene with bioreceptors was demonstrated by Dichtel and his co-workers [4, 5]. Pushing these results toward the functionalization of graphene-based SGFET devices for developing an highly sensitive, robust and efficient biosensing technology represented a tremendous challenge. Closing the gap between a simple graphene sample and a first proof of concept required a lot of development. A considerable part of this development consisted in establishing an SGFET fabrication process in our clean-room facilities. The robustness and reproducibility were identified as essential specification for achieving reliable and high device performance. In order to meet such specifications, a versatile chip design was proposed along with different fabrication methods. These alternatives to the classical process involved the use of THF for efficiently strip the PMMA supporting layer, and a Cu sacrificial layer to prevent the non-reproducible contamination of graphene by resist residues. Strong efforts were also dedicated to the passivation process optimization, for preserving the graphene integrity while insuring the lowest parasitic leakage current during the device operation in liquid environment.

First, the graphene cleanliness, doping effects and structural defects were probed through a set of AFM, XPS and Raman characterizations performed for assessing the fabrication process efficiency. It was demonstrated that the THF solvent removes PMMA residues more efficiently than acetone, which is typically used in the community. In our experience, patterning graphene using a resist mask in direct contact with its surface leaves a nanometer-thick homogeneous residue layer. Using a Cu sacrificial layer was found to be more reproducible and robust, while leaving graphene area virtually uncovered by residues. Eventually, these highly promising results could be improved by optimizing the Cu etching time and solution concentration, or using another etchant which could completely remove Cu without affecting the graphene integrity and properties. The passivation step with SU-8 leaves inevitable residues evidenced by the three characterization techniques. However, using a resist as a passivation material remains more advantageous than using a material that needs to be patterned by etching techniques such as oxide materials. In addition, the resist processing needs to be optimized for each application, especially when facing adhesion issues damaging graphene.

These characterizations were then completed with electrical measurements in both air and liquid environment. An experimental setup was fully developed for the electrical characterizations in liquid, including a sample holder, a PCB, as well as a data treatment program based on Python. Thanks to the bipotentiostat, the leakage current has been systematically studied, demonstrating the robustness and efficiency of the passivation design, and the associated fabrication process developed during this thesis. Optimized experimental conditions were also established in order to promote reproducible and stable conditions for the devices operation in liquid. The hysteresis minimization was notably achieved by optimizing the scan rate and gate potential window parameters.

As desired, the devices fabricated using this optimized process exhibited electrical sensitivity values among the best reported in the literature. These high performance were ascribed to the surface treatment performed to enhance the hydrophilicity of the substrate before the transfer of graphene. This surface treatment, which promote a clean graphene-metal interface and consequently a low contact resistivity, might also be the cause of the strong p-doping observed in back-gating measurements. Graphene grain boundaries were identified as one of the main limitation for achieving high charge carrier mobility. The role of Cu residues in this phenomenon can't be discarded and could be evidenced by optimizing the etching of the Cu sacrificial layer in combination with AFM, XPS and Raman characterizations. These promising electrical performance could also be improved using a graphene source with larger grain size.

The devices robustness resulting from the fabrication process optimization was also demonstrated by performing hundreds of gate potential scans over several days. A drift effect was evidenced and attributed to the intercalation of water between graphene and the substrate. AFM and Raman in-situ characterizations are proposed in order to clarify this effect. Strikingly, the devices didn't show a significant loss of performance during such critical tests, demonstrating the efficiency of the process developed during this thesis.

In a last part, the potential of these devices for biosensing applications was assessed by performing two experiments with both PBASE and tripod non-covalently functionalized SGFET sensors. The functionalization of graphene with aromatic linker molecules is a promising technique. In particular, PBASE is widely used in the literature, since it is commercially available. Comparing the electrical performance of both devices therefore provides an interesting insight of the effect of such linkers on graphene properties. These first measurements particularly showed two opposite doping effects, attributed to the (in)ability of these linkers to effectively project a functionality away from the surface. While the NHS moiety of PBASE induces graphene p-doping, the tripod functionality is maintained above the surface resulting in graphene n-doping. Such effect is still unclear and was attributed to modifications of both the dielectric constant at the graphene-electrolyte interface and the ionic distribution within the EDL. Performing EIS characterizations was proposed, as this technique seems particularly suited for explaining such doping mechanism by probing interfacial impedance modifications induced by variations of local physico-chemical properties. Further attempts to detect streptavidin by saturating both sensors showed the impact and the importance of the non-covalent functionalization on the device transduction mechanism. Again, contrary shifts of the transfer curve were observed, supporting the fact that the two sensors biorecognition layer differs in their structure. Negative control experiments were also proposed in order to demonstrate the sensors specificity which is crucial for a reliable analysis of the biosensors performance. Another interesting experiment for understanding the charge detection mechanism could consist in the detection of avidin and neutravidin, which are structurally similar to streptavidin while presenting a different net charge. Performing EIS characterizations at each step of these biosensing experiments in correlation with simulations would also provide a complete view of the biosensor operation, and help achieving high performance.

An additional crucial point would be the development of a microfluidic delivery system in order to precisely control the species mass transport toward the sensor surface, which would also enable the study of binding kinetics. Such implementation could also provide the possibility to perform multiplexing measurements, by controlling the functionalization of similar devices on the same chip. In addition to such microfluidic delivery system, QCM characterizations could provide complementary information based on mass sensing. Considering the timeline of this work, this next step in the biosensor development and integration was not considered during this thesis.

This groundwork paved the way to further promising development including the use of aptamer receptors. As already mentioned in the introduction, these short-stranded nucleotides can bind their target with high specificity and affinity, and present several advantages. Aptamers can be reversibly denatured, enabling the biorecognition layer regeneration for reusing the biosensor. They are also considerably smaller than antibodies ($\sim$2 nm), and have the ability to bring the target closer to the surface by conformational changes induced by the binding event, which is appealing for working in more concentrated solutions.

Nevertheless, the main contribution of this work consists in the development of a robust and reliable basis for fabricating highly sensitive graphene-based devices which can be operated and characterized in liquid. Benefiting from the versatile non-covalent functionalization of graphene with the highly promising tripod linker, these sensors could be used for various innovative biosensing applications.

Appendices

Devices design

A set of devices with versatile geometries has been designed with various W/L ratio for a fixed area and various area for a fixed W/L ratio (Figure 11).

Two sets of TLM devices are also included, consisting of transistors with a constant channel width of 50 µm, and length varying from 10 µm to 250 µm.

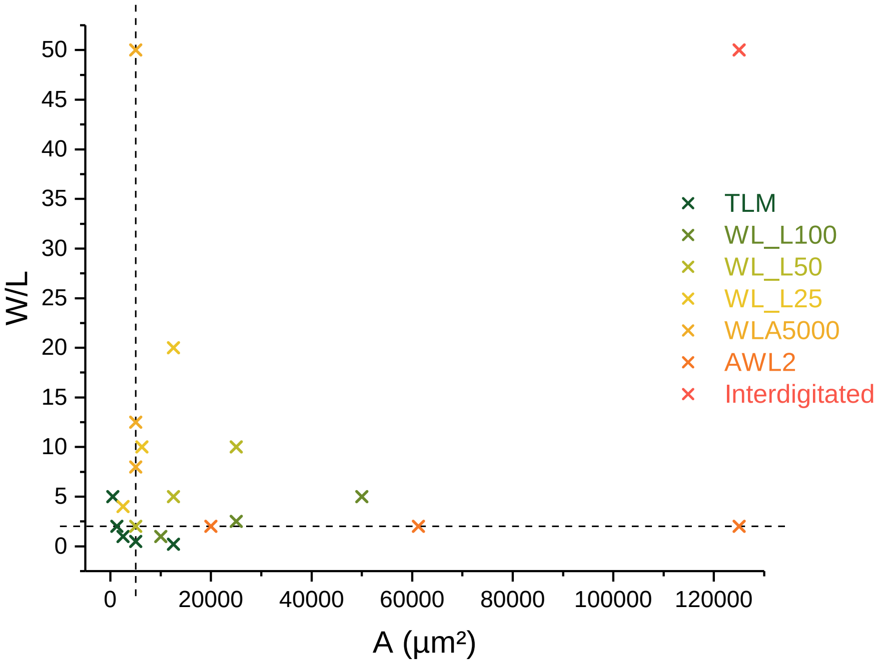

Figure 11: Representation of the different device designs realized, the dashed lines showing the devices with either equal W/L or area.

SU-8 passivation protocol

The optimized protocol for processing the SU-8 is the following:

- Spin-coating:
  - 1^{st} step: 500 rpm for 10 s
  - 2^{nd} step: 3000 rpm for 50 s
  - Acceleration: 500 rpm/s
- Soft-bake:
  - 1^{st} step: 65 °C for 60 s
  - 2^{nd} step: 95 °C for 120 s
  - 3^{rd} step: 65 °C for 60 s
- Exposure: UV (365 nm) for 25 s
- Post-bake:
  - 1^{st} step: 65 °C for 60 s
  - 2^{nd} step: 95 °C for 180 s
  - 3^{rd} step: 65 °C for 60 s
- Development:
  - 1^{st} step: 60 s in SU-8 developer with medium agitation
  - 2^{nd} step: 120 s in IPA
  - 3^{rd} step: 60 s in DIW
- Hard-bake:
  - 150 °C for 5 min

AFM methods

AFM experiments were carried out using a Bruker Dimension FastScan in amplitude modulation (Tapping mode). 512×512 pixels (step-height) and 2048×2048 pixels (2D maps) images were recorded at a scan rate of 1-2 Hz, using a FASTSCAN-A tip with a radius of 5 nm and a nominal spring constant of 18 N.m^{-1}. Feedback gains on Z feedback were adjusted to keep the amplitude error below 10% of the working amplitude.

Figure 12: AFM Dimension FastScan scanner (Brucker).

XPS methods

XPS experiments were carried out with a PHI 5000 Versa Probe II XPS spectrometer at a 10^{-9} mbar base pressure, using a monochromatic X-Ray source (1486.6 eV). The beam incident angle was fixed to 45° with respect to the sample surface, yielding to a probed depth of $\sim$5 nm [342]. The spot size was 50 µm, the overall energy resolution (high resolution spectra) was 550 meV, and the sample surface was neutralized using a double charge compensation by electron and low energy (<10 eV) ion beam.

The spectra were calibrated using the Au4f$_{7/2}$ and Si2p$_{3/2}$ peaks as references and fitted using standard procedures: the background was removed using the Shirley function, the sp^2 graphene-related component fitted with the asymmetric Doniach-Sunjic function and the other peaks with the Voigt function [272][273].

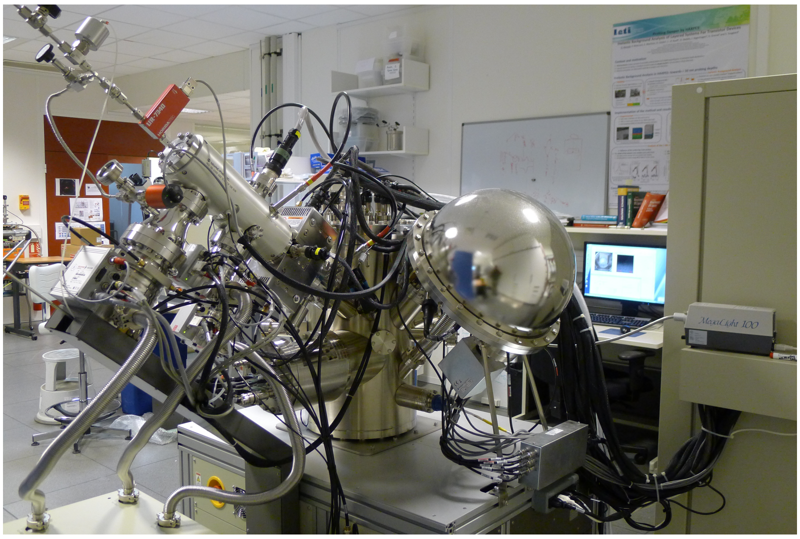

Figure 13: PHI 5000 Versa Probe II XPS spectrometer.

Raman microscopy methods

Raman measurements were performed with a confocal inVia Raman spectrometer (Renishaw) equipped with a 532 nm laser and a x50 objective (N.A 0.75) giving a laser spot size of about 0.9 µm. To avoid any heating effects or damaging the sample, the laser power was kept at 0.5 mW. The spectral resolution was 0.9 cm^{-1} and the 2D maps were recorded using a micro-controlled stage with a 1 µm step.

Figure 14: Raman inVia (Renishaw) spectrometer.

PBS buffer protocol

A buffer consists of a neutral salt, and an acid/base couple compensating pH variations in solution [343]:

$$\text{acid} \rightleftharpoons \text{base} + \text{H}^+ \tag{1}$$

At the equilibrium, the acid dissociation constant K_a is defined by:

$$K_a = \frac{[base]\,[H^+]}{[acid]} \tag{2}$$

The pH of the solution follows the Henderson-Hasselbalch equation:

$$pH \;=\; pK_a + \log_{10}\left(\frac{[base]}{[acid]}\right) \tag{3}$$

where $pH = -\log_{10}\left(\text{H}^+\right)$ and $pK_a = -\log_{10}\left(K_a\right)$. In particular, the pK_a is temperature and ionic strength dependant:

$$pK_{a,T} = \; pK_a + \frac{dpK_a}{dT}\left(T - 298.15K\right) \tag{4}$$

$$pK_{a,I} = pK_a + (2z_a - 1)\left[\frac{A_T\sqrt{I}}{\left(1+\sqrt{I}\right)} - 0.1 \cdot I\right] \tag{5}$$

where T is the temperature, A_T a temperature dependant constant, z_a the charge of the conjugate acid species, and I the total ionic strength comprising both contributions of the neutral salt and the buffer species:

$$I = I_{salt} + I_{buffer} \tag{6}$$

The protocol for preparing a buffer with both pH and I controlled consists in the following:

1. Specify pH, T and I
2. Set $[buffer] = [acid] + [base]$ at least 10-folds smaller than I so the ionic strength is maintained constant by the neutral salt and won't vary due to pH variations
3. Adjust pK_a for T and I using Equation 4 and Equation 5
4. Calculate $[acid]$ and $[base]$ using Equation 3 and $[buffer]$
5. Calculate I_{buffer}, and deduce $[salt]$ from I_{salt}

PBS buffer solutions were prepared using sodium dihydrogen phosphate (NaH_2PO_4) (>98%) and disodium hydrogen phosphate (Na_2HPO_4) (>99%) from VWR, and NaCl (>99.5%) from Sigma Aldrich.

Parameters [343]:

- $pKa\left(\mathrm{H_2PO_4^-/HPO_4^{2-}}\right) = 7.2$
- $\frac{dpK_a}{dT} = -0.0028\ K^{-1}$
- $A_T = 0,507$ at 20 °C

Bibliography

[1] Frost & Sullivan, “Key Opportunities and Trends in Biosensors,” Sep. 2019. (Page 1.)

[2] G. Roglic and World Health Organization, Eds., *Global Report on Diabetes*. Geneva, Switzerland: World Health Organization, 2016. (Page 1.)

[3] S. Mendis and World Health Organization, “Global status report on noncommunicable diseases 2014,” World Health Organization, Tech. Rep., 2014. (Page 1.)

[4] T. Alava, J. A. Mann, C. Théodore, J. J. Benitez, W. R. Dichtel, J. M. Parpia, and H. G. Craighead, “Control of the Graphene–Protein Interface Is Required To Preserve Adsorbed Protein Function,” *Analytical Chemistry*, vol. 85, no. 5, pp. 2754–2759, Mar. 2013. (Pages 1, 46, 51, 145, and 159.)

[5] J. A. Mann, J. Rodríguez-López, H. D. Abruña, and W. R. Dichtel, “Multivalent Binding Motifs for the Noncovalent Functionalization of Graphene,” *Journal of the American Chemical Society*, vol. 133, no. 44, pp. 17 614–17 617, Nov. 2011. (Pages 2, 49, 148, and 159.)

[6] L. C. Clark and C. Lyons, “Electrode Systems for Continuous Monitoring in Cardiovascular Surgery,” *Annals of the New York Academy of Sciences*, vol. 102, no. 1, pp. 29–45, 1962. (Page 5.)

[7] L. C. Clark, R. Wolf, D. Granger, and Z. Taylor, “Continuous Recording of Blood Oxygen Tensions by Polarography,” *Journal of Applied Physiology*, vol. 6, no. 3, pp. 189–193, Sep. 1953. (Page 5.)

[8] M. S. Thakur and K. V. Ragavan, “Biosensors in food processing,” *Journal of Food Science and Technology*, vol. 50, no. 4, pp. 625–641, Aug. 2013. (Page 5.)

[9] V. Scognamiglio, G. Pezzotti, I. Pezzotti, J. Cano, K. Buonasera, D. Giannini, and M. T. Giardi, “Biosensors for effective environmental and agrifood protection and commercialization: From research to market,” *Microchimica Acta*, vol. 170, no. 3, pp. 215–225, Sep. 2010. (Page 5.)

[10] Y. Fang, Ed., *Label-Free Biosensor Methods in Drug Discovery*, ser. Methods in Pharmacology and Toxicology. New York: Humana Press, 2015. (Page 5.)

[11] G. P. Tegos, "Biodefense," *Virulence*, vol. 4, no. 8, pp. 740–744, Nov. 2013. (Page 5.)

[12] D. R. Thévenot, K. Toth, R. A. Durst, and G. S. Wilson, "Electrochemical biosensors: Recommended definitions and classification," *Biosensors and Bioelectronics*, vol. 16, no. 1, pp. 121–131, Jan. 2001. (Page 6.)

[13] H. F. Lodish and P. L. Masson, *Biologie moléculaire de la cellule*. Bruxelles: De Boeck, 2014. (Pages 7 and 8.)

[14] P. L. Kastritis and A. M. J. J. Bonvin, "On the binding affinity of macromolecular interactions: Daring to ask why proteins interact," *Journal of the Royal Society Interface*, vol. 10, no. 79, Feb. 2013. (Page 8.)

[15] G. Schreiber and A. E. Keating, "Protein Binding Specificity versus Promiscuity," *Current opinion in structural biology*, vol. 21, no. 1, pp. 50–61, Feb. 2011. (Page 9.)

[16] J. L. Arlett, E. B. Myers, and M. L. Roukes, "Comparative advantages of mechanical biosensors," *Nature Nanotechnology*, vol. 6, no. 4, pp. 203–215, Apr. 2011. (Pages 9 and 15.)

[17] E. A. Moschou, B. V. Sharma, S. K. Deo, and S. Daunert, "Fluorescence Glucose Detection: Advances Toward the Ideal In Vivo Biosensor," *Journal of Fluorescence*, vol. 14, no. 5, pp. 535–547, Sep. 2004. (Page 9.)

[18] A. J. M. Barbosa, A. R. Oliveira, and A. C. A. Roque, "Protein- and Peptide-Based Biosensors in Artificial Olfaction," *Trends in Biotechnology*, vol. 36, no. 12, pp. 1244–1258, Dec. 2018. (Page 9.)

[19] A. M. Gonçalves, A. Q. Pedro, F. M. Santos, L. M. Martins, C. Maia, J. A. Queiroz, and L. A. Passarinha, "Trends in Protein-Based Biosensor Assemblies for Drug Screening and Pharmaceutical Kinetic Studies," in *Molecules*, 2014. (Page 9.)

[20] S. Damiati, M. Peacock, R. Mhanna, S. Søpstad, U. B. Sleytr, and B. Schuster, "Bioinspired detection sensor based on functional nanostructures of S-proteins to target the folate receptors in breast cancer cells," *Sensors and Actuators B: Chemical*, vol. 267, pp. 224–230, Aug. 2018. (Page 9.)

[21] E. Engvall and P. Perlmann, “Enzyme-Linked Immunosorbent Assay, Elisa: III. Quantitation of Specific Antibodies by Enzyme-Labeled Anti-Immunoglobulin in Antigen-Coated Tubes,” *The Journal of Immunology*, vol. 109, no. 1, pp. 129–135, Jul. 1972. (Page 9.)

[22] C. Moina and G. Ybarr, “Fundamentals and Applications of Immunosensors,” in *Advances in Immunoassay Technology*, N. Chiu, Ed. InTech, Mar. 2012. (Page 9.)

[23] B. Byrne, E. Stack, N. Gilmartin, and R. O’Kennedy, “Antibody-Based Sensors: Principles, Problems and Potential for Detection of Pathogens and Associated Toxins,” *Sensors*, vol. 9, no. 6, pp. 4407–4445, Jun. 2009. (Page 9.)

[24] M. S. Azam, M. R. T. Rahman, Z. Lou, Y. Tang, S. M. Raqib, and J. S. Jothi, “Review : Advancements and application of immunosensors in the analysis of food contaminants,” *Nusantara Bioscience*, 2016. (Page 9.)

[25] Rockland antibodies & assays, “Anti-Idiotypic Antibody Production Service,” https://rockland-inc.com/anti-idiotypic-antibody-production.aspx, Sep. 19. (Page 10.)

[26] K. Tawa and W. Knoll, “Mismatching base-pair dependence of the kinetics of DNA–DNA hybridization studied by surface plasmon fluorescence spectroscopy,” *Nucleic Acids Research*, vol. 32, no. 8, pp. 2372–2377, 2004. (Page 10.)

[27] J. A. Garrido-Cardenas, F. Garcia-Maroto, J. A. Alvarez-Bermejo, and F. Manzano-Agugliaro, “DNA Sequencing Sensors: An Overview,” *Sensors (Basel, Switzerland)*, vol. 17, no. 3, Mar. 2017. (Page 10.)

[28] P. Yáñez-Sedeño, L. Agüí, R. Villalonga, and J. M. Pingarrón, “Biosensors in forensic analysis. A review,” *Analytica Chimica Acta*, vol. 823, pp. 1–19, May 2014. (Page 10.)

[29] L. M. Moretto and K. Kalcher, Eds., *Environmental Analysis by Electrochemical Sensors and Biosensors: Fundamentals*, ser. Nanostructure Science and Technology. New York, NY: Springer New York, 2014. (Page 10.)

[30] M. Tichoniuk, M. Ligaj, and M. Filipiak, “Application of DNA Hybridization Biosensor as a Screening Method for the Detection of Genetically Modified Food Components,” *Sensors (Basel, Switzerland)*, vol. 8, no. 4, pp. 2118–2135, Mar. 2008. (Page 10.)

[31] V. C. Diculescu, A.-M. Chiorcea-Paquim, and A. M. Oliveira-Brett, “Applications of a DNA-electrochemical biosensor,” *TrAC Trends in Analytical Chemistry*, vol. 79, pp. 23–36, May 2016. (Page 10.)

[32] A. D. Ellington and J. W. Szostak, “In vitro selection of RNA molecules that bind specific ligands,” *Nature*, vol. 346, no. 6287, pp. 818–822, Aug. 1990. (Page 11.)

[33] C. Tuerk and L. Gold, “Systematic evolution of ligands by exponential enrichment: RNA ligands to bacteriophage T4 DNA polymerase,” *Science*, vol. 249, no. 4968, pp. 505–510, Aug. 1990. (Page 11.)

[34] I. Bazin, S. A. Tria, A. Hayat, and J.-L. Marty, “New biorecognition molecules in biosensors for the detection of toxins,” *Biosensors and Bioelectronics*, vol. 87, pp. 285–298, Jan. 2017. (Page 12.)

[35] A. D. Keefe, S. Pai, and A. Ellington, “Aptamers as therapeutics,” *Nature Reviews Drug Discovery*, vol. 9, no. 7, pp. 537–550, Jul. 2010. (Page 12.)

[36] S. Reverdatto, D. Burz, and A. Shekhtman, “Peptide Aptamers: Development and Applications,” *Current Topics in Medicinal Chemistry*, vol. 15, no. 12, pp. 1082–1101, Apr. 2015. (Page 12.)

[37] F. Pfeiffer and G. Mayer, “Selection and Biosensor Application of Aptamers for Small Molecules,” *Frontiers in Chemistry*, vol. 4, Jun. 2016. (Page 12.)

[38] R. L. Pereira, I. C. Nascimento, A. P. Santos, I. E. Y. Ogusuku, C. Lameu, G. Mayer, and H. Ulrich, “Aptamers: Novelty tools for cancer biology,” *Oncotarget*, vol. 9, no. 42, pp. 26 934–26 953, Apr. 2018. (Page 12.)

[39] H. Wang, E. Nakata, and I. Hamachi, “Recent Progress in Strategies for the Creation of Protein-Based Fluorescent Biosensors,” *ChemBioChem*, vol. 10, no. 16, pp. 2560–2577, 2009. (Page 13.)

[40] I. L. Medintz, H. T. Uyeda, E. R. Goldman, and H. Mattoussi, “Quantum dot bioconjugates for imaging, labelling and sensing,” *Nature Materials*, vol. 4, no. 6, pp. 435–446, Jun. 2005. (Page 13.)

[41] U. Resch-Genger, M. Grabolle, S. Cavaliere-Jaricot, R. Nitschke, and T. Nann, “Quantum dots versus organic dyes as fluorescent labels,” *Nature Methods*, vol. 5, no. 9, pp. 763–775, Sep. 2008. (Page 13.)

[42] D. S. Skelley, L. P. Brown, and P. K. Besch, “Radioimmunoassay,” *Clinical Chemistry*, vol. 19, no. 2, pp. 146–186, Feb. 1973. (Page 13.)

[43] G. V. Presnova, M. Y. Rybcova, and A. M. Egorov, "Electrochemical biosensors based on horseradish peroxidase," *Russian Journal of General Chemistry*, vol. 78, no. 12, pp. 2482–2488, Dec. 2008. (Page 13.)

[44] M. Čadková, V. Dvořáková, R. Metelka, Z. Bílková, and L. Korecká, "Alkaline phosphatase labeled antibody-based electrochemical biosensor for sensitive HE4 tumor marker detection," *Electrochemistry Communications*, vol. 59, pp. 1–4, Oct. 2015. (Page 13.)

[45] S. A. Lim, H. Yoshikawa, E. Tamiya, H. M. Yasin, and M. U. Ahmed, "A highly sensitive gold nanoparticle bioprobe based electrochemical immunosensor using screen printed graphene biochip," *RSC Advances*, vol. 4, no. 102, pp. 58 460–58 466, Nov. 2014. (Page 13.)

[46] X. Ren, X. Meng, D. Chen, F. Tang, and J. Jiao, "Using silver nanoparticle to enhance current response of biosensor," *Biosensors and Bioelectronics*, vol. 21, no. 3, pp. 433–437, Sep. 2005. (Page 13.)

[47] C. M. Martinez and L. H. Alvarez, "Application of redox mediators in bioelectrochemical systems," *Biotechnology Advances*, vol. 36, no. 5, pp. 1412–1423, Sep. 2018. (Page 13.)

[48] P. Fechner, O. Bleher, M. Ewald, K. Freudenberger, D. Furin, U. Hilbig, F. Kolarov, K. Krieg, L. Leidner, G. Markovic, G. Proll, F. Pröll, S. Rau, J. Riedt, B. Schwarz, P. Weber, and J. Widmaier, "Size does matter! Label-free detection of small molecule–protein interaction," *Analytical and Bioanalytical Chemistry*, vol. 406, no. 17, pp. 4033–4051, Jul. 2014. (Page 13.)

[49] I. Palchetti and M. Mascini, "Biosensor Technology: A Brief History," in *Sensors and Microsystems*, ser. Lecture Notes in Electrical Engineering, P. Malcovati, A. Baschirotto, A. d'Amico, and C. Natale, Eds. Springer Netherlands, 2010, pp. 15–23. (Page 14.)

[50] J. Homola, "Present and future of surface plasmon resonance biosensors," *Analytical and Bioanalytical Chemistry*, vol. 377, no. 3, pp. 528–539, Oct. 2003. (Page 14.)

[51] P. Schuck, "Reliable determination of binding affinity and kinetics using surface plasmon resonance biosensors," *Current Opinion in Biotechnology*, vol. 8, no. 4, pp. 498–502, Aug. 1997. (Page 14.)

[52] P. Nilsson, B. Persson, M. Uhlén, and P. A. Nygren, "Real-time monitoring of DNA manipulations using biosensor technology," *Analytical Biochemistry*, vol. 224, no. 1, pp. 400–408, Jan. 1995. (Page 14.)

[53] S. H. Han, S. K. Kim, K. Park, S. Y. Yi, H.-J. Park, H.-K. Lyu, M. Kim, and B. H. Chung, "Detection of mutant p53 using field-effect transistor biosensor," *Analytica Chimica Acta*, vol. 665, no. 1, pp. 79–83, Apr. 2010. (Page 14.)

[54] P. Damborský, J. Švitel, and J. Katrlík, "Optical biosensors," *Essays In Biochemistry*, vol. 60, no. 1, pp. 91–100, Jun. 2016. (Page 14.)

[55] A. Afzal, A. Mujahid, R. Schirhagl, S. Bajwa, U. Latif, and S. Feroz, "Gravimetric Viral Diagnostics: QCM Based Biosensors for Early Detection of Viruses," *Chemosensors*, vol. 5, no. 1, p. 7, Feb. 2017. (Page 14.)

[56] G. Sauerbrey, "Verwendung von Schwingquarzen zur Wägung dünner Schichten und zur Mikrowägung," *Zeitschrift für Physik*, vol. 155, no. 2, pp. 206–222, Apr. 1959. (Page 14.)

[57] n. Janshoff, n. Galla, and n. Steinem, "Piezoelectric Mass-Sensing Devices as Biosensors-An Alternative to Optical Biosensors?" *Angewandte Chemie (International Ed. in English)*, vol. 39, no. 22, pp. 4004–4032, Nov. 2000. (Page 15.)

[58] X. Zhou, L. Liu, M. Hu, L. Wang, and J. Hu, "Detection of hepatitis B virus by piezoelectric biosensor," *Journal of Pharmaceutical and Biomedical Analysis*, vol. 27, no. 1-2, pp. 341–345, Jan. 2002. (Page 15.)

[59] N. C. Pesquero, F. C. Carvalho, R. C. Faria, M.-C. Roque-Barreira, and P. R. Bueno, "ArtinM Binding Effinities and Kinetic Interaction with Leukemia Cells: A Quartz Crystal Microbalance Bioelectroanalysis on the Cytotoxic Effect," *Electroanalysis*, vol. 29, no. 6, pp. 1554–1558, 2017. (Page 15.)

[60] J. A. Capobianco, W. Y. Shih, G. P. Adams, and W.-H. Shih, "Label-free Growth Receptor-2 Detection and Dissociation Constant Assessment in Diluted Human Serum Using a Longitudinal Extension Mode of a Piezoelectric Microcantilever Sensor," *Sensors and actuators. B, Chemical*, vol. 160, no. 1, pp. 349–356, Dec. 2011. (Page 15.)

[61] D. Pizzoni, M. Mascini, V. Lanzone, M. Del Carlo, C. Di Natale, and D. Compagnone, "Selection of peptide ligands for piezoelectric peptide based gas sensors arrays using a virtual screening approach," *Biosensors and Bioelectronics*, vol. 52, pp. 247–254, Feb. 2014. (Page 15.)

[62] R. Raiteri, M. Grattarola, H.-J. Butt, and P. Skládal, "Micromechanical cantilever-based biosensors," *Sensors and Actuators B: Chemical*, vol. 79, no. 2, pp. 115–126, Oct. 2001. (Page 15.)

[63] U. Sampath, S. M. Heinrich, F. Josse, F. Lochon, I. Dufour, and D. Rebiere, “Study of viscoelastic effect on the frequency shift of microcantilever chemical sensors,” *IEEE Transactions on Ultrasonics, Ferroelectrics, and Frequency Control*, vol. 53, no. 11, pp. 2166–2173, Nov. 2006. (Page 15.)

[64] I. Dufour, F. Lochon, S. M. Heinrich, F. Josse, and D. Rebiere, “Effect of Coating Viscoelasticity on Quality Factor and Limit of Detection of Microcantilever Chemical Sensors,” *IEEE Sensors Journal*, vol. 7, no. 2, pp. 230–236, Feb. 2007. (Page 15.)

[65] M. Iqbal, M. A. Gleeson, B. Spaugh, F. Tybor, W. G. Gunn, M. Hochberg, T. Baehr-Jones, R. C. Bailey, and L. C. Gunn, “Label-Free Biosensor Arrays Based on Silicon Ring Resonators and High-Speed Optical Scanning Instrumentation,” *IEEE Journal of Selected Topics in Quantum Electronics*, vol. 16, no. 3, pp. 654–661, May 2010. (Page 15.)

[66] D. Sun, T. Guo, Y. Ran, Y. Huang, and B.-O. Guan, “In-situ DNA hybridization detection with a reflective microfiber grating biosensor,” *Biosensors and Bioelectronics*, vol. 61, pp. 541–546, Nov. 2014. (Page 15.)

[67] J.-N. Yih, Y.-M. Chu, Y.-C. Mao, W.-H. Wang, F.-C. Chien, C.-Y. Lin, K.-L. Lee, P.-K. Wei, and S.-J. Chen, “Optical waveguide biosensors constructed with subwavelength gratings,” *Applied Optics*, vol. 45, no. 9, pp. 1938–1942, Mar. 2006. (Page 15.)

[68] H. Shafiee, E. A. Lidstone, M. Jahangir, F. Inci, E. Hanhauser, T. J. Henrich, D. R. Kuritzkes, B. T. Cunningham, and U. Demirci, “Nanostructured Optical Photonic Crystal Biosensor for HIV Viral Load Measurement,” *Scientific Reports*, vol. 4, p. 4116, Feb. 2014. (Page 15.)

[69] P. Steglich, M. Hülsemann, B. Dietzel, and A. Mai, “Optical Biosensors Based on Silicon-On-Insulator Ring Resonators: A Review,” *Molecules*, vol. 24, no. 3, Jan. 2019. (Page 15.)

[70] H. Inan, M. Poyraz, F. Inci, M. A. Lifson, M. Baday, B. T. Cunningham, and U. Demirci, “Photonic crystals: Emerging biosensors and their promise for point-of-care applications,” *Chemical Society reviews*, vol. 46, no. 2, pp. 366–388, Jan. 2017. (Page 15.)

[71] D. Fariña, M. Álvarez, S. Márquez, C. Dominguez, and L. M. Lechuga, “Sensitivity analysis for improving nanomechanical photonic transducers biosensors,” *Journal of Physics D: Applied Physics*, vol. 48, no. 33, p. 335401, Aug. 2015. (Page 16.)

[72] M. K. Park, J. S. Kee, J. Y. Quah, V. Netto, J. Song, Q. Fang, E. M. La Fosse, and G.-Q. Lo, “Label-free aptamer sensor based on silicon microring resonators,” *Sensors and Actuators B: Chemical*, vol. 176, pp. 552–559, Jan. 2013. (Page 16.)

[73] M. Pohanka and P. Skládal, “Electrochemical biosensors - principles and applications,” *Journal of Applied Biomedicine*, vol. 6, no. 2, pp. 57–64, Jul. 2008. (Page 16.)

[74] A. Sassolas, L. J. Blum, and B. D. Leca-Bouvier, “Electrochemical Aptasensors,” *Electroanalysis*, vol. 21, no. 11, pp. 1237–1250, Jun. 2009. (Page 16.)

[75] M. Vestergaard, K. Kerman, and E. Tamiya, “An Overview of Label-free Electrochemical Protein Sensors,” *Sensors*, vol. 7, no. 12, pp. 3442–3458, Dec. 2007. (Page 16.)

[76] E. Farjami, R. Campos, J. S. Nielsen, K. V. Gothelf, J. Kjems, and E. E. Ferapontova, “RNA Aptamer-Based Electrochemical Biosensor for Selective and Label-Free Analysis of Dopamine,” *Analytical Chemistry*, vol. 85, no. 1, pp. 121–128, Jan. 2013. (Page 17.)

[77] A. K. H. Cheng, B. Ge, and H.-Z. Yu, “Aptamer-Based Biosensors for Label-Free Voltammetric Detection of Lysozyme,” *Analytical Chemistry*, vol. 79, no. 14, pp. 5158–5164, Jul. 2007. (Page 17.)

[78] X. Luo and J. J. Davis, “Electrical biosensors and the label free detection of protein disease biomarkers,” *Chemical Society Reviews*, vol. 42, no. 13, pp. 5944–5962, Jun. 2013. (Page 17.)

[79] E. B. Bahadır and M. K. Sezgintürk, “A review on impedimetric biosensors,” *Artificial Cells, Nanomedicine, and Biotechnology*, vol. 44, no. 1, pp. 248–262, Jan. 2016. (Page 17.)

[80] P. Bergveld, “Development of an Ion-Sensitive Solid-State Device for Neurophysiological Measurements,” *IEEE Transactions on Biomedical Engineering*, vol. BME-17, no. 1, pp. 70–71, Jan. 1970. (Page 17.)

[81] M. J. Schöning and A. Poghossian, “Recent advances in biologically sensitive field-effect transistors (BioFETs),” *Analyst*, vol. 127, no. 9, pp. 1137–1151, Sep. 2002. (Page 18.)

[82] K. Shoorideh and C. O. Chui, “On the origin of enhanced sensitivity in nanoscale FET-based biosensors,” *Proceedings of the National Academy of Sciences of the United States of America*, vol. 111, no. 14, pp. 5111–5116, Apr. 2014. (Pages 18 and 22.)

[83] X.-L. Luo, J.-J. Xu, W. Zhao, and H.-Y. Chen, "A novel glucose ENFET based on the special reactivity of MnO2 nanoparticles," *Biosensors and Bioelectronics*, vol. 19, no. 10, pp. 1295–1300, May 2004. (Page 18.)

[84] Y. Miyahara, T. Moriizumi, and K. Ichimura, "Integrated enzyme fets for simultaneous detections of urea and glucose," *Sensors and Actuators*, vol. 7, no. 1, pp. 1–10, Mar. 1985. (Page 18.)

[85] S. Caras and J. Janata, "Field effect transistor sensitive to penicillin," *Analytical Chemistry*, vol. 52, no. 12, pp. 1935–1937, Oct. 1980. (Page 18.)

[86] P. Casal, X. Wen, S. Gupta, T. Nicholson, Y. Wang, A. Theiss, B. Bhushan, L. Brillson, W. Lu, and S. C. Lee, "ImmunoFET feasibility in physiological salt environments," *Philosophical Transactions. Series A, Mathematical, Physical, and Engineering Sciences*, vol. 370, no. 1967, pp. 2474–2488, May 2012. (Page 18.)

[87] E. Souteyrand, J. P. Cloarec, J. R. Martin, C. Wilson, I. Lawrence, S. Mikkelsen, and M. F. Lawrence, "Direct Detection of the Hybridization of Synthetic Homo-Oligomer DNA Sequences by Field Effect," *The Journal of Physical Chemistry B*, vol. 101, no. 15, pp. 2980–2985, Apr. 1997. (Page 18.)

[88] J. Fritz, E. B. Cooper, S. Gaudet, P. K. Sorger, and S. R. Manalis, "Electronic detection of DNA by its intrinsic molecular charge," *Proceedings of the National Academy of Sciences*, vol. 99, no. 22, pp. 14 142–14 146, Oct. 2002. (Page 18.)

[89] W. Gumbrecht, W. Schelter, B. Montag, M. Rasinski, and U. Pfeiffer, "Online blood electrolyte monitoring with a ChemFET microcell system," *Sensors and Actuators B: Chemical*, vol. 1, no. 1, pp. 477–480, Jan. 1990. (Page 18.)

[90] S. Iijima, "Helical microtubules of graphitic carbon," *Nature*, vol. 354, no. 6348, pp. 56–58, Nov. 1991. (Page 19.)

[91] M. F. L. D. Volder, S. H. Tawfick, R. H. Baughman, and A. J. Hart, "Carbon Nanotubes: Present and Future Commercial Applications," *Science*, vol. 339, no. 6119, pp. 535–539, Feb. 2013. (Page 19.)

[92] M. Kumar and Y. Ando, "Chemical vapor deposition of carbon nanotubes: A review on growth mechanism and mass production," *J. Nanosci. Nanotechnol*, pp. 3739–3758, 2010. (Page 19.)

[93] K. Matsumoto, Y. Ohno, and K. Maehashi, "Utilizing research into electrical double layers as a basis for the development of label-free biosensors based on

nanomaterial transistors," *Nanobiosensors in Disease Diagnosis*, p. 1, Dec. 2015. (Page 20.)

[94] Y. Sun, Z. Peng, H. Li, Z. Wang, Y. Mu, G. Zhang, S. Chen, S. Liu, G. Wang, C. Liu, L. Sun, B. Man, and C. Yang, "Suspended CNT-Based FET sensor for ultrasensitive and label-free detection of DNA hybridization," *Biosensors and Bioelectronics*, vol. 137, pp. 255–262, Jul. 2019. (Page 20.)

[95] A. Sharma, S. Hong, R. Singh, and J. Jang, "Single-walled carbon nanotube based transparent immunosensor for detection of a prostate cancer biomarker osteopontin," *Analytica Chimica Acta*, vol. 869, pp. 68–73, Apr. 2015. (Page 20.)

[96] C. Tlili, N. V. Myung, V. Shetty, and A. Mulchandani, "Label-free, chemiresistor immunosensor for stress biomarker cortisol in saliva," *Biosensors and Bioelectronics*, vol. 26, no. 11, pp. 4382–4386, Jul. 2011. (Page 20.)

[97] T. Dastagir, E. S. Forzani, R. Zhang, I. Amlani, L. A. Nagahara, R. Tsui, and N. Tao, "Electrical detection of hepatitis C virus RNA on single wall carbon nanotube-field effect transistors," *Analyst*, vol. 132, no. 8, pp. 738–740, Jul. 2007. (Page 20.)

[98] C. Wang, K. Takei, T. Takahashi, and A. Javey, "Carbon nanotube electronics – moving forward," *Chemical Society Reviews*, vol. 42, no. 7, pp. 2592–2609, Mar. 2013. (Page 20.)

[99] R. Rao, C. L. Pint, A. E. Islam, R. S. Weatherup, S. Hofmann, E. R. Meshot, F. Wu, C. Zhou, N. Dee, P. B. Amama, J. Carpena-Nuñez, W. Shi, D. L. Plata, E. S. Penev, B. I. Yakobson, P. B. Balbuena, C. Bichara, D. N. Futaba, S. Noda, H. Shin, K. S. Kim, B. Simard, F. Mirri, M. Pasquali, F. Fornasiero, E. I. Kauppinen, M. Arnold, B. A. Cola, P. Nikolaev, S. Arepalli, H.-M. Cheng, D. N. Zakharov, E. A. Stach, J. Zhang, F. Wei, M. Terrones, D. B. Geohegan, B. Maruyama, S. Maruyama, Y. Li, W. W. Adams, and A. J. Hart, "Carbon Nanotubes and Related Nanomaterials: Critical Advances and Challenges for Synthesis toward Mainstream Commercial Applications," *ACS Nano*, vol. 12, no. 12, pp. 11 756–11 784, Dec. 2018. (Page 20.)

[100] E. S. Snow, J. P. Novak, P. M. Campbell, and D. Park, "Random networks of carbon nanotubes as an electronic material," *Applied Physics Letters*, vol. 82, no. 13, pp. 2145–2147, Mar. 2003. (Page 20.)

[101] V. Schroeder, S. Savagatrup, M. He, S. Lin, and T. M. Swager, "Carbon Nanotube Chemical Sensors," *Chemical reviews*, vol. 119, no. 1, pp. 599–663, Jan. 2019. (Page 20.)

[102] M. E. Roberts, M. C. LeMieux, and Z. Bao, “Sorted and Aligned Single-Walled Carbon Nanotube Networks for Transistor-Based Aqueous Chemical Sensors,” *ACS Nano*, vol. 3, no. 10, pp. 3287–3293, Oct. 2009. (Page 21.)

[103] G. Giancane, A. Ruland, V. Sgobba, D. Manno, A. Serra, G. M. Farinola, O. H. Omar, D. M. Guldi, and L. Valli, “Aligning Single-Walled Carbon Nanotubes By Means Of Langmuir–Blodgett Film Deposition: Optical, Morphological, and Photo-electrochemical Studies,” *Advanced Functional Materials*, vol. 20, no. 15, pp. 2481–2488, 2010. (Page 21.)

[104] S. Shekhar, P. Stokes, and S. I. Khondaker, “Ultrahigh Density Alignment of Carbon Nanotube Arrays by Dielectrophoresis,” *ACS Nano*, vol. 5, no. 3, pp. 1739–1746, Mar. 2011. (Page 21.)

[105] J. S. Walker, J. A. Fagan, A. J. Biacchi, V. A. Kuehl, T. A. Searles, A. R. Hight Walker, and W. D. Rice, “Global Alignment of Solution-Based Single-Wall Carbon Nanotube Films via Machine-Vision Controlled Filtration,” *Nano Letters*, vol. 19, no. 10, pp. 7256–7264, Oct. 2019. (Page 21.)

[106] C.-P. Li, C.-S. Lee, X.-L. Ma, N. Wang, R.-Q. Zhang, and S.-T. Lee, “Growth Direction and Cross-Sectional Study of Silicon Nanowires,” *Advanced Materials*, vol. 15, no. 7-8, pp. 607–609, 2003. (Page 21.)

[107] M.-J. Bañuls, R. Puchades, and Á. Maquieira, “Chemical surface modifications for the development of silicon-based label-free integrated optical (IO) biosensors: A review,” *Analytica Chimica Acta*, vol. 777, pp. 1–16, May 2013. (Page 21.)

[108] Y. Zhang, R. Chen, L. Xu, Y. Ning, S. Xie, and G.-J. Zhang, “Silicon Nanowire Biosensor for Highly Sensitive and Multiplexed Detection of Oral Squamous Cell Carcinoma Biomarkers in Saliva,” *Analytical Sciences*, vol. 31, no. 2, pp. 73–78, 2015. (Page 21.)

[109] N. Lu, A. Gao, P. Dai, H. Mao, X. Zuo, C. Fan, Y. Wang, and T. Li, “Ultrasensitive Detection of Dual Cancer Biomarkers with Integrated CMOS-Compatible Nanowire Arrays,” *Analytical Chemistry*, vol. 87, no. 22, pp. 11 203–11 208, Nov. 2015. (Page 21.)

[110] Y.-W. Huang, C.-S. Wu, C.-K. Chuang, S.-T. Pang, T.-M. Pan, Y.-S. Yang, and F.-H. Ko, “Real-Time and Label-Free Detection of the Prostate-Specific Antigen in Human Serum by a Polycrystalline Silicon Nanowire Field-Effect Transistor Biosensor,” *Analytical Chemistry*, vol. 85, no. 16, pp. 7912–7918, Aug. 2013. (Pages 21 and 22.)

[111] P. Namdari, H. Daraee, and A. Eatemadi, “Recent Advances in Silicon Nanowire Biosensors: Synthesis Methods, Properties, and Applications,” *Nanoscale Research Letters*, vol. 11, no. 1, p. 406, Dec. 2016. (Page 21.)

[112] A. C. M. De Moraes and L. T. Kubota, “Recent Trends in Field-Effect Transistors-Based Immunosensors,” *Chemosensors*, vol. 4, no. 4, p. 20, Dec. 2016. (Page 21.)

[113] P. Ambhorkar, Z. Wang, H. Ko, S. Lee, K.-i. Koo, K. Kim, and D.-i. D. Cho, “Nanowire-Based Biosensors: From Growth to Applications,” *Micromachines*, vol. 9, no. 12, Dec. 2018. (Page 22.)

[114] H. Shiigi, S. Tokonami, H. Yakabe, and T. Nagaoka, “Label-Free Electronic Detection of DNA-Hybridization on Nanogapped Gold Particle Film,” *Journal of the American Chemical Society*, vol. 127, no. 10, pp. 3280–3281, Mar. 2005. (Page 22.)

[115] S. Roy, H. Vedala, A. D. Roy, D.-h. Kim, M. Doud, K. Mathee, H.-k. Shin, N. Shimamoto, V. Prasad, and W. Choi, “Direct Electrical Measurements on Single-Molecule Genomic DNA Using Single-Walled Carbon Nanotubes,” *Nano Letters*, vol. 8, no. 1, pp. 26–30, Jan. 2008. (Page 22.)

[116] P. E. Sheehan and L. J. Whitman, “Detection Limits for Nanoscale Biosensors,” *Nano Letters*, vol. 5, no. 4, pp. 803–807, Apr. 2005. (Page 23.)

[117] T. M. Squires, R. J. Messinger, and S. R. Manalis, “Making it stick: Convection, reaction and diffusion in surface-based biosensors,” *Nature Biotechnology*, vol. 26, no. 4, pp. 417–426, Apr. 2008. (Pages 23, 143, and 146.)

[118] A. B. Dahlin, “Size Matters: Problems and Advantages Associated with Highly Miniaturized Sensors,” *Sensors*, vol. 12, no. 3, pp. 3018–3036, Mar. 2012. (Page 23.)

[119] P. R. Wallace, “The Band Theory of Graphite,” *Physical Review*, vol. 71, no. 9, pp. 622–634, May 1947. (Page 24.)

[120] K. S. Novoselov, A. K. Geim, S. V. Morozov, D. Jiang, Y. Zhang, S. V. Dubonos, I. V. Grigorieva, and A. A. Firsov, “Electric Field Effect in Atomically Thin Carbon Films,” *Science*, vol. 306, no. 5696, pp. 666–669, Oct. 2004. (Pages 24, 30, and 56.)

[121] N. D. Mermin, “Crystalline Order in Two Dimensions,” *Physical Review*, vol. 176, no. 1, pp. 250–254, Dec. 1968. (Page 24.)

[122] X. Du, I. Skachko, A. Barker, and E. Y. Andrei, “Approaching ballistic transport in suspended graphene,” *Nature Nanotechnology*, vol. 3, no. 8, pp. 491–495, Aug. 2008. (Page 25.)

[123] A. C. Neto, F. Guinea, and N. M. Peres, “Drawing conclusions from graphene,” *Physics World*, vol. 19, no. 11, pp. 33–37, Nov. 2006. (Page 25.)

[124] A. H. Castro Neto, F. Guinea, N. M. R. Peres, K. S. Novoselov, and A. K. Geim, “The electronic properties of graphene,” *Reviews of Modern Physics*, vol. 81, no. 1, pp. 109–162, Jan. 2009. (Page 25.)

[125] N. Petrone, C. R. Dean, I. Meric, A. M. van der Zande, P. Y. Huang, L. Wang, D. Muller, K. L. Shepard, and J. Hone, “Chemical Vapor Deposition-Derived Graphene with Electrical Performance of Exfoliated Graphene,” *Nano Letters*, vol. 12, no. 6, pp. 2751–2756, Jun. 2012. (Page 26.)

[126] J.-H. Chen, C. Jang, S. Xiao, M. Ishigami, and M. S. Fuhrer, “Intrinsic and extrinsic performance limits of graphene devices on SiO2,” *Nature Nanotechnology*, vol. 3, no. 4, pp. 206–209, Apr. 2008. (Page 26.)

[127] C. Lee, X. Wei, J. W. Kysar, and J. Hone, “Measurement of the Elastic Properties and Intrinsic Strength of Monolayer Graphene,” *Science*, vol. 321, no. 5887, pp. 385–388, Jul. 2008. (Page 26.)

[128] A. A. Balandin, S. Ghosh, W. Bao, I. Calizo, D. Teweldebrhan, F. Miao, and C. N. Lau, “Superior thermal conductivity of single-layer graphene,” *Nano Letters*, vol. 8, no. 3, pp. 902–907, Mar. 2008. (Page 26.)

[129] H. D. Young and F. W. Sears, *University Physics. Extended Version with Modern Physics*, 8th ed., ser. Addison-Wesley Series in Physics. Reading, Mass: Addison-Wesley Pub. Co, 1992. (Page 26.)

[130] R. R. Nair, P. Blake, A. N. Grigorenko, K. S. Novoselov, T. J. Booth, T. Stauber, N. M. R. Peres, and A. K. Geim, “Fine Structure Constant Defines Visual Transparency of Graphene,” *Science*, vol. 320, no. 5881, pp. 1308–1308, Jun. 2008. (Page 26.)

[131] C. D. English, G. Shine, V. E. Dorgan, K. C. Saraswat, and E. Pop, “Improved Contacts to MoS2 Transistors by Ultra-High Vacuum Metal Deposition,” *Nano Letters*, vol. 16, no. 6, pp. 3824–3830, Jun. 2016. (Page 26.)

[132] L. H. Li, T. Tian, Q. Cai, C.-J. Shih, and E. J. G. Santos, “Asymmetric electric field screening in van der Waals heterostructures,” *Nature Communications*, vol. 9, no. 1, pp. 1–11, Mar. 2018. (Page 26.)

[133] P. Blake, E. W. Hill, A. H. Castro Neto, K. S. Novoselov, D. Jiang, R. Yang, T. J. Booth, and A. K. Geim, “Making graphene visible,” *Applied Physics Letters*, vol. 91, no. 6, p. 063124, 2007. (Page 26.)

[134] K. S. Novoselov, V. I. Fal′ko, L. Colombo, P. R. Gellert, M. G. Schwab, and K. Kim, “A roadmap for graphene,” *Nature*, vol. 490, no. 7419, pp. 192–200, Oct. 2012. (Page 27.)

[135] H. Zheng, R. K. Smith, Y.-w. Jun, C. Kisielowski, U. Dahmen, and A. P. Alivisatos, “Large-Area Synthesis of High-Quality and Uniform Graphene Films on Copper Foils,” *Science*, vol. 324, no. 5932, pp. 1309–1312, Jun. 2009. (Page 27.)

[136] X. Li, L. Colombo, and R. S. Ruoff, “Synthesis of Graphene Films on Copper Foils by Chemical Vapor Deposition,” *Advanced Materials*, vol. 28, no. 29, pp. 6247–6252, Aug. 2016. (Page 27.)

[137] F. Veliev, “Interfacing neurons with nanoelectronics: From silicon nanowires to carbon devices,” Ph.D. dissertation, Université Grenoble Alpes, 2016. (Pages 28, 66, and 73.)

[138] W. Fang, A. L. Hsu, Y. Song, and J. Kong, “A review of large-area bilayer graphene synthesis by chemical vapor deposition,” *Nanoscale*, vol. 7, no. 48, pp. 20 335–20 351, Dec. 2015. (Page 28.)

[139] K. S. Kim, Y. Zhao, H. Jang, S. Y. Lee, J. M. Kim, K. S. Kim, J.-H. Ahn, P. Kim, J.-Y. Choi, and B. H. Hong, “Large-scale pattern growth of graphene films for stretchable transparent electrodes,” *Nature*, vol. 457, no. 7230, pp. 706–710, Feb. 2009. (Page 28.)

[140] S.-Y. Kwon, C. V. Ciobanu, V. Petrova, V. B. Shenoy, J. Bareño, V. Gambin, I. Petrov, and S. Kodambaka, “Growth of Semiconducting Graphene on Palladium,” *Nano Letters*, vol. 9, no. 12, pp. 3985–3990, Dec. 2009. (Page 28.)

[141] B. J. Kang, J. H. Mun, C. Y. Hwang, and B. J. Cho, “Monolayer graphene growth on sputtered thin film platinum,” *Journal of Applied Physics*, vol. 106, no. 10, p. 104309, Nov. 2009. (Page 28.)

[142] A. Cabrero-Vilatela, R. S. Weatherup, P. Braeuninger-Weimer, S. Caneva, and S. Hofmann, “Towards a general growth model for graphene CVD on transition metal catalysts,” *Nanoscale*, vol. 8, no. 4, pp. 2149–2158, Jan. 2016. (Page 28.)

[143] Z. Han, A. Kimouche, D. Kalita, A. Allain, H. Arjmandi-Tash, A. Reserbat-Plantey, L. Marty, S. Pairis, V. Reita, N. Bendiab, J. Coraux, and V. Bouchiat, “Homogeneous Optical and Electronic Properties of Graphene Due to the Suppression of Multilayer Patches During CVD on Copper Foils,” *Advanced Functional Materials*, vol. 24, no. 7, pp. 964–970, Feb. 2014. (Pages 28 and 60.)

[144] IDTechEx, “Graphene Enters High-volume Applications... And This Is Just The Start,” https://www.idtechex.com/en/research-article/graphene-enters-high-volume-applications-and-this-is-just-the-start/18416, Oct. 2019. (Page 28.)

[145] Aixtron, “Cost-effective, large scale graphene with AIXTRON systems,” https://phys.org/news/2019-06-cost-effective-large-scale-graphene-aixtron.html, Jun. 19. (Page 28.)

[146] Y. Chen, X.-L. Gong, and J.-G. Gai, “Progress and Challenges in Transfer of Large-Area Graphene Films,” *Advanced Science*, vol. 3, no. 8, p. 1500343, Aug. 2016. (Page 29.)

[147] J. W. Suk, A. Kitt, C. W. Magnuson, Y. Hao, S. Ahmed, J. An, A. K. Swan, B. B. Goldberg, and R. S. Ruoff, “Transfer of CVD-Grown Monolayer Graphene onto Arbitrary Substrates,” *ACS Nano*, vol. 5, no. 9, pp. 6916–6924, Sep. 2011. (Pages 29 and 35.)

[148] F. Schwierz, “Graphene transistors,” *Nature Nanotechnology*, vol. 5, no. 7, pp. 487–496, Jul. 2010. (Page 30.)

[149] F. Xia, V. Perebeinos, Y.-m. Lin, Y. Wu, and P. Avouris, “The origins and limits of metal-graphene junction resistance,” *Nature Nanotechnology*, vol. 6, no. 3, pp. 179–184, Mar. 2011. (Page 30.)

[150] D. B. Farmer, R. Golizadeh-Mojarad, V. Perebeinos, Y.-M. Lin, G. S. Tulevski, J. C. Tsang, and P. Avouris, “Chemical Doping and Electron-Hole Conduction Asymmetry in Graphene Devices,” *Nano Letters*, vol. 9, no. 1, pp. 388–392, Jan. 2009. (Page 30.)

[151] L. Gammelgaard, J. M. Caridad, A. Cagliani, D. M. A. Mackenzie, D. H. Petersen, T. J. Booth, and P. Bøggild, “Graphene transport properties upon exposure to PMMA processing and heat treatments,” *2D Materials*, vol. 1, no. 3, p. 035005, Nov. 2014. (Pages 30 and 125.)

[152] K. Nagashio, T. Yamashita, T. Nishimura, K. Kita, and A. Toriumi, “Electrical transport properties of graphene on SiO2 with specific surface structures,” *Journal of Applied Physics*, vol. 110, no. 2, p. 024513, 2011. (Page 30.)

[153] S. Das Sarma, S. Adam, E. H. Hwang, and E. Rossi, “Electronic transport in two-dimensional graphene,” *Reviews of Modern Physics*, vol. 83, no. 2, pp. 407–470, May 2011. (Page 31.)

[154] S. Kim, J. Nah, I. Jo, D. Shahrjerdi, L. Colombo, Z. Yao, E. Tutuc, and S. K. Banerjee, “Realization of a high mobility dual-gated graphene field-effect transistor with Al2O3 dielectric,” *Applied Physics Letters*, vol. 94, no. 6, p. 062107, Feb. 2009. (Page 31.)

[155] F. Giubileo and A. Di Bartolomeo, “The role of contact resistance in graphene field-effect devices,” *Progress in Surface Science*, vol. 92, no. 3, pp. 143–175, Aug. 2017. (Pages 32 and 71.)

[156] H. Zhong, Z. Zhang, H. Xu, C. Qiu, and L.-M. Peng, “Comparison of mobility extraction methods based on field-effect measurements for graphene,” *AIP Advances*, vol. 5, no. 5, p. 057136, May 2015. (Page 32.)

[157] P. Blake, R. Yang, S. Morozov, F. Schedin, L. Ponomarenko, A. Zhukov, R. Nair, I. Grigorieva, K. Novoselov, and A. Geim, “Influence of metal contacts and charge inhomogeneity on transport properties of graphene near the neutrality point,” *Solid State Communications*, vol. 149, no. 27-28, pp. 1068–1071, Jul. 2009. (Page 32.)

[158] S. Islam, S. Shukla, V. K. Bajpai, Y.-K. Han, Y. S. Huh, A. Ghosh, and S. Gandhi, “Microfluidic-based graphene field effect transistor for femtomolar detection of chlorpyrifos,” *Scientific Reports*, vol. 9, no. 1, pp. 1–7, Jan. 2019. (Page 32.)

[159] K. Islam, A. Suhail, and G. Pan, “A Label-Free and Ultrasensitive Immunosensor for Detection of Human Chorionic Gonadotrophin Based on Graphene FETs,” *Biosensors*, vol. 7, no. 3, p. 27, Sep. 2017. (Page 32.)

[160] A. Kakatkar, T. S. Abhilash, R. D. Alba, J. M. Parpia, and H. G. Craighead, “Detection of DNA and poly-l-lysine using CVD graphene-channel FET biosensors,” *Nanotechnology*, vol. 26, no. 12, p. 125502, Mar. 2015. (Page 32.)

[161] J. Ping, R. Vishnubhotla, A. Vrudhula, and A. T. C. Johnson, “Scalable Production of High-Sensitivity, Label-Free DNA Biosensors Based on Back-Gated Graphene Field Effect Transistors,” *ACS Nano*, vol. 10, no. 9, pp. 8700–8704, Sep. 2016. (Pages 32 and 33.)

[162] J. Ye, M. F. Craciun, M. Koshino, S. Russo, S. Inoue, H. Yuan, H. Shimotani, A. F. Morpurgo, and Y. Iwasa, “Accessing the transport properties of graphene and its multilayers at high carrier density,” *Proceedings of*

the National Academy of Sciences, vol. 108, no. 32, pp. 13 002–13 006, 2011. (Page 33.)

[163] C. Hébert, E. Masvidal-Codina, A. Suarez-Perez, A. B. Calia, G. Piret, R. Garcia-Cortadella, X. Illa, E. Del Corro Garcia, J. M. De la Cruz Sanchez, D. V. Casals, E. Prats-Alfonso, J. Bousquet, P. Godignon, B. Yvert, R. Villa, M. V. Sanchez-Vives, A. Guimerà-Brunet, and J. A. Garrido, "Flexible Graphene Solution-Gated Field-Effect Transistors: Efficient Transducers for Micro-Electrocorticography," *Advanced Functional Materials*, vol. 28, no. 12, p. 1703976, Mar. 2018. (Pages 34 and 81.)

[164] O. Stern, "Zur Theorie Der Elektrolytischen Doppelschicht," *Zeitschrift für Elektrochemie und angewandte physikalische Chemie*, vol. 30, no. 21-22, pp. 508–516, 1924. (Page 36.)

[165] A. J. Bard and L. R. Faulkner, *Electrochemical Methods: Fundamentals and Applications*, 2nd ed. New York: Wiley, 2001. (Pages 37, 40, 127, and 128.)

[166] J. Xia, F. Chen, J. Li, and N. Tao, "Measurement of the quantum capacitance of graphene," *Nature Nanotechnology*, vol. 4, no. 8, pp. 505–509, Aug. 2009. (Page 39.)

[167] N. Schwierz, D. Horinek, and R. R. Netz, "Reversed Anionic Hofmeister Series: The Interplay of Surface Charge and Surface Polarity," *Langmuir*, vol. 26, no. 10, pp. 7370–7379, May 2010. (Page 40.)

[168] L. H. Hess, M. Seifert, and J. A. Garrido, "Graphene Transistors for Bioelectronics," *Proceedings of the IEEE*, vol. 101, no. 7, pp. 1780–1792, Jul. 2013. (Pages 40, 41, 42, and 122.)

[169] C. Mackin, L. H. Hess, A. Hsu, Yi Song, Jing Kong, J. A. Garrido, and T. Palacios, "A Current–Voltage Model for Graphene Electrolyte-Gated Field-Effect Transistors," *IEEE Transactions on Electron Devices*, vol. 61, no. 12, pp. 3971–3977, Dec. 2014. (Pages 40, 41, 81, and 87.)

[170] D. Kireev, M. Brambach, S. Seyock, V. Maybeck, W. Fu, B. Wolfrum, and A. Offenhäusser, "Graphene transistors for interfacing with cells: Towards a deeper understanding of liquid gating and sensitivity," *Scientific Reports*, vol. 7, no. 1, Dec. 2017. (Pages 40, 41, and 132.)

[171] J. Ping and A. T. C. Johnson, "Quantifying the intrinsic surface charge density and charge-transfer resistance of the graphene-solution interface through bias-free low-level charge measurement," *Applied Physics Letters*, vol. 109, no. 1, p. 013103, Jul. 2016. (Page 40.)

[172] I. Heller, S. Chatoor, J. Männik, M. A. G. Zevenbergen, C. Dekker, and S. G. Lemay, "Influence of Electrolyte Composition on Liquid-Gated Carbon Nanotube and Graphene Transistors," *Journal of the American Chemical Society*, vol. 132, no. 48, pp. 17 149–17 156, Dec. 2010. (Pages 40, 42, and 137.)

[173] R. L. McCreery, "Advanced Carbon Electrode Materials for Molecular Electrochemistry," *Chemical Reviews*, vol. 108, no. 7, pp. 2646–2687, Jul. 2008. (Page 43.)

[174] D. A. C. Brownson, D. K. Kampouris, and C. E. Banks, "Graphene electrochemistry: Fundamental concepts through to prominent applications," *Chemical Society Reviews*, vol. 41, no. 21, p. 6944, 2012. (Page 43.)

[175] B. Ntsendwana, B. B. Mamba, S. Sampath, and O. A. Arotiba, "Electrochemical Detection of Bisphenol A Using Graphene- Modified Glassy Carbon Electrode," *Int. J. Electrochem. Sci.*, vol. 7, p. 12, 2012. (Page 43.)

[176] N. M. M. A. Edris, J. Abdullah, S. Kamaruzaman, and Y. Sulaiman, "Ultrasensitive Reduced Graphene Oxide-Poly(Procion)/Gold Nanoparticles Modified Glassy Carbon Electrode for Selective and Simultaneous Determination of Ascorbic Acid, Dopamine, and Uric Acid," *Journal of The Electrochemical Society*, vol. 166, no. 8, pp. B664–B672, Jan. 2019. (Page 43.)

[177] A. Navaee, A. Salimi, and H. Teymourian, "Graphene nanosheets modified glassy carbon electrode for simultaneous detection of heroine, morphine and noscapine," *Biosensors & Bioelectronics*, vol. 31, no. 1, pp. 205–211, Jan. 2012. (Page 44.)

[178] A. Mesaros, S. Papanikolaou, C. F. J. Flipse, D. Sadri, and J. Zaanen, "Electronic states of graphene grain boundaries," *Physical Review B*, vol. 82, no. 20, p. 205119, Nov. 2010. (Page 44.)

[179] F. Banhart, J. Kotakoski, and A. V. Krasheninnikov, "Structural Defects in Graphene," *ACS Nano*, vol. 5, no. 1, pp. 26–41, Jan. 2011. (Page 44.)

[180] W. Yuan, Y. Zhou, Y. Li, C. Li, H. Peng, J. Zhang, Z. Liu, L. Dai, and G. Shi, "The edge- and basal-plane-specific electrochemistry of a single-layer graphene sheet," *Scientific Reports*, vol. 3, p. 2248, Jul. 2013. (Page 44.)

[181] X. Tan, H.-J. Chuang, M.-W. Lin, Z. Zhou, and M. M.-C. Cheng, "Edge Effects on the pH Response of Graphene Nanoribbon Field Effect Transistors," *The Journal of Physical Chemistry C*, vol. 117, no. 51, pp. 27 155–27 160, Dec. 2013. (Pages 44 and 137.)

[182] W. Fu, C. Nef, O. Knopfmacher, A. Tarasov, M. Weiss, M. Calame, and C. Schönenberger, “Graphene Transistors Are Insensitive to pH Changes in Solution,” *Nano Letters*, vol. 11, no. 9, pp. 3597–3600, Sep. 2011. (Page 44.)

[183] Z. Hao, Y. Zhu, X. Wang, P. G. Rotti, C. DiMarco, S. R. Tyler, X. Zhao, J. F. Engelhardt, J. Hone, and Q. Lin, “Real-Time Monitoring of Insulin Using a Graphene Field-Effect Transistor Aptameric Nanosensor,” *ACS Applied Materials & Interfaces*, vol. 9, no. 33, pp. 27 504–27 511, Aug. 2017. (Page 45.)

[184] N. M. Andoy, M. S. Filipiak, D. Vetter, Ó. Gutiérrez-Sanz, and A. Tarasov, “Graphene-Based Electronic Immunosensor with Femtomolar Detection Limit in Whole Serum,” *Advanced Materials Technologies*, vol. 3, no. 12, p. 1800186, Oct. 2018. (Page 45.)

[185] S. Xu, S. Jiang, C. Zhang, W. Yue, Y. Zou, G. Wang, H. Liu, X. Zhang, M. Li, Z. Zhu, and J. Wang, “Ultrasensitive label-free detection of DNA hybridization by sapphire-based graphene field-effect transistor biosensor,” *Applied Surface Science*, vol. 427, pp. 1114–1119, Jan. 2018. (Page 45.)

[186] L. Zhou, K. Wang, H. Sun, S. Zhao, X. Chen, D. Qian, H. Mao, and J. Zhao, “Novel Graphene Biosensor Based on the Functionalization of Multifunctional Nano-bovine Serum Albumin for the Highly Sensitive Detection of Cancer Biomarkers,” *Nano-Micro Letters*, vol. 11, no. 1, p. 20, Mar. 2019. (Page 45.)

[187] G. T. Hermanson, “Silane Coupling Agents,” in *Bioconjugate Techniques.* Elsevier, 2013, pp. 535–548. (Page 45.)

[188] C. Rajesh, C. Majumder, H. Mizuseki, and Y. Kawazoe, “A theoretical study on the interaction of aromatic amino acids with graphene and single walled carbon nanotube,” *The Journal of Chemical Physics*, vol. 130, no. 12, p. 124911, Mar. 2009. (Page 46.)

[189] S. Gowtham, R. H. Scheicher, R. Ahuja, R. Pandey, and S. P. Karna, “Physisorption of nucleobases on graphene: Density-functional calculations,” *Physical Review B*, vol. 76, no. 3, p. 033401, Jul. 2007. (Page 46.)

[190] L. Ou, Y. Luo, and G. Wei, “Atomic-Level Study of Adsorption, Conformational Change, and Dimerization of an α-Helical Peptide at Graphene Surface,” *The Journal of Physical Chemistry B*, vol. 115, no. 32, pp. 9813–9822, Aug. 2011. (Page 46.)

[191] G. Zuo, X. Zhou, Q. Huang, H. Fang, and R. Zhou, “Adsorption of Villin Headpiece onto Graphene, Carbon Nanotube, and C60: Effect of Contacting

Surface Curvatures on Binding Affinity," *The Journal of Physical Chemistry C*, vol. 115, no. 47, pp. 23 323–23 328, Dec. 2011. (Page 46.)

[192] Z. E. Hughes and T. R. Walsh, "Structural Disruption of an Adenosine-Binding DNA Aptamer on Graphene: Implications for Aptasensor Design," *ACS sensors*, Nov. 2017. (Page 46.)

[193] R. Campos, J. Borme, J. R. Guerreiro, G. Machado, M. F. Cerqueira, D. Y. Petrovykh, and P. Alpuim, "Attomolar Label-Free Detection of DNA Hybridization with Electrolyte-Gated Graphene Field-Effect Transistors," *ACS Sensors*, Feb. 2019. (Pages 47, 48, and 152.)

[194] J. Park and M. Yan, "Covalent Functionalization of Graphene with Reactive Intermediates," *Accounts of Chemical Research*, vol. 46, no. 1, pp. 181–189, Jan. 2013. (Pages 47 and 48.)

[195] J. Shen, B. Yan, M. Shi, H. Ma, N. Li, and M. Ye, "Synthesis of graphene oxide-based biocomposites through diimide-activated amidation," *Journal of Colloid and Interface Science*, vol. 356, no. 2, pp. 543–549, Apr. 2011. (Page 47.)

[196] N. Mohanty and V. Berry, "Graphene-Based Single-Bacterium Resolution Biodevice and DNA Transistor: Interfacing Graphene Derivatives with Nanoscale and Microscale Biocomponents," *Nano Letters*, vol. 8, no. 12, pp. 4469–4476, Dec. 2008. (Page 47.)

[197] N. Mohanty, M. Fahrenholtz, A. Nagaraja, D. Boyle, and V. Berry, "Impermeable Graphenic Encasement of Bacteria," *Nano Letters*, vol. 11, no. 3, pp. 1270–1275, Mar. 2011. (Page 47.)

[198] S. J. Park, O. S. Kwon, S. H. Lee, H. S. Song, T. H. Park, and J. Jang, "Ultrasensitive Flexible Graphene Based Field-Effect Transistor (FET)-Type Bioelectronic Nose," *Nano Letters*, vol. 12, no. 10, pp. 5082–5090, Oct. 2012. (Page 47.)

[199] E. J.-C. Amieva, J. López-Barroso, A. L. Martínez-Hernández, and C. Velasco-Santos, "Graphene-Based Materials Functionalization with Natural Polymeric Biomolecules," *Recent Advances in Graphene Research*, Oct. 2016. (Page 47.)

[200] A. Bhaumik, A. Haque, M. Taufique, P. Karnati, R. Patel, M. Nath, and K. Ghosh, "Reduced Graphene Oxide Thin Films with Very Large Charge Carrier Mobility Using Pulsed Laser Deposition," *Journal of Material Science & Engineering*, vol. 06, no. 04, 2017. (Page 48.)

[201] Y. Wang, Y. Chen, S. D. Lacey, L. Xu, H. Xie, T. Li, V. A. Danner, and L. Hu, "Reduced graphene oxide film with record-high conductivity and mobility," *Materials Today*, vol. 21, no. 2, pp. 186–192, Mar. 2018. (Page 48.)

[202] X. Wang, Z. Hao, T. R. Olsen, W. Zhang, and Q. Lin, "Measurements of aptamer–protein binding kinetics using graphene field-effect transistors," *Nanoscale*, vol. 11, no. 26, pp. 12 573–12 581, 2019. (Pages 48 and 147.)

[203] S. Xu, J. Zhan, B. Man, S. Jiang, W. Yue, S. Gao, C. Guo, H. Liu, Z. Li, J. Wang, and Y. Zhou, "Real-time reliable determination of binding kinetics of DNA hybridization using a multi-channel graphene biosensor," *Nature Communications*, vol. 8, p. 14902, Mar. 2017. (Pages 48 and 147.)

[204] S. Mukherjee, X. Meshik, M. Choi, S. Farid, D. Datta, Y. Lan, S. Poduri, K. Sarkar, U. Baterdene, C.-E. Huang, Y. Y. Wang, P. Burke, M. Dutta, and M. A. Stroscio, "A Graphene and Aptamer Based Liquid Gated FET-Like Electrochemical Biosensor to Detect Adenosine Triphosphate," *IEEE Transactions on NanoBioscience*, vol. 14, no. 8, pp. 967–972, Dec. 2015. (Page 48.)

[205] R. Zhao and R.-Q. Zhang, "A new insight into π–π stacking involving remarkable orbital interactions," *Physical Chemistry Chemical Physics*, vol. 18, no. 36, pp. 25 452–25 457, 2016. (Page 49.)

[206] J. A. Mann, T. Alava, H. G. Craighead, and W. R. Dichtel, "Preservation of Antibody Selectivity on Graphene by Conjugation to a Tripod Monolayer," *Angewandte Chemie International Edition*, vol. 52, no. 11, pp. 3177–3180, Mar. 2013. (Pages 50, 51, 52, and 145.)

[207] J. A. Mann and W. R. Dichtel, "Improving the Binding Characteristics of Tripodal Compounds on Single Layer Graphene," *ACS Nano*, vol. 7, no. 8, pp. 7193–7199, Aug. 2013. (Pages 50, 51, and 150.)

[208] J. Rodríguez-López, N. L. Ritzert, J. A. Mann, C. Tan, W. R. Dichtel, and H. D. Abruña, "Quantification of the Surface Diffusion of Tripodal Binding Motifs on Graphene Using Scanning Electrochemical Microscopy," *Journal of the American Chemical Society*, vol. 134, no. 14, pp. 6224–6236, Apr. 2012. (Page 50.)

[209] C. Sun, K. L. Walker, D. L. Wakefield, and W. R. Dichtel, "Retaining the Activity of Enzymes and Fluorophores Attached to Graphene Oxide," *Chemistry of Materials*, vol. 27, no. 12, pp. 4499–4504, Jun. 2015. (Page 51.)

[210] B. K. Bharadwaj, D. Nath, R. Pratap, and S. Raghavan, “Making consistent contacts to graphene: Effect of architecture and growth induced defects,” *Nanotechnology*, vol. 27, no. 20, p. 205705, 2016. (Pages 56 and 57.)

[211] A. Gahoi, S. Wagner, A. Bablich, S. Kataria, V. Passi, and M. C. Lemme, “Contact resistance study of various metal electrodes with CVD graphene,” *Solid-State Electronics*, vol. 125, pp. 234–239, Nov. 2016. (Page 57.)

[212] K. Nagashio, T. Nishimura, K. Kita, and A. Toriumi, “Metal/graphene contact as a performance Killer of ultra-high mobility graphene analysis of intrinsic mobility and contact resistance,” in *2009 IEEE International Electron Devices Meeting (IEDM)*, Dec. 2009, pp. 1–4. (Pages 57 and 71.)

[213] J. A. Robinson, M. LaBella, M. Zhu, M. Hollander, R. Kasarda, Z. Hughes, K. Trumbull, R. Cavalero, and D. Snyder, “Contacting graphene,” *Applied Physics Letters*, vol. 98, no. 5, p. 053103, Jan. 2011. (Page 57.)

[214] O. Balci and C. Kocabas, “Rapid thermal annealing of graphene-metal contact,” *Applied Physics Letters*, vol. 101, no. 24, p. 243105, 2012. (Page 57.)

[215] L. Wang, I. Meric, P. Y. Huang, Q. Gao, Y. Gao, H. Tran, T. Taniguchi, K. Watanabe, L. M. Campos, D. A. Muller, J. Guo, P. Kim, J. Hone, K. L. Shepard, and C. R. Dean, “One-Dimensional Electrical Contact to a Two-Dimensional Material,” *Science*, vol. 342, no. 6158, pp. 614–617, Nov. 2013. (Page 57.)

[216] S. Min Song, T. Yong Kim, O. Jae Sul, W. Cheol Shin, and B. Jin Cho, “Improvement of graphene–metal contact resistance by introducing edge contacts at graphene under metal,” *Applied Physics Letters*, vol. 104, no. 18, p. 183506, May 2014. (Page 57.)

[217] S. M. Song, J. K. Park, O. J. Sul, and B. J. Cho, “Determination of Work Function of Graphene under a Metal Electrode and Its Role in Contact Resistance,” *Nano Letters*, vol. 12, no. 8, pp. 3887–3892, Aug. 2012. (Page 57.)

[218] M. Houssa, A. Dimoulas, and A. Molle, *2D Materials for Nanoelectronics*. Crc Press, Taylor & Francis Group, 2016. (Page 58.)

[219] X. Li, Y. Zhu, W. Cai, M. Borysiak, B. Han, D. Chen, R. D. Piner, L. Colombo, and R. S. Ruoff, “Transfer of Large-Area Graphene Films for High-Performance Transparent Conductive Electrodes,” *Nano Letters*, vol. 9, no. 12, pp. 4359–4363, Dec. 2009. (Pages 60 and 67.)

[220] J.-Y. Hong, Y. C. Shin, A. Zubair, Y. Mao, T. Palacios, M. S. Dresselhaus, S. H. Kim, and J. Kong, “A Rational Strategy for Graphene Transfer on Substrates with Rough Features,” *Advanced Materials*, vol. 28, no. 12, pp. 2382–2392, Mar. 2016. (Pages 61, 66, and 68.)

[221] X. Liang, B. A. Sperling, I. Calizo, G. Cheng, C. A. Hacker, Q. Zhang, Y. Obeng, K. Yan, H. Peng, Q. Li, X. Zhu, H. Yuan, A. R. Hight Walker, Z. Liu, L.-m. Peng, and C. A. Richter, “Toward Clean and Crackless Transfer of Graphene,” *ACS Nano*, vol. 5, no. 11, pp. 9144–9153, Nov. 2011. (Pages 61 and 66.)

[222] M. C. Prado, D. Jariwala, T. J. Marks, and M. C. Hersam, “Optimization of graphene dry etching conditions via combined microscopic and spectroscopic analysis,” *Applied Physics Letters*, vol. 102, no. 19, p. 193111, May 2013. (Page 62.)

[223] H. H. Kim, S. K. Lee, S. G. Lee, E. Lee, and K. Cho, “Wetting-Assisted Crack- and Wrinkle-Free Transfer of Wafer-Scale Graphene onto Arbitrary Substrates over a Wide Range of Surface Energies,” *Advanced Functional Materials*, vol. 26, no. 13, pp. 2070–2077, 2016. (Page 63.)

[224] K. Hermansson, U. Lindberg, B. Hok, and G. Palmskog, “Wetting properties of silicon surfaces,” in *TRANSDUCERS ’91: 1991 International Conference on Solid-State Sensors and Actuators. Digest of Technical Papers*, Jun. 1991, pp. 193–196. (Page 64.)

[225] S. B. Habib, E. Gonzalez, and R. F. Hicks, “Atmospheric oxygen plasma activation of silicon (100) surfaces,” *Journal of Vacuum Science & Technology A: Vacuum, Surfaces, and Films*, vol. 28, no. 3, p. 476, 2010. (Page 64.)

[226] J. Song, F.-Y. Kam, R.-Q. Png, W.-L. Seah, J.-M. Zhuo, G.-K. Lim, P. K. H. Ho, and L.-L. Chua, “A general method for transferring graphene onto soft surfaces,” *Nature Nanotechnology*, vol. 8, no. 5, pp. 356–362, Apr. 2013. (Page 66.)

[227] L. H. Hess, M. Jansen, V. Maybeck, M. V. Hauf, M. Seifert, M. Stutzmann, I. D. Sharp, A. Offenhäusser, and J. A. Garrido, “Graphene Transistor Arrays for Recording Action Potentials from Electrogenic Cells,” *Advanced Materials*, vol. 23, no. 43, pp. 5045–5049, Nov. 2011. (Page 66.)

[228] W. Regan, N. Alem, B. Alemán, B. Geng, Ç. Girit, L. Maserati, F. Wang, M. Crommie, and A. Zettl, “A direct transfer of layer-area graphene,” *Applied Physics Letters*, vol. 96, no. 11, p. 113102, Mar. 2010. (Page 66.)

[229] Z. T. Wu, W. W. Zhao, W. Y. Chen, J. Jiang, H. Y. Nan, X. T. Guo, Z. Liang, Y. M. Chen, Y. F. Chen, and Z. H. Ni, “The influence of chemical solvents on the properties of CVD graphene,” *Journal of Raman Spectroscopy*, vol. 46, no. 1, pp. 21–24, Jan. 2015. (Page 66.)

[230] Y. Yu Wang and P. J. Burke, “A large-area and contamination-free graphene transistor for liquid-gated sensing applications,” *Applied Physics Letters*, vol. 103, no. 5, p. 052103, 2013. (Pages 66 and 120.)

[231] Z. Han, “Graphène pour la nanoélectronique : De la croissance CVD jusqu’à la suparconductivité de proximité à deux dimensions,” Thesis, Grenoble, Sep. 2013. (Page 66.)

[232] A. Ambrosi and M. Pumera, “The CVD graphene transfer procedure introduces metallic impurities which alter the graphene electrochemical properties,” *Nanoscale*, vol. 6, no. 1, pp. 472–476, 2014. (Page 66.)

[233] L.-H. Lee and W.-C. Chen, “High Refractive Index Thin Films Prepared from Trialkoxysilane-Capped Poly(methyl methacrylate)-Titania Materials,” *Chemistry of Materials*, vol. 13, no. 3, pp. 1137–1142, Mar. 2001. (Page 67.)

[234] S. K. Varshney, J. P. Hautekeer, R. Fayt, R. Jerome, and P. Teyssie, “Anionic polymerization of (meth)acrylic monomers. 4. Effect of lithium salts as ligands on the "living" polymerization of methyl methacrylate using monofunctional initiators,” *Macromolecules*, vol. 23, no. 10, pp. 2618–2622, May 1990. (Page 67.)

[235] D. W. van Krevelen and K. te Nijenhuis, *Properties of Polymers: Their Correlation with Chemical Structure: Their Numerical Estimation and Prediction from Additive Group Contributions*, 4th ed. Amsterdam: Elsevier, 2009. (Page 68.)

[236] R. Kohli and K. L. Mittal, *Developments in Surface Contamination and Cleaning. Vol. 4, Vol. 4,*. Waltham, MA; Oxford: William Andrew, 2012, oCLC: 1100665383. (Page 68.)

[237] Y.-C. Lin, C.-C. Lu, C.-H. Yeh, C. Jin, K. Suenaga, and P.-W. Chiu, “Graphene Annealing: How Clean Can It Be?” *Nano Letters*, vol. 12, no. 1, pp. 414–419, Jan. 2012. (Pages 73 and 101.)

[238] W. Choi, Y.-S. Seo, J.-Y. Park, K. B. Kim, J. Jung, N. Lee, Y. Seo, and S. Hong, “Effect of Annealing in Ar/H2 Environment on Chemical Vapor Deposition-Grown Graphene Transferred With Poly (Methyl Methacrylate),”

IEEE Transactions on Nanotechnology, vol. 14, no. 1, pp. 70–74, Jan. 2015. (Page 73.)

[239] Z. Cheng, Q. Zhou, C. Wang, Q. Li, C. Wang, and Y. Fang, "Toward Intrinsic Graphene Surfaces: A Systematic Study on Thermal Annealing and Wet-Chemical Treatment of SiO $_2$ -Supported Graphene Devices," *Nano Letters*, vol. 11, no. 2, pp. 767–771, Feb. 2011. (Page 73.)

[240] K. Kumar, Y.-S. Kim, and E.-H. Yang, "The influence of thermal annealing to remove polymeric residue on the electronic doping and morphological characteristics of graphene," *Carbon*, vol. 65, pp. 35–45, Dec. 2013. (Page 73.)

[241] C. W. Jang, J. H. Kim, J. M. Kim, D. H. Shin, S. Kim, and S.-H. Choi, "Rapid-thermal-annealing surface treatment for restoring the intrinsic properties of graphene field-effect transistors," *Nanotechnology*, vol. 24, no. 40, p. 405301, Oct. 2013. (Page 73.)

[242] M. Jang, T. Q. Trung, J.-H. Jung, B.-Y. Kim, and N.-E. Lee, "Improved performance and stability of field-effect transistors with polymeric residue-free graphene channel transferred by gold layer," *Physical Chemistry Chemical Physics*, vol. 16, no. 9, p. 4098, 2014. (Pages 73 and 100.)

[243] X. Wang and H. Dai, "Etching and narrowing of graphene from the edges," *Nature Chemistry*, vol. 2, no. 8, pp. 661–665, Aug. 2010. (Page 73.)

[244] A. Hsu, H. Wang, K. K. Kim, J. Kong, and T. Palacios, "Impact of Graphene Interface Quality on Contact Resistance and RF Device Performance," *IEEE Electron Device Letters*, vol. 32, no. 8, pp. 1008–1010, Aug. 2011. (Page 73.)

[245] C. A. Joiner, T. Roy, Z. R. Hesabi, B. Chakrabarti, and E. M. Vogel, "Cleaning graphene with a titanium sacrificial layer," *Appl. Phys. Lett.*, p. 4, 2014. (Page 73.)

[246] N. C. Wang, E. A. Carrion, M. C. Tung, and E. Pop, "Reducing graphene device variability with yttrium sacrificial layers," *Applied Physics Letters*, vol. 110, no. 22, p. 223106, May 2017. (Page 73.)

[247] T. N. Trung, D.-O. Kim, J.-H. Lee, V.-D. Dao, H.-S. Choi, and E.-T. Kim, "Simple and Reliable Lift-Off Patterning Approach for Graphene and Graphene?Ag Nanowire Hybrid Films," *ACS Applied Materials & Interfaces*, Jun. 2017. (Page 79.)

[248] F. Scholz, *Electroanalytical Methods: Guide to Experiments and Applications.* Springer Berlin, 2002. (Pages 81, 122, and 126.)

[249] M. Calleja, M. Nordström, M. Álvarez, J. Tamayo, L. M. Lechuga, and A. Boisen, "Highly sensitive polymer-based cantilever-sensors for DNA detection," *Ultramicroscopy*, vol. 105, no. 1, pp. 215–222, Nov. 2005. (Page 81.)

[250] R. Marie, S. Schmid, A. Johansson, L. Ejsing, M. Nordström, D. Häfliger, C. B. Christensen, A. Boisen, and M. Dufva, "Immobilisation of DNA to polymerised SU-8 photoresist," *Biosensors and Bioelectronics*, vol. 21, no. 7, pp. 1327–1332, Jan. 2006. (Page 81.)

[251] K. V. Nemani, K. L. Moodie, J. B. Brennick, A. Su, and B. Gimi, "In vitro and in vivo evaluation of SU-8 biocompatibility," *Materials science & engineering. C, Materials for biological applications*, vol. 33, no. 7, Oct. 2013. (Page 81.)

[252] B. F. E. Matarèse, P. L. C. Feyen, A. Falco, F. Benfenati, P. Lugli, and J. C. deMello, "Use of SU8 as a stable and biocompatible adhesion layer for gold bioelectrodes," *Scientific Reports*, vol. 8, no. 1, p. 5560, Apr. 2018. (Page 81.)

[253] P. Abgrall, V. Conedera, H. Camon, A.-M. Gue, and N.-T. Nguyen, "SU-8 as a structural material for labs-on-chips and microelectromechanical systems," *Electrophoresis*, vol. 28, no. 24, pp. 4539–4551, Dec. 2007. (Page 81.)

[254] W. Fu, L. Feng, G. Panaitov, D. Kireev, D. Mayer, A. Offenhäusser, and H.-J. Krause, "Biosensing near the neutrality point of graphene," *Science Advances*, vol. 3, no. 10, p. e1701247, 2017. (Pages 81, 118, and 132.)

[255] F. Veliev, A. Cresti, D. Kalita, A. Bourrier, T. Belloir, Anne Briançon-Marjollet, M. Albrieux, S. Roche, V. Bouchiat, and C. Delacour, "Sensing ion channel in neuron networks with graphene field effect transistors," *2D Materials*, vol. 5, no. 4, p. 045020, 2018. (Page 81.)

[256] S. Keller, G. Blagoi, M. Lillemose, D. Haefliger, and A. Boisen, "Processing of thin SU-8 films," *Journal of Micromechanics and Microengineering*, vol. 18, no. 12, p. 125020, Nov. 2008. (Pages 82 and 86.)

[257] J. D. Williams and W. Wang, "Study on the postbaking process and the effects on UV lithography of high aspect ratio SU-8 microstructures," *Journal of Micro/Nanolithography, MEMS, and MOEMS*, vol. 3, no. 4, pp. 563–569, Oct. 2004. (Page 83.)

[258] J. F. Gaynor and S. B. Desu, "Stress measurement as a new technique for determining glass transition temperatures and other thermomechanical properties of polymers," *Journal of Materials Science Letters*, vol. 13, no. 4, pp. 236–237, Jan. 1994. (Page 83.)

[259] X. Li, R. Zhang, W. Yu, K. Wang, J. Wei, D. Wu, A. Cao, Z. Li, Y. Cheng, Q. Zheng, R. S. Ruoff, and H. Zhu, “Stretchable and highly sensitive graphene-on-polymer strain sensors,” *Scientific Reports*, vol. 2, no. 1, p. 870, Dec. 2012. (Page 83.)

[260] F. C. Nix and D. MacNair, “The Thermal Expansion of Pure Metals: Copper, Gold, Aluminum, Nickel, and Iron,” *Physical Review*, vol. 60, no. 8, pp. 597–605, Oct. 1941. (Page 85.)

[261] G. A. Lager, J. D. Jorgensen, and F. J. Rotella, “Crystal structure and thermal expansion of *A*-quartz SiO2 at low temperatures,” *Journal of Applied Physics*, vol. 53, no. 10, pp. 6751–6756, Oct. 1982. (Page 85.)

[262] D. Yoon, Y.-W. Son, and H. Cheong, “Negative Thermal Expansion Coefficient of Graphene Measured by Raman Spectroscopy,” *Nano Letters*, vol. 11, no. 8, pp. 3227–3231, Aug. 2011. (Page 85.)

[263] “SU-8 2000 datasheet,” http://www.microchem.com/pdf/SU-82000DataSheet2000_5thru2015Ver4.pdf, Jul. 2019. (Page 85.)

[264] T. Tasaki, T.-F. M. Chang, C. Ishiyama, and M. Sone, “Study on delamination mechanism of SU-8 micropillars on a Si-substrate under bend loading by Weibull analysis,” *Microelectronic Engineering*, vol. 88, no. 8, pp. 2132–2134, Aug. 2011. (Page 86.)

[265] Sang Jeen Hong, Seungkeun Choi, Yoonsu Choi, M. Allen, and G. S. May, “Characterization of low-temperature SU-8 photoresist processing for MEMS applications,” in *2004 IEEE/SEMI Advanced Semiconductor Manufacturing Conference and Workshop (IEEE Cat. No.04CH37530)*, May 2004, pp. 404–408. (Page 86.)

[266] “OMNICOAT datasheet,” http://microchem.com/pdf/OMNICOAT.pdf, Sep. 2018. (Page 86.)

[267] H. Darmstadt and C. Roy, “Surface spectroscopic study of basic sites on carbon blacks,” *Carbon*, vol. 41, no. 13, pp. 2662–2665, 2003. (Page 100.)

[268] K. A. Wepasnick, B. A. Smith, J. L. Bitter, and D. Howard Fairbrother, “Chemical and structural characterization of carbon nanotube surfaces,” *Analytical and Bioanalytical Chemistry*, vol. 396, no. 3, pp. 1003–1014, Feb. 2010. (Page 100.)

[269] H. Ago, T. Kugler, F. Cacialli, W. R. Salaneck, M. S. P. Shaffer, A. H. Windle, and R. H. Friend, “Work Functions and Surface Functional Groups of Multiwall Carbon Nanotubes,” *The Journal of Physical Chemistry B*, vol. 103, no. 38, pp. 8116–8121, Sep. 1999. (Page 100.)

[270] J. Penuelas, A. Ouerghi, D. Lucot, C. David, J. Gierak, H. Estrade-Szwarckopf, and C. Andreazza-Vignolle, “Surface morphology and characterization of thin graphene films on SiC vicinal substrate,” *Physical Review B*, vol. 79, no. 3, p. 033408, Jan. 2009. (Page 100.)

[271] K. V. Emtsev, F. Speck, T. Seyller, L. Ley, and J. D. Riley, “Interaction, growth, and ordering of epitaxial graphene on SiC{0001} surfaces: A comparative photoelectron spectroscopy study,” *Physical Review B*, vol. 77, no. 15, p. 155303, Apr. 2008. (Page 100.)

[272] G. Cunge, D. Ferrah, C. Petit-Etienne, A. Davydova, H. Okuno, D. Kalita, V. Bouchiat, and O. Renault, “Dry efficient cleaning of poly-methyl-methacrylate residues from graphene with high-density H2 and H2-N2 plasmas,” *Journal of Applied Physics*, vol. 118, no. 12, p. 123302, Sep. 2015. (Pages 100, 101, and 171.)

[273] D. Ferrah, O. Renault, C. Petit-Etienne, H. Okuno, C. Berne, V. Bouchiat, and G. Cunge, “XPS investigations of graphene surface cleaning using H $_2$ - and Cl $_2$ -based inductively coupled plasma: XPS investigations of graphene surface dry-cleaning,” *Surface and Interface Analysis*, vol. 48, no. 7, pp. 451–455, Jul. 2016. (Pages 100 and 171.)

[274] A. Pirkle, J. Chan, A. Venugopal, D. Hinojos, C. W. Magnuson, S. McDonnell, L. Colombo, E. M. Vogel, R. S. Ruoff, and R. M. Wallace, “The effect of chemical residues on the physical and electrical properties of chemical vapor deposited graphene transferred to SiO2,” *Applied Physics Letters*, vol. 99, no. 12, p. 122108, 2011. (Pages 100, 101, and 118.)

[275] G. Beamson, A. Bunn, and D. Briggs, “High-resolution monochromated XPS of poly(methyl methacrylate) thin films on a conducting substrate,” *Surface and Interface Analysis*, vol. 17, no. 2, pp. 105–115, 1991. (Page 100.)

[276] S. Kaya, P. Rajan, H. Dasari, D. C. Ingram, W. Jadwisienczak, and F. Rahman, “A Systematic Study of Plasma Activation of Silicon Surfaces for Self Assembly,” *ACS Applied Materials & Interfaces*, vol. 7, no. 45, pp. 25 024–25 031, Nov. 2015. (Page 101.)

[277] Y. Ahn, J. Kim, S. Ganorkar, Y.-H. Kim, and S.-I. Kim, “Thermal annealing of graphene to remove polymer residues,” *Materials Express*, vol. 6, no. 1, pp. 69–76, Feb. 2016. (Page 101.)

[278] N. Peltekis, S. Kumar, N. McEvoy, K. Lee, A. Weidlich, and G. S. Duesberg, “The effect of downstream plasma treatments on graphene surfaces,” *Carbon*, vol. 50, no. 2, pp. 395–403, Feb. 2012. (Page 101.)

[279] K. S. Kim, H.-K. Hong, H. Jung, I.-K. Oh, Z. Lee, H. Kim, G. Y. Yeom, and K. N. Kim, “Surface treatment process applicable to next generation graphene-based electronics,” *Carbon*, vol. 104, pp. 119–124, Aug. 2016. (Page 101.)

[280] H. J. Hwang, Y. Lee, C. Cho, and B. H. Lee, “Facile process to clean PMMA residue on graphene using KrF laser annealing,” *AIP Advances*, vol. 8, no. 10, p. 105326, Oct. 2018. (Page 101.)

[281] J. D. Andrade, *Surface and Interfacial Aspects of Biomedical Polymers: Volume 1 Surface Chemistry and Physics.* Boston, MA: Springer US, 1985. (Page 106.)

[282] F. Walther, P. Davydovskaya, S. Zürcher, M. Kaiser, H. Herberg, A. M. Gigler, and R. W. Stark, “Stability of the hydrophilic behavior of oxygen plasma activated SU-8,” *Journal of Micromechanics and Microengineering*, vol. 17, no. 3, pp. 524–531, Feb. 2007. (Page 106.)

[283] S. Ashraf, C. G. Mattsson, M. Fondell, A. Lindblad, and G. Thungström, “Surface modification of SU-8 for metal/SU-8 adhesion using RF plasma treatment for application in thermopile detectors,” *Materials Research Express*, vol. 2, no. 8, p. 086501, Aug. 2015. (Page 106.)

[284] T. M. G. Mohiuddin, A. Lombardo, R. R. Nair, A. Bonetti, G. Savini, R. Jalil, N. Bonini, D. M. Basko, C. Galiotis, N. Marzari, K. S. Novoselov, A. K. Geim, and A. C. Ferrari, “Uniaxial Strain in Graphene by Raman Spectroscopy: G peak splitting, Gruneisen Parameters and Sample Orientation,” *Physical Review B*, vol. 79, no. 20, p. 205433, May 2009. (Page 107.)

[285] J. E. Lee, G. Ahn, J. Shim, Y. S. Lee, and S. Ryu, “Optical separation of mechanical strain from charge doping in graphene,” *Nature Communications*, vol. 3, p. 1024, Aug. 2012. (Pages 107, 112, and 113.)

[286] A. Das, S. Pisana, B. Chakraborty, S. Piscanec, S. K. Saha, U. V. Waghmare, K. S. Novoselov, H. R. Krishnamurthy, A. K. Geim, A. C. Ferrari, and A. K.

Sood, “Monitoring dopants by Raman scattering in an electrochemically top-gated graphene transistor,” *Nature Nanotechnology*, vol. 3, no. 4, pp. 210–215, Apr. 2008. (Pages 107, 108, and 112.)

[287] C. Casiraghi, S. Pisana, K. S. Novoselov, A. K. Geim, and A. C. Ferrari, “Raman fingerprint of charged impurities in graphene,” *Applied Physics Letters*, vol. 91, no. 23, p. 233108, 2007. (Page 107.)

[288] I. Calizo, A. A. Balandin, W. Bao, F. Miao, and C. N. Lau, “Temperature Dependence of the Raman Spectra of Graphene and Graphene Multilayers,” *Nano Letters*, vol. 7, no. 9, pp. 2645–2649, Sep. 2007. (Pages 107 and 112.)

[289] D. Yoon, Y.-W. Son, and H. Cheong, “Strain-Dependent Splitting of the Double-Resonance Raman Scattering Band in Graphene,” *Physical Review Letters*, vol. 106, no. 15, p. 155502, Apr. 2011. (Page 107.)

[290] I. Calizo, F. Miao, W. Bao, C. N. Lau, and A. A. Balandin, “Variable temperature Raman microscopy as a nanometrology tool for graphene layers and graphene-based devices,” *Applied Physics Letters*, vol. 91, no. 7, p. 071913, Aug. 2007. (Page 107.)

[291] A. Eckmann, A. Felten, A. Mishchenko, L. Britnell, R. Krupke, K. S. Novoselov, and C. Casiraghi, “Probing the Nature of Defects in Graphene by Raman Spectroscopy,” *Nano Letters*, vol. 12, no. 8, pp. 3925–3930, Aug. 2012. (Page 107.)

[292] W. Su and D. Roy, “Visualizing graphene edges using tip-enhanced Raman spectroscopy,” *Journal of Vacuum Science & Technology B*, vol. 31, no. 4, p. 041808, Jul. 2013. (Page 107.)

[293] D. Graf, F. Molitor, K. Ensslin, C. Stampfer, A. Jungen, C. Hierold, and L. Wirtz, “Spatially Resolved Raman Spectroscopy of Single- and Few-Layer Graphene,” *Nano Letters*, vol. 7, no. 2, pp. 238–242, Feb. 2007. (Page 108.)

[294] S. D. Costa, A. Righi, C. Fantini, Y. Hao, C. Magnuson, L. Colombo, R. S. Ruoff, and M. A. Pimenta, “Resonant Raman spectroscopy of graphene grown on copper substrates,” *Solid State Communications*, vol. 152, no. 15, pp. 1317–1320, Aug. 2012. (Page 108.)

[295] C. Neumann, S. Reichardt, P. Venezuela, M. Drögeler, L. Banszerus, M. Schmitz, K. Watanabe, T. Taniguchi, F. Mauri, B. Beschoten, S. V. Rotkin, and C. Stampfer, “Raman spectroscopy as probe of nanometre-scale strain variations in graphene,” *Nature Communications*, vol. 6, no. 1, p. 8429, Dec. 2015. (Page 112.)

[296] M. B. B. S. Larsen, D. M. A. Mackenzie, J. M. Caridad, P. Bøggild, and T. J. Booth, “Transfer induced compressive strain in graphene: Evidence from Raman spectroscopic mapping,” *Microelectronic Engineering*, vol. 121, pp. 113–117, Jun. 2014. (Page 112.)

[297] N. S. Mueller, S. Heeg, M. P. Alvarez, P. Kusch, S. Wasserroth, N. Clark, Fredrik Schedin, J. Parthenios, K. Papagelis, C. Galiotis, M. Kalbáč, Aravind Vijayaraghavan, U. Huebner, R. Gorbachev, O. Frank, and S. Reich, “Evaluating arbitrary strain configurations and doping in graphene with Raman spectroscopy,” *2D Materials*, vol. 5, no. 1, p. 015016, 2018. (Page 112.)

[298] S. Ryu, L. Liu, S. Berciaud, Y.-J. Yu, H. Liu, P. Kim, G. W. Flynn, and L. E. Brus, “Atmospheric Oxygen Binding and Hole Doping in Deformed Graphene on a SiO $_2$ Substrate,” *Nano Letters*, vol. 10, no. 12, pp. 4944–4951, Dec. 2010. (Page 113.)

[299] S. Goniszewski, M. Adabi, O. Shaforost, S. M. Hanham, L. Hao, and N. Klein, “Correlation of p-doping in CVD Graphene with Substrate Surface Charges,” *Scientific Reports*, vol. 6, no. 1, p. 22858, Mar. 2016. (Pages 113 and 118.)

[300] S. D. Costa, J. Ek Weis, O. Frank, M. Fridrichová, and M. Kalbac, “Monitoring the doping of graphene on SiO 2 /Si substrates during the thermal annealing process,” *RSC Advances*, vol. 6, no. 76, pp. 72 859–72 864, 2016. (Page 113.)

[301] H. Al-Mumen, L. Dong, and W. Li, “SU-8 doped and encapsulated n-type graphene nanomesh with high air stability,” *Applied Physics Letters*, vol. 103, no. 23, p. 232113, Dec. 2013. (Page 113.)

[302] Y. Shi, X. Dong, P. Chen, J. Wang, and L.-J. Li, “Effective doping of single-layer graphene from underlying SiO 2 substrates,” *Physical Review B*, vol. 79, no. 11, p. 115402, Mar. 2009. (Page 118.)

[303] R. A. Nistor, M. A. Kuroda, A. A. Maarouf, and G. J. Martyna, “Doping of adsorbed graphene from defects and impurities in SiO 2 substrates,” *Physical Review B*, vol. 86, no. 4, p. 041409, Jul. 2012. (Page 118.)

[304] L. H. Hess, M. V. Hauf, M. Seifert, F. Speck, T. Seyller, M. Stutzmann, I. D. Sharp, and J. A. Garrido, “High-transconductance graphene solution-gated field effect transistors,” *Applied Physics Letters*, vol. 99, no. 3, p. 033503, 2011. (Pages 118 and 123.)

[305] J. D. Buron, F. Pizzocchero, P. U. Jepsen, D. H. Petersen, J. M. Caridad, B. S. Jessen, T. J. Booth, and P. Bøggild, “Graphene mobility mapping,” *Scientific Reports*, vol. 5, p. 12305, Jul. 2015. (Page 118.)

[306] H. S. Song, S. L. Li, H. Miyazaki, S. Sato, K. Hayashi, A. Yamada, N. Yokoyama, and K. Tsukagoshi, “Origin of the relatively low transport mobility of graphene grown through chemical vapor deposition,” *Scientific Reports*, vol. 2, no. 1, p. 337, Dec. 2012. (Page 118.)

[307] R. Ma, Q. Huan, L. Wu, J. Yan, W. Guo, Y.-Y. Zhang, S. Wang, L. Bao, Y. Liu, S. Du, S. T. Pantelides, and H.-J. Gao, “Direct Four-Probe Measurement of Grain-Boundary Resistivity and Mobility in Millimeter-Sized Graphene,” *Nano Letters*, Aug. 2017. (Page 118.)

[308] K. Nagashio and A. Toriumi, “DOS-Limited Contact Resistance in Graphene FETs,” *arXiv*, p. 9, Apr. 2011. (Page 119.)

[309] T. Cusati, G. Fiori, A. Gahoi, V. Passi, M. C. Lemme, A. Fortunelli, and G. Iannaccone, “Electrical properties of graphene-metal contacts,” *Scientific Reports*, vol. 7, no. 1, p. 5109, Dec. 2017. (Page 119.)

[310] P. K. Ang, M. Jaiswal, C. H. Y. X. Lim, Y. Wang, J. Sankaran, A. Li, C. T. Lim, T. Wohland, Ö. Barbaros, and K. P. Loh, “A Bioelectronic Platform Using a Graphene-Lipid Bilayer Interface,” *ACS Nano*, vol. 4, no. 12, pp. 7387–7394, Dec. 2010. (Page 120.)

[311] H. Wang, Y. Wu, C. Cong, J. Shang, and T. Yu, “Hysteresis of electronic transport in graphene transistors,” *ACS nano*, vol. 4, no. 12, pp. 7221–7228, 2010. (Page 125.)

[312] B. K. Bharadwaj, H. Chandrasekar, D. Nath, R. Pratap, and S. Raghavan, “Intrinsic limits of channel transport hysteresis in graphene-SiO 2 interface and its dependence on graphene defect density,” *Journal of Physics D: Applied Physics*, vol. 49, no. 26, p. 265301, 2016. (Page 125.)

[313] L. Shahriary and A. Athawale, “Graphene oxide synthesized by using modified Hummers approach,” *Renew. Energy Environ. Eng.*, vol. 2, Jan. 2014. (Page 127.)

[314] S. Falina, M. Syamsul, Y. Iyama, M. Hasegawa, Y. Koga, and H. Kawarada, “Carboxyl-functionalized graphene SGFET: pH sensing mechanism and reliability of anodization,” *Diamond and Related Materials*, vol. 91, pp. 15–21, Jan. 2019. (Page 128.)

[315] S. S. Kwon, J. Choi, M. Heiranian, Y. Kim, W. J. Chang, P. M. Knapp, M. C. Wang, J. M. Kim, N. R. Aluru, W. I. Park, and S. Nam, “Electrical Double Layer of Supported Atomically Thin Materials,” *Nano Letters*, vol. 19, no. 7, pp. 4588–4593, Jul. 2019. (Page 132.)

[316] D. Kireev, I. Zadorozhnyi, T. Qiu, D. Sarik, F. Brings, T. Wu, S. Seyock, V. Maybeck, M. Lottner, B. M. Blaschke, J. Garrido, X. Xie, S. Vitusevich, B. Wolfrum, and A. Offenhäusser, “Graphene Field-Effect Transistors for In Vitro and Ex Vivo Recordings,” *IEEE Transactions on Nanotechnology*, vol. 16, no. 1, pp. 140–147, Jan. 2017. (Page 132.)

[317] W. Fu, C. Nef, A. Tarasov, M. Wipf, R. Stoop, O. Knopfmacher, M. Weiss, M. Calame, and C. Schönenberger, “High mobility graphene ion-sensitive field-effect transistors by noncovalent functionalization,” *Nanoscale*, vol. 5, no. 24, p. 12104, 2013. (Page 132.)

[318] M. A. Brown, M. S. Crosser, M. R. Leyden, Y. Qi, and E. D. Minot, “Measurement of high carrier mobility in graphene in an aqueous electrolyte environment,” *Applied Physics Letters*, vol. 109, no. 9, p. 093104, Aug. 2016. (Page 132.)

[319] G. Bepete, E. Anglaret, L. Ortolani, V. Morandi, K. Huang, A. Pénicaud, and C. Drummond, “Surfactant-free single-layer graphene in water,” *Nature Chemistry*, vol. 9, no. 4, pp. 347–352, Apr. 2017. (Page 133.)

[320] D. Li, M. B. Müller, S. Gilje, R. B. Kaner, and G. G. Wallace, “Processable aqueous dispersions of graphene nanosheets,” *Nature Nanotechnology*, vol. 3, no. 2, pp. 101–105, Feb. 2008. (Page 133.)

[321] D. Lee, G. Ahn, and S. Ryu, “Two-Dimensional Water Diffusion at a Graphene–Silica Interface,” *Journal of the American Chemical Society*, vol. 136, no. 18, pp. 6634–6642, May 2014. (Page 136.)

[322] S.-K. Hu, F.-Y. Lo, C.-C. Hsieh, and L. Chao, “Sensing Ability and Formation Criterion of Fluid Supported Lipid Bilayer Coated Graphene Field-Effect Transistors,” *ACS Sensors*, Feb. 2019. (Page 136.)

[323] U.-T. Chiu, B.-F. Lee, S.-K. Hu, T.-F. Yu, W.-Y. Lee, and L. Chao, “Graphene Memory Based on a Tunable Nanometer-Thin Water Layer,” *The Journal of Physical Chemistry C*, vol. 123, no. 17, pp. 10 842–10 848, May 2019. (Page 136.)

[324] Z. Xiao, Q. Wan, and C. Durkan, “Cleaning Transferred Graphene for Optimization of Device Performance,” *Advanced Materials Interfaces*, p. 1801794, Apr. 2019. (Page 137.)

[325] M. H. Lee, B. J. Kim, K. H. Lee, I.-S. Shin, W. Huh, J. H. Cho, and M. S. Kang, “Apparent pH sensitivity of solution-gated graphene transistors,” *Nanoscale*, vol. 7, no. 17, pp. 7540–7544, 2015. (Page 137.)

[326] L. Zuccaro, J. Krieg, A. Desideri, K. Kern, and K. Balasubramanian, "Tuning the isoelectric point of graphene by electrochemical functionalization," *Scientific Reports*, vol. 5, p. 11794, Jul. 2015. (Page 137.)

[327] B. Dominy, D. Perl, F. Schmid, and C. Brooks, "The Effects of Ionic Strength on Protein Stability: The Cold Shock Protein Family," *Journal of molecular biology*, vol. 319, pp. 541–54, Jun. 2002. (Page 138.)

[328] M. Dufrechou, C. Poncet-Legrand, F.-X. Sauvage, and A. Vernhet, "Stability of White Wine Proteins: Combined Effect of pH, Ionic Strength, and Temperature on Their Aggregation," *Journal of Agricultural and Food Chemistry*, vol. 60, no. 5, pp. 1308–1319, Feb. 2012. (Page 138.)

[329] E. Sahin, A. O. Grillo, M. D. Perkins, and C. J. Roberts, "Comparative Effects of pH and Ionic Strength on Protein–Protein Interactions, Unfolding, and Aggregation for IgG1 Antibodies," *Journal of Pharmaceutical Sciences*, vol. 99, no. 12, pp. 4830–4848, Dec. 2010. (Page 138.)

[330] T. Wang, O. S. Kumru, L. Yi, Y. J. Wang, J. Zhang, J. H. Kim, S. B. Joshi, C. R. Middaugh, and D. B. Volkin, "Effect of ionic strength and pH on the physical and chemical stability of a monoclonal antibody antigen-binding fragment," *Journal of Pharmaceutical Sciences*, vol. 102, no. 8, pp. 2520–2537, 2013. (Page 138.)

[331] J. Zhang, "Protein-Protein Interactions in Salt Solutions," in *Protein-Protein Interactions - Computational and Experimental Tools*, W. Cai, Ed. InTech, Mar. 2012. (Page 138.)

[332] E. Stern, R. Wagner, F. J. Sigworth, R. Breaker, T. M. Fahmy, and M. A. Reed, "Importance of the Debye Screening Length on Nanowire Field Effect Transistor Sensors," *Nano Letters*, vol. 7, no. 11, pp. 3405–3409, Nov. 2007. (Page 142.)

[333] J. Sun and Y. Liu, "Matrix Effect Study and Immunoassay Detection Using Electrolyte-Gated Graphene Biosensor," *Micromachines*, vol. 9, no. 4, p. 142, Mar. 2018. (Page 142.)

[334] O. H. Laitinen, V. P. Hytönen, H. R. Nordlund, and M. S. Kulomaa, "Genetically engineered avidins and streptavidins," *Cellular and Molecular Life Sciences*, vol. 63, no. 24, pp. 2992–3017, Dec. 2006. (Page 142.)

[335] F. Liu, J. Z. H. Zhang, and Y. Mei, "The origin of the cooperativity in the streptavidin-biotin system: A computational investigation through molecular

dynamics simulations," *Scientific Reports*, vol. 6, no. 1, pp. 1–11, Jun. 2016. (Page 142.)

[336] I. Konstantinov, "Antibody Immunoglobulin G (IgG) — scientific illustration," https://www.visual-science.com/projects/antibody-immunoglobulin-G/illustration/, Nov. 2019. (Page 143.)

[337] X. Duan, Y. Li, N. K. Rajan, D. A. Routenberg, Y. Modis, and M. A. Reed, "Quantification of the affinities and kinetics of protein interactions using silicon nanowire biosensors," *Nature nanotechnology*, vol. 7, no. 6, pp. 401–407, May 2012. (Page 143.)

[338] Y. Liu, L. Yuan, M. Yang, Y. Zheng, L. Li, L. Gao, N. Nerngchamnong, C. T. Nai, C. S. S. Sangeeth, Y. P. Feng, C. A. Nijhuis, and K. P. Loh, "Giant enhancement in vertical conductivity of stacked CVD graphene sheets by self-assembled molecular layers," *Nature Communications*, vol. 5, p. 5461, Nov. 2014. (Page 147.)

[339] N. Gao, T. Gao, X. Yang, X. Dai, W. Zhou, A. Zhang, and C. M. Lieber, "Specific detection of biomolecules in physiological solutions using graphene transistor biosensors," *Proceedings of the National Academy of Sciences*, vol. 113, no. 51, pp. 14 633–14 638, Dec. 2016. (Pages 147 and 148.)

[340] Y. Ohno, S. Okamoto, K. Maehashi, and K. Matsumoto, "Direct Electrical Detection of DNA Hybridization Based on Electrolyte-Gated Graphene Field-Effect Transistor," *Japanese Journal of Applied Physics*, vol. 52, no. 11R, p. 110107, Oct. 2013. (Page 147.)

[341] A. Star, J.-C. P. Gabriel, K. Bradley, and G. Grüner, "Electronic Detection of Specific Protein Binding Using Nanotube FET Devices," *Nano Letters*, vol. 3, no. 4, pp. 459–463, Apr. 2003. (Page 152.)

[342] H. Shinotsuka, S. Tanuma, C. J. Powell, and D. R. Penn, "Calculations of electron inelastic mean free paths. X. Data for 41 elemental solids over the 50 eV to 200 keV range with the relativistic full Penn algorithm," *Surface and Interface Analysis*, vol. 47, Oct. 2015. (Page 171.)

[343] R. J. Beynon and J. S. Easterby, *Buffer Solutions*, ser. The Basics. Oxford ; New York: IRL Press at Oxford University Press, 1996. (Pages 175 and 176.)

Résumé

Avec l'augmentation du nombre de cancers et des maladies infectieuses et cardiovasculaires, la détection précoce et/ou en temps réel des biomarqueurs associés est particulièrement cruciale afin de permettre un diagnostic et un traitement efficace. Compte tenu du vieillissement de la population mondiale, et de la nécessité de perfectionnement des services médicaux dans les pays émergents comme l'Inde ou la Chine, la demande de dispositifs de diagnostic médical représente un domaine d'application majeur pour les capteurs biologiques.

Les transistors à grille liquide à base de graphène (SGFET) représentent une génération de biocapteurs très prometteuse, dans la lignée des biocapteurs à haute sensibilité s'appuyant sur les propriétés exceptionnelles des nanofils et nanotubes de carbone. Transformer un dispositif SGFET en biocapteur nécessite d'immobiliser des biorécepteurs à la surface du graphène. Les techniques de fonctionnalisation non covalente sont les plus efficaces, car elles permettent de préserver à la fois l'intégrité structurelle et les propriétés électriques du graphène. Dans cette perspective, le PBASE est largement utilisé, puisque cette molécule peut s'adsorber sur le graphène par des interactions π-π, tout en exposant un groupement chimique réactif servant d'ancrage pour le greffage de récepteurs biologiques. Cependant, il n'est pas systématiquement démontré que les biorécepteurs restent fonctionnels lorsqu'ils sont greffés au PBASE, car cette molécule est incapable d'empêcher les biorécepteurs de s'adsorber sur le graphène et d'être par conséquent dénaturés. Le "tripod" est une molécule se liant de manière multivalente au graphène grâce à trois pieds en pyrène, projetant efficacement toute fonctionnalité active loin de la surface, et formant une couche de reconnaissance biologique prévisible et robuste sur le graphène.

Dans ce contexte, ces travaux de thèse ont visé à développer un SGFET à base de graphène fonctionnalisé avec le tripod pour des applications de détection biologique très robustes, fiables et sensibles. Différentes méthodes ont été explorées afin d'établir un procédé de fabrication stable et reproductible. Ce procédé a notamment été caractérisé par un ensemble de mesures AFM, XPS et Raman. La performance des dispositifs fabriqués a été évaluée avant la fonctionnalisation non covalente par des mesures électriques sous air et en milieu liquide, et une première preuve du concept de détection de la streptavidine a été présentée.

Abstract

With the rise of cancers, infectious and cardiovascular diseases, the early and/or real-time robust detection of the associated biomarkers is particularly crucial for establishing a diagnosis and an efficient treatment. Considering a worldwide ageing population and the growing need for an improved healthcare in emerging countries such as India or China, the demand for point-of-care diagnostics represents a major field of applications for biosensors.

Graphene-based solution-gated field-effect-transistors (SGFET) represent a highly promising generation of biosensors, in line with the superior sensitivity of biosensors benefiting from the exceptional properties of nanowires and carbon nanotubes. Transforming a SGFET device into a biosensor requires to immobilize bioreceptors at the graphene surface. The non-covalent functionalization is the most efficient technique, since it can preserve both graphene structural integrity and electrical properties. In this perspective, PBASE is widely used, since this molecule can adsorb onto graphene by π-π interactions, while exposing a reactive moiety serving as an anchor for grafting biological receptors. However, it is not systematically demonstrated that bioreceptors remains functional when grafted to PBASE, since this molecule lacks the ability to prevent bioreceptors from stacking onto graphene and consequently being denaturated. The "tripod" is a molecule binding multivalently to graphene thanks to three pyrene feet, effectively projecting any active functionality away from the surface, and forming a predictable and robust biorecognition layer on graphene.

In this context, this thesis work aimed at developing a tripod functionalized graphene-based SGFET for highly robust, reliable and sensitive biosensing applications. Different methods were explored in order to establish a stable and reproducible fabrication process. In particular, this process was characterized through a set of AFM, XPS and Raman measurements. The performance of the as-fabricated devices was assessed before non-covalent functionalization, through electrical measurements in air and in liquid environments, and a first proof of concept of streptavidin detection was presented.